Novel Antenna Beamsteering for Wireless Applications

João Ricardo Vitorino Reis

Faculty of Computing, Engineering & Science
University of South Wales

This thesis is submitted for the degree of
Doctor of Philosophy

December 2018

Novel Antenna Beamsteering for Wireless Applications

João Ricardo Vitorino Reis, Faculty of Computing, Engineering & Science
University of South Wales

Director of Studies: Nigel Copner[1]

Supervision team: Akram Hammoudeh[1]
Zaid Al-Daher[1]
Rafael Caldeirinha[1,2]
Telmo Fernandes[1,2]

[1]Faculty of Computing, Engineering & Science, University of South Wales (USW), Pontypridd, Wales, United Kingdom

[2]Instituto de Telecomunicações (IT), Delegação de Leiria and Instituto Politécnico de Leiria (IPL), Leiria, Portugal

Summary

This thesis highlights the research carried out on novel antenna beam steering techniques for wireless applications. This work is part of a research program registered at the University of South Wales submitted in partly fulfilment of transferring registration to that of the degree of Doctor of Philosophy and in collaboration with Instituto de Telecomunicações in Leiria, Portugal.

This page is intentionally left blank.

Certificate of Research

This is to certify that, except where specific reference is made, the work described in this thesis is the result of the candidate. Neither this thesis, nor any part of it, has been presented, or is currently submitted, in candidature for any degree at any other University.

(João Ricardo Vitorino Reis)

December 2018

This page is intentionally left blank.

This thesis is dedicated to my parents, sister and girlfriend.

This page is intentionally left blank.

Acknowledgements

I would like to start by expressing my gratitude to all the members of my supervision team, Doctors Nigel Copner, Akram Hammoudeh, Zaid Al-Daher, Rafael Caldeirinha and Telmo Fernandes, for their continuous advice, enthusiastic support and many fruitful discussions during these years of study and scientific research.

In particular, I would like to address a word to Doctors R. Caldeirinha and T. Fernandes that introduce me in the first place to University of South Wales and who were the igniters to this successful collaboration. Thanks for their constant encouragement, guidance and most of all for their support that went way beyond the academic life. A special thanks to Dr. Akram Hammoudeh for his support and continuous stimulation, his energy was contagious.

To Rodolfo Gomes, my cousin and my colleague in this journey, I would like to send a very special regard and thank all the good and bad moments that we went through together and for always being there when I most needed.

I would like to acknowledge the University of South Wales for providing me the facilities, financial support and a grant which allowed me to carry out my research work with the necessary peace of mind. I would also like to acknowledge Instituto de Telecomunicações - Leiria and Instituto Politécnico de Leiria for providing me all material and facilities when working in Portugal and for hosting me since 2016 to date, and in particular, to projects *E-beaming (UID/EEA/50008/2013)* and *RETIOT (SAICT-45-2015-03 / Projeto nº 16432)* for funding my latest developments.

To the people who worked in the Wireless and Optoelectronic Research and Innovation Centre during my stay, in particular Mr. A. Alfadreek, Mr. M. Abdurahman, Mr. A. Buba, Dr. Y. Gong, Dr. J. Huang and Dr. K. Li, I would like to thank the friendly environment and their sympathy. Particular thanks to Dr. Jurgen Ritcher and Mr. John Williams for the many chats and technical discussion we had. I also thank my colleagues from Instituto Politécnico de Leiria, David Ferreira and Nuno Leonor for their help and support and to the technician Marco Santos who always helped me with the hardware related issues.

My very special thanks goes to my parents and sister that were the first to push me to this journey, having always believed in me and supported all my decision. I owe them much more than I could ever write in this paragraph. Finally, to my love Marisa for the unconditional support, encouragement and simply for having waited for me all the years I was far from her.

This page is intentionally left blank.

Abstract

This thesis presents the author's work on the design and development of novel antenna capable of electronic beamsteering[1] for various wireless applications. Such antennas aim to change the direction of their radiation patterns and directivities, electronically and dynamically, in a fast and efficient manner without the need of mechanical aid.

In particular, Metamaterials (MM) and, more specifically, Frequency Selective Surfaces (FSS), are introduced as base materials on novel beamsteering antenna designs. When these are structured as a transmitarray, *i.e.* a structure positioned in the near-field of a directive radiating element, such "artificial" materials allow to control the direction of the propagating electromagnetic wave providing the desired beamsteering capability.

The innovative work developed in this Ph.D. yielded to the fabrication of two FSS-inspired transmitarray antenna prototypes with Two-Dimensional (2D) beamsteering capability using a single Radio Frequency (RF) front-end. Following mathematical workout and proper model validation using a full-wave electromagnetic simulator, the transmitarrays have experimentally been characterised in terms of their beamsteering capability and finally tested under several real-case scenarios.

The use transmitarrays in novel antenna beamsteering is attractive to many wireless applications, specially in the scope of the 5^{th} Generation (of mobile network) (5G) and novel hybrid transmission schemes such as Spatial Diversity (SD) and Multiple-input Multiple-output (MIMO) with beamsteering. The reduction of the RF fronted burden associated to the use of a single radiation element, instead of many elements as used in other beamsteering techniques, the reduced implementation costs and the compact and light weight form factors, opens a new window for the deployment of transmitarray antennas in several top-notch wireless applications. This is considered to be a leap contribution to the antennas' community with practical relevance to emerging industries in this field.

[1] Also spelled as *"beam steering"*.

This page is intentionally left blank.

List of acronyms and abbreviations

1D	One-Dimensional
2D	Two-Dimensional
3D	Three-Dimensional
5G	5^{th} Generation (of mobile network)
ADC	Analogue-to-digital Converter
AF	Array Factor
AMC	Artificial Magnetic Conductor
AR	Axial Ratio
ASIC	Application Specific Integrated Circuit
AWGN	Additive White Gaussian Noise
Az	Azimuth
BER	Bit Error Rate
BsC	Beamsteering Controller
BST	Barium-Strontium-Titanate
BW	Bandwidth
CST	Computer Simulation Technology
D2D	Device-to-device
DAC	Digital-to-analogue Converter
DC	Direct Current
DOA	Direction-of-arrival
DSP	Digital Signal Processor
DUT	Device Under Test
EBG	Electromagnetic Band Gap
EC	Equivalent Circuit
EIRP	Effective Isotropic Radiated Power
El	Elevation
EM	Electromagnetic
eRT	Electronically Reconfigurable Transmitarray

EVM	Error Vector Magnitude
E-field	Electric-field
FPGA	Field Programmable Gate Array
FSL	Free-space Loss
FSS	Frequency Selective Surfaces
GPIB	General Purpose Interface Bus
GUI	Graphical User Interface
HIS	High Impedance Surface
HPBW	Half Power Beamwidth
H-field	Magnetic-field
IC	Integrated Circuit
IEEE	Institute of Electrical and Electronics Engineers
IoT	Internet-of-Things
IPL	Instituto Politécnico de Leiria
IT	Instituto de Telecomunicações
LC	Liquid Crystal
LHCP	Left-hand Circular Polarisation
LNA	Low Noise Amplifier
LOS	Line-of-sight
LTCC	Low Temperature Co-fired Ceramic
LTE	Long Term Evolution
M2M	Machine-to-machine
MEMS	Micro Electromechanical Systems
MIMO	Multiple-input Multiple-output
MM	Metamaterials
MU	Multi-user
MWS	Microwave Studio
NRI	Negative Refractive Index
OFDM	Orthogonal Frequency Division Multiplexing
OpAmp	Operational Amplifier
PA	Power Amplifier
PC	Personal Computer
PCB	Printed Circuit Board
PD	Power Driver
PIN	p-i-n junction diode

PTFE	Polytetrafluoroethylene
QAM	Quadrature Amplitude Modulation
QPSK	Quadrature Phase-shift Keying
RADAR	Radio Detection And Ranging
RF	Radio Frequency
RHCP	Right-hand Circular Polarisation
Rx	Receiver
SD	Spatial Diversity
SDR	Software-defined Radio
SIR	Signal-to-inference Ratio
SISO	Single-input Single-output
SLL	Side-to-main Lobe Level
SMD	Surface-mount Device
SNR	Signal-to-noise Ratio
SRR	Split-ring Resonator
TDMA	Time Division Multiple Access
TE	Transverse-electric
TTD	True Time Delay
Tx	Transmitter
USW	University of South Wales
VNA	Vector Network Analyser

This page is intentionally left blank.

Contents

List of figures

This page is intentionally left blank.

List of tables

CHAPTER 1

Introduction

1.1 Background of study and motivation

The antenna is an essential part of any wireless communication system, transforming electromagnetic energy from its guided form to free-space radiation, and vice versa [1]. Antennas can be designed with several sizes and shapes, depending on the intended application, *e.g.* cellular handsets have different design requirements when compared with parabolic antennas for satellite communications.

Although the shape is an important consideration in antenna engineering, beam reconfigurability, *i.e.* beamsteering, is also crucial to some applications where high-directivity apertures need to be scanned or antennas need to keep track of particular objects to provide adaptation to dynamic environments with multipath and moving scatterers.

The concept of antenna beamsteering is not new. By definition, beamsteering is the capability of changing the direction of the radiation pattern main lobe enabling to focus the energy toward the intended users or devices, instead of directing it into unnecessary directions [1].

In fact, beamsteering has been used since the 1970's in Radio Detection And Ranging (RADAR) applications [2, 3] and even though such systems have considerably evolved since then, the core of its implementation still rely on a distributed network of controlled phase shifters, feeding each element in an antenna array [4–6]. The arrays of antennas will not only require distributed bulky beamsteering controllers but also a substantial amount of parallel processing to meet reconfiguration agility and radio frequency performance requirements. Such systems will therefore become costly, heavy and bulky, especially in large arrays consisting of tens and hundreds of elements [5, 6], hindering its integration for consumer or daily applications.

This clearly becomes a limitation for future wireless technologies that are emerging in the scope of the 5th Generation (of mobile network) (5G) [7–10] such as: Internet-of-Things (IoT), Device-to-device (D2D) or Machine-to-machine (M2M) communications. They will require direct and uninterrupted wireless links to connect simultaneously all kind of devices, at any place, at any time, in a concept of an all-connected-world. In that sense, antennas should evolve to a point where (beam) reconfigurability is a fundamental requirement while maintaining them compact and low-cost.

1.2 Aims and objectives

To this extent, the focus of this research programme aims at the development of novel antennas capable of electronic beamsteering for various wireless communication applications. Such antennas would be capable of changing the direction of their radiation patterns and directivities, electronically and dynamically, in a fast and efficient manner without the need of mechanical or motorised components.

In particular, transmitarrays, *i.e.* a radome located in the near-field of a directional antenna acting as a microwave lens, are introduced as structures which can control the properties of an incident Electromagnetic (EM) wave and accomplish beamsteering.

This beamsteering method aims to eliminate the need of phase shifters and complex digital topologies, by using artificial structured materials inspired on Metamaterials (MM) [11, 12] and Frequency Selective Surfaces (FSS) [13, 14], for a customised phase response and a personalised electromagnetic interaction. These artificial manufactured structures exhibit distinct resonant characteristics depending on the appearance and on the dimensions of geometries, *e.g.*: band-pass, band-stop, high-pass or low-pass filtering characteristics. Moreover, when loaded with discrete capacitors or varactors diodes, it is possible to modify the capacitance value (C) of the associated LC equivalent circuit characteristic of each FSS, and consequently tuning the resonant frequency and control the phase response.

To this extent, transmitarrays composed of MM or FSS are able to be electronically control the scanning angle of a single directive antenna, overcoming the limitations imposed by traditional array systems regarding to the burden of the Radio Frequency (RF) front-end. This feature allied to the inexpensive Printed Circuit Board (PCB) manufacturing costs, allow to significantly reduce weight, power consumption and the dimensions of assemblies, making these structures promising for beamsteering antenna fabrication and, very attractive for inclusion in a large number of applications associated to future 5G networks [7–10].

At the outset, the main key objectives are as follows:

1. Identification of the main techniques presented in the literature to perform antenna beamsteering, understanding their advantages and limitations;

2. Getting familiarised with transmitarray structures including, mode-of-operation, building materials and construction techniques and also their direct applications besides antenna beamsteering;

3. Construction of specific mechanical rigs to support the measurement systems including the antennas and the transmitarray structures. Development of the necessary measurement techniques for radiation pattern measurement. Appropriate calibration and sensitivity analysis of the experimental setup within an anechoic chamber. Development of the necessary post-processing scripts for data analysis and experimental beamsteering characterisation;

4. Study of the theoretical model for One-Dimensional (1D) antenna beamsteering using a transmitarray (limited to steering on a single antenna plane), improving it to enable 2D antenna beamsteering, *i.e.* by allowing the steering of the main lobe of the antenna's radiation pattern in two orthogonal planes (elevation and azimuth);

5. Familiarisation with various tools and programs for PCB design and electromagnetic simulation. Consequent, development and optimisation of a proper simulation models for unit-cell and transmitarray evaluation and characterisation;

6. Study of metamaterials with particular dedication to frequency selective surfaces. Revision of the theoretical concepts, identification of the design procedures and comprehension of the electromagnetic phenomena associated to several design configurations and dimensions, factors which govern their electromagnetic response;

7. Implementation of a passive, non-reconfigurable, transmitarray for 2D beamsteering composed of FSS to prove the concept. Electromagnetic simulation and validation against measurements performed inside an anechoic chamber. Investigation of factors influencing the performance and behaviour of the beamsteering performance;

8. Implementation of an active, reconfigurable, transmitarray for 2D beamsteering composed of FSS including a proper feeding strategy. Development of the necessary complementary hardware, namely the controller/driver, that would allow electronically controlled beamsteering. Implementation of a Graphical User Interface (GUI) to control the transmitarray via software. Electromagnetic simulation and validation against measurements performed inside an anechoic

chamber. Investigation of factors influencing the performance of the prototype, giving emphasis to the impact caused by the chosen feeding strategy;

9. Experimental tests and prove-of-concept of the developed active prototype, under several real-case application scenarios to validate its usefulness on several wireless communication.

10. Timely dissemination of the work being performed, in several conferences and journal publications with relevant scientific reputation and peer-reviewed, to validate the outcomes and importantly obtain expertise feedback on the field.

Despite of no tecnical requirements such as frequecy of operation, bandwidth, beamsteering angular range or angular resolution were defined at the outset, rather than the necessity of performing electronically contrallable 2D antenna beamsteering, consideration will be given to sub-6GHz frequency bands envisaging emerging applications of 5G, such D2D, M2M or IoT [7–10] and, facilitating prototype construction with low implementation costs.

1.3 Thesis outline

This thesis is structured as follows:

Chapter 2 starts by presenting a literature review covering some relevant concepts on antennas and propagation necessary for the subsequent chapters. Namely, antenna arrays are introduced as one methodology of performing antenna beamsteering while the Array Factor (AF) that characterises such devices is presented and analysed. Moreover, in addition to a critical review on the most common techniques for beamsteering implemented to date, *e.g.* switched-beam antennas and true time delay systems, a state-at-art on transmitarray antennas is also presented, highlighting the importance of such structures in wave-front control and, in particular, for beamsteering purposes.

Chapter 3 describes in detail the measurement systems utilised in the experimental part of this research work. A complete characterisation of the hardware and techniques used for measuring antenna radiation pattern are presented. Moreover, the measurement setup utilised to obtain antenna radiation patterns is characterised, starting with a link budget calculation and followed by a detailed explanation of the system calibration and normalization procedures. Subsequently, the standard gain horn antenna used as reference for transmitarray beamsteering analysis is characterised in terms of absolute gain, S_{11}, and 3D radiation pattern, for the frequencies of interest for this work. Finally, the software developed in-house, to enable automated measurements, as well as the post-processing scripts utilised for results interpretation, are also presented herein.

Chapter 4 introduces the theoretical formulation necessary to realise the beamsteering using a generic transmitarray. In particular, theoretical models for 1D and 2D beamsteering are thoroughly described followed by proper model validation on an ideal dielectric slab, using a full-wave electromagnetic simulator. The simulations carried out on the models provided a good level of confidence either on the simulation tool but also on the developed theoretical model.

Chapter 5 is devoted to the work realised on a passive transmitarray with 2D beamsteering capability. It starts by introducing the transmitarray unitary element composed of stacked layers of square-slot FSS, loaded with discrete capacitors. A thorough parametric study carried out in Computer Simulation Technology (CST) Microwave Studio (MWS), a full wave electromagnetic solver, is presented. The study particularly aims to characterise the phase variation of the element against unit-cell dimensions, number of stacked layers and layer separation distance. Furthermore, the beamsteering algorithm which estimates the necessary values of progressive phase to apply throughout a 5×5 transmitarray, based on the previous parametric study, is detailed. Finally, simulation results are compared against the ones obtained experimentally on a fabricated prototype, validating the proposed theoretical model for 2D beamsteering using a FSS-inspired transmitarray.

Chapter 6 provides the design and full characterisation of an Electronically Reconfigurable Transmitarray (eRT) for 2D beamsteering. In the sequence of the work presented on the previous chapter, a novel active FSS-inspired transmitarray element is introduced, enabling the electronic control of the elementary phase-shift. This is accomplished due to the use of varactor diodes loaded in each unit-cell and due to the proposed feeding strategy, also described in this chapter. Furthermore, the design, implementation and characterisation of a Beamsteering Controller (BsC) which drives the necessary control signal to the transmitarray is presented, followed by the presentation of the GUI that enables the control of the scanning angle direction, remotely, from a host computer. A complete experimental characterisation is performed on a prototype of the eRT comparing both simulation and experimental results followed by a critical analysis.

Chapter 7 is dedicated to the continuous characterisation of the eRT with 2D beamsteering capability. In particular, two distinct case studies representing possible real-life applications are considered to prove the usefulness of the developed prototype. Each case study is disseminated in a specific section. Therefore, the first section, evaluates the eRT under fast beamsteering angular requests. The device is characterised experimentally in terms of steering-rate response evaluating its agility when bouncing between distinct scanning angles, aiming fast track applications. Finally, in the second section, the prototype is evaluated when integrated in a realistic Long Term Evolution (LTE) wireless communication system. In particular, the eRT is utilised as the transmitter antenna of a top-notch Orthogonal Frequency Division Multiplexing (OFDM) software

defined radio, operating at 5.2 GHz. Figures of merit Bit Error Rate (BER) and Error Vector Magnitude (EVM) curves are obtained experimentally and compared, with and without the transmitarray.

Chapter 8 presents a summary and main conclusive remarks of this complete research work. An overview of all reported developments is provided and compared with initial aims and objectives, as well as the identification of all major contributions to the scientific community. Consideration is also given regarding topics that require further investigation, or are envisaged as possible relevant developments in the near future, and as an extension of the work presented in this thesis.

CHAPTER 2

Literature review

2.1 Introduction

The antenna is fundamental for any wireless communication system being the interface between the guided radio waves and the free-space propagation. According to the Institute of Electrical and Electronics Engineers (IEEE), the Standard Definitions of Terms for Antennas (IEEE Std. 145–1983) defines an *antenna* or *aerial* as a means for radiating or receiving radio waves [15].

Antennas can be designed with several sizes and shapes to meet either (both) configuration or (and) performance requirements, always aiming the application in which they will operate [1]. *E.g.* antennas for mobile phones have different design requirements than the ones for satellite communications. While in a mobile handset (Fig. 2.1a), antennas are designed with a very small form-factor to be easily embedded inside the device and typically aim multi-frequency and wideband operation, antennas for satellite communication (Fig. 2.1b) are often composed by very wide parabolic dishes to achieve high gain and directivities typically operating at single frequencies bands.

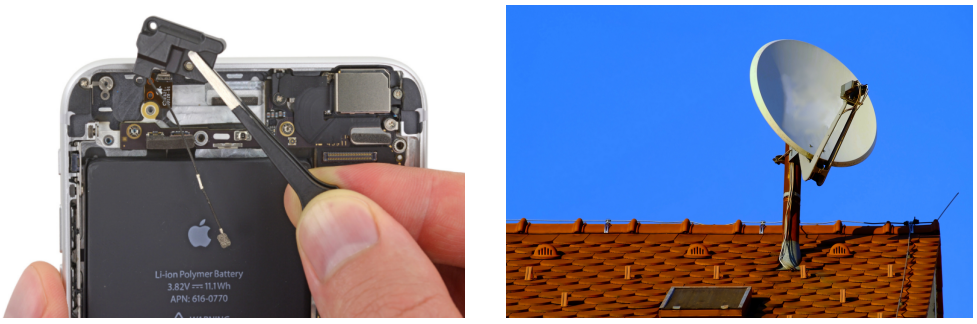

(a) (b)

FIGURE 2.1: (a) Internal antenna of a modern mobile handset and (b) parabolic dish antenna for satellite television (images extracted from [16] and [17], respectively).

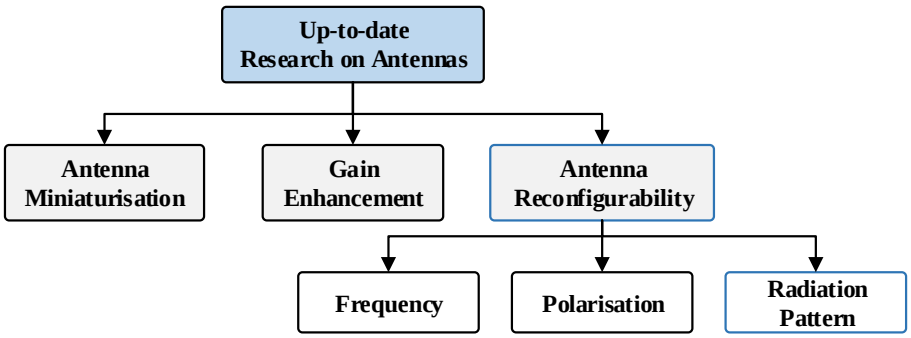

FIGURE 2.2: Research areas of novel antenna designs.

In the literature, many textbooks [1, 18, 19] are readily available as guidance for antenna design and characterisation, presenting the necessary mathematical relation between antenna shape and dimensions, electromagnetic properties, construction materials and antenna's performance. The majority start by introducing simple antennas designs that serve as the basis to more sophisticated antennas. For example, for a microstrip patch, which consists of a metallic patch etched on a grounded substrate by using printed circuit board (PCB) technology, the dimensions of the etched geometry are presented against the electromagnetic properties of substrate, *i.e.* relative permittivity (ϵ_r) and permeability (μ_r), to define the frequency of operation of this type of antennas. Such antennas can be further aggregated in an array to compose more elaborated antenna designs [5, 6].

Thus, it is clear that standard antennas elements are deeply founded in the literature and, nowadays, the major trend in antenna engineering rely on the increase of the antenna's performance, *e.g.* by enabling them with the capability to adapt themselves to the environment where they would operate. This is even more crucial with the appearance of novel 5G use cases (IoT, D2D, M2M) that aim direct and reliable wireless links to connect thousands of devices simultaneously, any time, anywhere [7–10].

The work being presented in the literature allow to group the research on antennas in three distinct categories, as highlighted in Fig.2.2, including: *i)* antenna miniaturisation, *ii)* gain enhancement, and finally *iii)* antenna reconfigurability, where this Ph.D. work relies on. These categories are detailed as follows:

i) Antenna miniaturisation: this category leans on the study and development of novel antenna designs or reduction techniques which allow to reduce the physical size of an antenna, while its bandwidth and efficiency are unaltered or even sometimes improved. Techniques for reduction comprises the use of metamaterials [11, 12, 20, 21], magnet-dielectric substrates [22, 23], or even by including resonant elements in antenna designs to alter its electromagnetic properties, *e.g.* by utilising Artificial Magnetic Conductor (AMC) or Split-ring Resonator (SRR) structures [24, 25]. Their application

aim the integration in portable devices such as mobile phones, tablets, computers, laptops, *etc.*, which require antennas to be small, lightweight, and low profile;

ii) Gain enhancement: the gain is probably one of the most determinant feature to take into consideration when choosing an antenna. It is a measure that takes into account the efficiency of the antenna as well as its directional capabilities (directivity) . The gain of an antenna can be defined as *"the ratio of the intensity, in a given direction, to the radiation intensity that would be obtained if the power accepted by the antenna were radiated isotropically"* [1]. Antennas with high gains are always desirable since they allow to relax the front-end design of an RF-chain, *e.g.* by reducing the gain on the power amplifiers and consequently, its impairments on the system. Therefore, ways of increasing antenna's gain have always been an hot topic within the scientific community. The most common way to increase the gain of an antenna is by increasing its effective area (aperture) [1], *e.g.* by using antenna arrays. However, many other techniques have been reported in the literature namely, by altering antennas resonant behaviour and radiation characteristics. In particular, one can find examples of gain enhanced antennas employing: superstates of dielectric materials [26, 27] and metamaterials [28]; enhanced ground planes based on High Impedance Surface (HIS) [29]; Electromagnetic Band Gap (EBG) [30] and FSS [31]; or even by applying SRR elements as antenna directors [32, 33];

iii) Antenna reconfigurability: this topic has become a crucial and desired feature of modern, agile, RF systems for wireless communications. Reconfiguring an antenna is achieved through deliberately changing some of its parameters. This change is achieved by many techniques that redistribute the antenna currents and thus alter the electromagnetic fields of the antenna's effective aperture [34]. Depending on the parameters being reconfigured, antennas can be classified as :

- *Frequency reconfigurable antenna:* the resonance frequency of an antenna and its bandwidth[1], are typically related to the antenna's physical dimensions and differ from design to design [1]. While there are some types of antennas that exhibit wide frequency bandwidth, *e.g.* horn antennas, there are others much narrower. A microstrip patch antenna typically exhibit less than 5% of bandwidth relative to its resonance frequency [18]. For this type of antennas, frequency reconfigurability is an important feature since it allows to (electronically) match the antenna to different frequencies of operation by tuning its reflection coefficient. Novel antenna designs for frequency reconfigurable antennas have been implemented using *e.g.* Micro Electromechanical Systems (MEMS) [18], p-i-n junction diode (PIN) [35, 36] or even variable capacitors (also known as varactor diodes)[36, 37], to electrically modify the characteristics of the radiating element or alter the properties of

[1]Conventionally obtained by difference between the upper and lower frequencies given by the points where the antenna S_{11} intersects with a -10dB line. [1]

the antenna's feeding line. Alternatively, tunable dielectric materials such as Liquid Crystal (LC) [38, 39] and Low Temperature Co-fired Ceramic (LTCC) [40], among others, are also employed for this purpose. Such materials can have their electromagnetic properties (ϵ_r, μ_r) altered by an external stimulus (bias or voltage) enabling frequency tunability in an antenna, as in [39, 40]. The major application of this feature is on systems that require to operate in multi-frequency bands.

- *Polarisation reconfigurable antenna:* polarisation of an antenna is defined as *"the polarisation of the wave transmitted by the antenna"* [1], and it describes the time-varying direction and relative magnitude of the Electric-field (E-field) vector of the radiated EM wave. Depending on the figure traced as a function of time by the extremity of the E-vector, at a fixed location in space, polarisation can be classified either as linear, circular, or elliptical [19]. For example, if the vector that describes the E-field at a point in space as a function of time is always directed along a line, the field is said to be linearly polarised [1, 15, 19]. An antenna with the capability of changing its polarisation (horizontal/vertical, slant 45, left-hand or right-hand circular polarised, *etc.*) is called polarisation reconfigurable antenna [34]. Many examples can be found in the literature by employing some switching mechanism (using MEMS, PIN diodes, varactors or RF-switches) that alter the feeding path or the position of the antenna's feeding point [41–45] or alternatively, by using surfaces composed of metamaterials (also known as metasurfaces) placed over the radiating element [46, 47] acting as a polariser. Notwithstanding, while the last approach requires to mechanically rotate the metasurfaces to generate a specific polarisation, the use of any switching mechanism enables the antennas to be electronically reconfigurable.

- *Radiation pattern (or beam) reconfigurable antenna:* the topic where this Ph.D work leans on. The radiation pattern is a mathematical/ graphical tool that helps to visualize the radiation properties of an antenna as a function of space coordinates [15]. Although several parameters could be represented (power flux density, field strength, directivity, phase or polarisation)[1], the radiation pattern conventionally displays, in two- or three- dimensions, the distribution of the radiation intensity of an antenna as observing it from the far-field [1, 19]. Besides of giving an insight of the radiation shape, as depicted in Fig. 2.3, the radiation pattern also allows to characterise an antenna in terms of performance. Relevant parameters such as: the direction of maximum radiation intensity and its value (commonly represented by gain or directivity), the number of side lobes and their direction and amplitude, the Side-to-main Lobe Level (SLL) and the Half Power Beamwidth (HPBW), among other properties, can be characterised [1, 15, 19].

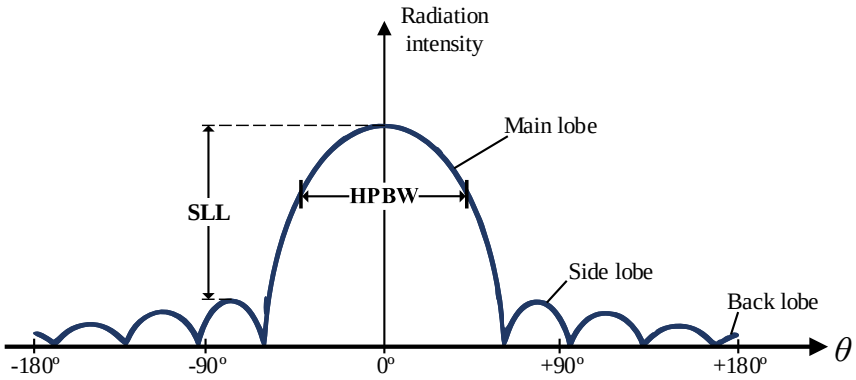

FIGURE 2.3: Linear plot of power pattern and its associated lobes and beamwidth (image adapted from [1]).

An antenna in which its radiation pattern may be reconfigurable, assumes that its radiation properties can be (intentionally) manipulated in terms of direction or in terms of shape or gain. In the first case, it is said that the antenna has beamsteering capability, *i.e.* it can steer the main beam of the radiation pattern towards a direction of more convenience, whereas in the second case it can realise beamforming, *i.e.* the antenna can form and shape its own radiation pattern to illuminate a specific solid angle [1]. Figure 2.4 helps to visualise the difference between beamsteering and beamforming. Both these schemes are very useful and desirable in any wireless communication system since they allow to dynamically adjust the antenna pattern and consequently enhance reception. Such feature is crucial to some applications that require tracking of objects and adaptation to dynamic scenarios with multi-path and moving scatterers, *e.g.* base-station dynamic antenna alignment, wireless back-haul links auto-alignment due to pole swaying and twisting in the wind or mobile user tracking [48, 49]. Since such antenna systems are focusing their energy toward the receiver, they are increasing the useful received signal level and thus, lowering the interference level. *I.e.* an higher Signal-to-inference Ratio (SIR) increases the capacity of the system and improves range and the coverage area.

Many techniques have been employed in the development of beam reconfigurable antennas. The most traditional manner of implementing such feature is by using arrays of antennas. Nevertheless, some novel techniques have been emerging in the the last couple of years. Some of those will be reviewed in detail, particularity aiming antenna beamsteering.

To this end, it is presented in this chapter an overview of the existing techniques for antenna beamsteering. It starts by introducing the principle of operation of the most conventional methods of implementing beamsteering, *i.e.* by employing antenna array. Subsequently, smart antennas and switched-beam antennas are described. A

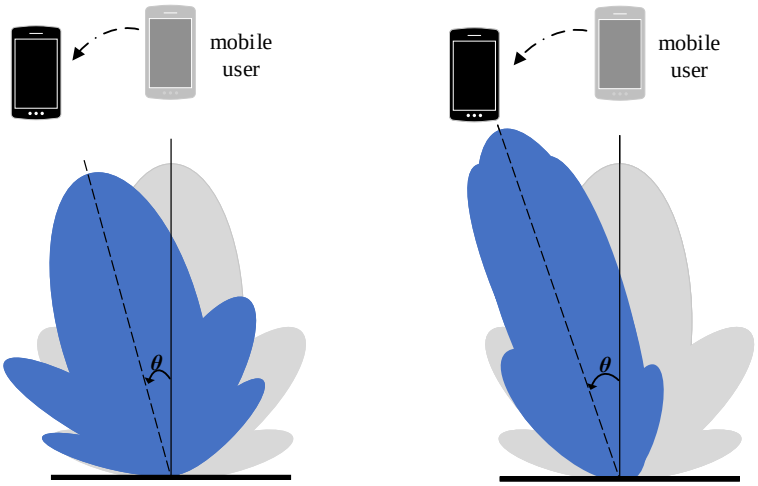

(a) (b)

FIGURE 2.4: Illustration of (a) beamsteering and (b) beamforming reconfigurability schemes.

literature review on alternative techniques, to the use antenna arrays for beamsteering implementation, is also presented. This leads to the introduction of antenna Transmit-arrays, where an overview on the current state-of-the-art is then outlined.

2.2 Traditional antenna beamsteering systems

Usually, antennas as individual elements do not meet the requirements to perform beamsteering (nor beamforming). Commonly, it is necessary to aggregate several antenna elements in more complex structures to accomplish such feature. It is the case of the well known antenna arrays and switched-beam antennas. Such devices are presented in this section, as the most traditional techniques to steer the main lobe of an antenna radiation pattern.

2.2.1 Antenna arrays and array factor formula

Antenna arrays have been known for years [2–4]. Such systems are probably the most common and utilised technique to perform reconfigurable control of beam direction and achieve very directive characteristics (very high gains). Understanding the concept behind antenna arrays is crucial to interpret the phenomena associated to beamsteering.

Antenna array consists of a number of identical antenna elements physically arranged in a certain manner, usually in the same plane, forming an array of antennas. Depending on several factors, the electric fields produced by each antenna element that composes

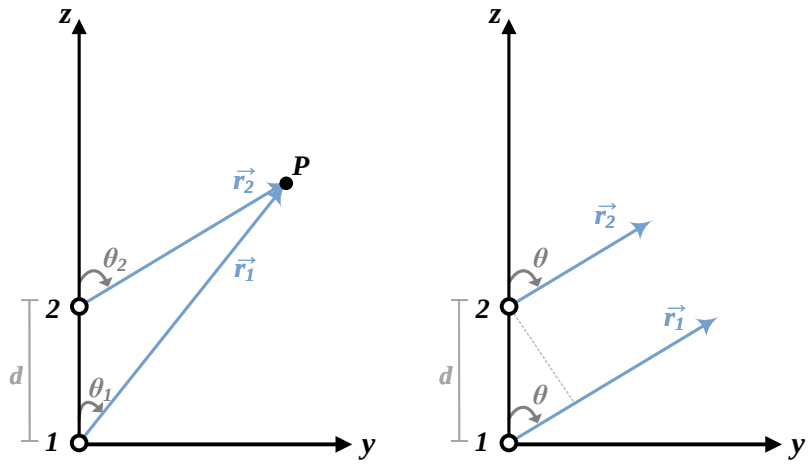

FIGURE 2.5: Two *Hertzian* dipole antenna array observed (a) from a generic local point "P" and (b) from a far-field distance (image adapted from [1]).

the array, interfere constructively in the some directions and, interfere destructively in others. Hence, total radiation could be manipulated and beamsteering and/ or beamforming could be realised. These factors are: the geometrical configuration of the array, the separation distance between elements, the amplitude and phase of the excitation signal applied to each individual element and, finally, its relative radiation pattern [1]. Such parameters may be used to characterise an antenna array.

Two-element array

Therefore, let us consider the simplest case where two *Hertzian* Dipoles [1] are equality separated along the z-axis by a distance d, as shown in Fig. 2.5. The dipoles are fed by currents of equal amplitude I_o and with a phase difference β so that, $I_1 = I_o$ and $I_2 = I_o e^{j\beta}$.

According to Fig. 2.5a, the total electric field ($\vec{E}_{total}$), at a generic observation point "P", is the vector sum of the contribution of each element, expressed by (2.1),

$$\vec{E}_{total} = \vec{E}_1 + \vec{E}_2 = j\eta \, \frac{kl}{4\pi} \left[I_1 \, \frac{e^{-jkr_1}}{r_1} \, \cos\theta_1 \;\; \hat{a}_{\theta_1} + I_2 \, \frac{e^{-jkr_2}}{r_2} \, \cos\theta_2 \;\; \hat{a}_{\theta_2} \right] \tag{2.1}$$

where $k = 2\pi/\lambda$ is the wavenumber and $\eta = \sqrt{\mu/\epsilon}$ is the intrinsic impedance of the medium [1].

However, at a region sufficiently away from the antenna, so that far-field conditions may be satisfied [1, 15, 19], the fields from each dipole can be considered nearly parallel, as depicted in Fig. 2.5b.

When taking into account the far field approximations [1], the following approximation can be done:

$$\theta_1 \simeq \theta_2 \simeq \theta; \quad \underbrace{r_1 \simeq r_2 \simeq r}_{\text{(for amplitude)}}; \quad \underbrace{r_1 \simeq r, \;\; r_2 \simeq r - d\cos\theta}_{\text{(for phase)}};$$

in which the electric field vectors have the same direction and, consequently, (2.1) may be simplified as shown in (2.2).

$$\begin{aligned}\vec{E}_{total} &= j\eta \, \frac{kl}{4\pi}\left[I_0 \, \frac{e^{-jkr}}{r} \;\; \cos\theta \;\; \hat{a}_\theta + I_0 \, \frac{e^{-jk(r-d\cos\theta)}}{r} \;\; \cos\theta \; e^{j\beta} \;\; \hat{a}_\theta\right] = \\ &= \hat{a}_\theta \;\; j\eta \, \frac{klI_o\cos\theta}{4\pi r}\left[e^{-jkr} + e^{-jkr}e^{jkd\cos\theta}e^{j\beta}\right] = \\ &= \underbrace{\hat{a}_\theta \;\; j\eta \, \frac{klI_o\cos\theta e^{-jkr}}{4\pi r}}_{\text{Element Factor}} \underbrace{\left[1 + e^{j(kd\cos\theta+\beta)}\right]}_{\text{Array Factor}}. \end{aligned} \quad (2.2)$$

From the analysis of (2.2), it is possible to conclude that the total E-field created by an array composed by two dipoles (in the far-field), is equal to E-field produced by one dipole (element factor) multiplied by an antenna factor, known as Array Factor (AF).

The AF is an important feature of antenna array theory since it relates the (physical) properties of the array using a closed-form expression (second term of eq. (2.2)). Each array has its own array factor that depends on the geometry, excitation phase, separation d and/or the phase β between the elements. By varying any of these parameters, the characteristics of the array factor and, consequently, the total field of the array can be controlled.

N-element linear array

Furthermore, it is possible to generalise the previous example to an array with N identical antennas, linearly positioned along the same axis and spaced by a distance d, as illustrated in Fig. 2.6.

By applying the concepts referred in the aforementioned case and assuming all elements have identical amplitudes, but each succeeding element has a β progressive phase lead current excitation relative to the preceding one (*i.e.* the array is uniform), whereby, $I_1 = I_0$, $I_2 = I_0 e^{j\beta}$, $I_3 = I_0 e^{j2\beta}$, ... , $I_N = I_0 e^{j(N-1)\beta}$, the AF takes the form of (2.3) [1],

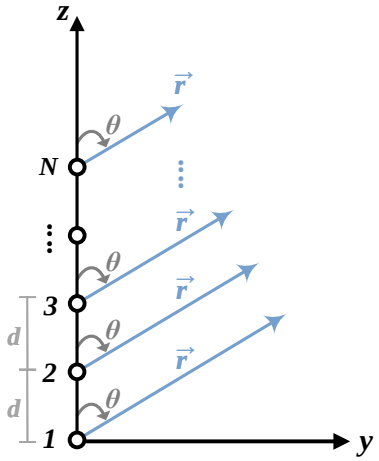

FIGURE 2.6: Linear distribution N array elements (image adapted from [1]).

$$AF = \left[1 + e^{j(kdcos\theta+\beta)} + e^{j2(kdcos\theta+\beta)} + ... + e^{j(N-1)(kdcos\theta+\beta)}\right] = \sum_{n=1}^{N} e^{j(n-1)\psi}, \quad (2.3)$$

where $\psi = k\ d\ cos(\theta) + \beta$, represents the progressive phase between adjacent elements.

Alternatively, with some mathematical arrangement [1], the array factor can be expressed by (2.4) as the the vector sum of N phasors, each of unit amplitude and progressive phase ψ,

$$AF = e^{j(N-1)\frac{\psi}{2}}\left[\frac{\sin\frac{N\psi}{2}}{\sin\frac{\psi}{2}}\right]. \quad (2.4)$$

When the reference point of the array is its physical centre, and the formula is normalised in order to the maximum value be unitary, (2.4) takes the form of (2.5),

$$AF_n = \frac{1}{N}\frac{\sin\frac{N\psi}{2}}{\sin\frac{\psi}{2}}. \quad (2.5)$$

Through the (generic) AF formula represented by (2.5), it is possible to characterise the antenna array and extract some relevant information about it, such as: the maximum, the nulls, the side lobes, and the beamwidth, only by mathematical manipulation. Such properties are thoroughly described in [1], however for the sake of the interpretation, let us focus on the maximum of the array factor.

The maximum of the AF, which corresponds to the maximum of radiation (*i.e.* main lobe), is one of the most important characteristic of the array factor, and therefore, of the antenna array. The maximum values of (2.5) occur when $\psi = 0$, as per (2.6),

$$\frac{\psi}{2} = \frac{1}{2}(kd\cos\theta + \beta)|_{\theta=\theta_m} = \pm\pi m \Rightarrow \theta_m = cos^{-1}\left[\frac{-\beta \pm 2\pi m}{kd}\right], \quad m = 0, 1, 2, ... \quad (2.6)$$

from which it can be extracted the location of the maximum (θ_m) that depends on the phase between adjacent elements. This is in fact one of the fundamental principals of phased antenna arrays, wherein is possible to steer the position of the main lobe of the radiation pattern, to a direction θ_x, by applying a progressive phase shift between adjacent elements of $\beta_x = -kd\cos\theta_x$. Such feature is illustrated in Fig. 2.7, for a progressive phase between elements of $\beta = 0$, $\beta = \pi/3$ (60°) and $\beta = -kd$ (90°), applied to an array composed of 10 *Hertzian* dipoles, spaced by $d = \lambda/4$, according to the geometry of Fig. 2.6.

From the depicted results (Fig. 2.7), it can be noticed that by progressively increasing β from 0 to kd, the main lobe of the AF is being steered away from $\theta = 0°$ in direction of $\theta = \pi/2$ (90°) (and $-\pi/2$ since element pattern and AF are symmetrical). This proves that beamsteering can be realised only by varying the progressive phase between elements and an *End-Fire* array – an array whose the maximum radiation is directed along its axis ($\theta_0 = 0°$ *or* 180°), can be converted to a *Broadside* array – where the maximum radiation is directed normal to the array axis ($\theta_0 = 90°$) [1].

Nevertheless, it should be mentioned that although the AF has a maximum pointing at ±90° for the case where $\beta = -kd$ (Fig. 2.7h), the total pattern (Fig. 2.7i) exhibits a null, forced by the null of the radiation pattern of a single element, at the same direction. Therefore, to optimize the design of any antenna array, the maxima of the single element and of the array factor should both be directed toward the same direction. In practice, this may be accomplished by carefully selecting the right type of radiators utilised as single single elements proceeded by the proper separation and individual excitation.

$N \times M$ - Element planar array

It is patent that the last example only supports one-dimensional beamsteering (steer is only performed in one orthogonal plane) since elements are linearly distributed along a single line. To withdraw such limitation and achieved beamsteering in two dimensions, the planar array of Fig. 2.8 should be considered.

In a planar array the elements are arranged in a plane defined by two axes, commonly respecting rectangular or square geometries. Such arrays, typically by increasing the number of elements, provide higher versatility enabling the beam shaping or the radiation

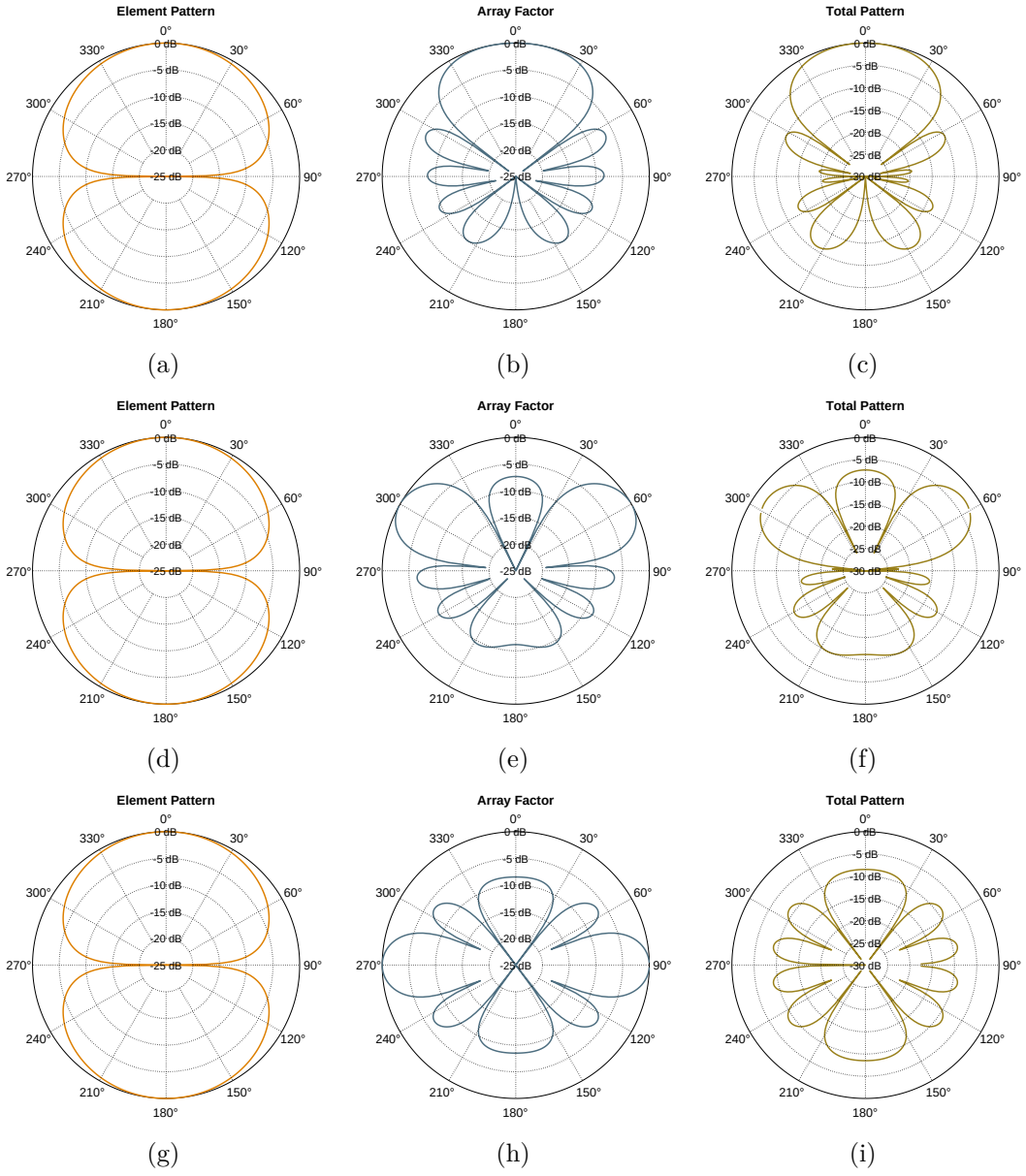

FIGURE 2.7: Element pattern, array factor and total pattern, for a linear antenna array composed of 10 *Hertzian* dipoles, spaced by $d = \lambda/4$, according to the geometry of Fig. 2.6 , for: (a-c) $\beta = 0$, (d-f) $\beta = \pi/3$ (60°) and (g-i) $\beta = -kd$, respectively.

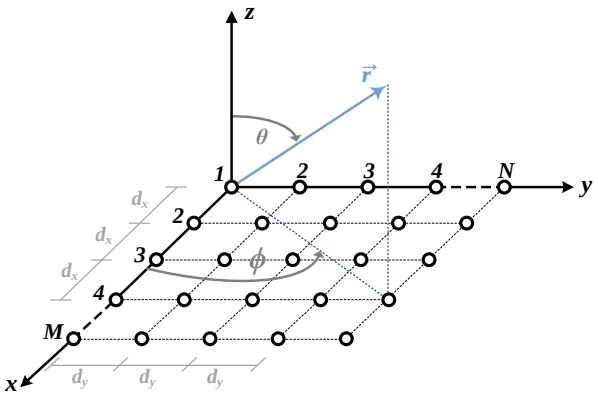

FIGURE 2.8: Planar distribution of $N \times N$ array elements (image adapted from [1]).

pattern in the two main planes, increasing gain and directivity. More importantly, they are doted with the capability of steering the radiation pattern, pointing towards a direction defined by (θ, ϕ) coordinates, *i.e.* by performing 2D-beamsteering.

A uniform planar array in the *xoy*-plane, can be analysed as an uniform linear array of N elements spaced by d_x, along the x-axis, where each of its elements is thereof a uniform linear array of M elements spaced by d_y, along the y-axis. This is a simple rule to obtain the expression of the total array factor that allow to characterise this type of antenna arrays. If each element is fed with an amplitude a_{xn}, a_{ym} and with a progressive phase shift β_x, β_y, respectively, the AF can be represented by (2.7), per axis,

$$\begin{cases} AF_x = \sum_{n=1}^{N} a_{xn}\ e^{j(n-1)\psi_x}, \quad \psi_x = k\ d_x\ \sin\theta\cos\phi + \beta_x \\ AF_y = \sum_{m=1}^{M} a_{ym}\ e^{j(m-1)\psi_y}, \quad \psi_y = k\ d_y\ \sin\theta\sin\phi + \beta_y \end{cases}, \tag{2.7}$$

then, the array factor of the $N \times M$ array is given by (2.8),

$$AF_{MN} = AF_x \times AF_y = \sum_{n=1}^{N} a_{xn} \left[\sum_{m=1}^{M} a_{ym}\ e^{j(m-1)\psi_y} \right] e^{j(n-1)\psi_x}. \tag{2.8}$$

If the planar array is uniform, *i.e.* all the elements have the same amplitude ($a_{nm} = a_{xn} \times a_{ym}$), then from (2.8), the normalised array factor can be represented by (2.9),

$$AF(\theta,\phi)_n = \left[\frac{1}{N} \frac{\sin\frac{N\psi_x}{2}}{\sin\frac{\psi_x}{2}} \right] \left[\frac{1}{M} \frac{\sin\frac{M\psi_y}{2}}{\sin\frac{\psi_y}{2}} \right] \tag{2.9}$$

2.2.2 Antenna phased arrays

In the previous analysis, it has been shown (Fig. 2.7) that the major lobe of the radiation pattern generated by an array of antennas can be directed to a desired direction, by simply controlling the phase excitation in each unitary element [1]. If a specific progressive phase (phase difference) exists uniformly between adjacent elements, the maximum radiation can be steered in any desired direction to perform beamsteering. In fact, this is the basic principle of operation of the so called antenna phased arrays [1, 4–6].

In antenna phased arrays, each radiating element of the array is usually connected to a phase-shifter that modifies the phase of the input signal [5, 6], as depicted in Fig. 2.9. Subsequently, the phase relation between adjacent elements of the array leads to the main (directional) beam to be scanned in a progressive manner to a given direction, following the theoretical background already presented in this document.

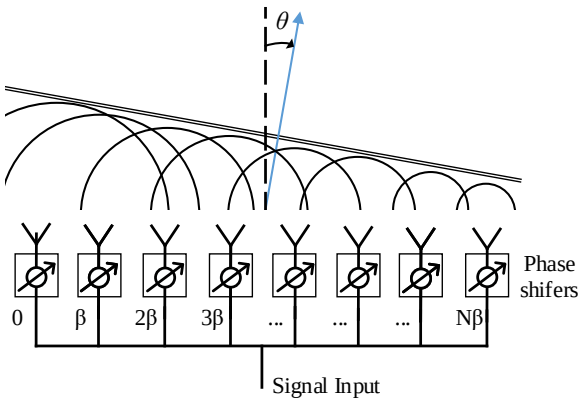

FIGURE 2.9: Principle of operation of a linear antenna phased arrays (image adapted from [5]).

Phase-shifters are devices that have the capability of (electronically) controlling the phase of an RF signal, by producing a shift on the phase between the input and output port of the device [50]. In practice, many types of phase-shifters can be employed, *e.g.* ferroelectric, PIN diodes based, MEMS based *etc.* [51]. For example, for a diode phase-shifter using balanced, hybrid-coupled varactors, the actual phase shift is controlled either by varying the analogue bias Direct Current (DC) voltage (typically 0–30 volts) or by a digital command through a Analogue-to-digital Converter (ADC) [1]. These phase-shifters, when controlled using a computer, may add to an antenna system capabilities of self-controlling the direction of their radiation patterns (refer to Smart Antennas - Section 2.3).

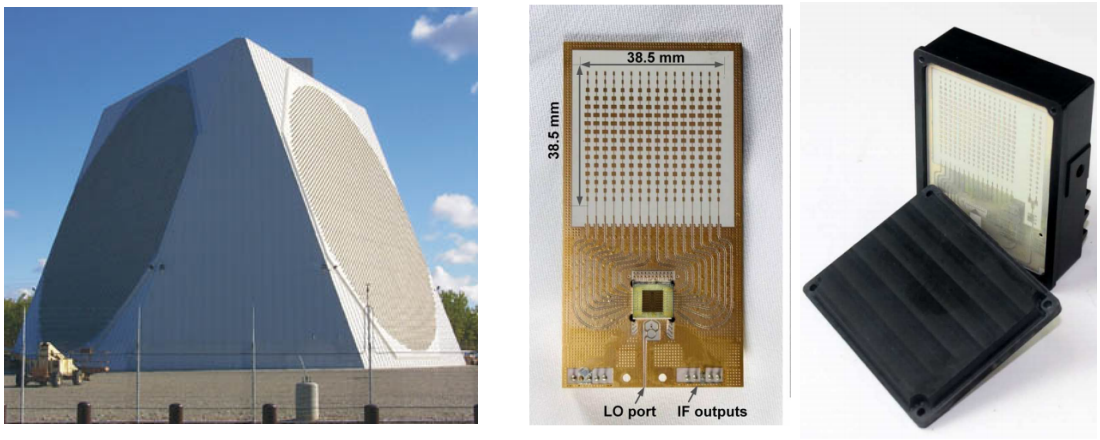

(a) (b) (c)

FIGURE 2.10: (a) Photography of the military RADAR PAVE PAWS phased array system (image extracted from [52]) and, (b,c) microstrip phased array for advanced automotive radars (images extracted from the work presented in [53]).

Particularly, antenna phased arrays are widely used in many applications that range from RADAR, broadcasting, space communication, *etc.*, either for civil or military use, that can exhibit large dimensions comparable to the size of buildings (Fig.2.10a [52]) or small comparable to the palm of the hand (Figs. 2.10b and 2.10c [53]).

A good reference that compiles a great amount of information about large phased antenna arrays and its application can be found in [54]. However, this thesis will be mostly concerned about phased arrays built in microstrip technology, as the ones from [55–57], due to their design simplicity, ease of implementation and manufacture (mostly used in PCB techniques) and, consequently, relatively low implementation costs.

Notwithstanding, there is one common factor to all types of phased antenna arrays: the use of a phase-shifter per element of an array quickly becomes a limitation for larger arrays resulting in bulky, electronically complex and expensive systems [6]. Since each element in the array needs to be individually fed, the length of the transmission lines increases with the size of the array, leading to an increase of transmission line losses and space requirements. Therefore, the characteristics of the feeding network becomes the major disadvantage of phased arrays, even more accentuated at high frequencies (millimetre wave frequencies), where the size of the radiating elements tend to be small and of comparable size to the feeding lines, as in fact, it can be seen for the array depicted in Fig. 2.10b [53].

However, phased arrays as the one of Fig. 2.11 [57], can simply be implemented by replacing the phase-shifters by fixed length transmission lines to feed each array element. Since the phase shift is proportional to the electric length of the feeding line [50], antenna arrays can be build with the radiation pattern steered in a pre-defined (fixed)

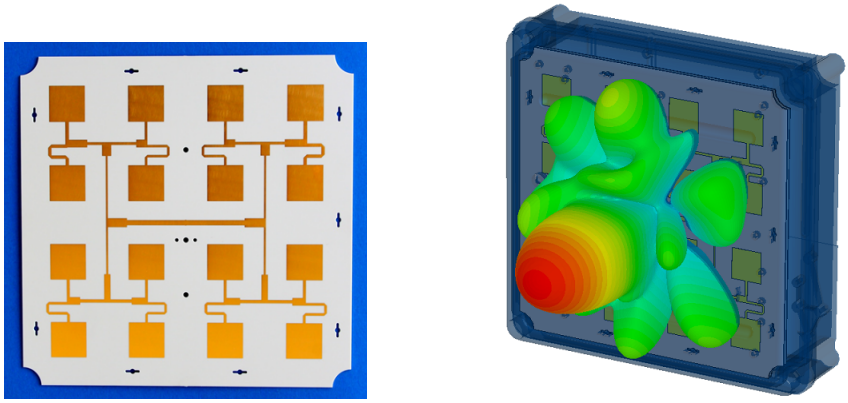

(a) (b)

FIGURE 2.11: Microstrip planar antenna phased array composed by 4×4 elements: (a) prototype of the PCB and (b) full simulation model in an electromagnetic solver (images extracted from CST website [57]).

direction. Nonetheless, this methodology exhibits the same disadvantages regarding feeding network for large arrays of antennas.

2.2.3 Switched-beam antennas

Switched-beam antennas can be seen as an alternative to phased arrays as far as beamsteering capability is concerned. Similarly, this type of antennas are composed by more than one radiating element (or array of radiating elements) that are alternately switched on or off (and thus the name of switched-beam), depending on the direction of the radiation pattern is intended to be aimed at.

Although not mandatory, switched-beam antennas can be designed respecting the physical distribution of elements utilised in antenna arrays [58–61]. The major difference between this type of antennas and phased arrays rely on design of the feeding network. While phased arrays typically use phase-shifters to control the phase in each element and, consequently, the scanning angle, the switched-beam antennas possesses a RF mechanism that selects which antenna elements are radiating.

An example of the implementation of such technology is disseminated in [58]. The authors have implemented and characterised experimentally a 2D dimensional beam steerable antenna based on the switched-beam principle depicted in Fig. 2.12a. The prototype of the antenna (Fig.2.12b) comprises of a feed array of 16 aperture coupled microstrip patches, covered with a *quartz* lens. A feeding network (Fig. 2.12c) that employs active RF switches, on a chip, selects the antenna element to be active and, consequently, the direction and shape of the resultant radiation pattern that is defined by the antenna element displacement relative to the lens axis. The antenna was designed

to operate in the 77 and 85 GHz frequency band and exhibits a directive gain higher than 16 dBi and scanning angles that can go up to 27°, as depicted in Fig. 2.12d.

Other designs can be found in the literature also reporting the use of switching devices [62–65], such as PIN-diodes, varactors and MEMS to implement this type of antennas.

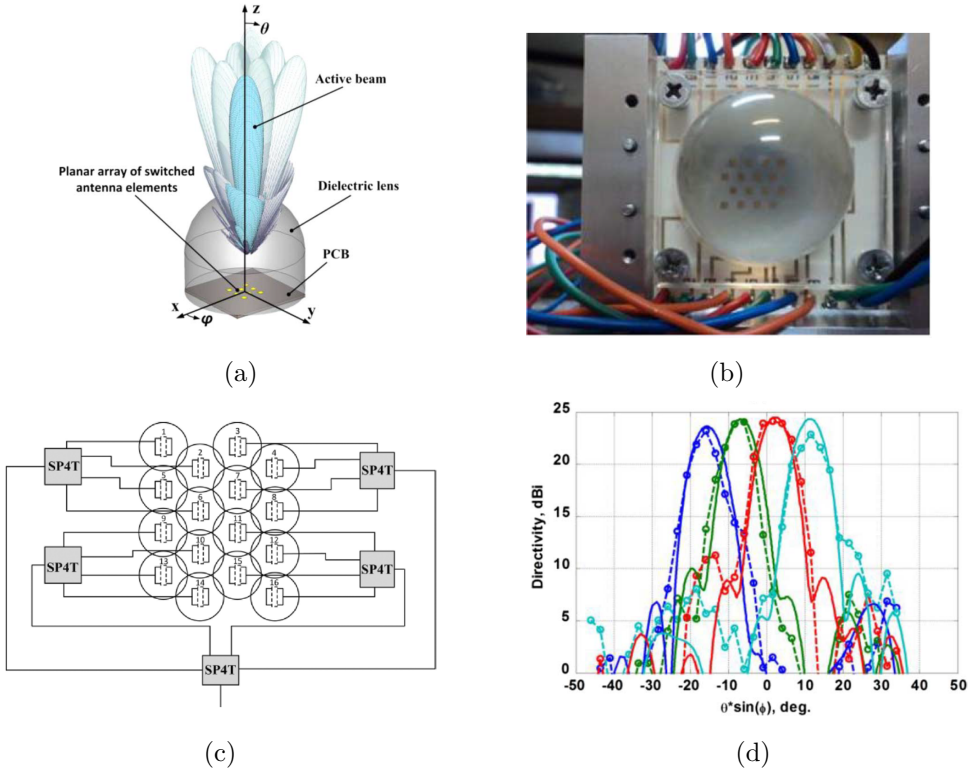

FIGURE 2.12: Switched-beam lens antenna: (a) switched-beam principle, (b) prototype of the antenna, (c) proposed feeding network and (d) measured radiation patterns (images extracted from the work presented in [58]).

However, a different design for the feeding network which enables antenna beam switching properties can be found in [59]. The antenna developed by *Wang et. al.* in the latter is depicted in Fig. 2.13b. It is composed of 6 array panels of microstrip patch antennas each responsible to illuminate a 60° sector in the azimuth plane, and thus provide 360° of overall coverage. The feeding network, illustrated in both Figs. 2.13b and 2.13c was implemented using power dividers, directional couplers and $\lambda/4$ impedance transformers on microstrip technology [1, 50], in a way that each sectoral arrays panel is provided with an optimised phase and amplitude distribution so side lobes could be minimised.

In fact, the work presented in [59] has a beamforming network developed based on the well known *Butler* matrix [5, 6, 66–68]. The *Butler* matrix is one of the most

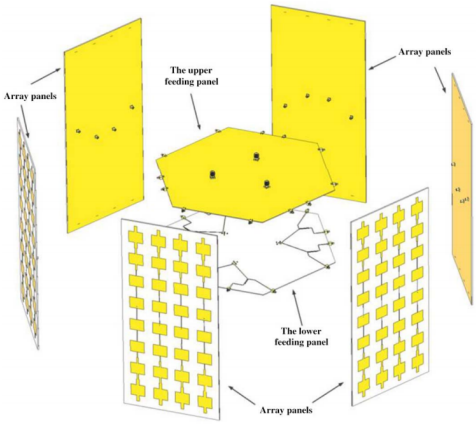

(a)

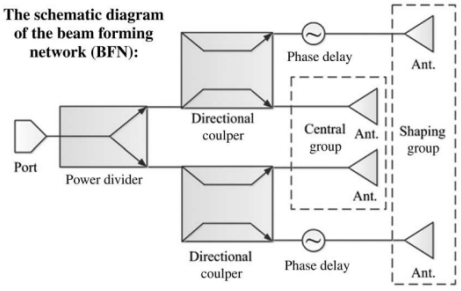

(b)

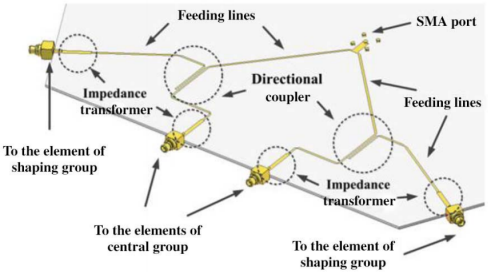

(c)

FIGURE 2.13: Switched-beam antenna composed of array panels of microstrip patch antennas: (a) antenna exploded-view, (b) block diagram and (c) microstrip design of the beamforming network (images extracted from the work presented in [59]).

common method used to feed a switched-beam antenna. A wide range of switched-beam and multi-beam antenna designs employing *Butler* matrices can be found in [66–68] besides the ones presented in [59]. This feeding strategy is a circuit implementation for a spatial Fast Fourier Transform and allow to radiate orthogonal sets of beams with uniform aperture illumination [5, 6, 66–68]. It is a N-input and N-output feeding network that when connected to N radiating elements (antennas), allow multiple beams pointing at distinct directions depending on which input port is the excitation signal being applied [5, 6, 66–68]. The direction of the beams are set by the amplitude and by specified relative-phase differences in each radiating element.

For a generic 4×4 matrix (Fig. 2.14) [68] typically composed of fixed phase-shifters, hybrid junction or directional couplers and crossovers, each output signal S_n, at port n is given by (2.10) [67],

$$S_n = \sum_{m=1} A_m.\exp(j.\alpha_m), \tag{2.10}$$

TABLE 2.1
RELATIVE PHASE FOR A GENERIC 4×4 *Butler* MATRIX.

		Input n			
		Port 1	Port 2	Port 3	Port 4
Output m	Port 1	45°	90°+ 45°	90°	90°+ 90°
	Port 2	90°	0°	90°+ 45°+ 90°	45°+ 90°
	Port 3	45°+ 90°	90°+ 45°+ 90°	0°	90°
	Port 4	90°+ 90°	90°	90° + 45°	45°

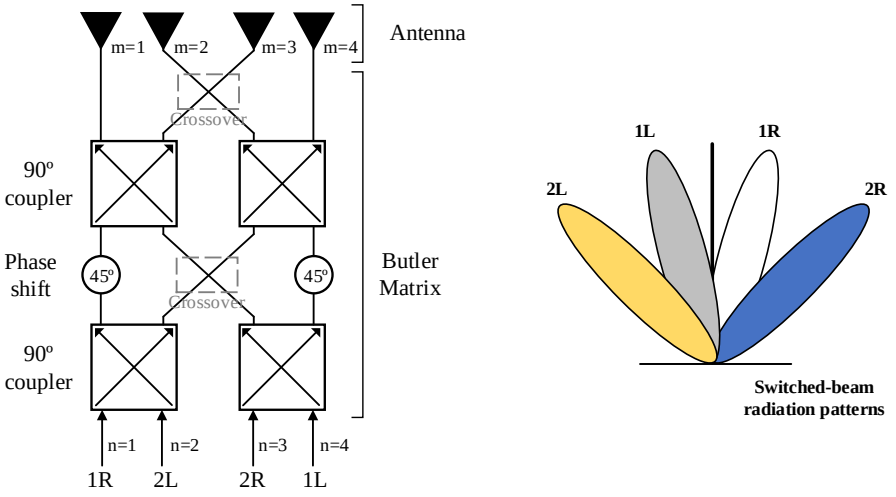

(a) (b)

FIGURE 2.14: (a) Block diagram of a generic 4×4 *Butler* matrix and (b) respective output beam directions (images adapted from [68]).

where A_m is input signal at the input port m, and α_m is the phase difference between the input m and the output signals n [67]. For the particular example depicted in Fig. 2.14, the relative phase lag introduced by each path is detailed in Table 2.1, where each phase-shifter introduces 45° of phase delay, the directional couplers 90° in a cross path (0° in straight line) and the crossovers act as a jumper that allow to select the desire patch introducing no phase delay.

A similar alternative to the one proposed by the *Butler* matrix is given by the *Rotman* lens [69]. Both methods operate similarly, however, while the *Butler* matrix is typically constructed in microstrip technology using passive elements (fixed phase-shifters, hybrid junction or directional couplers), whose theoretical background relies on the transmission lines theory [1, 50], the *Rotman* lens relies on the effect of the EM propagation trapped inside of a enclosed structure, typical employed using microwave waveguides or also microstrip structures. Several examples and guidelines for *Rotman* lens design can be found in [69, 70].

2.2.4 True time delay systems

One limiting factor inherent to the design and implementation of phased antenna arrays is the beam squinting. This phenomenon, very well described and characterised in [71] and [72], is known by severely affecting phased array antenna systems due to their non-linear phase-frequency characteristic, causing the beamsteering output angle direction to deviate as a function of the operating frequency. Consequently, the main lobe of the radiation pattern is forced to point to $\theta_p = \theta_0 + \Delta\theta_{bs}$ at a frequency $f = f_0 + \Delta f$, instead of pointing at θ_0 [71]. Thus, beam squint may become critical for array systems that exhibit broadband and/ or narrow beamwidth characteristics, causing to steer off at the target [71]. In fact, such angular deviation ($\Delta\theta_{bs}$) in function of the frequency is, according to [72], characterised by (2.11),

$$\Delta\theta_{bs} = \theta_p - \theta_0 = sin^{-1}\left(\frac{f_0}{f} sin\theta_0\right) - \theta_0, \tag{2.11}$$

To compensate for this impairment, True Time Delay (TTD) devices may be used as an alternative to traditional phase-shifters in antenna arrays implementation. A TTD device differs from a traditional phase-shifter by delaying by the same amount of time, all spectral components of the input RF signal. This ensures the entire bandwidth of the signal is steered by the same angle [71, 72], instead of which produce a constant phase shift. The effect between both these methods and its impact on the radiation pattern is well characterised in [72] and observed in the radiation patterns of Fig. 2.15.

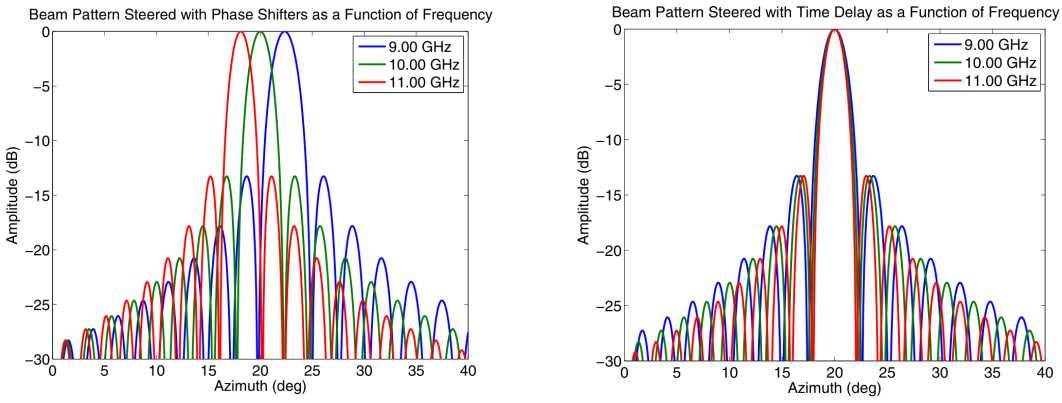

(a) (b)

FIGURE 2.15: Example of the effect of beam squint in antenna radiation pattern using (a) phase-shifter against (b) a TTD system, for different frequencies points (images extracted from the work presented in [72]).

In fact, TTD systems itself are a hot topic in the scientific community and much research work have been performed [73–76], namely, by exploring photonics[2] in the implementation delay lines in the optical domain. The basic idea behind the use of optics in the implementation and development of TTD devices is to modulate the bias current of a laser diode with the RF signal. The light is delayed by a length of the optical fibre and then converted back to an electronic signal with a photo-detector. Compared to delay devices based on pure electrical techniques, controllable delay lines using photonic or optical techniques could operate with broader bandwidths and eliminating the beam squinting effect [76]. These system though, are highly limited by the losses inherent to the conversion of the RF-to-optics, and *vice-versa*, which may be a huge limitation factor for the application of this technology.

2.3 Smart-antennas

Although phased arrays or switched-beam antennas can be designed with the capability of electronically control the direction of propagation, *i.e.* enabling beam-steering, it becomes clear that such systems typically do not possess any type of intelligence that enables the beam to be aimed towards a specific direction. An antenna that possess this capability is designated as Smart-Antenna [1, 77].

Smart-antenna is the conventional name given to an antenna system with some sort of digital processing, which in addition to the radiating elements, make the system to be "smart". In fact, such antennas employ the theory of antenna array reported in Section 2.2.1. In addition to feedback scheme for detection of Direction-of-arrival (DOA) [77], such systems can adapt themselves to the scenario where they are deployed.

A smart-antenna uses powerful controllers for digital signal processing, such as Digital Signal Processor (DSP), Field Programmable Gate Array (FPGA) or Application Specific Integrated Circuit (ASIC). These usually run heavy computation algorithms [77, 78] that estimate the necessary phase and the amplitude (weights) to apply in each element that composes the antenna array, automatically shaping a radiation pattern in real-time, as illustrated in Fig.2.16. Depending on the application scenario, they can simply realise beamsteering to redirect the main or a side lobe of the radiation pattern to any desired direction (smart switched-beam antenna), or on the other hand, they can implement beamforming by adapting the shape of the radiation pattern as convenient (adaptive beamforming) [1]. For example, smart-antenna systems are employed in mobile cellular networks, for cell sectoring (Fig. 2.16b), in which the sector coverage is composed of multiple beams, and the number of beams in the sector (*e.g.* in 120°) is a

[2] the science that studies the physical effect of light

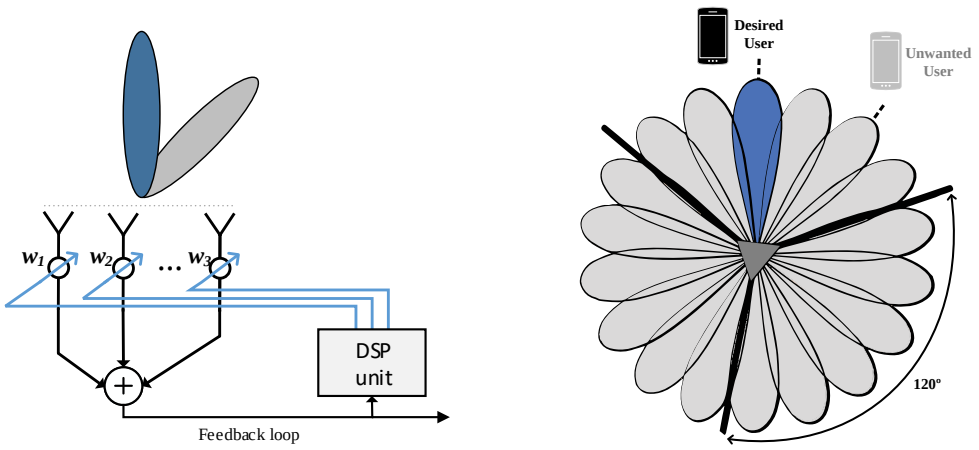

(a) (b)

FIGURE 2.16: Switched beamsteering for cell sectoring: (a) block diagram of the backbone and (b) illustrative switched-beam cell sectoring (images adapted from [1]).

function of the array geometry. Since they can focus their radiation pattern toward the desired users while rejecting unwanted interferences, they can provide greater coverage area, yielding higher rejection interference and, consequently, lower the BER, and finally increase the capacity of the system.

2.4 Alternative beamsteering techniques

Although phase antenna arrays and switched-beam antenna have been considered as the most important techniques to steer the main lobe of the antenna radiation pattern, there are a few alternative methods to perform beamsteering. Some of those are detailed in this section.

2.4.1 Mechanical alignment systems

Considered as a rough approach to beamsteering systems, mechanical motorised mounts can be used to implement beamsteering by rotating a directive antenna on its own axis and therefore align the main lobe towards an intended direction. Traditionally known as pan/tilt positioners (or headers), they are employed for tracking applications or in laboratory environment to help with the alignment of antennas and obtain their radiation patterns. An example of a pan/tilt motorised head available at Instituto de Telecomunicações (IT) laboratory, is illustrated in Fig. 2.17.

However, mechanical systems suffers from several drawbacks that cause them to be not appealing for antenna beamsteering [48, 49]. Firstly, they require periodic maintenance due to the wear and tear of the mechanical parts and thus, they are prone

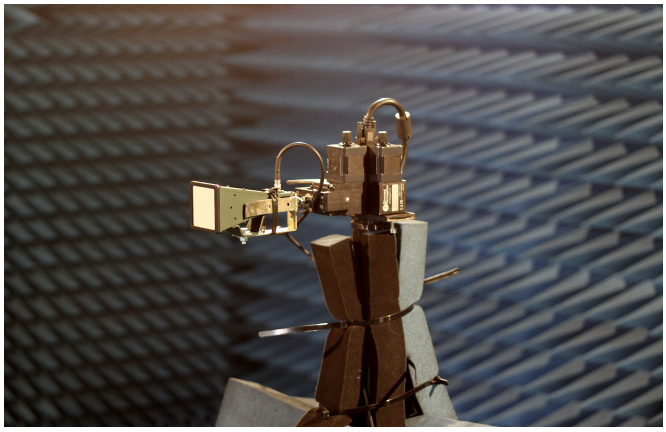

FIGURE 2.17: Example of a pan/till motorised mount for antenna scanning.

to failure over time, becoming undesirable in the commercial point of view. Secondly, even using high speed/torque mounts, these systems present always an intrinsic delay associated to the rotation of the motors, specially limited to steer heavy and bulky antennas. Thirdly, extra hardware is always needed since such motors require an high voltage power supply and respective motor drivers. Finally, its use aggregated to an antenna always results in a bulky system, not suitable for all types of applications [49].

2.4.2 Microfluidics beamsteering antennas

A novel approach has been recently explored by using conductive fluids in antenna design. This approach aims to use metallic-based liquids to modify the physical or electrical properties of the antennas, due to the electrically conductive and electromagnetic reflective characteristics associated to metals. By exploring such properties, it is possible to create new radiating elements, reflectors or director elements of an antenna. The antennas that use conductive fluids on its composition are therefore referred as microfluidics antennas.

In particular, some examples of microfluidic antennas can be found in the literature [79–82] aiming at the development of antenna beamsteering. In [79], a novel planar Yagi-Uda antenna uses parasitics elements made of liquid metal (Mercury–Hg), acting as reflector and directors. The beamsteering is accomplished by rotating the liquid parasitics elements, in a circular microfluidics channel, around the driven element by means of a flow, generated and controlled by a piezoelectric micro-pump. The proposed antenna, depicted in Fig.2.18, operates at 1.8 GHz enabling an electrically controlled beamsteering of 360°, in one plane only, with 4% of bandwidth.

Following a similar approach, *A. Gheethan et. al.* have demonstrated in [80], a microfluidics focal plane array with beamsteering ranges up to ±25° in a single plane, at a frequency of operation of 30 GHz. In their application, squared volumes separated

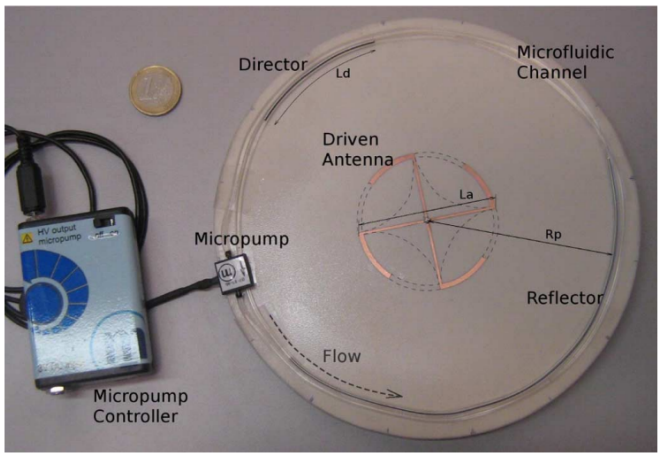

FIGURE 2.18: Prototype of a microfluidics reconfigurable (image extracted from the work presented in [79]).

by multiples of wavelength are placed in line with the microfluidic channel, forming an array of connected empty spaces. A micro-pump moves the conductive liquid inside the channel (bi-directional) filling each volume once at a time. From an electric perspective, these models behave like a square patch antenna moving in space every time liquid is pumped to the next empty space. Beamsteering is accomplished therefore, by spatially moving the origin of the radiated EM field.

Moreover, authors in [81, 82] are working on a circularly polarised X-band microfluidics unit-cell for transmitarray applications. The unit-cell comprises double layer nested ring-split rings formed as microfluidics channels in the *Polydimethylsiloxane* material using soft lithography techniques. The current work is patent pending and thus, specific details are not yet available, despite initial results can be found in [82].

Although microfluidics antennas have been successfully prototyped with experimental tests showing the merit of such technology [79–82], the use of metallic fluids in antenna design still have some limitations. These systems not only rely on electric/ motorised parts to pump the liquid, subject to wear and tear of the mechanical parts, but also represent a risk by using hazardous conductive liquids. These liquids are hazardous by nature presenting a risk in case of a leak in the conductive channel, either by destroying the equipment but most importantly for public health. In technical perspective, it is not clear how much would be the angular precision of the proposed antennas since it is not possible to know the correct position of the liquid within the microfluidic channel, and this may alter antenna performance.

2.4.3 Transmitarrays and reflectarrays

To overcome some of the issues in design and implementation of the complex and costly feeding networks, the research community have started to study alternatives to antenna

array systems. Spatial feeding techniques have been seen as a feasible alternative offering numerous advantages to the technologies. It is the case of the Transmitarray [83, 84] and Reflectarray antennas [85, 86].

Transmitarray and reflectarray are the conventional names given to structures that can modify the original radiation pattern of a directional antenna source, *e.g.* horn antenna, when placed at a distance sufficiently away from the its aperture [87]. To the set composed by the structure and the radiating source, it is referred either as transmitarray antenna [83, 84] or as reflectarray antenna [85, 86], depending whether a transmit– or a reflect– type of structure is being employed. Due to their electromagnetic properties, such structures are be capable of modifying the characteristics of the incident EM wave emitted by the source, and perform beamsteering, focusing or even polarisation control, either by re-transmission using a transmitarray or by reflection using a reflectarray [83–86]. Thus, one can imagine a reflectarray acting, in a sense, like a mirror by reflecting the incident EM wave to a specific direction, while a transmitarray acts similarly to a lens, allowing to pass-through the incident wave with an alteration (or not) of its direction of propagation. The differences between both antennas topologies are depicted in Fig. 2.19.

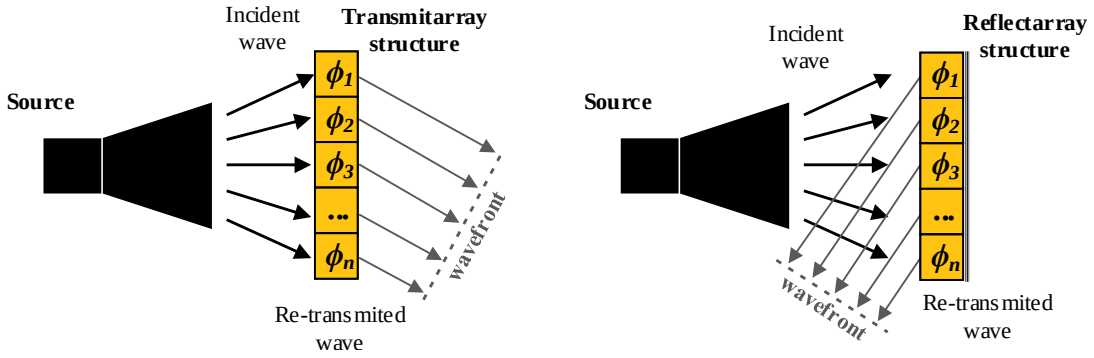

FIGURE 2.19: Generic model of (a) a transmitarray and (b) a reflectarray antenna.

The direction to which the incident wave is being re-radiated depends on the design of the structure. These structures are commonly composed by several resonant unitary elements (unit-cells) with a spatial periodicity forming a planar array [87]. The unit-cells are typically based on simple microstrip patches, or inspired by metamaterials and frequency selective surfaces, as the ones depicted in Fig. 2.20.

By definition metamaterials are artificial man-made structured materials (Fig. 2.20a), able to produce electromagnetic properties (permittivity, permeability and refractive

index) which are unusual or non-existent in nature [11, 12, 88, 89], and such properties can be explored for transmitarray and reflectarray designs. Moreover, due to its spatial filtering capability and particular phase response, FSS [13, 14, 90] (Fig. 2.20b), a particular case study of MM, may also be used as elementary unit-cells of these structures.

Notwithstanding, these unitary elements are designed so that the portion of the EM wave that illuminates each cell can be modified, with an enhanced control of the transmission phase-shift. For example, if a progressive phase progression is applied throughout the entire structure, much like an antenna phased array (Section 2.2.1), beamsteering is possible to be realised [83–86].

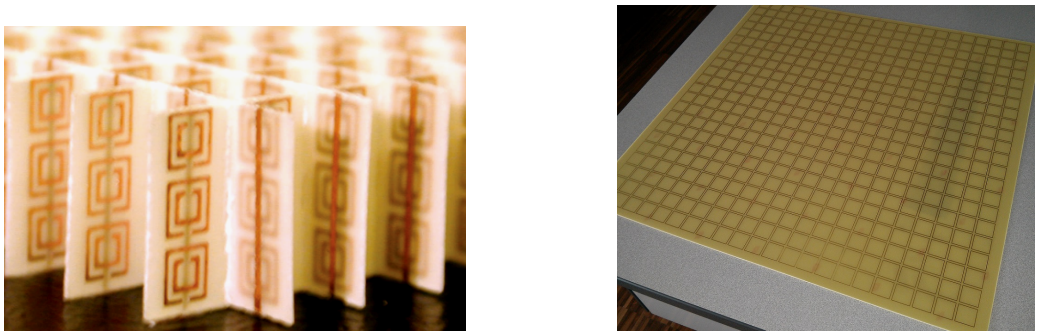

(a) (b)

FIGURE 2.20: (a) Image of the first negative refractive index MM synthesised by *Shelby et. al* and (b) prototype of a FSS structure with band-reject frequency response (images extracted from [89] and [90], respectively).

The most significant difference between a transmitarray and reflectarray is that, in the latter, all power is re-radiated independent on the frequency or cell design. If the unit-cells are not matched to the frequency of operation, the elements will have small effect on the array response and the reflecting ground plane will predominate. In the worst case scenario, the reflected wave could have the same direction of the original one [85, 86]. On the other hand, for a transmitarray, if the structure is not well matched to the free-space or if the unit-cells are not adapted to the frequency of operation, the incident EM wave will be totally reflected back, resulting in no transmission through the structure [83, 84]. Therefore, a transmitarray is desirable to be the most "transparent" as possible, introducing very low loss so the EM field of the propagating wave is not severely attenuated, whereas the reflectarray is desirable to be a perfect reflecting surface so the incident wave can be entirely reflected.

From a practical point of view, since both transmitarray and reflectarray structures are mostly implemented using PCB technology [87], by etching the unit-cell geometries

on a copper covered substrate, they benefit from being planar and thus easy to integrate with other peripherals. Furthermore, they are compatible with discrete Surface-mount Device (SMD) allowing to reduce the size of assemblies, and finally, since they have the electromagnetic feeding source separated from the beamsteering network, they offer higher degree of modularity to the system as opposed to traditional antenna array.

Even though reflectarrays have been studied for years and its design characteristics and procedures are well reported, *e.g.* in [85, 86], the major challenge in its design remains on the independent phase control of each array element.

Traditionally, a microstrip patch is used as single element in reflectarrays [86], as the example presented in Fig. 2.21. However slots, loops, and other element shapes can also be employed [87]. In order to implement an automated control of beam direction, *i.e.* electronic beamsteering, the phase in each element must be reconfigurable, behaving like a phase-shifter in an antenna phased array.

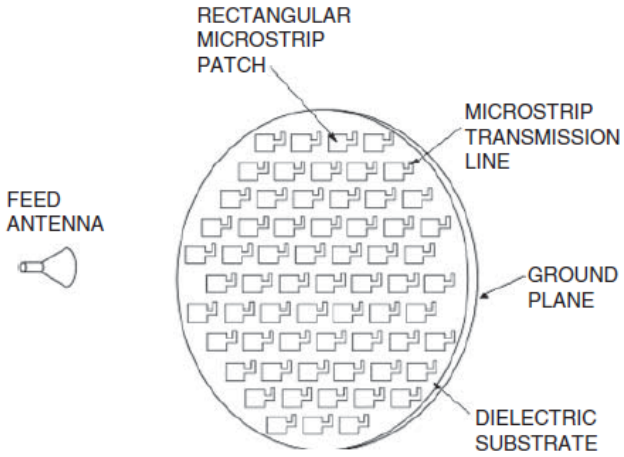

FIGURE 2.21: Reflectarray using printed patch elements (images extracted from [86]).

Remarkably in 2002, *Sievenpiper et. al.* [91, 92], introduced an HIS-based reflector for antenna beamsteering at 4 GHz. The proposed method, comprising a two-dimensional lattice of small resonators with an LC behaviour, provides 2–Dimensional beamsteering by varying, electronically, the capacitance C of such resonators using varactor diodes.

Likewise, electronic reconfigurable reflectarrays have been implemented in [93] and [94], by using PIN diodes and MEMS coupled to delay lines to implement beamsteering, respectively. A prototype of the reflectarray antenna with switched-beam using PIN diodes is depicted in Fig. 2.22 [93], where it is possible to observe the in-layers that possesses the active feeding lines implemented behind the ground plane (Fig. 2.22a) and

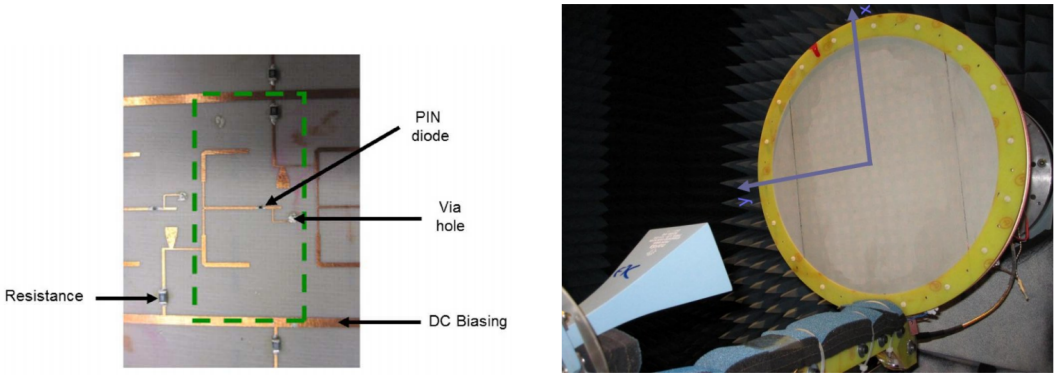

(a) (b)

FIGURE 2.22: Prototype of a reflectarray antenna: (a) antenna during the measurements campaign and (b) image of the in-layer biasing lines loaded the diodes for beam reconfigurability (images extracted from the work presented in [93]).

the complete prototype of the reflectarray spatially separated from the horn antenna (Fig. 2.22b) inside the anechoic chamber for testing. This prototype meritoriously validated the beamsteering ranges achieved in simulation, by steering the beam towards $+5°$ and $-5°$ in a single plane, limited by the 1-bit states provided by the PIN diodes.

Moreover, in [95], *Pozar, D. et. al.* have constructed a fixed beam reflectarray operating at millimetre waves (28 and 70 GHz) using microstrip patch printed over a grounded substrate. In particular, the use of reflectarrays at mmWaves is successfully proven through experiments carried out in prototypes, pointing out the issues of these type of structures, such as phase errors and reduced bandwidth. Also in [96], a prototyped 20×20 reflectarray antenna, with a fixed beam shifted to $45°$ in H plane at 25 GHz, is also presented and a proposal for its electronically control is introduced using MEMS distributed phase-shifters.

Importantly in [97], a reflectarray antenna employing FSS is introduced. The authors use double square ring FSS as unit-cell elements. The square ring shape of the cell are very well known and characterised in the FSS's world since they are one of the most basic shapes characterised so far [13, 14, 90]. Although it is not electronically controlled, in [97], measurements results on a 60 element array achieving 10% of bandwidth at 20 GHz, and an additional steer of the main beam up to $30°$ in azimuth, by varying the length of the double square rings.

Although reflectarrays have been successfully implemented in [85–87, 91–97], the feed blockage remains a challenge in implementation of such type of antennas since the feeding source is on the same side of the radiated field. This may be a challenging depending on the final application that can be overcome with the use of a transmitarray.

Alternatively to reflectarrays, transmitarrays may also be utilised to control the wavefront direction emitted by a source. In fact, this topology has been utilised in

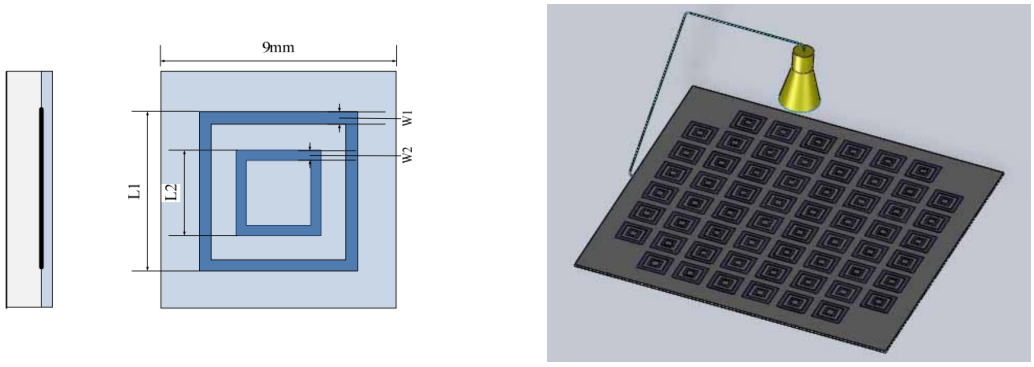

(a) (b)

FIGURE 2.23: (a) FSS unit-cell and (b) respective reflectarray with switch-beam capability (images extracted from the work presented in [97]).

this Ph.D. as the core of novel antenna methods for beamsteering. Due to this fact, a dedicated state-of-the-art on transmitarray is presented in the following section while theoretical background is further introduced in detail in Chapter 4.

Disclosure note

The term Metamaterials has been utilised in some of the author's initial publications. It is the author opinion that work being presented herein, fits the "broad" definition of Metamaterials:

"The word meta, in metamaterials, is a Greek word that means beyond/after, and the term has been coined to represent materials that are artificially fabricated so that they have EM properties that go beyond those found readily in nature. In fact, the word has been used to represent materials, which usually are constructed to exhibit periodic formations whose period is much smaller than the free-space and/or guided wavelength. (. . .) ", in "Advanced Engineering Electromagnetics", Balanis, C.A., 2012 [88].

For this reason, it has been considered that the structures presented in this research work, when seen as a whole, could be considered as a Metamaterial (although its unit-cells elements are inspired in FSS).

However, it was called to the authors attention that the term Metamaterial could have been misused since, in this work, the unit-cell doesn't have dimensions "much smaller than the wavelength" (considering much smaller x10) nor exhibits a Negative Refractive Index (NRI) properties, conditions that according to the definition, are usually essential to define a MM.

Due to this fact, the author have abandoned the term Metamaterials and refer to the structures being developed along this work as "FSS-inspired", giving more emphasis to what is being proposed as base of novel transmitarray designs.

2.5 State-of-the-art on transmitarray antennas

In 1986, *McGrath* firstly introduced in his paper [98] a microwave lens with focusing and scanning capabilities, by simply connecting two microstrip patch antennas using vias in both sides of a planar structure, forming a spatial array of microstrip patches, *i.e.* a transmitarray. Since then, transmitarray have been seen as a feasible alternative to phased antenna arrays and the focus of novel and extensive research. Due to their design simplicity and, more importantly, due to the low manufacture costs (manufactured using PCB techniques), they have been extensively utilised for numerous antenna applications, including wavefront polarisation control and beam reconfigurability. Since these devices are the core of the work presented in this thesis, a dedicated literature review followed by a critical analysis on the most relevant transmitarray designs proposed by other authors, is presented in this section.

2.5.1 Transmitarrays for polarisation control

As already introduced, a transmitarray is a structure spatially separated from a directional feeding RF source, in which the incident EM wave propagates through, experiencing different phase shift or amplitude control. Consequently, the re-radiated field exhibits different characteristics from the incident one. Depending on the design of the structure and on the characteristics of the unit-cells, the transmitarray will behave distinctly. This includes the control of the polarisation of the re-radiated EM wave.

First introduced in [99] and further in [100], the authors have presented a transmitarray with the objective of controlling the polarisation of the wavefront. The proposed structure is based on microstrip patch antennas, whose elements in the outer side of the structure are physically rotated ($\alpha = 0°$, $90°$, $180°$, and $270°$) relative to the patch feeding point), to tilt the polarisation of the re-transmitted wave. The implemented unit-cells and the respective transmitarray are depicted in Fig. 2.24 [100]. The polarisation of the re-radiated wave is forced by tilting of each unit-cell enabling the developed transmitarray to produce a circularly polarised wave. Since the polarisation control is performed through sequential rotation and no other mechanism was implemented to automatically modify the properties of the transmitarray, rather than mechanical movement, the suggested model is considered discrete (passive).

Following the same approach, a novel passive transmitarray was latter introduced in [101] by the same research group. This particular device exhibits an enhanced unit-cell also based on microstrip patch with etched corners. A prototype of the device measured a broadside gain of 22.8 dBi at the simulated frequency with a 3 dB bandwidth of 20% in Right-hand Circular Polarisation (RHCP) and 3 dB axial ratio with bandwidth of 24.4%.

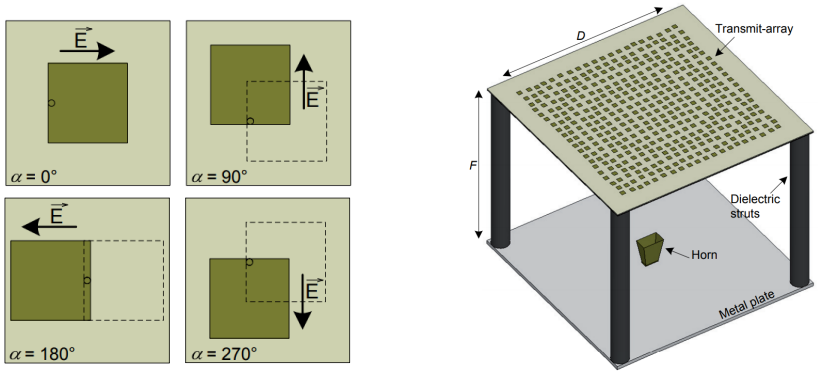

(a) (b)

FIGURE 2.24: (a) Patch unit-cell and (b) transmitarray model for polarisation control (images extracted from the work presented in [100]).

With a novel unit-cell design but following a slightly different methodology, a novel transmitarray was introduced in [102]. The design was implemented by using cascading metallic surfaces to provide polarisation and wavefront control. Two transmitarrays were developed and tested experimentally both based on a quarter-wave plate design that transforms a linearly polarised incident wave into a circularly polarised transmitted wave. Since the phase difference between two orthogonal E-field components is a quarter of the wavelength (90°), when an incident field is linearly polarised at (45°) relative to its axes, the quarter-wave plate converts the transmitted field to circular polarisation. Other passive transmitarray, can be found in [103] by stacking together several layers of rectangle ring slot unit-cells, separated by an air gap. The proposed device is capable of realising Left-hand Circular Polarisation (LHCP), RHCP and linear polarisations, when excited by a linearly polarised feeding source (*Vivaldi* antenna). This is achieved due to the enhanced phased control given by the stacked layers but also by varying the size of the unit-cell throughout the array. By varying the X and Y dimensions of the rectangle ring slot element, transmission magnitude and phase shift for both polarisations can be achieved. Therefore, it is possible to perform a change in polarisation by adjusting the rotation angles of the feeding antenna through the phase of the linearly polarised incoming wave.

Alternatively, it is possible to find in the literature reconfigurable (tunable) transmitarray devices capable of changing their electromagnetic properties electronically, through an external stimulus (bias or voltage). Such designs are typically denoted with the use of PIN diodes, RF-switches, varactors, MEMS, *etc.* as have been reported in some other applications throughout this thesis. It is the case of the reconfigurable circularly polarised transmitarray of Fig. 2.25, presented by *Huang, C. et. al.* in [104]. The authors have suggested two designs of unit-cells for 1-bit phase resolution transmitarray, to operate around 10 GHz. The most complete design presented by the authors consists of two-layer metallic patterns connected by a metallized via-hole as

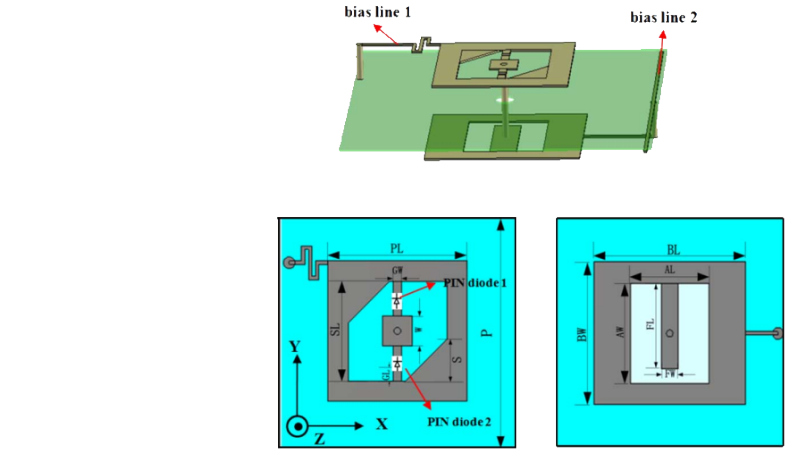

(a)

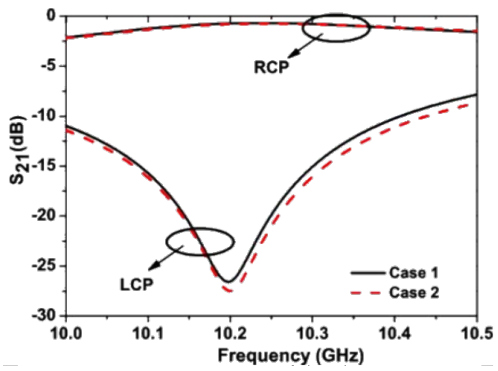

(b)

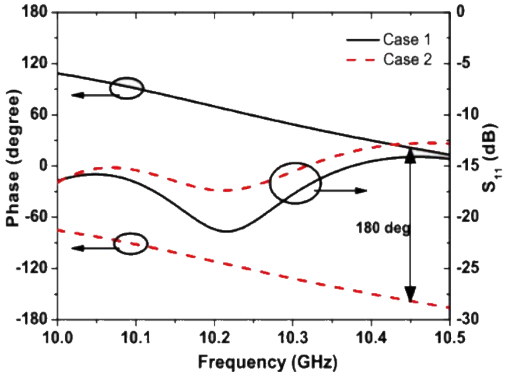

(c)

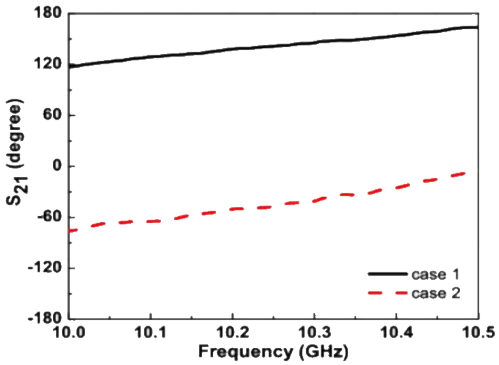

(d)

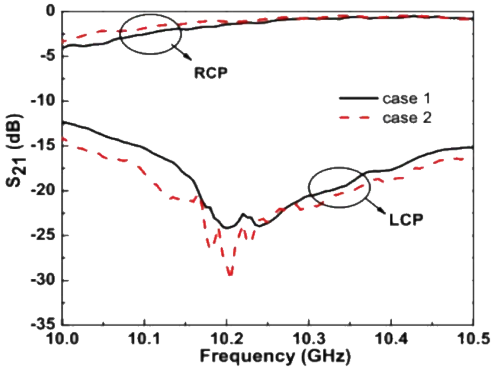

(e)

FIGURE 2.25: (a) Transmitarray unit-cell design loaded with PIN diodes; S_{21} amplitude and phase response for: (b,c) simulated and (d,e) experimental results, respectively. (images extracted from the work presented in [104]).

depicted in Fig. 2.25a. A U-slot rectangular patch is used in one side of the structure to receive the incident wave. On the other side, a square ring patch with two triangular corners and loaded with 2 PIN diodes is utilised to produce circular polarisation. The PIN diodes were used to dynamically select between LHCP and RHCP. The unit-cell operates under two cases: case 1 - PIN diode 1 is switched on while 2 is off; case 2 - PIN diode 1 is switched off while 2 is on. Simulated results (Fig. 2.25b, Fig. 2.25c) on the unit-cell were further validated on a 8×8 transmitarray prototype against experimental results (Fig. 2.25d, Fig. 2.25e). While in case 1, the transmitarray converts a vertically polarised incident wave to RHCP, in case 2 the transmission phase of the outgoing wave is also shifted by 180°. Based on the previous unit-cell design [104], the same research group have introduced and characterised in [105], a transmitarray with both reconfigurable polarisation control and beamsteering capabilities. Besides of controlling the polarisation of the re-transmited EM wave, the proposed transmitarray also has the capability of realising beamsteering in a range of ±45° in both elevation an azimuth planes at 4.8 GHz, exhibiting however insertion losses of 5.6 dB over a small bandwidth of 100 MHz, obtained experimentally on a manufactured prototype.

Similarly in [106] , it has been presented a 20×20 element fully reconfigurable transmitarray based on a 1-bit linear polarisation unit-cell model operating in the Ka-band (27-GHz). A snapshot of both unit-cells and the reconfigurable transmitarray are depicted in Fig. 2.26. The unit-cell is formed in a multi-layer design with a central ground plane (Fig. 2.26a) loaded with PIN diodes to obtain a wideband constant phase shift between the two phase states. Circular polarisation is achieved by using the sequential rotation tecnique previously described, while PIN diodes enable LHCP /RHCP polarisation switching. However, due to the control of the phase shift by switching on and off the PIN diodes, the control of the direction of the outcoming wave is also possible with reported steering ranges of ±60° in azimuth and elevation planes.

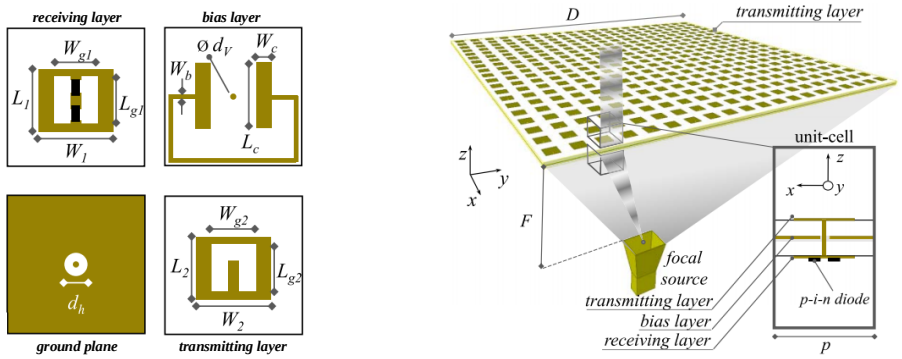

(a) (b)

FIGURE 2.26: Snapshot of (a) the active unit-cell and (b) transmitarray for beamsteering and polarisation control (images extracted from the work presented in [106]).

2.5.2 Transmitarrays for antenna beamsteering

Several examples can be found in the literature for transmitarrays aiming antenna beamsteering. They comprise the use of different materials, unit-cells designs and implementation approaches. However, there is one requirement that must be satisfied to use such structures to steer the main beam of an antenna radiation pattern. The unitary element that composes the transmitarray must have transmission phase that can be varied (tunable) up to 360°, while the transmission magnitude (desirably) remains constant over the bandwidth. This follows in a way, the concept utilised for beamsteering in phased antenna arrays with the use of phase-shifters. Therefore, this section is focused on the review of transmitarrays structures and unit-cell elements, with reconfigurable capabilities that enable electronic beamsteering.

Reconfigurable based on microstrip patches

Particularly in [107], a reconfigurable transmitarray for beamsteering is proposed. The device is composed of a set of patch antennas placed on each side of the array structure and connected by an electronically tunable phase-shifter, where the innovation of this work relies on. The phase-shifter is developed in transmission line technology and consists of a microstrip directional coupler terminated with reflective LC circuits, whose capacitance (C) is controlled by a varactor diode. Consequently, by tuning the value of C, it is possible to selected whether the terminations of the coupler are open- or short- circuit and thus, control the phase-shift between the input and the output of the transmitarray. Nevertheless, this solution turned out to be limited in terms of phase range and since several couplers are cascaded together to overcome this issue, the size and complexity of the phase-shift network is consequently increased. This forced a large separation between the radiating elements, that were arranged in groups of 4 elements and separated by 1.4 wavelengths, leading to the reduction in the scan capability and to the appearing of grating lobes. Therefore, a maximum of 9° of angular shift is reported on the azimuth plane. The proposed solution presents 700 MHz of bandwidth and 3 dB of insertion losses but such values are advertised for the phase-shifter alone and not for the complete transmitarray.

Remarkably in their work, *Lau, J. et. al.* [83, 108–111] have introduced several models of active unit-cells and of electronically controlled transmitarray. Specifically aiming antenna beamsteering, it is presented and characterised in [108] and further improved in [109] a transmitarray element (Fig. 2.27a) that consists of two microstrip patches on either side of a ground plane coupled to a small slot aperture. Each patch is split in half with a small gap in between, and varactor diodes inserted to connect the two halves, while another varactor diode is inserted at the centre of the slot, connecting the two sides of the slot. Together, all these parts act as three coupled tunable resonators

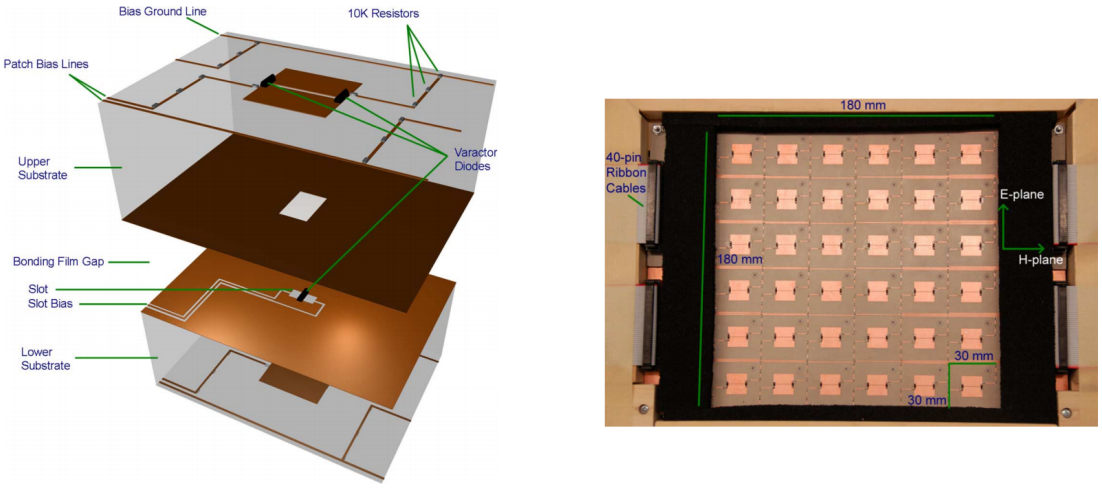

(a) (b)

FIGURE 2.27: (a) Reconfigurable element (exploded-view) and (b) respective transmitarray prototype (images extracted from the work presented in [109]).

that provides a variable phase-shift over 360° with 3 dB of insertion losses, as reported in [109]. However, the losses are slightly increased to 4.8 dB (over the same bandwidth), when the proposed element is composing a 6×6 array and the biasing network to control the varactors are included, as depicted in Fig. 2.27b [109]. Nonetheless, the developed prototype achieved ±25° of electronically controlled beam scanning, in azimuth and elevation planes independently, with a broadside directivity of 20.8 dBi.

As alternative, a different unitary element is proposed and characterised by the same authors in [110]. The unit-cell for transmitarray applications explores the properties of proximity-coupled feeding and aperture coupling [1]. In this solution, the array element is implemented with microstrip patches in both sides of the structure separated by a ground plane. Each patch fed a differential microstrip transmission line by mutual coupling. In one of the sides, possess a differential bridged-T phase-shifter composed by varactor diodes and DC blocking capacitors. Both sides of the structure are further interconnected also by aperture coupling through two open slots etched in the ground plane. According to experiments realised on a single unit-cell using the waveguide method[3], it is notably achieved a tunable phase range of around 425° and insertion loss in average of 3.4 dB at 4.86 GHz. This model is however limited by the narrow bandwidth of the radiating elements and such drawback is mitigated, on a final prototype by employing a stack of microstrip patches. The final array element exhibits insertion losses of around 3.6 dB with a phase range over 400°, but the bandwidth was increased from 100 to 500 MHz at the same central frequency. Subsequently, a 6×6 reconfigurable transmitarray composed of active elements previously described [110] is presented and evaluated in terms of beamsteering performance in [111]. The prototype of the

[3]The waveguide melhod consist of a sample of the unit-cell enclosed between two waveguide flanges.

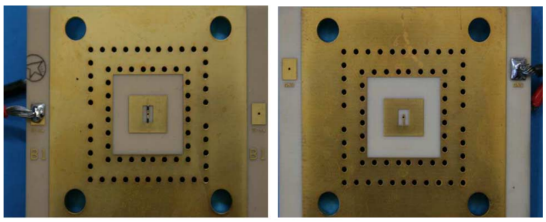

(a)

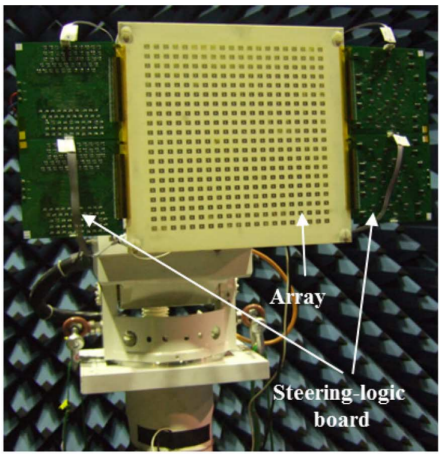

(b)

FIGURE 2.28: (a) Unit-cell design and (b) transmitarray prototype for antenna beamsteering (images extracted from the work presented in [112] and [113], respectively).

transmitarray provides a scanning range of ±50° in both elevation and azimuth planes, with 2.2 dB of insertion losses and 10% bandwidth (500 MHz) at 5 GHz.

Moreover, in [112], a novel unit-cell design is proposed and characterised for an electronic control of the wave direction using a transmitarray. It is composed of a passive microstrip patch antenna with U-shape slot etched on the reception plane, and an active patch with an etched O-shape slot in the re-transmission plane, as depicted in Fig. 2.28a. The active O-shape is loaded with two PIN diodes (and in an alternative design with RF-MEMS) that allow to control the transmission phase by alternatively activating diode states. A 15% of bandwidth and around 3 dB of insertion losses at 10 GHz are reported experimentally on a single unit-cell, evaluated using the waveguide method also employed in [110]. Later in [114], the same unit-cell design using MEMS presents a bandwidth of 16% but 4 dB of insertions losses. In [113] the authors presented a full characterisation of a 20×20 transmitarray comprising 800 PIN diodes and the respective feeding mesh. The prototype is depicted in Fig. 2.28b. The authors state that the proposed transmitarray exhibits a 2D beamsteering capability with maximum ranges of ±40° in elevation and ±70° in azimuth.

Reconfigurable based on tunable metamaterials

Transmitarrays composed of MM to perform antenna beamsteering are also reported in the literature. It is the case of the work described in [115] and [116] , where 1D beamsteering, *i.e.* main lobe limited to steering in a single plane, is demonstrated using such type of materials. Both works [115, 116] suggest new steerable antennas by using controllable MM (electronically reconfigurable) to form the transmitarray. Although implemented with different resonant unit-cell designs (Fig. 2.29), they both respect the same physical principle: tunable refractive index structures are utilised to electronically control the direction of the outcoming wave. The steering is achieved when the refractive index of the MM structure is tuned, leading to a progressive phase distribution along the structure, acting as a linear phased array.

In particular, the proposed transmitarray structures are composed of staked layers of periodically printed sub-wavelength metallic resonators with embedded microwave varactors. By adjusting the varactor diode, the resonant characteristics of the unit-cell is modified controlling, in fact, the associated phase-delay between the first and the last layer of the transmitarray. Consequently, the associated effective refractive index of a single transmitarray element is being adjusted. Accordingly, if a progressive phase between adjacent elements is applied through the array in order to perform beamsteering, the metamaterial exhibits a gradient index of refraction, when seen as an whole.

Therefore in [115], 6 stacked layers of a double-layer I-shaped unit-cell (Fig. 2.29a) are suggested as array element, exhibiting 360° of phase-shift at 1.6 GHz while the varactor is tuned from 0.1 pF to 1.9 pF, with insertion losses of 4 dB (averaged). Bandwidth is not referred by the authors. A continuous scanning range of ±30° in the azimuth plane is achieved using a full wave simulator. Although it is stated that experimental results obtained on a prototype are consistent with simulation ones, the paper lacks a more elaborated and physically grounded analysis of the results.

Notably in [116], a complete characterisation of a metamaterial transmitarray composed by the unit cell presented in Fig. 2.29b was performed. In addition to the transmitarray, an array of microstrip patch antennas was also developed to serve as feeding source. The prototype, implemented on a stacked layer structure (Fig. 2.30a), presents an angular steering range of ±30° in azimuth verified under experiments at 4.7 GHz. Some samples of radiation pattern are demonstrated by the authors in their paper and illustrated in Fig. 2.30b.

Although introduced as metamaterials by analysing the refractive index of the array element, it can be noticed that such structures are in fact frequency selective surfaces. While the unit-cell presented in [115] exhibits a low-pass filtering frequency response, the unit-cell of reference [116] possesses a band-pass filtering type. Herein, is when the term metamaterials could be misleading as disclosed at the beginning of this thesis.

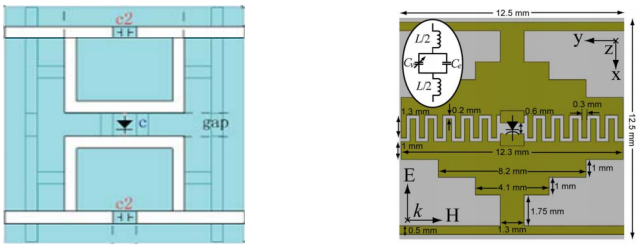

(a) (b)

FIGURE 2.29: Metamaterial unit-cells for transmitarray antennas presented by (a) *Yongzhi S. et. al.* and by (b) *Jiang T. et. al.* (images extracted from the work presented in [115] and [116], respectively).

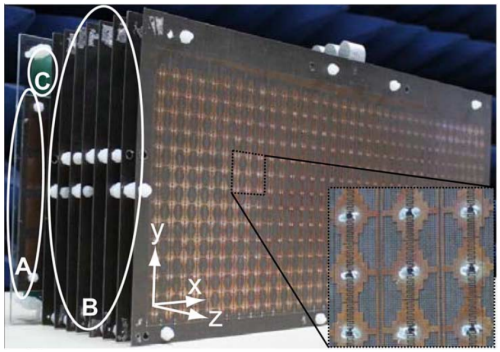

(a)

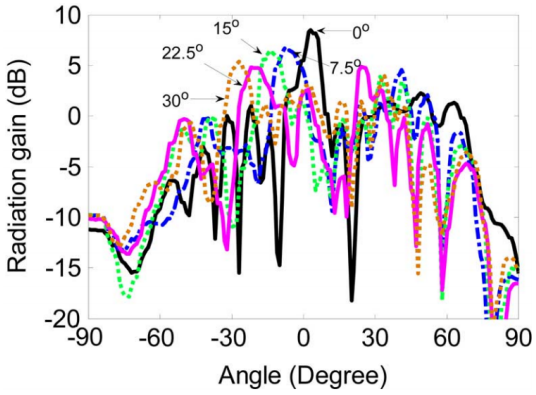

(b)

FIGURE 2.30: (a) Prototype of the MM beamsteering antenna and (b) measured radiation pattern for different steering angles (images extracted from the work presented in [116]).

Reconfigurable based on FSS

Frequency Selective Surfaces are, per se, a timely topic on the field of (antennas and) propagation that have been studied for years. A FSS is a spacial filter that exhibits distinct resonant filtering characteristics *e.g.*: band-pass, band-stop, high-pass or low-pass, that depend on the format and on the dimensions of periodic resonant geometries etched over a metallic coated substrate [13, 14]. As a spacial filter, these structures are able to allow or block the propagation of an incident EM wave within a specific frequency band and even control its propagation phase.

Much of the work about FSS relies on the study and development of novel unit-cell designs for EM blockage (shielding) or radio coverage enhancement [13, 14, 90, 117, 118]. However, new applications have recently emerged by exploring the use FSS in new antenna designs [119–121], and in various transmitarray implementations [122–127].

For example in [122], a wideband transmitarray is suggested by using a FSS of double square rings unit-cells. The authors have demonstrated that the phase-shift introduced by the transmitarray can be varied by simply modifying the physical size of the squares, and such can be further improved by stacking several layers of FSS on top of each others. In fact, the concept of stacked layers separated by an air gap is widely used for transmitarrays implemented with FSS since it allows to increase both the bandwidth and the transmission phase of the structure, as reported in [13, 83, 125, 128].

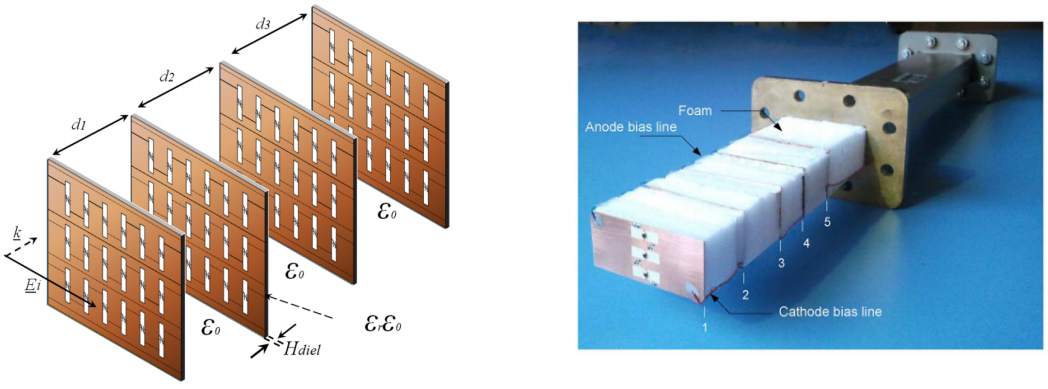

(a) (b)

FIGURE 2.31: (a) FSS transmitarray model and (b) respective unit-cell prototype evaluated using the waveguide method (images extracted from the work presented in [124] and [125], respectively).

In particular, some examples can be found in [123–127] by presenting reconfigurable transmitarrays of FSS for antenna beamsteering. The majority of the work utilises

varactor diodes to electronically control the capacitance of the equivalent LC circuit that characterises the resonant unit-cell design, as presented by *Russo et. al.* in [123–125]. In their work, a tunable pass-band FSS suitable for beamsteering operations is proposed. The suggested FSS, depicted in Fig. 2.31a, is evaluated by simulations in [123, 124] and experimentally characterised in [125], also using the waveguide method (Fig. 2.31b), previously described. The proposed structure is capable of bandwidths ranging from 1% to 10% (with a few modifications in original design) at 4 GHz, with a transmission amplitude that remains above 3 dB within the varactor tuning range. Although the transmission phase obtained from experiments varies by approximately 360° over the whole bandwidth, making this design suitable for beamsteering, the paper does not include the implementation of a complete transmitarray and respective beamsteering characterisation.

In [126], an active FSS based on the traditional squared-slot design with band-pass filtering characteristics is implemented for antenna beamsteering, as depicted in Fig. 2.32. Varactor diodes are used to tune the FSS and control the phase-shift, with range up to 360°, of a structure composed of 5 stacked layers. In fact, the authors have demonstrated on a physical prototype, illustrated in Fig. 2.32b, that through different configurations of the bias voltages applied to the varactors, a gradient phase distribution along the transmitarray can be utilised to steer the radiation pattern of a horn antenna. This corroborates with the facts presented for MM transmitarrays introduced in last section. Although the work show its merits by presenting a tunable steering range of ±30° in both azimuth and elevation plans at 5.3 GHz, as depicted in Fig. 2.32c and Fig. 2.32d respectively, it is a fact that such scanning angle can only satisfy one steering direction at the time. Therefore, two-dimensional beamsteering, *i.e.* steer the main lobe to a direction with two spatial components as a planar array (presented in Section 2.2.1) is still unachievable with this device.

Alternatively in [127], a tunable FSS with beam steering capability is presented. The FSS is used as a transmitarray with a bandpass characteristic centred at 12 GHz. The novelty of the work relies on the FSS design which is composed of capacitive (parallel electrodes) and inductive (vertical wires) structures printed on a Barium-Strontium-Titanate (BST) thick-film ceramic, as illustrated in Fig. 2.33. The tunability is performed due to the properties of the BST substrate that can be tuned by applying an external electrostatic field across the material, and not by using discrete components such varactors or PIN diodes. By applying a DC field between the electrodes of the capacitor, the effective permittivity is reduced resulting also in a capacitance reduction. Experiments realised on a 40×40 FSS transmitarray (Fig. 2.33b), report a maximum phase difference of 121° at 12 GHz when the bias voltage is ranging from 0 V (untuned state) and 120 V (maximum tuning state). Within such voltage range, the main beam of a feeding horn antenna is steered up to ±10° in the azimuth plane, due to the

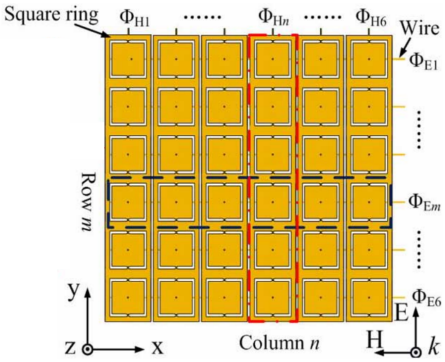

(a)

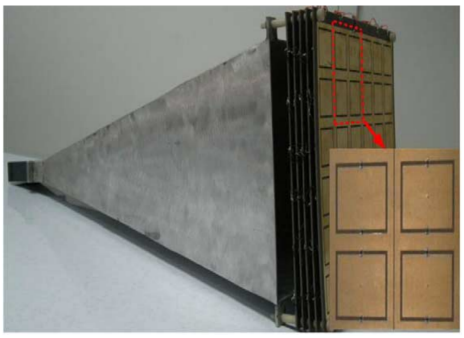

(b)

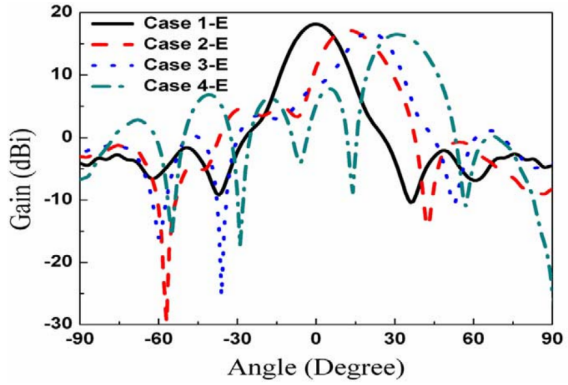

(c)

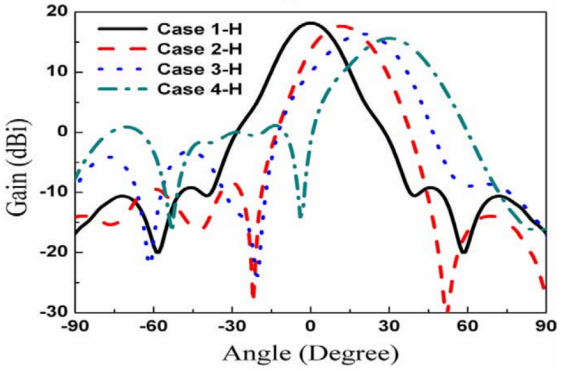

(d)

FIGURE 2.32: (a) 6×6 square slot FSS model, (b) transmitarray antenna prototype, (c,d) measured radiation pattern in azimuth and elevation planes, respectively (images extracted from the work presented in [126]).

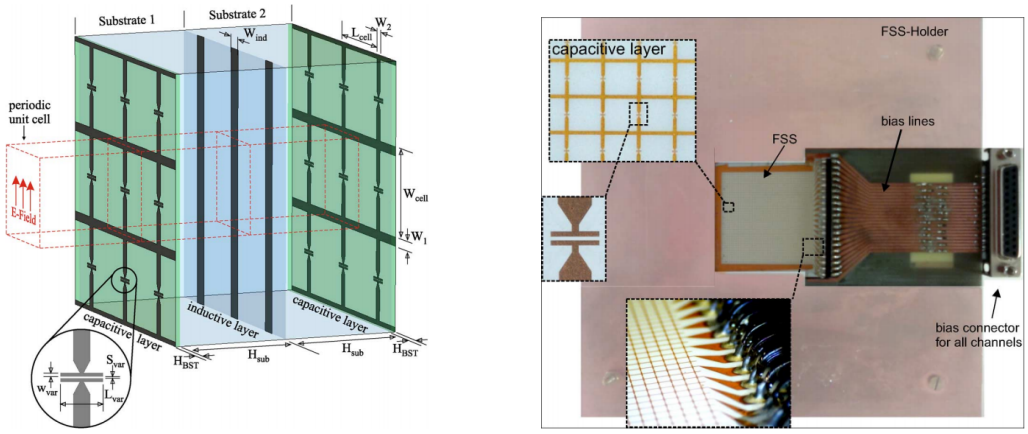

(a) (b)

FIGURE 2.33: (a) FSS transmitarray model and (b) respective transmitarray prototype (images extracted from the work presented in [127]).

low phase-shift (121°) produced by the structure. Although showing its merits, the proposed solution is one of a type in the literature, possible due to the impractical voltage values necessary to apply for tuning the structure and perform beamsteering limited 1-Dimension, in comparison with other state-of-the-art proposals.

The references presented in this review of the literature are summarised in Table 2.2, listed by their main feature (polarisation control and beamsteering), mode of operation (P - passive, A - active), unit-cell (UC) design format and size, reconfigurability control mechanism, frequency of operation, bandwidth, insertion losses and beamsteering angular ranges with respective steering planes, when applicable.

2.6 Interim conclusions

This chapter presents an extensive literature review addressing the most relevant topics for this research work. It reviews antenna beamsteering technologies for wireless systems, giving particular emphasis to the realisation of antenna beamsteering by using transmitarrays devices.

A fundamental overview on the concept of beamsteering is introduced and supported by theoretical analysis of antenna arrays, as the most common systems that can realise beamforming and steer the main lobe of an antenna's radiation pattern. Besides the physical factors (element spacing, element shape and dimensions, *etc.*) that characterise an array of antennas, it is verified that the phase and amplitude of the RF signal applied to each element that composes the array also play an important role in array performance. In fact, this is disseminated through the mathematical computation of

Table 2.2
Summary table of references for polarisation control (Pol.) and beamsteering (BS) transmitarrays

Ref.	Feature	Mode†	UC type	UC size	Control mechanism	Freq. band	Bandwidth	Loss	BS Range
[99, 100]	Pol.	P	microstrip patch	$0.5\lambda \times 0.5\lambda$*	cell rotation	60 GHz*	5.6 GHz*	0.46 dB*	n/a
[101]		P	microstrip patch	$0.5\lambda \times 0.5\lambda$	cell rotation	30 GHz	6.5 GHz	n/a	n/a
[102]		P	multi-layer PCB	$0.28\lambda \times 0.28\lambda$	cascading surfaces	77 GHz	13 GHz	n/a	n/a
[103]		P	cascaded rectangle ring slot	$0.6\lambda \times 0.6\lambda$	feeding source rotation	6 GHz	1.8 GHz	n/a	n/a
[104]		A	U-slot patch	$0.47\lambda \times 0.47\lambda$	PIN diodes	10 GHz	320 MHz	1.4 dB	n/a
[105]	BS & Pol.	A	U-slot coupled feed patch	$0.488\lambda \times 0.488\lambda$	PIN diodes	4.8 GHz	100 MHz	5.6 dB	$\pm 45°(Az\ and\ El)$
[106]		A	rectangle ring slot	$0.46\lambda \times 0.46\lambda$	PIN diodes	27 GHz	4.2 GHz	3 dB	$\pm 60°(Az\ and\ El)$
[107]	BS	A	microstrip patch	n/a	varactor diodes	12 GHz	700 MHz	3 dB	$+9°(Az\ only)$
[108, 109]		A	microstrip patch	$0.55\lambda \times 0.55\lambda$	varactor diodes	5.7 GHz	n/a	4.8dB	$\pm 25°\star(Az\ or\ El)$
[110]		A	coupled feed patch	$0.55\lambda \times 0.55\lambda$*	varactor diodes	5 GHz*	500 MHz*	3.6 dB*	n/a
[111]		A	coupled feed patch	$0.55\lambda \times 0.55\lambda$	varactor diodes	5 GHz	500 MHz	2.2 dB	$\pm 50°\star(Az\ and\ El)$
[112–114]		A	microstrip patch	$0.5\lambda \times 0.5\lambda$	PIN diodes (and MEMS)	10 GHz	1.5 GHz	3 dB	$\pm 70°(Az)\ and\ \pm 40°(El)$
[115]		A	metamaterials	$0.17\lambda \times 0.17\lambda$	varactor diodes	1.7 GHz	n/a	4 dB	$\pm 30°\star(Az\ only)$
[116]		A	metamaterials	$0.61\lambda \times 0.61\lambda$	varactor diodes	4.7 GHz	250 MHz	n/a	$\pm 30°\star(Az\ only)$
[123–125]		A	freq. selective surface	$0.5\lambda \times 0.5\lambda$*	varactor diodes	4 GHz*	400 MHz*	3 dB*	n/a
[126]		A	freq. selective surface	$0.58\lambda \times 0.58\lambda$	varactor diodes	5.3 GHz	180 MHz	6.5 dB	$\pm 30°\star(Az\ or\ El)$
[127]		A	freq. selective surface	$\lambda/25 \times \lambda/25$	tunable ferroelectric film	12 GHz	n/a	2.9 dB	$\pm 10°(Az\ only)$

† modes for unit-cells: P - passive, A - active;
* considering the best case of 2 proposed designs;
⋆ steering range with SLL<12dB;
n/a - not available.

the Array Factor formula, for an ideal linear array, excited with different progressive phase patterns between its elements. With this analysis, it was verified that to perform beamsteering with an array of antennas, the phase must be varied, progressively and equally, throughout the entire array. Section 2.2.2 was then dedicated to antenna phased arrays that can enable beamsteering, just by varying the phase in each element, *e.g.* by using a phase-shifter of fixed delay lines, while the amplitude of the input signal is maintained constant (uniform). As alternative, but also capable of enabling beamsteering, switched-beam antennas were also covered in this review. These are implemented using a switching mechanism to select which element(s) of an array are radiating, *e.g.* to aim at distinct locations in space, instead of controlling the phase-shift per element.

Although beamsteering and beamforming systems based on arrays of radiating elements are widely used (phased arrays and switched-beam antennas), they have a relatively high implementation costs and energy consumption, that grow exponentially with the number elements of the array and also with the frequency of operation. Moreover, their feeding network complexity also suffers from large number of feeding lines needed to redistribute the RF signal to all array elements, which rapidly may become a drawback of theses systems.

Subsequently, smart-antennas are introduced in Section 2.3. Such systems, usually deployed over an array of antennas, provide intelligence to the antenna's physical layer enabling "smart" decisions regarding the direction of radiation. The decision is made in real time by very powerful digital processors, running heavy computation algorithms. They estimate the direction of arrival and compensate, in-the-loop, the necessary phase and the amplitude (weights) to attribute in each antenna branch for a specific steering case.

After having introduced the most common manners of controlling the direction of an antenna radiation pattern, other possible techniques to realise beamsteering are presented in Section 2.4. Such comprehend the use of mechanical mounts for antenna rotation, novel antenna designs based on microfluidics, or even the use reflectarray and transmitarray structures for antenna implementation. Mechanical mounts for antenna orientation tend to be bulky and subjected to intense wear and tear and thus, impractical for most of applications. Microfluidic antennas have a huge potential for beamsteering and beamforming, but the technology is not mature (yet) and their acceptance is unpredictable. Additional, such method is still risky since the of leakage of the hazard fluids utilised in their composition, may be a danger for equipments and public health. Finally, reflectarray antennas suffer from feed blockage since the feeding source is placed on the same side of the re-radiated wave.

Thus, transmitarray antennas are seen as a feasible alternative to the techniques referred so far, overcoming some of the presented limitations. By employing transmit-

array for antenna beamsteering, it withdraws the requirements of mechanical components or complex beamsteering networks. In particular, phase-shifters can be replaced by other phasing control mechanisms, such as artificial structured materials inspired in FSS for a customised phase response and a personalised EM interaction. Since transmitarray are mostly employing using PCB techniques, they will significantly reduce weight, power consumption and the dimensions of assemblies, making them very attractive for inclusion in a large number of applications and, *e.g.* ready to embedded in future 5G devices.

Therefore, in Section 2.5, a detailed state-of-the-art literature review is presented on transmitarray antennas, including several examples of its application for wavefront control. Namely, transmitarrays for polarisation conversion of the incident EM wave and beamsteering are presented. Special attention was given to the design of the unit-cells, that can be either discrete (passive) or reconfigurable (active), and inspired on simple microstrip patch antennas, metamaterials, frequency selective surfaces or having other more complex designs. Finally, the references presented in this review of the literature are summarised in Table 2.2.

CHAPTER 3

Overview of the measurement systems

3.1 Introduction

A wide range of measurements were performed in this research work in order to validate and characterise the developed prototypes. The experiments were always conducted in an electromagnetic controlled environment, *i.e.* inside an anechoic chamber, aiming to characterise the FSS transmitarrays in terms of electromagnetic radiation and beamsteering performance.

The measurement campaign was conducted in two phases corresponding to two physically distinct facilities, namely:

- **Stage1:** characterisation of a passive and of an electronically reconfigurable (active) transmitarrays, held in the Radio and Propagation Laboratory at the University of South Wales (USW), Treforest, Wales;
- **Stage2:** characterisation of a second active transmitarray, held in the Radio Systems Laboratory of Instituto de Telecomunicações – Leiria located at the Instituto Politécnico de Leiria (IPL), Leiria, Portugal.

In this chapter, the measurement setups and techniques are identified and characterised, therefore guaranteeing the validity of all measurement results and hence of this research work. The description covers the test environment, mechanical rigs, developed measuring techniques, RF measurement equipment, antennas, cables and all other relevant peripherals. An overall measurement system analysis is also provided in this chapter, reporting relevant metrics such as dynamic range, accuracy and repeatability of results.

3.2 Methodology

In particular, antenna radiation patterns have been measured to study the changes caused in the shape of the main beam of a reference standard gain horn antenna, when using the prototypes of the transmitarrays coupled to the antenna's aperture. The majority of the radiation patterns were obtained using a frequency broadband technique, retrieving all the information about amplitude and phase of the EM signal in a frequency band defined between 4 and 6 GHz, and over an angular range defined between $-90° \leq Az \leq 90°$ and $-30° \leq El \leq 30°$. However, to assist with system calibration and for a quick inspection of the output angle direction, radiation patterns for a single frequency point (using a continuous scan technique) were also obtained within the same angular range. The implementation of both frequency broadband and single frequency continuous scan techniques are further described in this chapter.

The radiation patterns were therefore obtained for a single antenna configuration, as follows:

- **Reference measurement** – the measurement considered as reference for all single antenna measurements. The radiation pattern of a well characterised standard gain horn antenna was measured for further comparison and to assist with results normalisation;
- **Single antenna measurements** – the measurements conducted when the passive or the reconfigurable (active) transmitarray prototypes were attached to the reference standard horn antenna.

These configurations were mostly used to characterise the experiments reported in Chapter 5 and 6 of this document.

Through the analysis of the measured results, the beamsteering capability was further characterised by analysing the obtained radiation patterns in terms of:

- **Main lobe steering direction** – considering the higher absolute gain direction in dBi;
- **Half power beamwidth (HPBW)** – the width of the main lobe at -3 dB below the maximum gain;
- **Side-to-main lobe level (SLL)** – the amplitude difference between the main lobe and the higher side lobe of the radiation pattern.

In addition to antenna radiation pattern, reflection coefficient S_{11} /S_{22} (antenna matching) were also obtained for a complete system characterisation. All the measurement were performed inside an anechoic chamber.

3.3 Anechoic chamber and peripherals

In this work, all the measurements were conducted inside the anechoic chamber present in both USW (Fig. 3.6) and IT laboratories. The anechoic chamber was used for indoor measurements enabling experiments to be performed in a controlled, electromagnetically quiet and reflection free radio environment.

In the USW facilities, the chamber offered an usable length of 5.25 m, a width of 2.15 m and a height of 2.5 m while at IT it offered an usable length of 5.7 m, a width of 4.8 m and height of 2.9 m.

Both chambers, installed by the same supplier *"Emerson & Cumming, Inc"*, have their interior walls, ground and ceiling, completely shielded from possible exterior RF interferences by a protective metal foil. These are also covered with very high performance broadband pyramidal absorbers *"Eccosorb VHP-8"* and *"Eccosorb VHP-12"*. The absorbers pyramids, composed by urethane foam loaded with carbon, offer a minimum reflection coefficient of -25 dB for RF signals above 500 MHz [129], covering the range of frequencies used throughout this research work.

An *"Agilent PNA 5320A"* and a *"Rhode & Schwartz ZVM"* Vector Network Analysers were used in USW and IT laboratories, respectively, for S-parameter measuring.

The turntables from the manufacturer *"Parker, Inc"* model *"200RT"*, described in the arrangements of Section 3.4, were utilised to rotate the Device Under Test (DUT) and assist with radiation pattern measurement. These turntables, also similar in both USW and IT facilities, are controlled using two independent indexers and the corresponding stepper drives.

In order to keep the environment inside the anechoic chambers undisturbed, while minimising possible human errors during the measurement experiments, the Vector Network Analyser (VNA) and tables indexers were located outside the chamber and remotely controlled through a control computer, via General Purpose Interface Bus (GPIB) and RS-232 serial link, respectively. Figure 3.1 illustrates the apparatus for measurement in USW laboratory.

A measurement software, specifically developed in MATLAB, was used to control and monitor the entire measurement process. The software application, which was installed in the control computer, took care of all the measurement procedure. The actions being performed, as well as the measurement results, were displayed to the user in real time, therefore allowing the user to completely monitor the measurement process.

In order to prevent an undesirable measurement and configuration data loss in the event of a power supply failure, the initialisation configurations and the measurement

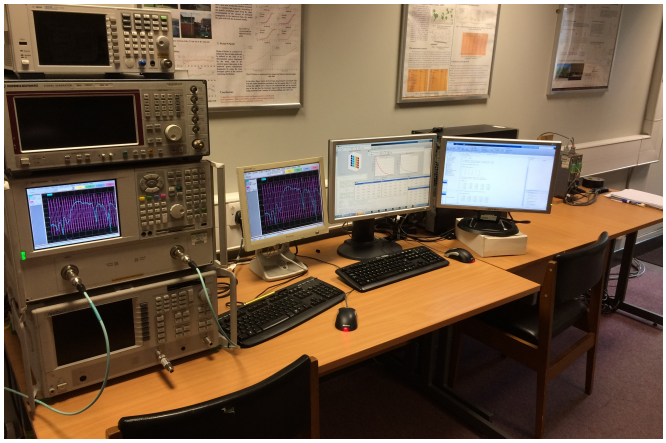

FIGURE 3.1: Measurement apparatus in the USW laboratory facilities.

results were saved in MATLAB data files using an appropriate data structure, allowing them to be retrieved later in the measurement software or in other MATLAB applications.

All the measurements were taken over a sufficiently large time, and averaged to allow a stable mean signal level to be obtained. A margin of ± 0.5 dB error in $S - parameter$ aquisition is considered which correspond to the typical uncertanty associated to the utilised Vector Network Analysers.

3.4 Antenna radiation pattern measurement setup

In order to obtain antenna radiation patterns, a measurement setup for a single antenna measuring was implemented and characterised. The measurement setup were designed so radiation patterns were obtained in the antenna's far-field distance by the means of S-parameter readings. The experimental setup and the fundamental concepts for its interpretation are thoroughly described as herein.

3.4.1 Scattering parameters

Linear two-port networks may be characterised by several equivalent circuit parameters, namely: transfer, impedance or scattering matrices [19]. With respect to Fig. 3.2, which represents a generalized two-port network, the transfer matrix relates the voltage and current at port 1, to those at port 2, as is defined by (3.1).

$$\begin{bmatrix} V_1 \\ I_2 \end{bmatrix} = \begin{bmatrix} A & B \\ C & D \end{bmatrix} \begin{bmatrix} V_2 \\ I_2 \end{bmatrix} \tag{3.1}$$

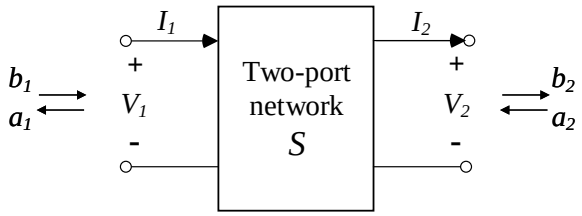

FIGURE 3.2: Block diagram of a two-port network (image adapted from [19]).

The impedance matrix, in (3.2), relates the voltages $V_!$ and V_2 to the currents I_1 and I_2.

$$\begin{bmatrix} V_1 \\ V_2 \end{bmatrix} = \begin{bmatrix} Z_{11} & Z_{12} \\ Z_{21} & Z_{22} \end{bmatrix} \begin{bmatrix} I_1 \\ I_2 \end{bmatrix} \tag{3.2}$$

The scattering matrix relates the outgoing waves, b_1 and b_2, to the incoming waves, a_1 and a_2, as depicted in (3.3).

$$\begin{bmatrix} b_1 \\ b_2 \end{bmatrix} = \begin{bmatrix} S_{11} & S_{12} \\ S_{21} & S_{22} \end{bmatrix} \begin{bmatrix} a_1 \\ a_2 \end{bmatrix}, \quad S = \begin{bmatrix} S_{11} & S_{12} \\ S_{21} & S_{22} \end{bmatrix} \tag{3.3}$$

In the scattering parameters (S-parameters), S_{11} and S_{22} are reflection coefficients, where S_{21} and S_{12} are transmission coefficients. A two-port VNA performing a transmission measurement typically operates by transmitting a frequency-swept pulse, of known amplitude and phase, followed by measuring the received signal on the other of its ports, as depicted in Fig. 3.3.

This way, one can obtain the specific frequency response of the network it was connected to, at the instant of time the measurement was being performed. All measurements obtained in the anechoic chamber follow this description, in which the frequency response of the radio channel is extracted in the form of its S-parameters. By performing two measurements, one without a DUT, and another with the DUT, one can normalise the frequency response, therefore obtaining the particular impact that the DUT has on the radio channel.

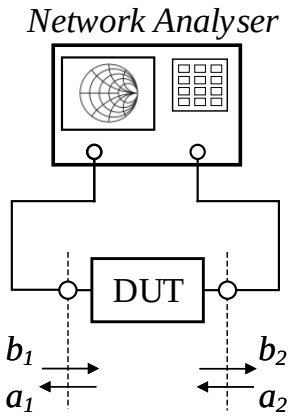

FIGURE 3.3: Network analyser connected to DUT (image adapted from [19]).

3.4.2 The far-field distance

The far-field or *Fraunhofer* region is defined as the region where the angular field distribution of an antenna is essentially independent of the radial distance from the antenna [1]. Consequently, it is also the region where the radiation pattern no longer varies with the radial distance from the antenna. This region extends from a minimum radial distance R boundary to infinity. The lower radial distance limit for the *Fraunhofer* region is given by (3.4),

$$R = \frac{2D^2}{\lambda}, \tag{3.4}$$

where D is the largest linear dimension of the antenna and λ is the signal wavelength.

The minimum far-field distances corresponding to the various antennas used during this project are presented in Table 3.1. The values are presented for $f = 5$ GHz ($\lambda = 60$ mm), which corresponds to the centre frequency defined of the sweep range considered for broadband measurements (4 to 6 GHz). Moreover, R is considered the dimension defined by the diagonal of the horn antenna aperture.

TABLE 3.1
ANTENNAS MINIMUM FAR-FIELD DISTANCE OBTAINED AT $f = 5\ GHz$.

Manufacturer	Model	Type	Aperture dim.	D_{max}	R
"The Waveguide Solution"	20 dBi S.G.*	Horn	230 mm × 170 mm	286 mm	2.73 m
"Flann Microwave"	DP241	Horn	50 mm × 50 mm	70.7 mm	167 mm

S.G.* - Standard Gain

3.4.3 Single antenna setup

The single antenna setup was designed to measure the 3D radiation pattern of an individual antenna, at the time. The block diagram of the setup is illustrated in Fig. 3.4, as a side-view representation. This setup allowed to obtain the radiation patterns for the reference horn antenna (20 dBi Standard gain manufactured by *"The Waveguide Solutions"*) and also the radiation patterns when the prototypes of the transmitarrays were attached to this reference horn antenna, for characterisation. Both cases are herein considered as DUT, for simplification.

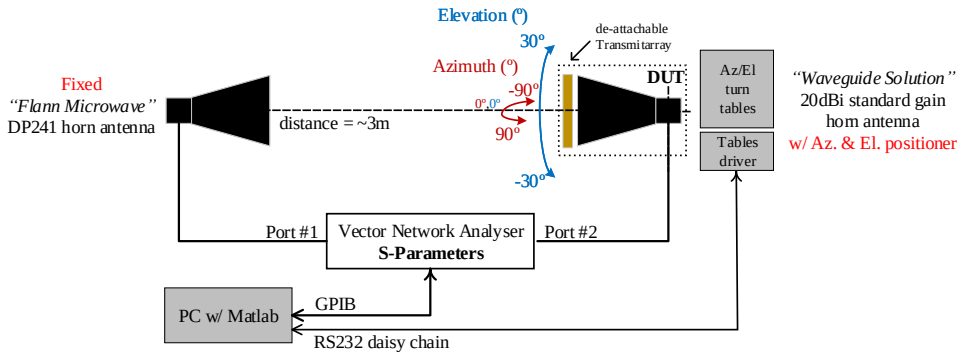

FIGURE 3.4: Side-view representation of the setup for single antenna radiation pattern measurements.

The measurement was performed by reading the S_{21} or the S_{12} parameters using a VNA. While a well characterised antenna from *"Flann Microwave"* [130], connected to VNA's port #1, was kept fixed throughout all measurements, the DUT connected to VNA's port #2, was made to rotate in its own axis by using set of motorised turntables. The tables disposed in an *Azimuth-over-Elevation* fashion (Fig 3.5), were able to accurately rotate the DUT with an angular resolution of at least 0.004 degrees, in both Azimuth and Elevation planes. However, in this measurement campaign, only 1 degree of resolution was considered since this value was found to be a relatively good agreement between angular detail and measurement time.

The DUT was fixed to the vertical table, and aligned to the centre of motion, by using a double L-shape bracket. However, due to the physical limits imposed by the mechanical rig, the radiation patterns were only able to be obtained within the angular range defined between $-90° \leq Az \leq 90°$ and $-30° \leq El \leq 30°$. This angular range was however sufficient large to characterise experientially the DUT and have a fair comparison with simulated results.

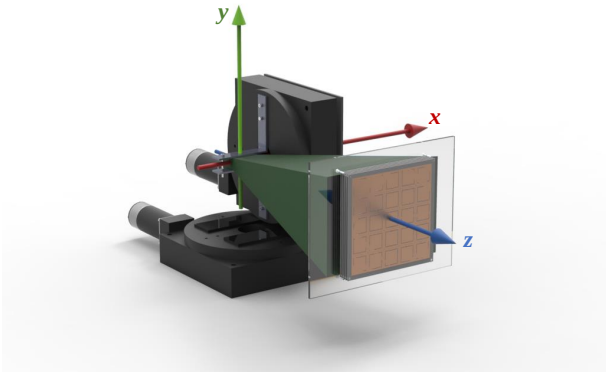

(a)

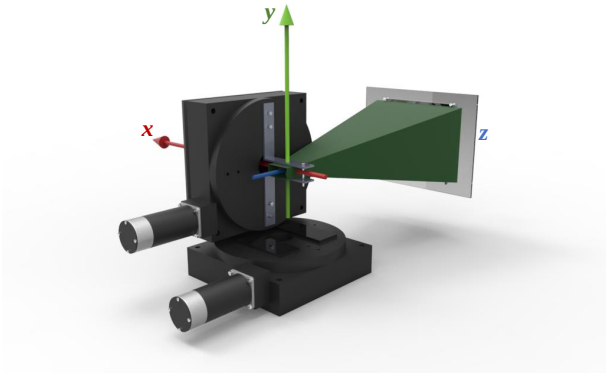

(b)

FIGURE 3.5: (a) Front-view and (b) back-view of the *Azimuth-over-Elevation* setup for single radiation pattern measurements.

The attribution of the transmitter and receiver antennas' position were defined by the type of S-parameter being read from the VNA. To this extent, when the S_{21} was acquired, the transmitter was set at Port #1 while receiver was set at Port #2. On the other hand, when reading the S_{12} the transmitter was set at Port #2 while the receiver was at #1. This feature enabled to study and characterise the reciprocity of the DUT, either as a transmitting and receiving antenna. The default setting was set to read the S_{21} parameter, and only this is consider from now on in schematic representations and system description.

The distance between both transmitter and receiver was set to approximately 3 meters to ensure that the measurements were carried out within the far-field region of the horn antennas (Section 3.4.2). Moreover, the distance between the antennas to the chamber walls and floor was set to at least 1 m. This ensures that the location of the measurement devices remains in the quiet zone of the anechoic chamber. Figure 3.6 shows the arrangement for single radiation pattern measurement inside the anechoic chamber at USW facilities.

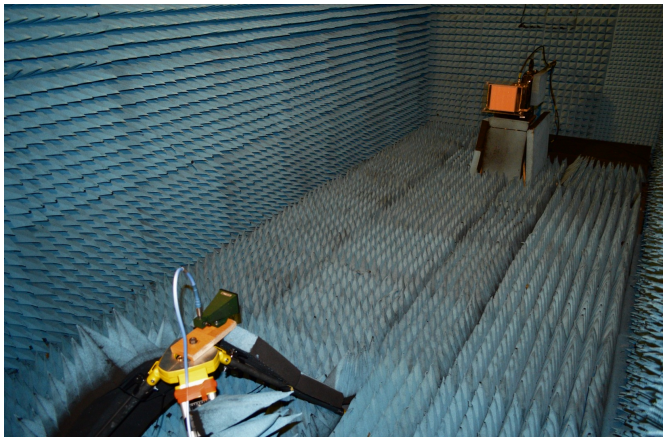

FIGURE 3.6: Setup inside the anechoic chamber (USW) for single radiation pattern measurements.

To obtain data, a VNA previously calibrated was used and controlled remotely via GPIB-bus from a control computer while synchronized with the tables motion, these in turn, controlled via serial-port (RS-232 link). Measurement data was recorded in MATLAB. The way data is extracted and synchronized with tables motion define the measuring techniques described in Section 3.6.

3.4.4 The *Perspex* mount

In order to fix the transmitarray in front of the reference horn antenna a supporting mount was developed. The mount, composed of two sheets of *Perspex* material, with dimensions of 300 mm × 230 mm and 5 mm of thickness, allowed to easily attach/ de-attach the transmitarray to the antenna's aperture.

The perspex mount is depicted in Fig. 3.7. One of the *Perspex* sheets was trimmed in the centre with the dimension of the reference horn aperture (230 mm × 170 mm) and glued to reference antenna next to the aperture's edge. This frame was always considered throughout the measurements including the reference one.

Likewise, the second perspex sheet was trimmed in the centre with a square of dimension 165 mm × 165 mm, corresponding to the area of the FSS covered by copper. The transmitarray was fixed to the perspex by using 3 mm nylon screws and 0.5 mm Teflon (Polytetrafluoroethylene (PTFE)) washers.

At the time of the measurements and when necessary, the two perspex frames were attached to each other also by using 4 mm nylon screws.

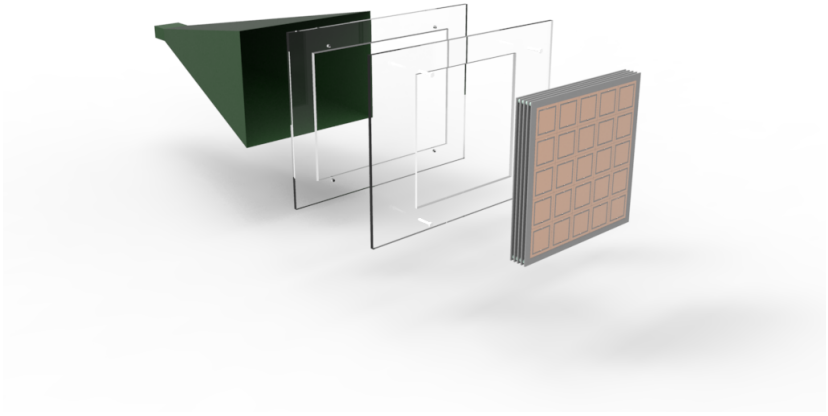

FIGURE 3.7: Exploded-view of the *Perspex* mount.

All the building materials, whose electromagnetic characteristics are detailed in Table 3.2, were carefully selected by having low impact in electromagnetic performance, *i.e.* dielectric materials with low loss tangent were chosen. Even though its impact in antenna performance was studied by simulations a set of measurements was conducted to assess the performance of the antenna loaded with the perspex mount.

TABLE 3.2
EM CHARACTERISTICS OF THE MATERIALS USED IN THE SUPPORTING MOUNT.

Material	ϵ_r	$tan\delta$
Perspex	2.22	0.02
Nylon	3	0.001
Teflon	2.1	0.0001

In Fig. 3.8 is presented and compared the normalised broadband S_{21} parameter for the case where the reference antenna has no perspex attached to it, and for the case when both *Perspex* frames are assembled to the antenna and fixed with the nylon screws. No transmitarray was considered. From the results, it is possible to conclude that the developed mount introduces, in average, less than 0.5 dB of insertion losses for the considered frequency band.

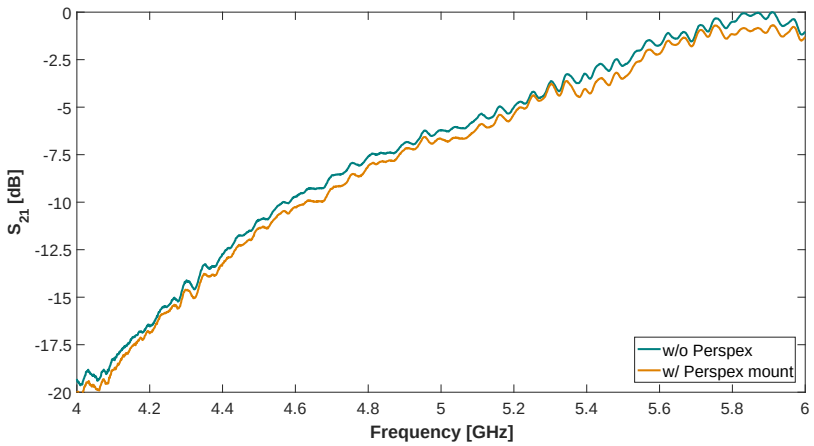

FIGURE 3.8: Comparison of the (normalised) S_{21} parameter with and without the *Perspex* mount attached to the reference horn antenna.

Nevertheless, since the antenna measurement for reference was performed in the presence of the perspex and further measurements are normalised to it, the effect of the *Perspex* mount have always been taken into account. The reference antenna is characterised in detail in Section 3.8.

3.5 Measurement setup characterisation

In this section, the experimental setup is being characterised in terms of power handling and dynamic range by presenting a link budget calculation for the entire measurement system. Moreover, the methodology utilised for system calibration and subsequent results normalisation is introduced.

3.5.1 Link budget for the single antenna reference measurement

The link budget of a radio communication system accounts for all gains and losses present in the RF chain. Therefore, it is possible to quantify the communication link's performance while accounting for the system's power, gains, and losses of both the transmitter and receiver. In particular, it is crucial to characterise the limits of the received power and ensure an overall system dynamic range of (at least) 40 dB that would provide sufficient resolution for the examination of the side lobes of interest, as indicated in [15].

The link budget can be calculated through the *Friis formula* given by (3.5) [1, 19],

$$\frac{P_r}{P_t} = G_t.G_r.\left(\frac{\lambda}{4.\pi.d}\right)^2, \tag{3.5}$$

where P_t and P_r are the power of the transmitted and received signal, G_t and G_r the gain of the transmitting and receiving antennas (with respect to an isotropic radiator), respectively, λ is the wavelength. Moreover, d is the separation distance between antennas where it is assumed they are reflection and polarisation-matched and aligned for maximum directional radiation and reception [1, 19].

The effect of the propagation path can be quantified by defining the *free-space loss* (L_f) and *gain* (G_f) as in (3.6) [19], respectively,

$$L_f = \left(\frac{4.\pi.d}{\lambda}\right)^2, \qquad G_f = \frac{1}{L_f} = \left(\frac{\lambda}{4.\pi.d}\right)^2. \tag{3.6}$$

The *free-space loss*[1] characterises the loss in signal strength of an EM wave that would result from a line-of-sight path through free space. It is proportional to the square of the separation distance between antennas and to the square of the frequency of the EM wave [1, 19].

Equation (3.5) can be written as the product of the transmit and receive gains and the propagation loss factor, as in (3.7) [19],

$$P_r = P_t.G_t.G_r.\left(\frac{\lambda}{4.\pi.d}\right)^2 = P_t.G_t.G_r.G_f, \tag{3.7}$$

and customised by adding any necessary loss or gain factor [19].

In fact, to complete the link budget calculation for the reference measurement, depicted in Fig. 3.9, the losses in cables and connectors (L_{cc}) and the losses inserted by the *i.e.* mount (L_{mnt}) (characterised in Section 3.4.4) were taken into account.

Hence, the link budget formula for the reference measurement takes the form of (3.8), when represented in *decibels*,

$$P_{r_{[dBm]}} = P_{t_{[dBm]}} + G_{t_{[dBi]}} + G_{r_{[dBi]}} - L_{f_{[dB]}} - L_{cc_{[dB]}} - L_{mnt_{[dB]}} \qquad [dB] \tag{3.8}$$

The link budget estimation for the reference measurement for a single antenna radiation pattern setup was are presented in Table 3.3. This was considered in the

[1] also referred as Path Loss in this document

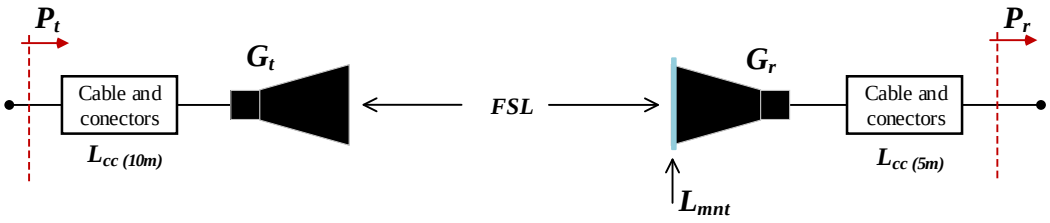

FIGURE 3.9: Illustration of the *Friis formula* for the reference measurement.

design and implementation of the experimental setups in both USW and IT facilities. Since both laboratories have similar RF equipments, the measurement conditions were easily replicated in both labs. According to the table, the estimated received power was around -39.3 dBm assuring an effective dynamic range of +50.7 dB. The dynamic range was calculated by the difference (in dB) between the maximum received power and the VNA noise floor. A margin of 10.7 dB above the required 40 dB was intentionally considered, to allow room for the insertion of the transmitarray within the system.

TABLE 3.3
LINK BUDGET ESTIMATION FOR THE REFERENCE MEASUREMENT SYSTEM AT 5.2GHZ.

Parameter	Value	Units
Transmitted power	+10	dBm
Transmitter antenna gain	+19.5	dBi
Receiver antenna gain	+1.5	dBi
Cable (∼15m) & connectors losses	+13.5	dB
Perspex mount insertion loss	+0.5	dB
Estimated Free-space Loss (FSL) (3m)	+56.3	dB
Estimated received power	-39.3	dBm
VNA noise floor	-90	dBm
Effective system dynamic range	+50.7	dB

3.5.2 System calibration

The radiation pattern measurements were performed through the acquisition of S_{21} (or S_{12}) parameter using a VNA, as previously mentioned. All the measurements were carried out after the proper equipment calibration. The VNAs utilised in every

measurement setup were calibrated using a TOSM (through, open, short and match) procedure at the end of the RF cables and before the antennas, as illustrated in Fig. 3.10.

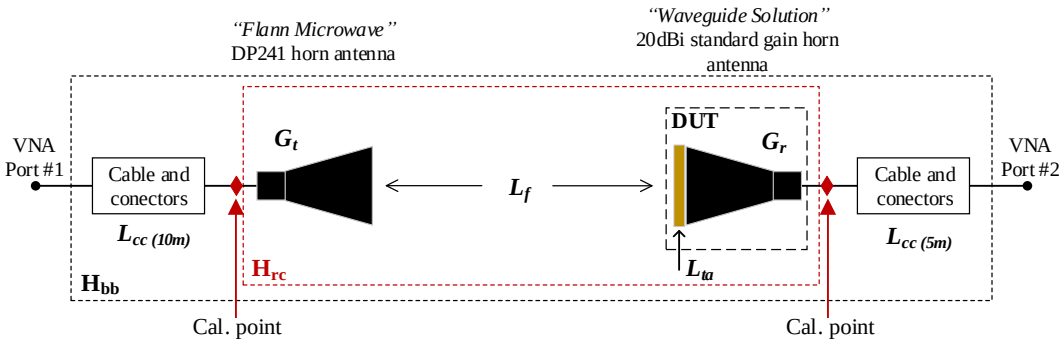

FIGURE 3.10: Block diagram for single antenna reference setup calibration (*Perspex* insertion loss (L_{mnt}) not represent for convenience).

The normalised frequency response of the radio channel (H_{rc_n}), is then given by (3.9),

$$H_{rc_n}(f) = \frac{H_{rc}(f)}{H_{bb}(f)}, \tag{3.9}$$

where $H_{bb}(f)$ is the frequency response of the system when connected back-to-back and $H_{rc}(f)$ is the frequency response of the radio channel that includes the information about the transmitting antenna, free space losses and the DUT. Therefore, all the effects introduced by connectors and cables (*i.e.* insertion losses) were included in the calibration and consequently its effect included in the measured data. The normalised response of the radio channel $H_{rc_n}(f)$ is then obtained by the reading of the complex-valued S_{21}, herein denominated as $S_{21_{|rc}}$.

3.5.3 Measurements normalisation

After proceeding with the system calibration as indicated in the previous section, the $S_{21_{|rc}}$ extracted using the VNA from the radio channel respects (3.10),

$$S_{21_{|rc\ [dB]}} = G_{t_{[dBi]}} - L_{f_{[dB]}} + G_{dut_{[dBi]}}, \quad where, \tag{3.10}$$

$$G_{dut_{[dBi]}} = G_{r_{[dBi]}} - L_{mnt_{[dB]}} - L_{ta_{[dB]}}, \tag{3.11}$$

and L_{ta} represents the insertion loss of a prototype of the transmitarray, when it is coupled to the reference horn antenna for characterisation (otherwise $L_{ta} = 0$).

Since the absolute gain (G_r) of the horn antenna utilised as reference (20 dBi standard gain horn antenna from *"Waveguide Solution"*) is well characterised and provided by the supplier, and a reference measurement was always performed in the absence of the transmitarray ($L_{ta} = 0$), it is possible to isolate by the comparison of results, the insertion loss of the developed prototypes or the absolute gain of the entire aggregate, *i.e.* reference antenna coupled with transmitarray.

In fact, this follows the *"gain-transfer method"* for linearly polarised antennas, described in *IEEE Standard Test Procedures for Antennas* [15]: *"This method is one in which the unknown power gain of a test antenna is measured by comparing it to that of a gain standard antenna. Ideally the test antenna is illuminated by a plane wave which is polarization matched to it, and the received power is measured into a matched load. The test antenna is replaced by a gain standard, leaving all other conditions the same."*

Thus, the radiation pattern results (for single antenna) presented throughout this research work are normalised either to the maximum of the reference measurement (represented by the normalised gain G_n) or normalised to the absolute gain of the reference standard gain horn antenna (represented by G_a), provided by the supplier. The results normalisation were then performed depending if:

- The transmitarray prototype is not coupled to the reference horn antenna, normalisation procedure follows (3.12),

$$\begin{cases} S21_{|ref[dB]} = S21_{|rc[dB]} \quad when \quad L_{ta} = 0, \\ G_{n_{|ref[dB]}} = S21_{|ref[dB]} + \mid max(S21_{|ref[dB]}) \mid, \\ G_{a_{|ref[dBi]}} = G_{n_{|ref[dB]}} + G_{r_{[dBi]}}, \end{cases} \tag{3.12}$$

  assuming that both receiver and transmitter antennas are aligned to their maximum power direction, *i.e.* ($Az = 0°$, $El = 0°$);

- A transmitarray prototype is coupled to the reference horn antenna, normalisation is calculated by (3.12),

$$\begin{cases} S21_{|ta[dB]} = S21_{|rc[dB]} \quad when \quad L_{ta} \neq 0, \\ G_{n_{|ta[dB]}} = S21_{|ta[dB]} + \mid max(S21_{|ref[dB]}) \mid, \\ G_{a_{|ta[dBi]}} = G_{n_{|ta[dB]}} + G_{r_{[dBi]}}. \end{cases} \tag{3.13}$$

It is worthwhile to mention that although the S_{21} parameters are used to measure power gain over a frequency band (when using the frequency broadband technique described next section), the indicated procedures are performed for a single frequency point, in a point-to-point normalisation.

3.6 Radiation pattern measuring techniques

As previously mentioned, two distinct techniques were implemented to obtained the antenna radiation patterns: the frequency broadband and the single frequency continuous scan techniques. Those, described in this section, depend on the way data was obtained and extracted from the VNA and synchronized with tables motion.

3.6.1 Frequency broadband

The frequency broadband technique assumes the VNA is configured and pre-calibrated for the frequency band of interest before any measuring. Particularly, the settings of Table 3.4 were used in the current configuration.

The antenna radiation pattern was obtained, by capturing the broadband S_{21} (or S_{12}) parameter (with amplitude and phase information over the frequency) for each angular point defined within the announced angular range.

Table 3.4
VNA settings used in frequency broadband measurements.

Setting	Value	Unit
f_{start}	4	GHz
f_{stop}	6	GHz
Sweep points	1601	
IF. bandwidth	10	kHz
Sweep time	auto	
Power	+10	dBm

The measurement started from $+90°$ to $-90°$ in Azimuth, with intercalate sweeps in Elevation from $+30°$ to $-30°$, with 1 degree of resolution in each plane, making a total of 11,041 spatial points. In each point the S-parameter values were averaged over (at least) 5 samples, to allow a stable mean signal level to be obtained. This operation

took around 4 seconds per single point meaning that a complete 3D radiation pattern was obtained in approximately 12 hours.

Before a set of measurements, an one-time fine-tuning was performed to aligned the antennas to their maximum gain direction. This procedure, typically known as *"home compensation"*, allow to obtain a well centred and referenced to origin of the axis radiation pattern.

In Fig. 3.11 is illustrated an example of a normalised 3D radiation pattern obtained with frequency broadband measurement, with the respective cuts in the main planes (Azimuth and Elevation) for the reference horn antenna at 5.29 GHz.

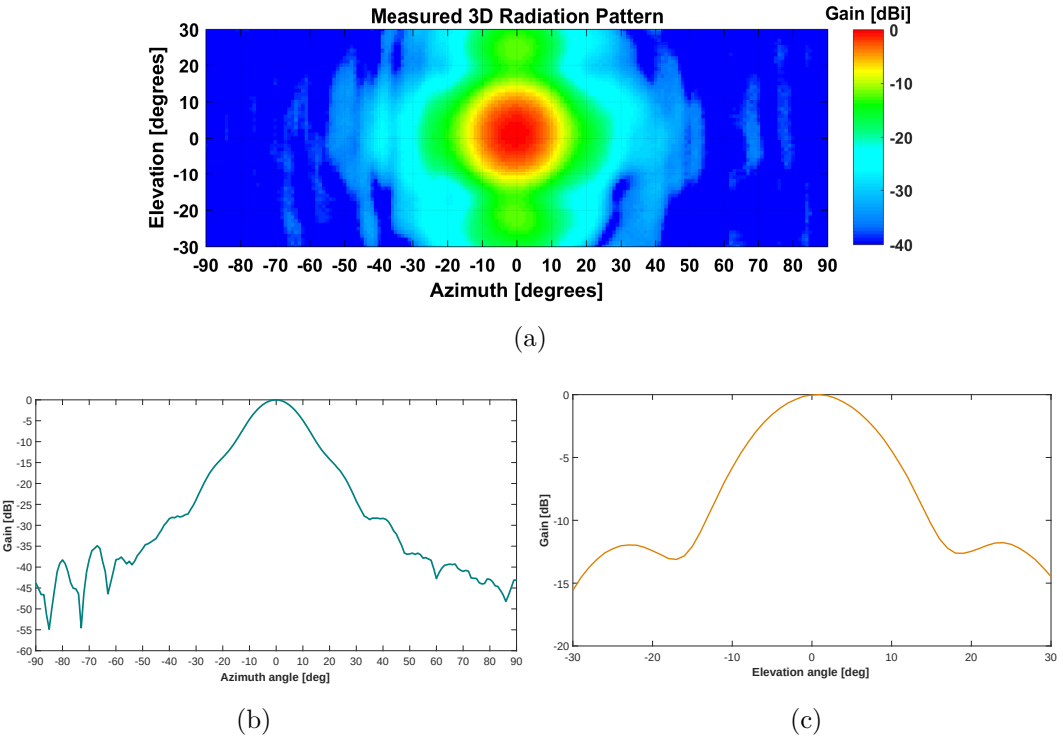

(a)

(b) (c)

FIGURE 3.11: (a) Example of a (normalised) 3D radiation pattern of the reference horn antenna with the respective cut in (b) azimuth and (c) elevation planes, at 5.29 GHz.

Although the detailed information about amplitude and phase along a frequency band is available, this method turned to be very time consuming even if reducing the measured angular range. Therefore, an new measurement technique to obtain antenna radiation patterns was developed to overcome this constraint.

3.6.2 Single frequency continuous scan

In alternative to the frequency broadband method, the single frequency continuous scan technique drastically reduced the data acquisition time while preserving the accuracy of the measurement. However, only information of amplitude was recorded (phase was neglected) due to equipment limitation.

In this technique, the VNA was previously calibrated and set to Time Series Mode. Hence, it was able to record any changes in signal amplitude, during a pre-defined period of time (defined by the sweep time), for a single frequency point (f_0). The VNA settings utilised in single frequency continuous scan measurements are detailed in Table 3.5.

TABLE 3.5
VNA SETTINGS USED IN SINGLE FREQUENCY CONTINUOUS SCAN MEASUREMENTS.

Setting	Value	Unit
f_{start}	f_0	GHz
f_{stop}	f_0	GHz
Time samples	1601	
IF. bandwidth	10	kHz
Sweep time	11	s
Power	+10	dBm

The initial instant of a measurement was activated by the VNA external trigger associated to two mechanical limit-switches fixed at the position corresponding to $+90°$ and $-90°$, in the horizontal turntable, as depicted in Fig. 3.12.

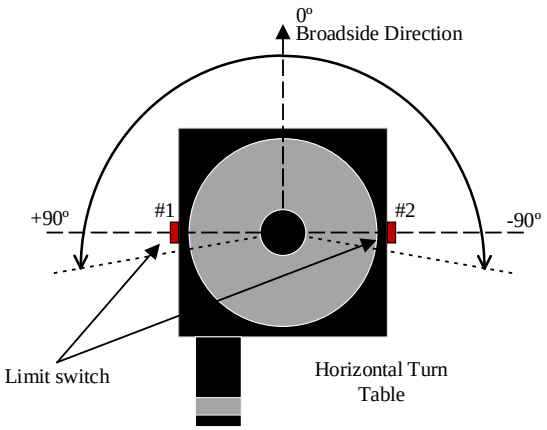

FIGURE 3.12: Mechanical turntable for 3D radiation pattern measurements, using the single frequency continuous scan technique.

Since the sweep time was intentionally set to a value longer than the time taken by the turntable to rotate from $+90°$ to $-90°$ (or *vice-versa*), antenna radiation patterns could be obtained by correlating and averaging the signal measured from two different motions (Fig. 3.13):

- Antenna rotating from left to right: horizontal turntable started its movement slightly beyond $+90°$ in direction to $-90°$. As soon as it passed by the first limit-switch (#1), the VNA started measuring and recording the amplitude of S_{21} until the sweep time was elapsed. At this instant, the antenna was stopped slightly beyond $-90°$ and a radiation pattern was obtained in function of time (Fig. 3.13a), but physically referenced to the limit-switch position #1 (*i.e.* $+90°$);
- Antenna rotating from right to left: subsequently, the turntable started a second motion from where it was stopped (beyond $-90°$) in direction to $+90°$. The VNA started a new recording as soon as the limit-switch #2 was triggered. Similarly, a new radiation pattern was obtained (Fig. 3.13a), but this time referenced to the physical position of the limit-switch #2 (*i.e.* $-90°$).

Since the channel was assumed to be static (anechoic chamber), the movement of the tables between $+90°$ and $-90°$ constant and linear and, the initial physical position of each measurement known, the radiation patterns obtained from both motions were then:

- Oriented to match the movement direction, as depicted in Fig. 3.13b;
- Aligned to each other by exploring the mathematical properties of the cross-correlation and, truncated between the begin of each measurement and the maximum lag of the correlation, to discard the time the VNA was still measuring beyond the physical limits, as illustrated in Fig. 3.13c;
- Finally, the patterns were averaged to obtain the final radiation pattern for a single azimuthal cut, as depicted in Fig. 3.13d.

Using this technique, a single radiation pattern in the azimuth plane (between $\pm 90°$) were obtained in approximately 25 seconds while a Three-Dimensional (3D) radiation pattern was obtained in 30 minutes (by taking several cuts between $\pm 30°$ in the Elevation plane), against the 12 hours using the frequency broadband method.

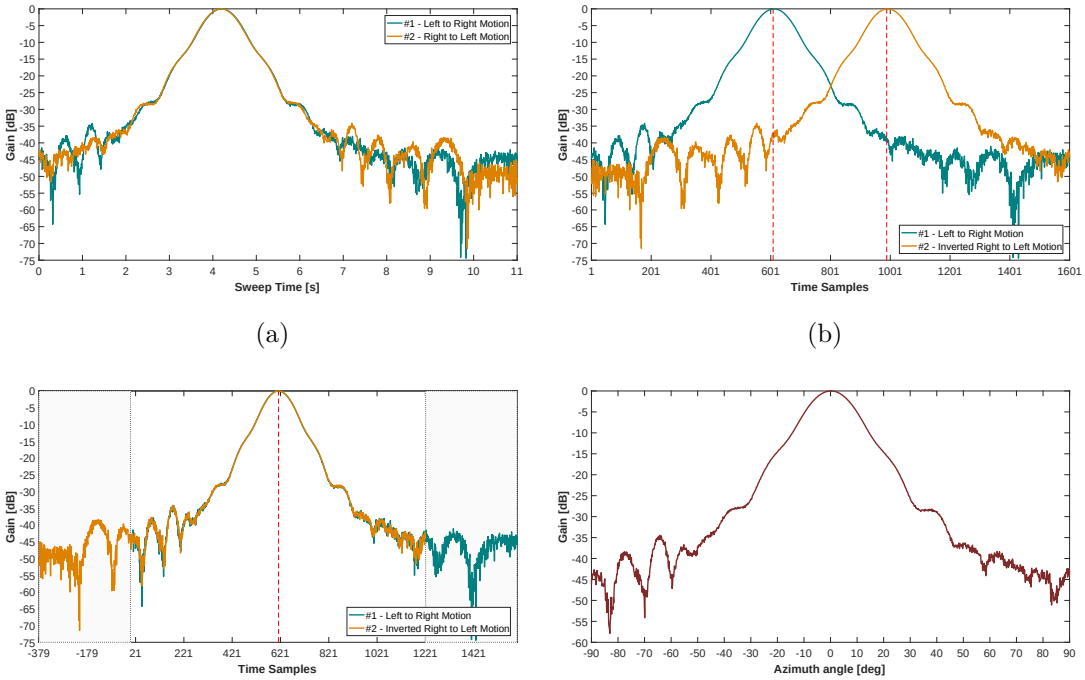

FIGURE 3.13: Single frequency continuous scan – measured radiation patterns for different stages of the data acquisition process: (a) raw data over the time, (b) rotated data, (c) data truncation to the maximum lag of correlation and (d) final radiation pattern.

3.6.3 Accuracy between measurement techniques

Each of the described measurement techniques was implemented to have its own purpose. While the frequency broadband technique was able to provide information of amplitude and phase over a broad frequency band, it was very time consuming. On the other hand, the single frequency continuous scan technique provided a quick inspection of an antenna radiation pattern, but limited to a single frequency point and with no phase information.

To validate them, a set of measurements was performed under the same experimental circumstances and radiation patterns for the reference standard gain horn antenna were obtained, independently, using both techniques. The results of the measurements are depicted in Fig. 3.14 illustrating the radiation pattern for the Az plane (El = 0) at $f = 5.29$ GHz.

According to the results, the antenna radiation patterns obtained using both measuring techniques are converging. The difference between the results present a root mean squared error of 1.44 dB when calculated over the entire angular range, but it is drastically reduced to 0.16 dB if considering only the range from $-60°$ and $+60°$.

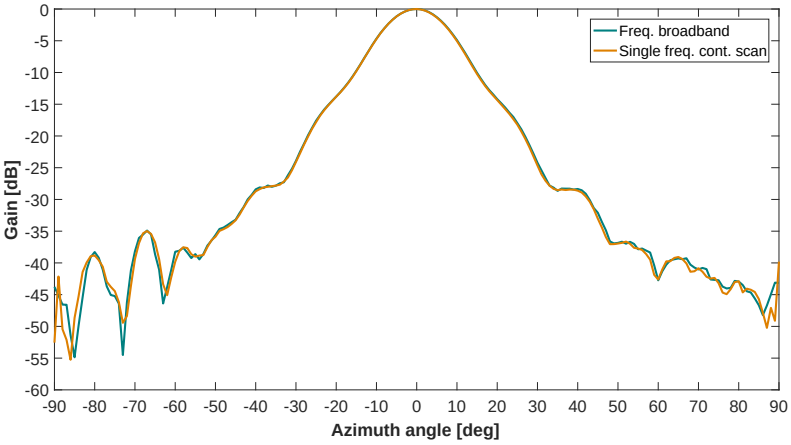

FIGURE 3.14: Antenna radiation pattern comparison using both frequency broadband and single frequency continuous scan techniques.

3.7 Post-processing scripts

A wide range of post-processing scripts were specifically developed, in MATLAB, to treat the raw data obtained from a radiation pattern measurement. These were developed to normalise the experimental raw data according to the procedures described in Section 3.5.3 and to simplify its analysis since a large amount of data was recorded during a measurement.

It is worthwhile to mention that an S_{21} with a resolution of 1601 sweep points was recorded for all angles defined between $-90° \leq Az \leq 90°$ and $-30° \leq El \leq 30°$ (11,041 spatial points), leading to a massive amount of data to be interpreted.

Therefore, the scripts are divided in two main categories: data normalisation and data analysis and plotting. After the raw had been normalised, the implemented scripts allowed the user to:

- plot the S_{21} (phase and amplitude) per angular point defined within the measured range;
- plot a radiation pattern for any frequency point within the data set;
- estimate, automatically, the main lobe direction and the HPBW per frequency point;
- estimate the best case scenario based on the higher gain at the main lobe direction, within the frequency points of the data set;
- calculate, automatically, the direction of the higher side lobe and its HPBW as well as the SLL;

- and finally, create an excel file summarising in a table all the information of the data set.

In figure 3.15 it is shown a snapshot of the post-processing program running in MATLAB, with a plot of a 3D radiation pattern and the excel table obtained for a measurement of the reference standard gain horn antenna.

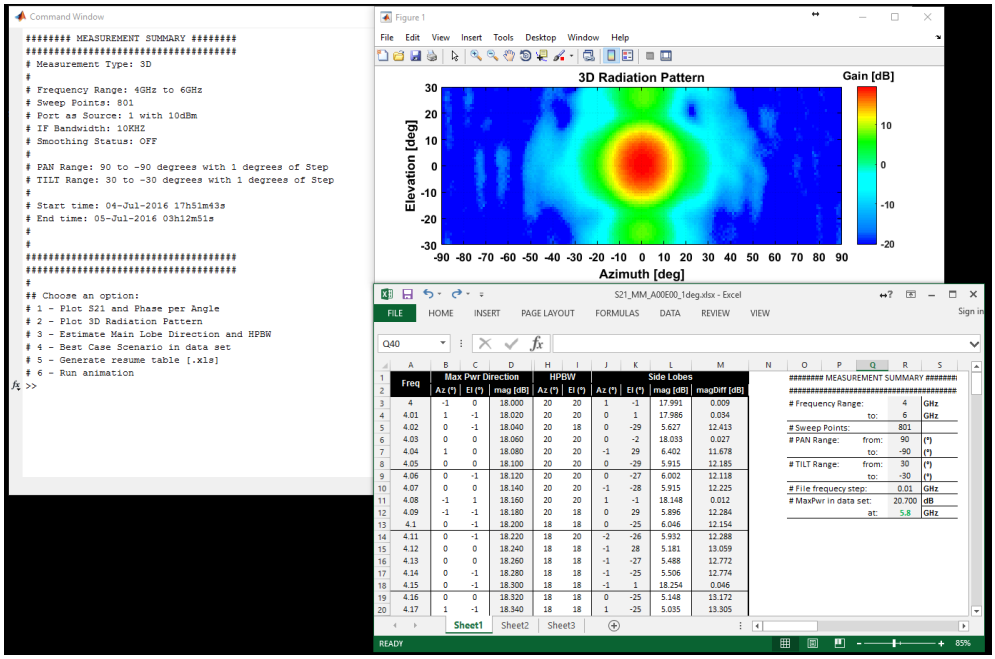

FIGURE 3.15: Snapshot of the post-processing program running in MATLAB.

3.8 Characterisation of the reference horn antenna

A standard gain horn antenna, supplied by "The Waveguide Solution", was used as reference antenna to all radiation pattern measurements. The horn has an overall length of 421 mm and aperture dimension of 230 mm × 170 mm and it was designed to operate in the frequency band between 3.95 to 5.85 GHz. Since the antenna terminates in a WG12 waveguide flange, an adaptor from waveguide to SMA connector was used. The horn presents a relatively good impedance matching with a S_{11} below -10dB, within the indicated frequency band, obtained experimentally and in simulations (using CST), as depicted in Fig. 3.16a. Although there is a difference between both experimental and simulated S_{11} curves, this is explained by the fact that the waveguide to SMA adaptor was not considered in the simulation environment. The absolute gain of the horn antenna, provided by the manufacturer, is depicted in Fig. 3.16b.

To characterise the horn antenna in terms of radiation performance, its 3D radiation pattern have been measured using the techniques described in this chapter and compared against EM simulations carried out on a realistic model of the antenna, in CST MWS. This action helps to validate the solver comparing the obtained results to real experiments. Although radiation patterns have been measured within the entire antenna's operation range, only a few radiation patterns have been selected to be depicted in this document (Fig. 3.17), corresponding to the frequency points necessary to further sections of this thesis. After proper analyse, the results obtained from both simulation and experiments were compiled in Table 3.6.

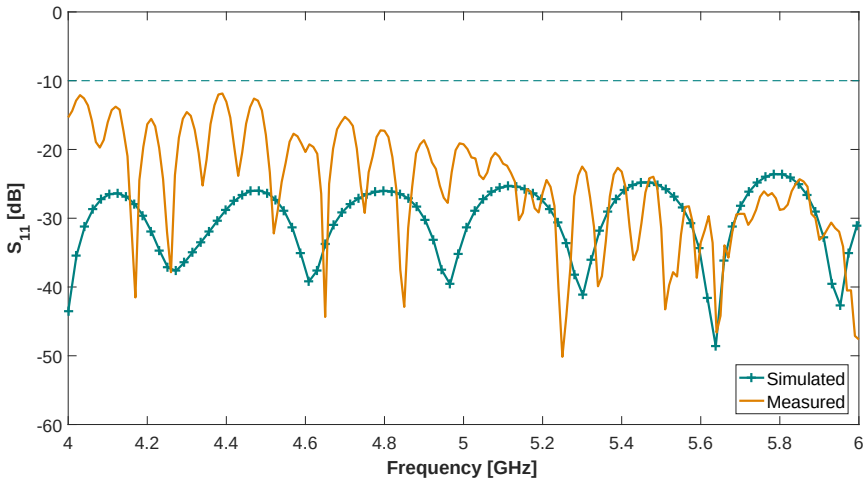

(a)

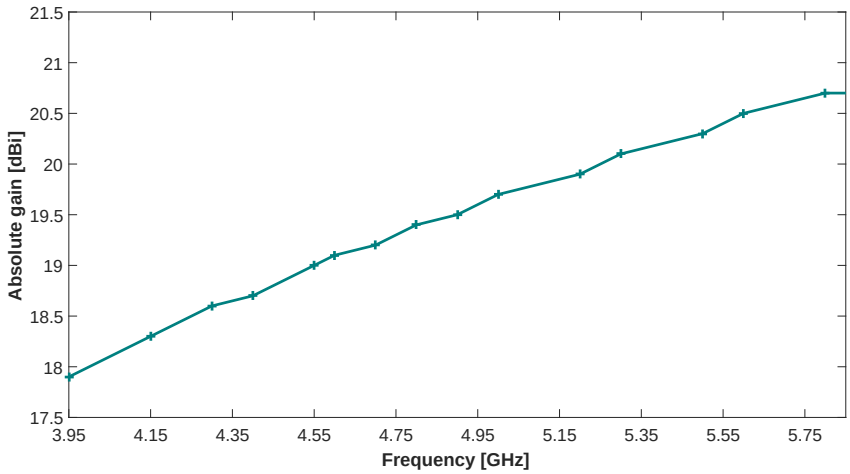

(b)

FIGURE 3.16: Reference horn antenna: (a) simulated *vs.* measured S_{11} and (b) absolute standard gain provided by the antenna supplier.

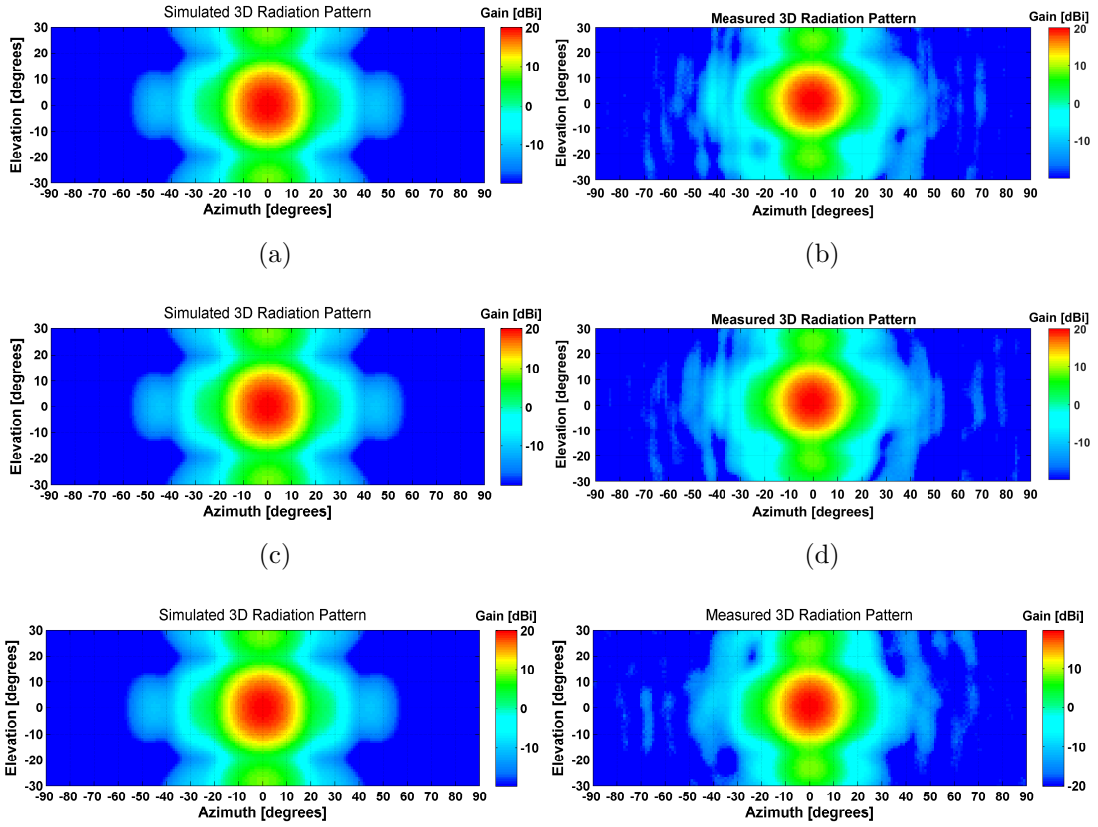

FIGURE 3.17: Simulated and measured 3D radiation pattern at: (a,b) 5.38 GHz, (c,d) 5.29 GHz and (e,f) 5.2 GHz, respectively, for the reference standard gain horn antenna.

TABLE 3.6
ANALYSE OF 3D RADIATION PATTERNS OF THE REFERENCE HORN ANTENNA.

	Simulated				Measured			
Frequency (GHz)	Gain (dBi)	HPBW Az(°)	HPBW El(°)	SLL (dB)	Gain (dBi)	HPBW Az(°)	HPBW El(°)	SLL (dB)
5.38	20.6	17	17	-12.6	20.2	16	15	-11.7
5.29	20.4	17	17	-12.1	20.1	16	14	-11.9
5.2	20.2	17	17	-11.6	19.9	16	16	-11.3

3.9 Interim conclusions

This chapter presents a detailed analysis of the experimental setup and technical procedures employed during the measurement campaign carried out in this research work. All the experiments took place inside an anechoic chamber to ensure measurements were performed in a electromagnetic controlled environment. The majority rely in the acquisition of 3D antenna radiation patterns to evaluate the beamsteering capability of the developed prototypes.

In particular the mechanical rig utilised for a single-antenna is described followed by the characterisation of the measuring systems, which include a complete link budget calculation to quantify the systems' the dynamic range. The methodology used for calibration and the description of the procedure for measurements normalisation are also presented. In addition, the techniques implemented for data acquisition, namely, frequency broadband and single frequency continuous scan techniques, are being thoroughly described. Subsequently, post processing scripts utilised for measured data treatment and analyses are presented. Finally, the standard gain horn antenna utilised as reference antenna throughout this work is properly characterised in terms of S_{11}, absolute gain and radiation pattern for the frequencies of more interest for this work.

This page is intentionally left blank.

CHAPTER 4

Beamsteering with a transmitarray

4.1 Introduction

This chapter introduces the theoretical background for antenna beamsteering using a transmitarray. In particular, the mode of operation of a conventional 1–Dimensional beamsteering transmitarray is described and compared against a typical linear antenna array. Additionally, a novel theoretical approach to perform 2–Dimensional beamsteering using a transmitarray is presented. The theoretical background is validated against electromagnetic simulations using a commercially available EM solver (CST MWS), running on an ideal model of a transmitarray composed of dielectric material, excited by an incident Gaussian plane wave. Finally, frequency selective surfaces are introduced as alternative to dielectric transmitarray elements with the capability of inserting transmission phase per element, and consequently controlling the progressive phase throughout the array leading to the beamsteering of a radiation pattern.

4.2 Transmitarray operation mode for 1D-beamsteering

The principle of beamsteering using a traditional transmitarray can be compared to the one using a linear antenna array. Figure 4.1 depicts both configurations for comparison. In a linear antenna array, the phase shifting is applied to the signal in each individual branch using a phase shifter [1, 5, 6], whilst in a transmitarray the phase shifting is obtained by controlling the phase delay introduced by each individual elements of the transmitarray, as reported in [83, 84, 107–116, 123–127].

When an incident Electromagnetic (EM) wave propagates through a transmitarray of length l, composed by N elements of periodicity p (Fig. 4.1b), it experiences a different phase shifting γ_n expressed by (4.1), after penetrating each of the elements of the array

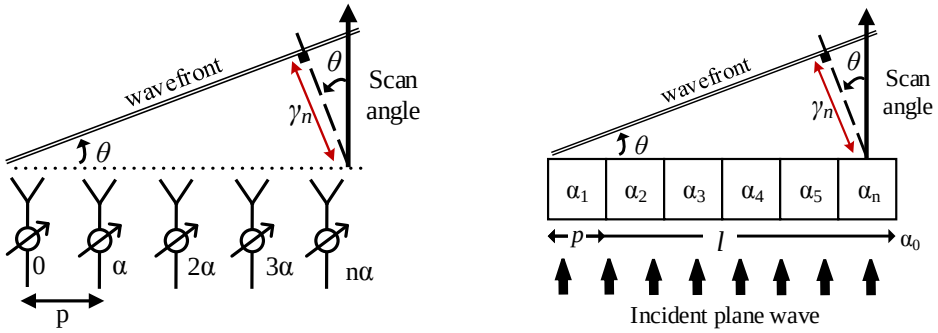

FIGURE 4.1: (a) Model of linear antenna array and (b) model of a transmitarray for 1D beamsteering analysis.

in the steering direction theta (θ),

$$\gamma_n = \frac{2\pi}{\lambda_0}.p.n.sin\theta = k_0.p.n.sin\theta, \tag{4.1}$$

where $k_0 = \frac{2\pi}{\lambda_0}$ is the wave number in free space.

Consequently, the transmission phase α_n in the n^{th} element, can be defined by (4.2),

$$\alpha_n = -\gamma_n + \alpha_0 + 2\pi i, \qquad i = 0, 1, 2, ... \tag{4.2}$$

where α_0 is the phase of the incident EM wave at the input of the transmitarray.

Therefore, the re-transmitted wave direction θ can be expressed as a function of the phase difference ψ between adjacent elements, *i.e.* progressive phase, using (4.3),

$$\begin{aligned} \psi = \alpha_n - \alpha_{n-1} = -\gamma_n + \gamma_{n-1} = \\ = -k_0.p.n.sin\theta + k_0.p.(n-1).sin\theta = \\ = -k_0.p.sin\theta. \end{aligned} \tag{4.3}$$

Thus, by varying the phase α_n of each array element in a progressive way, the incident wave can be steered to a desired direction θ relative to the normal of the structure, defined by (4.4),

$$\psi = -k_0.p.sin\theta \Leftrightarrow \theta = -sin^{-1}\left(\psi.\frac{\lambda}{2\pi.p}\right) \tag{4.4}$$

However, since the phase distribution in the array is applied along a single direction only, the model for a linear transmitarray limits its application to 1D beamsteering.

Therefore, the main lobe of the radiation pattern of the original antenna in which the transmitarray is applied, only has the capability to be steered towards the output angle with θ component, as reported in some of the references included in the literature review [107–109, 115, 116, 126, 127].

4.3 The proposed 2D–beamsteering theoretical model

In order to extend the concept to 2–D beamsteering using a transmitarray, it is proposed by this thesis to characterise the model by analogy with a planar antenna array. This vision enable the transmitarray to have the control over the two angular components theta (θ) and phi (ϕ) of the output angle direction, simultaneously, raising the limitation of 1D beamsteering of the previous model. The transmitarray model for 2D beamsteering is depicted in Fig. 4.2.

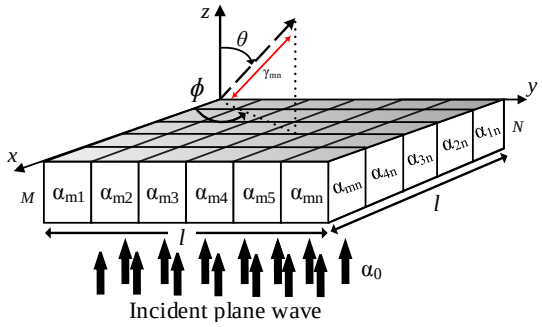

FIGURE 4.2: Proposed model for a transmitarray with 2D beamsteering.

Built on the theory of planar antenna arrays presented in [1] and [6], and overviewed in Section 2.2.1, a progressive phase shift between adjacent elements should occur along the X and Y directions of the $M \times N$ array so 2D beamsteering could be enabled. Thus, by expanding from (4.3), the relation between the two dimensional output directions (θ,ϕ) and the progressive phase delay, is given by (4.5),

$$\begin{cases} \psi_x = -k_0.p.sin(\theta).cos(\phi) \\ \\ \psi_y = -k_0.p.sin(\theta).sin(\phi) \end{cases}, \tag{4.5}$$

where ψ_x and ψ_y are the progressive phase along X and Y axis, respectively, and p is the periodicity of the $p \times p$ array elements.

Therefore, a $M \times N$ transmitarray would exhibit a relative phase distribution that can be represented by the matrix (4.6),

$$\begin{array}{c} \\ \psi_y \downarrow \end{array} \begin{array}{c} \longrightarrow \psi_x \\ \begin{bmatrix} \alpha_{1,1} & .. & .. & .. & .. & \alpha_{1,n} \\ .. & .. & .. & .. & .. & .. \\ .. & .. & .. & .. & .. & .. \\ \alpha_{m,1} & .. & .. & .. & .. & \alpha_{m,n} \end{bmatrix} \end{array} \tag{4.6}$$

where $\alpha_{m,n}$ is the phase delay introduced by each individual (m,n) element of the transmitarray. This representation is proposed herein to facilitate the understanding of the progressive phase along the transmitarray and will be further considered in this work.

From this analysis, it can be concluded that the output steering direction (θ,ϕ) depends on the transmission phase $\alpha_{m,n}$ of each element of the 2–D transmitarray, and similarly to (4.2) (linear case), the phase shifting in each individual element can be described by (4.7),

$$\alpha_{m,n} = -\gamma_{m,n} + \alpha_0 + 2\pi i, , \qquad i = 0, 1, 2, ..., \tag{4.7}$$

where the phase shifting of each element $\alpha_{m,n}$ is a periodic function, and $\alpha_{m,n} \subset [0, 2\pi]$ such as in the 1-D case. Thus, each element of the transmitarray must always be capable to achieve at least 360° (2π) of transmission phase shift, to ensure a complete control of the output angle.

Notwithstanding, in order to directly match the output angle direction obtained from the theory with the output angle direction given either by simulation and experiments, it is proposed, by this work, to apply in the theoretical model a coordinate system conversion from Spherical coordinates (represented by θ and ϕ components) to *Azimuth-over-Elevation* (represented by the pair *Az/El*). Therefore, the mathematical relation between spherical and *Az/El* coordinates well detailed in [131], given by (4.8), has been applied here:

$$\begin{cases} sin(\theta).cos(\phi) = cos(El).sin(Az) \\ \\ sin(\theta).sin(\phi) = sin(El) \end{cases} . \tag{4.8}$$

The main differences between both coordinate systems rely on the origin of the axis, as depicted in Fig. 4.3. In Table 4.1 are represented a few examples of converted output

angle directions for comparison. These will be from this point on, the coordinate system used as reference in this thesis.

From the mathematical workout resultant of replacing (4.8) in (4.5), this thesis contributes with a generic formula to calculate the output angle direction with *Az/El* components provided by a 2D transmitarray, as given by (4.9),

$$\begin{cases} \psi'_x = -k_0.p.cos(El).sin(Az) \\ \\ \psi'_y = -k_0.p.sin(El) \end{cases} . \tag{4.9}$$

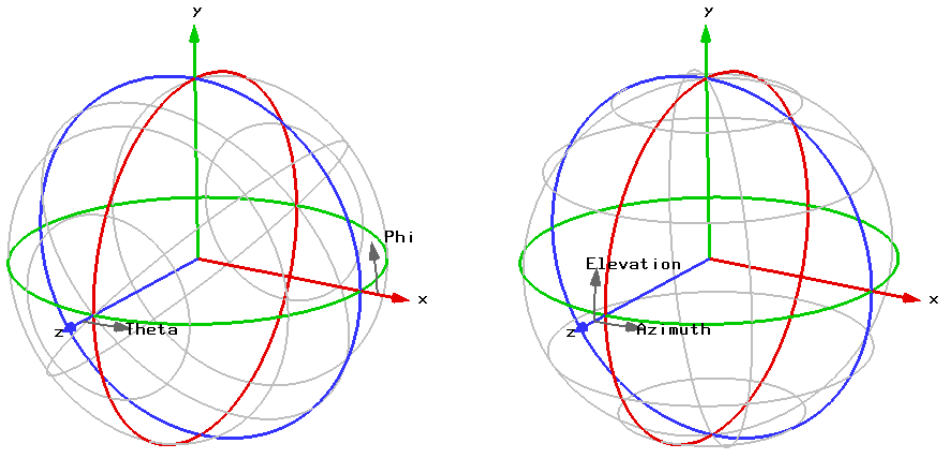

(a) (b)

FIGURE 4.3: Axial representation of the (a) spherical coordinate system (θ/ϕ) and (b) *Azimuth-over-Elevation* coordinate system (Az, El).

TABLE 4.1
EXAMPLE OF COORDINATES TRANSFORMATION.

Spherical		*Az/El*	
$\theta(°)$	$\phi(°)$	$Az(°)$	$El(°)$
0	25	0	0
25	0	25	0
25	90	0	25
25	25	22.9	10.3

4.4 Model validation with an ideal dielectric transmitarray

To validate the 1D and 2D beamsteering techniques proposed in the last sections of this chapter, both theoretical models were applied to an ideal transmitarray composed of variable dielectric material. After proper mathematical adjustment, the ideal transmitarray was designed and tested under EM simulations as presented next:

4.4.1 Ideal transmitarray model for 1D beamsteering

The ideal transmitarray model for 1D beamsteering is illustrated in Fig.4.4. It is composed of $N \times N$ dielectric elements of thickness t and periodicity $p = l/N$, where l is the total length of the dielectric slab.

For instance, it was considered that array elements of the same column were composed by the same dielectric material, characterised by a refractive index n (and consequently by an electric permittivity ϵ_r) [88], approximating the model to the one for 1D beamsteering reported in Section 4.2. In fact, this approach was inspired by the work presented in [115] and [116] and it is employed here.

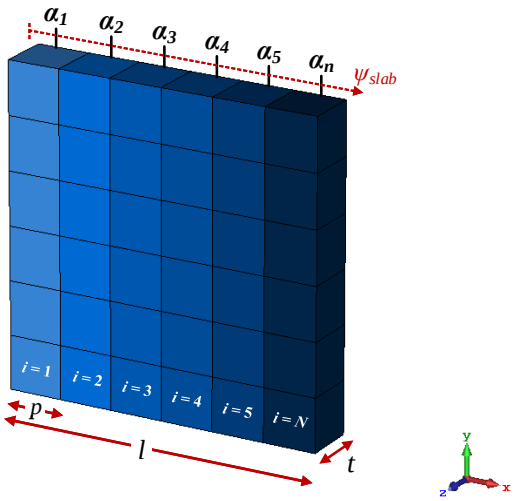

FIGURE 4.4: Dielectric slab utilised as transmitarray.

Accordingly, due to the EM properties of a dielectric material, each element that composes transmitarray introduces a phase delay (α_i) proportional to its electrical

length, that could be expressed by (4.10),

$$\alpha_i = \frac{2\pi}{\lambda_{m_i}}.t, \tag{4.10}$$

where λ_{m_i} is the wavelength in the dielectric medium that could be related to the wavelength in free-space (λ_0), according to (4.11),

$$n_i = \frac{\lambda_0}{\lambda_{m_i}}, \tag{4.11}$$

being n_i the refractive index of the material of the i^{th} column of the array.

Therefore, the phase delay α_i introduced by a dielectric array element is given by (4.12),

$$\alpha_i = \frac{2\pi}{\lambda_o}.t.n_i = k_o.t.n_i, \tag{4.12}$$

where k_o is the wave number in free space.

Consequently, the progressive phase ψ_{slab} calculated by the phase difference between adjacent elements, can be obtained using (4.13) which corroborates with [115, 116],

$$\psi_{slab} = \alpha_i - \alpha_{i-1} = [k_o.t.n_i] - [k_o.t.n_{i-1}] = k_o.t.\Delta n, \tag{4.13}$$

where Δn is the increment of the refractive index between two consecutive elements. Moreover, equation (4.13) can also be expressed as function of the refractive index of the first transmitarray element, using (4.14),

$$\Delta n = \frac{n_i - n_1}{i-1}. \tag{4.14}$$

as suggested by the authors in [115, 116].

However, it is proposed here to consider the relation between refractive index and dielectric permittivity, *i.e.* $n = \sqrt{\epsilon_r.\mu_r}$, with $\mu_r = 1$ (for non-ferromagnetic materials [50]), where (4.14) takes the form of (4.15),

$$\Delta n = \frac{\sqrt{\epsilon_{r_i}} - \sqrt{\epsilon_{r_1}}}{i-1}. \tag{4.15}$$

Accordingly, by substituting (4.15) in (4.13), the progressive phase for a dielectric transmitarray, as function of element's permittivity, is given by (4.16),

$$\psi_{slab} = k_o.t.\frac{\sqrt{\epsilon_{r_i}} - \sqrt{\epsilon_{r_1}}}{i-1}. \tag{4.16}$$

Thus, in analogy to theoretical formulation presented in Section 4.2, the output steering angle direction (θ) can be estimated by replacing (4.16) in (4.4), as expressed in (4.17),

$$\begin{aligned} \psi = \psi_{slab} \Leftrightarrow \\ \Leftrightarrow -k_0.p.sin\theta = k_o.t.\frac{\sqrt{\epsilon_{r_i}} - \sqrt{\epsilon_{r_1}}}{i-1} \Leftrightarrow \\ \Leftrightarrow \theta = -sin^{-1}\left(\frac{t}{p}.\frac{\sqrt{\epsilon_{r_i}} - \sqrt{\epsilon_{r_1}}}{i-1}\right). \end{aligned} \tag{4.17}$$

In the sequence of the presented theoretical formulation, a dielectric transmitarray composed of 6×6 elements, with $t = p = 33$ mm and $l = 198$ mm is considered. Moreover, 4 case studies corresponding to output angles of $\theta = 0°$, $5°$, $10°$ and $20°$ have been implemented. Those cases are detailed in Table 4.2, where the values of progressive phase, increment of refractive index and electric permittivity per transmitarray column are also presented.

Table 4.2
Case studies for 1D beamsteering with a dielectric slab transmitarray.

Case	$\theta(°)$	$\psi(°)$	Δn	ϵ_{r_1}	ϵ_{r_2}	ϵ_{r_3}	ϵ_{r_4}	ϵ_{r_5}	ϵ_{r_6}
#1	0	0	0	1	1	1	1	1	1
#2	5	17.26	0.087	1	1.18	1.37	1.59	1.82	2.06
#3	10	34.38	0.174	1	1.38	1.82	2.31	2.87	3.49
#4	20	67.72	0.342	1	1.80	2.84	4.10	5.61	7.34

The transmitarray model was designed and simulated in CST MWS, to evaluate the output steering direction for all the cases studies. Each transmitarray element has associated a material with the dielectric characteristics represented in the table, however, no losses in dielectric were taken into account for this simulations (loss tangent = 0). The transmitarray was simulated at 5 GHz using open boundaries and excited by an impinging wave propagating with +Z direction and, with an E-field and Magnetic-field (H-field) distribution as depicted in Fig. 4.5a and Fig. 4.5b, respectively.

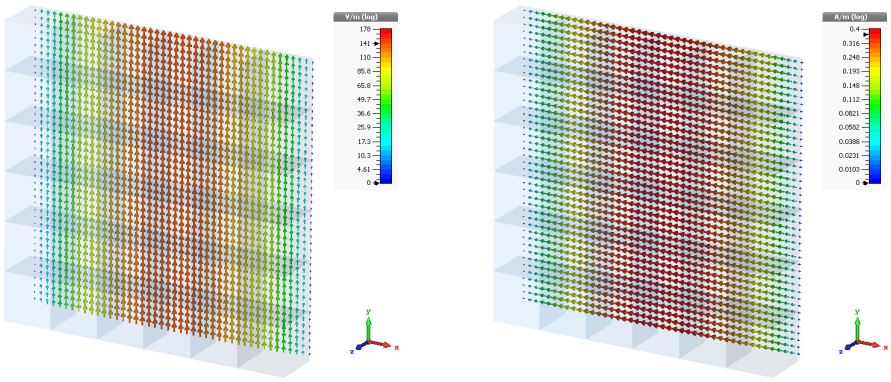

(a) (b)

FIGURE 4.5: Direction of the (a) E-field and (b) H-field of the propagating wave.

The simulation results were obtained as a far-field plot (Fig. 4.6) and as both electric (Fig. 4.7) and magnetic (Fig. 4.8) near-field distributions. According to the results depicted in Fig. 4.7 and Fig. 4.8, it can be noticed that for the cases where $\theta \neq 0°$ the direction of both E-field and H-field is being affected when it is propagating through the dielectric slab. Particularly, the field lines lose their parallel orientation relative to the structure. This effect indicates that in the far-field, the original main lobe will steer in direction. In fact, this is proven by the analysis of the radiation patterns depicted in Fig. 4.6, where the main lobe is being re-directed towards the expected angle.

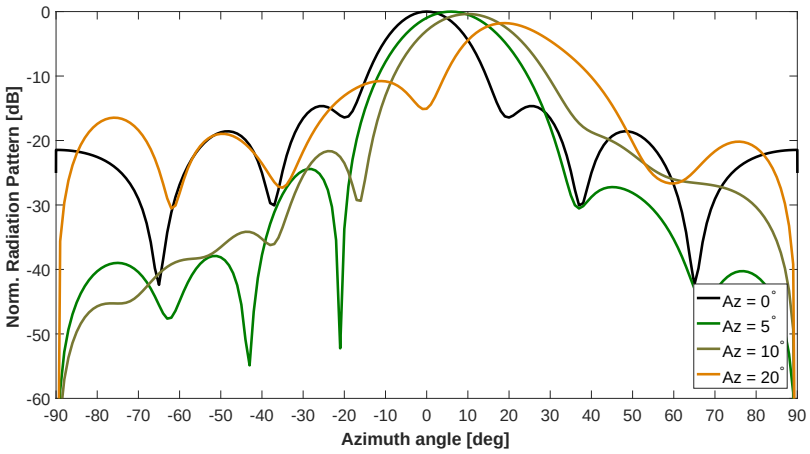

FIGURE 4.6: Simulated radiation pattern (azimuth cut) for the output angles $Az = 0°$, $5°$, $10°$ and $20°$.

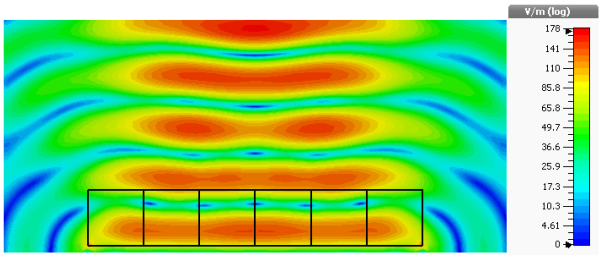

(a)

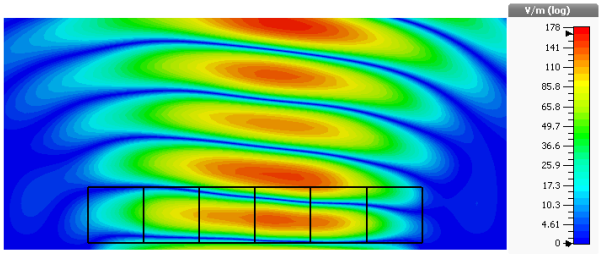

(b)

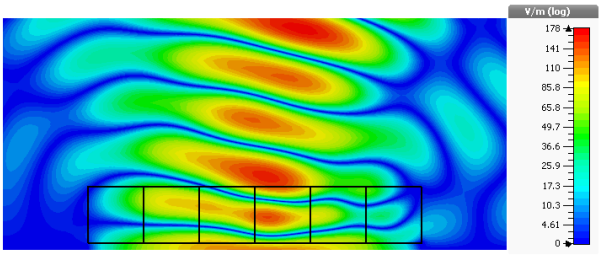

(c)

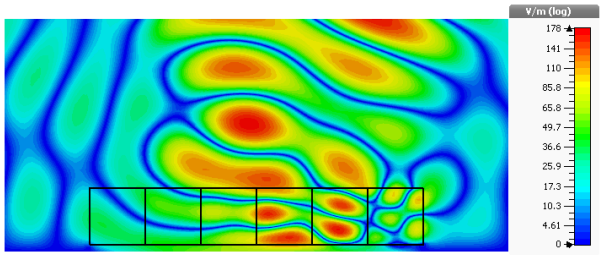

(d)

FIGURE 4.7: E-field propagation through the dielectric slab (top-view), when permittivity values are set to: (a) keep broadside direction; steer towards towards (b) 5°, (c) 10° and, (d) 20°.

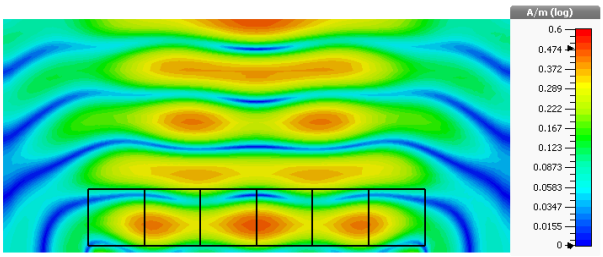

(a)

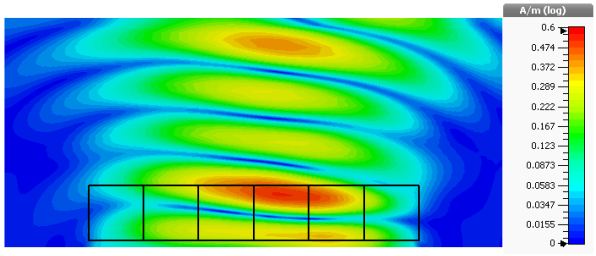

(b)

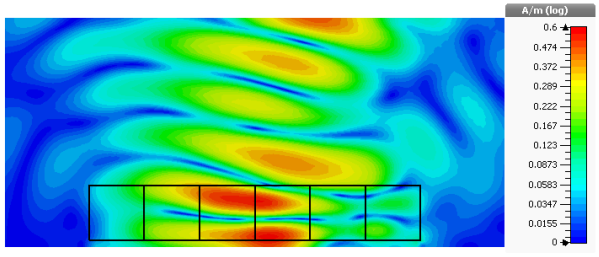

(c)

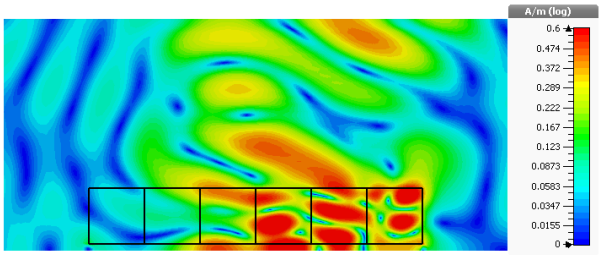

(d)

FIGURE 4.8: H-field propagation through the dielectric slab (top-view), when permittivity values are set to: (a) keep broadside direction; steer towards towards (b) 5°, (c) 10° and, (d) 20°.

4.4.2 Ideal transmitarray model for 2D beamsteering

Following the same methodology utilised in the previous analyse, a new ideal model of a dielectric slab will be considered, this time for evaluating the functionality of the 2D beamsteering theorectical model proposed in this Ph.D. work (Section 4.3). To this end, it is presented here the mathematical workout necessary to relate the output steering in two components (Az, El), with the progressive phase of the planar dielectric slab of Fig. 4.9. This model differs from the model of Fig. 4.4 by having each transmitarray element associated to an independent and controllable dielectric permittivity instead of being grouped in columns with the similar values.

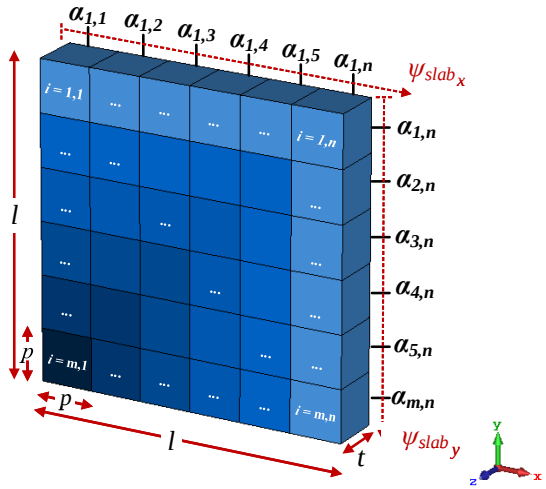

FIGURE 4.9: Dielectric slab utilised as transmitarray.

Accordingly, the elements of the transmitarray are mapped with an $\epsilon_{r_{mn}}$ that resulted in permittivity distribution with the format of (4.18),

$$\psi_y \downarrow \begin{bmatrix} & \longrightarrow \psi_x & & & & \\ \epsilon_{r_{1,1}} & .. & .. & .. & .. & \epsilon_{r_{1,n}} \\ .. & .. & .. & .. & .. & .. \\ .. & .. & .. & .. & .. & .. \\ \epsilon_{r_{m,1}} & .. & .. & .. & .. & \epsilon_{r_{m,n}} \end{bmatrix} \tag{4.18}$$

where the position of first element of the matrix corresponds to the top left element of the transmitarray.

In fact, when matching (4.18) with the phase matrix (4.6) presented in theory of Section 4.3, it is possible to extract the progressive phase (ψ) in function of the permittivity of each individual array elements, according to (4.19),

$$\begin{cases} \psi_{slab_x} = k_o.t.\dfrac{\sqrt{\epsilon_{r_m}} - \sqrt{\epsilon_{r_1}}}{m-1} \\ \\ \psi_{slab_y} = k_o.t.\dfrac{\sqrt{\epsilon_{r_n}} - \sqrt{\epsilon_{r_1}}}{n-1} \end{cases}, \tag{4.19}$$

where ψ_{slab_x} and ψ_{slab_y} correspond to the progressive phase in X and Y direction of the slab, respectively. The phase pattern to apply through the 2D array, could be related to the output angle direction with Az and El components, by substituting (4.19) in (4.9), and given by (4.20),

$$\begin{cases} \psi'_x = \psi_{slab_x} \\ \\ \psi'_y = \psi_{slab_y} \end{cases} \Leftrightarrow \begin{cases} cos(El).sin(Az) = -\dfrac{t}{p}.\dfrac{\sqrt{\epsilon_{r_m}} - \sqrt{\epsilon_{r_1}}}{m-1} \\ \\ sin(El) = -\dfrac{t}{p}.\dfrac{\sqrt{\epsilon_{r_n}} - \sqrt{\epsilon_{r_1}}}{n-1} \end{cases}. \tag{4.20}$$

To evaluate the 2D beamsteering, the dielectric transmitarray of Fig. 4.9 (6×6 elements with $t = p = 33$ mm and $l = 198$ mm) was simulated under new testing conditions, corresponding to 3 distinct output steered angles. The output angles are represented by their 2D components (*Az,El*) in Table 4.3, alongside with the respective progressive phase and refractive index increment.

Table 4.3
Case studies for beamsteering with a dielectric slab transmitarray.

Case	$Az(^\circ)$	$El(^\circ)$	$\psi'_x(^\circ)$	$\psi'_y(^\circ)$	Δn_x	Δn_y
#1	5	5	17.192	17.257	0.0868	0.0872
#2	10	10	33.860	34.382	0.1710	0.1737
#3	20	20	63.636	67.720	0.3214	0.3421

Additionally, the phase and permittivity matrices are also represented in (4.21) and (4.22) for case #1, in (4.23) and (4.24) for case #2 and, finally, in (4.25) and (4.26) for case #3, respectively. These representations allow to better illustrate the phase and permittivity distribution along the dielectric slab, for all the considered case studies.

$$\underset{\text{case \#1}}{\overline{P}_{m,n}} = \begin{bmatrix} 86.3 & 103.5 & 120.7 & 137.9 & 155.1 & 172.2 \\ 69.0 & 86.2 & 103.1 & 120.6 & 137.8 & 155.0 \\ 51.8 & 68.9 & 86.2 & 103.3 & 120.6 & 137.7 \\ 34.5 & 51.7 & 68.9 & 86.1 & 103.3 & 120.5 \\ 17.3 & 34.5 & 51.6 & 68.8 & 86.0 & 103.2 \\ 0 & 17.2 & 34.4 & 51.6 & 68.8 & 85.9 \end{bmatrix} \tag{4.21}$$

$$\underset{\text{case \#1}}{\epsilon_{r_{m,n}}} = \begin{bmatrix} 2.06 & 2.32 & 2.59 & 2.88 & 3.18 & 3.49 \\ 1.82 & 2.06 & 2.32 & 2.59 & 2.88 & 3.18 \\ 1.59 & 1.82 & 2.06 & 2.32 & 2.59 & 2.87 \\ 1.37 & 1.59 & 1.82 & 2.06 & 2.32 & 2.59 \\ 1.18 & 1.38 & 1.59 & 1.82 & 2.06 & 2.31 \\ 1.00 & 1.18 & 1.37 & 1.59 & 1.82 & 2.06 \end{bmatrix} \tag{4.22}$$

$$\underset{\text{case \#2}}{\overline{P}_{m,n}} = \begin{bmatrix} 171.9 & 205.8 & 239.6 & 273.5 & 307.4 & 341.2 \\ 137.5 & 171.4 & 205.3 & 239.1 & 272.9 & 306.8 \\ 103.2 & 137.0 & 170.9 & 204.7 & 238.6 & 272.5 \\ 68.8 & 102.6 & 136.5 & 170.3 & 204.2 & 238.1 \\ 34.4 & 68.3 & 102.1 & 135.9 & 169.8 & 203.7 \\ 0 & 33.9 & 67.7 & 101.6 & 135.4 & 169.3 \end{bmatrix} \tag{4.23}$$

$$\underset{\text{case \#2}}{\epsilon_{r_{m,n}}} = \begin{bmatrix} 3.49 & 4.16 & 4.89 & 5.67 & 6.51 & 7.42 \\ 2.87 & 3.48 & 4.15 & 4.87 & 5.66 & 6.5 \\ 2.31 & 2.86 & 3.47 & 4.14 & 4.86 & 5.65 \\ 1.82 & 2.31 & 2.85 & 3.46 & 4.13 & 4.85 \\ 1.38 & 1.81 & 2.3 & 2.84 & 3.45 & 4.12 \\ 1.00 & 1.37 & 1.8 & 2.29 & 2.84 & 3.44 \end{bmatrix} \tag{4.24}$$

$$\underset{\text{case \#3}}{\overline{P}_{m,n}} = \begin{bmatrix} 338.6 & 402.2 & 465.9 & 529.5 & 593.1 & 656.8 \\ 270.9 & 334.5 & 398.2 & 461.8 & 525.4 & 589.1 \\ 203.2 & 266.8 & 330.4 & 394.1 & 457.7 & 521.3 \\ 135.4 & 199.1 & 262.7 & 326.4 & 389.9 & 453.6 \\ 67.7 & 131.4 & 194.9 & 258.6 & 322.3 & 385.9 \\ 0 & 63.6 & 127.3 & 190.9 & 254.5 & 318.2 \end{bmatrix} \tag{4.25}$$

$$\underset{\text{case \#3}}{\epsilon_{r_{m,n}}} = \begin{bmatrix} 7.34 & 9.19 & 11.24 & 13.5 & 15.9 & 18.6 \\ 5.61 & 7.23 & 9.07 & 11.1 & 13.4 & 15.8 \\ 4.1 & 5.51 & 7.12 & 8.94 & 10.9 & 13.2 \\ 2.84 & 4.02 & 5.41 & 7.01 & 8.8 & 10.8 \\ 1.8 & 2.77 & 3.94 & 5.32 & 6.9 & 8.7 \\ 1.00 & 1.75 & 2.7 & 3.86 & 5.2 & 6.8 \end{bmatrix} \tag{4.26}$$

All the cases studies were evaluated under EM simulations in CST. The resultant 3D radiation patterns are illustrated in Fig. 4.10 in both perspective and planar views. According to the results, it is possible to observe that the main lobe direction is steered pointing towards the requested output angles defined by the pair (Az, El): $(5°, 5°)$, $(10°, 10°)$, $(20°, 20°)$, respectively. With this evidence, it is possible to conclude that 2D beamsteering can be realised when applying the proposed theoretical model to an ideal dielectric slab.

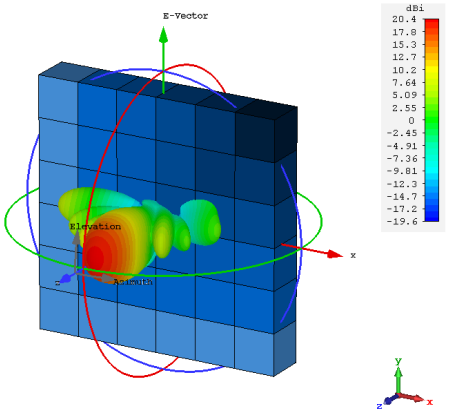

(a)

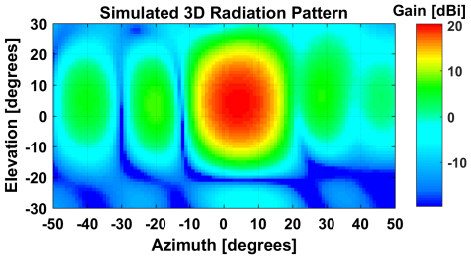

(b)

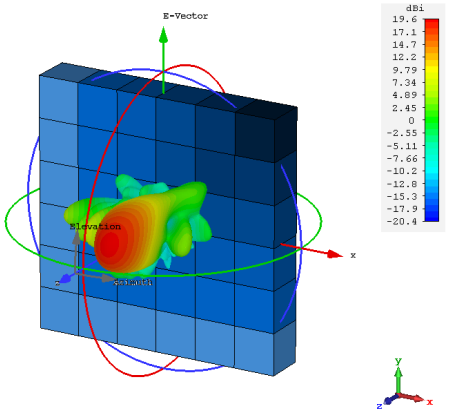

(c)

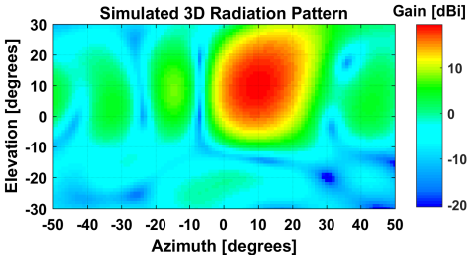

(d)

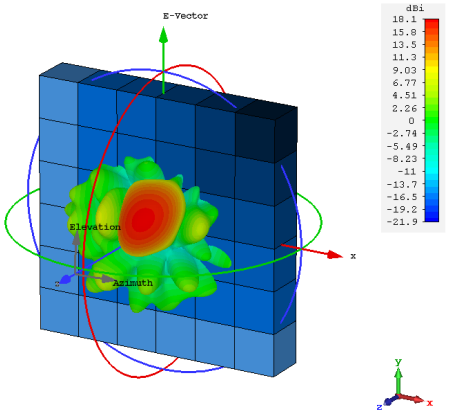

(e)

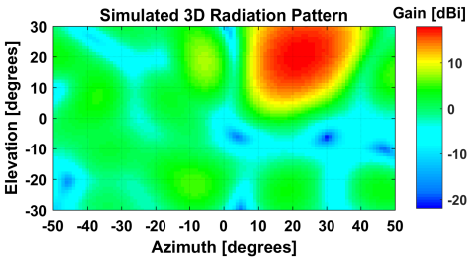

(f)

FIGURE 4.10: Simulated 3D radiation pattern (perspective and planar view) with main lobe steered towards (Az, El): (a) $(5°, 5°)$, (b) $(10°, 10°)$ and (c) $(20°, 20°)$, using a dielectric transmitarray.

4.4.3 Impact of transmitarray size on main lobe direction

Although 2D antenna beamsteering has been validated on a 6×6 dielectric slab, the proposed theoretical model can also be employed to different array dimensions. Thus, a new set of simulations running on dielectric slab models composed of 2×2, 4×4, 8×8 and 10×10 elements were performed, in addition to the 6×6 one, to evaluate the impact of the transmitarray size (*i.e.* number of elements) on main lobe direction. A snapshot of the considered models in CST MWS environment is depicted in Fig. 4.11.

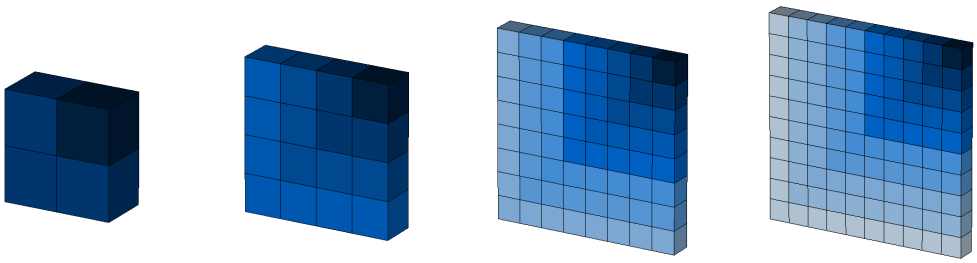

(a) (b) (c) (d)

FIGURE 4.11: (a-d) Snapshot of the 2×2, 4×4, 8×8 and 10×10 dielectric slab, in CST, for beamsteering analyse.

The simulations were performed on the slabs of Fig. 4.11, while dielectric materials properties, boundaries conditions and unitary element dimensions were preserved from the previous analysis, thus increasing the overall size of the samples. In particular, every transmitarray model was simulated for the output angles set to steer to (Az, El): $(0°, 0°)$, $(5°, 5°)$, $(10°, 10°)$ and $(20°, 20°)$, respectively. The radiation patterns obtained from the simulations were analysed and, the gain, the coordinates of the main lobe direction and respective HPBW, were compiled in Table 4.4. From the analyse of the table, it is immediately observed that the simulated main lobe direction was steered towards the expected direction, matching coordinates set in the theoretical model, for all dielectric slabs dimensions. In fact, just for a few cases, *e.g.* for 10×10 with $(20°, 20°)$, an error of $1°$ is observed, that may be related with angular accuracy of the simulation environment. Notwithstanding, these results clearly evidence that:

i) The direction of radiation patterns obtained by simulation corroborates with the expected angle direction, validating once again, the proposed 2D theoretical model against the EM solver;

ii) Consequently, this fact generates a relatively good level of confidence on the theory-to-simulation methodology utilised herein;

iii) The size of the transmitarray does not impact the main lobe direction, at a given output angle.

TABLE 4.4
IMPACT OF TRANSMITARRAY SIZE ON MAIN LOBE DIRECTION.

Array size	Expected		Main lobe			HPBW	
	$Az(°)$	$El(°)$	$Az(°)$	$El(°)$	Gain (dB)	$Az(°)$	$El(°)$
2×2	0	0	0	0	10.7	53.6	54.2
4×4	0	0	0	0	16.6	30.1	23.9
6×6	0	0	0	0	20.3	19	16.2
8×8	0	0	0	0	22.9	11.5	15.4
10×10	0	0	0	0	24.9	11.7	9.5
2×2	5	5	5	5	11	52.5	52.5
4×4	5	5	5	5	16.9	22.2	29.5
6×6	5	5	5	5	20.4	14.9	19.9
8×8	5	5	5	5	22.7	15.2	11.3
10×10	5	5	5	5	24.2	9.4	12.6
2×2	10	10	10	10	11.3	49.3	50.2
4×4	10	10	9	10	16.7	30.3	21.8
6×6	10	10	10	10	19.6	15.9	20.4
8×8	10	10	10	10	21.7	14.5	11.8
10×10	10	10	10	10	23.6	9.7	12.2
2×2	20	20	20	19	11.1	42.9	49.9
4×4	20	20	20	20	14.8	29.4	32
6×6	20	20	21	20	18.1	19.1	20
8×8	20	20	20	20	19.9	14.3	16.6
10×10	20	20	21	21	22.1	13.7	10.4

However for this particular set of simulations, two major effects are interestingly noticed when the dielectric slab are enlarged. Firstly, the gain at the main direction (merely indicative) increases. Secondly, the HPBW decreases indicating that the main lobe of the radiation is becoming narrower.

Although both these effects are in agreement with the theory of antenna arrays (refer to Section 2.2.1), which indicates that the gain at the main lobe direction increase while its beamwidth becomes narrower for larger antenna arrays (due to the array factor) [5, 6], in this particular case, such effect is associated to the simulation setup in CST MWS. Since the dielectric slab was excited by a impinging wave (with E- and H-fields orientation depicted in Fig. 4.5) proportional to the size of the dielectric slabs, this increases the integration area of the EM problem. Consequently, the total radiated gain is higher and the radiation pattern in the far-field narrower. Nonetheless, this does not invalidate the characterisation of the steering angles present in Table 4.4. For a comparative analyse, in Appendix A there are present a set of simulations for the excitation source.

4.4.4 Model stability to small ϵ_r variations

In order to analyse the sensitivity of the proposed model to small variations of substrate's permittivity (ϵ_r), a parametric study was performed under EM simulations. This test intends to evaluate the impact of a small change in permittivity, on element's transmission phase ($\Delta\alpha$) and, consequently, on the output angle direction. A maximum variation of 5% of ϵ_r was considered, which corresponds to approximately $\times 2$ the typical tolerance for permittivity, of a commercial available substrate (*e.g.* 2% in Nelco NX9250 [132]).

According to Fig. 4.12, which plots the relative transmission phase against ideal element relative permittivity (considering an element with dimensions $t = p = 33$ mm, at 5 GHz), it becomes clear that the transmission phase is impacted with any change in dielectric permittivity. For example, a +5% of tolerance for a substrate with an $\epsilon_r = 6$ ($\Delta\epsilon_r = 0.2$), results on a phase discrepancy $\Delta\alpha$ of around 9°. The transmission phase difference is then proportional to the permittivity on each element as detailed Table 4.5.

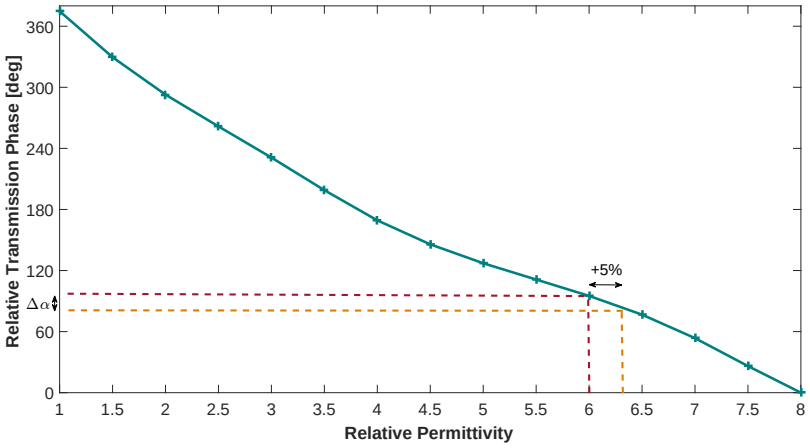

FIGURE 4.12: Simulated transmission phase in function of element's relative permittivity, for a transmitarray element with dimension of $t = p = 33$ mm at 5 GHz.

Therefore, to analyse the impact of the phase variation associated to the tolerances of substrate's permittivity on the output angle direction, two tests have been performed on the dielectric model of the transmitarray:

i) by forcing every dielectric element to have the same $\Delta\epsilon_r$ variation of +5% throughout the transmitarray, *i.e.* $\epsilon_{r_{m,n}} = \epsilon_{r_{m,n}} + 5\%$;

ii) by forcing a random $\pm\Delta\epsilon_r$ ($\pm 5\%$) distribution of through the array, *i.e.* $\epsilon_{r_{m,n}} = \epsilon_{r_{m,n}} \pm \text{random}(\pm 5\%)$.

TABLE 4.5
RELATIVE PHASE VARIATION ASSOCIATED TO SUBSTRATE TOLERANCES.

ϵ_r	$\Delta\epsilon_r$ @ $+5\%$	$\Delta\alpha$ (°)
1	0.05	3
2	0.1	6
4	0.2	12
6	0.3	9
8	0.4	25

The results were obtained using the 6×6 dielectric slab model in CST MWS presented for the 2D beamsteering analyse (Section 4.4.2). The maximum power direction of the resultant radiation patterns was used as figure of merit for characterisation. Several sets of output angles were considered and are summarised in Table 4.6.

TABLE 4.6
SIMULATED RESULTS FOR MODEL STABILITY TO SMALL ϵ_r VARIATIONS.

	Expected	Original	+5% tol.	dev.	Rand. dist.	dev.
Gain* (dBi)	—	20.4	20.3	-0.1	20.3	-0.1
Az (°)	5	5	5.1	+0.1	5.1	+0.1
El (°)	5	5	4.9	-0.1	4.9	-0.1
Gain* (dBi)	—	19.7	19.6	-0.1	19.6	-0.1
Az (°)	10	10.1	9.9	-0.2	10	-0.1
El (°)	10	10.1	9.9	-0.2	10	-0.1
Gain* (dBi)	—	18.1	17.5	+0.6	17.8	-0.3
Az (°)	20	21	23	+2.0	21	0.0
El (°)	20	20.7	23	+1.7	20.5	-0.2
Gain* (dBi)	—	17.3	16.8	-0.5	17.2	-0.1
Az (°)	30	30	33	+3.0	30	0.0
El (°)	30	30.6	33	+2.4	31	+0.4

* Gain given by CST MWS, just for reference.

As it can be concluded from the results of the Table 4.6, a clear deviation of the main lobe direction is noticed (+3°), specially for the cases with high output amplitude (20°,20°) and (30°,30°), when +5% of tolerance is applied uniformly throughout the array (test case *i*). This effect is explained since higher amplitude output angles require higher permittivity values (as in (4.26)), and consequently, the increment of phase associated to permittivity is also higher (Table 4.5). Additionally, since the transmission phase is uniformly incremented throughout the transmitarray, this impacts the progressive phase

(phase difference) between adjacent elements and thus, the output angle direction. For cases with lower output amplitude, the effect of small ϵ_r variations is not significantly noticeable.

Interestingly, for the random distribution (test case *ii*), the output angle direction is also not significantly impacted, remaining at its original position. This is valid for all the selected sets of angles. In fact, this can be explained by the non-uniform (random) distribution of the variations along the transmitarray. Since there are a non-uniform progressive phase distribution in the array, *i.e.* the random distribution do not allow all adjacent elements to have the same phase difference, this does not produce significant changes on the output angle directions.

With this study is then concluded that the tolerance of the substrate affects the angles direction with higher output resolutions. However, such alteration may be neglected in a real case due to the low tolerances in permittivity of commercial available substrates.

4.4.5 Final considerations on models validation

Even though both 1D and 2D beamsteering theoretical models were successfully implemented and validated against EM simulations on the dielectric transmitarray, there are a few considerations that deserve particular attention.

Firstly, it should be pointed out that the validation of the proposed theory under the slab models is only possible due to the use of ideal materials with permittivity values that may not be found in any particular dielectric in reality. As depicted in Fig. 4.12, an ϵ_r that varies from 1 and 8 is needed (considering element's dimensions of previous examples), to achieve a relative transmission phase that ranges from 0° to 360° necessary to enable beamsteering.

Not only would be impractical to physically implement a dielectric transmitarray with so many different materials (*i.e.* 6×6 array = 36 elements) that would be almost impossible to rapidly find materials that would fit within the required permittivity range. Even if possible to overcome these impracticalities, a single slab would enable beamsteering towards a single direction only since the relative permittivity of materials is typically constant (for the same frequency), limiting the application of tunable beamsteering.

Although there are some known electrically tunable dielectric materials, *e.g.* BST and Lead Strontium Titanate (PST), those are mainly based on ferroelectric materials associated to relatively high dielectric loss tangents becoming also impractical for this application [133].

Therefore, to make the concept of a transmitarray applicable to antenna beamsteering new approaches should be taken in consideration for controlling the associated transmission phase. In the next section, Frequency Selective Surfaces are introduced as elements that under specific conditions can exhibit an enhanced and controllable transmission phase.

4.5 Interim conclusions

This chapter introduces the theoretical background for antenna beamsteering using a transmitarray. After the presenting the theoretical model for 1D beamsteering using a transmitarray, a new approach for the analysis of a transmitarray with 2D beamsteering has been introduced.

The theoretical models for both 1D and 2D beamsteering have been validated by EM simulations running on an ideal model of a transmitarray composed of ideal dielectric materials. A critical analysis on the obtained simulated radiation pattern is performed in order to validate the both the theoretical formulation and the simulation environment.

Moreover, a parametric simulation is presented to characterise the impact that small variations of permittivity of the dielectric materials that compose the ideal transmitarray might have on the beamsteering direction. The variations on the substrate were in-line with the ones typically associated to the tolerance values of real dielectric substrates.

The work presented herein confirms the utility model and proves the feasibility of using transmitarray structures in antenna beamsteering.

This page is intentionally left blank.

CHAPTER 5

FSS-inspired transmitarray for 2D-beamsteering

5.1 Introduction

In this chapter, a novel transmitarray with two-dimensional beamsteering capability inspired on Frequency Selective Surfaces is presented. Following the requirements of the theoretical model introduced in last chapter, a controlled phase shift is applied to each individual transmitarray element, to enable the steering of the main lobe of an original antenna pattern in both elevation and azimuth planes. This is accomplished using a 5×5 stacked layer structure of square-loop FSS unit-cells loaded with discrete surface mount capacitors when coupled to the aperture of a standard gain horn antenna.

A complete parametric study based on electromagnetic simulations using CST MWS, is presented to evaluate and characterise unit-cell parameters. In particular, the phase characterisation in terms of its variation and response with layer stacking and distance separation and its impact on beamsteering resolution is studied. Antenna beamsteering with ranges up to $Az = 25°$ and $El = 25°$ are achieved by means of EM simulations and validated against experimental results performed on a physical prototype at 5.3 GHz.

5.2 FSS-inspired transmitarray design

As it has been presented in Section 2.5, FSS can be employed for many purposes including transmitarray implementation for antenna beamsteering. Specifically due to their filtering capability, enhanced phase response when stacked together and due to the relatively low implementation costs, they have been chosen to compose the transmitarray presented in this chapter.

5.2.1 The FSS-inspired unit-cell

In particular, to comply with the re-transmission necessities of a transmitarray type of structure, a square-slot design with pass-band capability was selected to compose the transmitarray. The square-slot unit-cell, whose geometry and Equivalent Circuit (EC) are presented in Fig. 5.1, is one of the canonical forms of FSS when it comes to understanding the behaviour of this type of structures. Such form is deeply characterised in the literature in [13, 14, 90, 134–136].

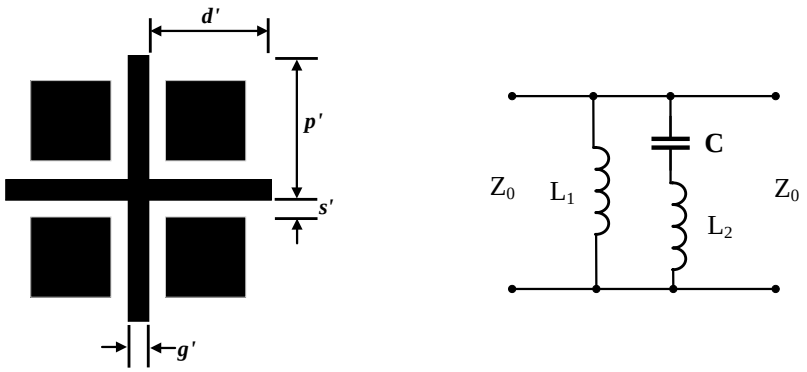

(a) (b)

FIGURE 5.1: Canonical model of a square slot FSS and respective EC model, presented in [90].

The frequency response of any FSS, depends on the dimensions of the geometry and of the physical properties (ϵ_r) of the substrate, and can be estimated by a set of equations relating together all these properties. For the unit-cell presented in Fig. 5.1, those equations are detailed in [134–136] and more recently revised in [90]. In particular, the pass-band frequency response (f_{ec}) obtained from the analysis of the equivalent resonant LC circuit, is given by (5.1),

$$f_{ec} = \frac{1}{2\pi\sqrt{(L_1 + L_2).C}}, \tag{5.1}$$

where,

$$\frac{X_{L_1}}{Z_0} = \omega L_1 = \cos\theta \; F(p', g', \lambda, \theta), \tag{5.2}$$

$$\frac{X_{L_{2int}}}{Z_0} = \frac{p' - 2s'}{p'} \; \cos\theta \; F(p', d' - 2s', \lambda, \theta), \tag{5.3}$$

$$\frac{X_{L_2}}{Z_0} = \omega L_2 = \frac{X_{L_{2int}}}{Z_0} + \frac{s'}{d' - 2s' + g'} \; \frac{X_{L_1}}{Z_0}, \tag{5.4}$$

$$\frac{B_{C_1}}{Y_0} = 4 \; \sec\theta \; F(p', g', \lambda, \theta), \tag{5.5}$$

$$\frac{B_{C_2}}{Y_0} = 4 \; \sec\theta \; F(d' - s', s', \lambda, \theta), \tag{5.6}$$

$$\frac{B_C}{Y_0} = \omega C = \left(1.75\frac{B_{C_1}}{Y_0} + 0.6\frac{B_{C_2}}{Y_0}\right) \; \epsilon_{eff} \tag{5.7}$$

$$\epsilon_{eff} = \frac{\epsilon_r + 1}{2} \tag{5.8}$$

The equations above translate the resonant effect that each part of the geometry has in the presence of an incident vertically polarised (Transverse-electric (TE) mode) EM field. Thus, in (5.2), X_{L_1} represents the inductance of the lines with g' width. X_{L_2} in (5.3) represents the inductance of the inner squares (with $d' - 2s'$ sides) with the lines with g' width, multiplied by a scaling factor defined by $\frac{(p'-2s')}{p'}$, which represents the s' length discontinuities. This X_{L_2} is, however, influenced by X_{L_1}, with a relation depicted in (5.4). Moreover, the capacitance value is obtained from two intermediate calculations. Equation (5.5) depicts the equivalent capacitor between the parallel lines with g' thickness and length d'. Equation (5.6) represents the capacitor between the inner square and the g' thickness lines. Finally, in (5.7), the overall value is calculated using the obtained and depicted relation. The ϵ_{eff} given by (5.8) represents the effective medium permittivity [13].

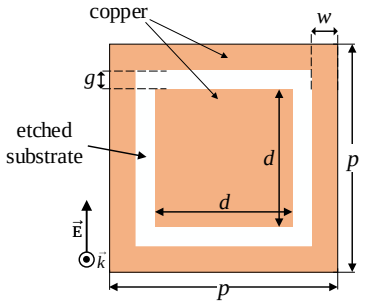

FIGURE 5.2: Square-slot unit-cell layout.

TABLE 5.1
UNIT-CELL DIMENSIONS AND SUBSTRATE CHARACTERISTICS.

Unit-cell dimensions (mm)				Generic Substrate	
p	d	g	w	*thickness*	ε_r
33	24	1.5	3	1.5 mm	2.5

For example, when considering the square slot unit-cell of Fig. 5.2 [90], whose substrate characteristics and dimensions (considering $w = g'/2$, $g = s'$, $p = p'$ and $d = d' - 2g'$ for ease of interpretation), are presented in Table 5.1, the S_{21} parameter obtained from the EC analyse is proved to be in good agreement with the one obtained from an EM simulation using CST MWS. From the mathematical work out (using (5.2) to (5.8)), one can obtain an $L_1 = 22.9$ nH, $L_2 = 2.67$ nH and $C = 0.13$ pF, generating a pass-band filtering characteristic whose resonant frequency is around 2.6 GHz, as depicted in Fig. 5.3.

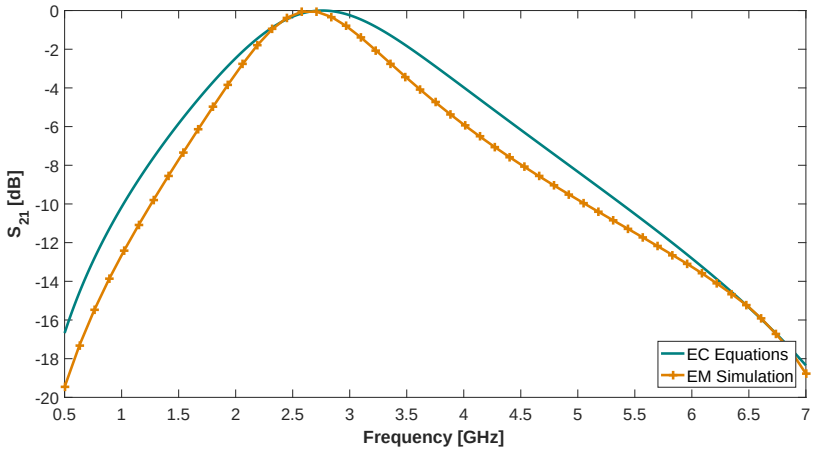

FIGURE 5.3: Comparison of the frequency response of the canonical FSS square slot geometry, when analysed using the EC equations *vs.* full wave simulation.

5.2.2 Proposed unit-cell design

As it can be concluded from the previous analysis, FSSs exhibit a resonant behaviour that typically depend on the shape and dimensions of the unit-cell. However, with the objective of having control over the resonant characteristics, alternative unit-cell models are presented in the literature by having their electromagnetic properties controllable by an external stimulus, *i.e.* voltage or current. For example, in the work presented in [126] and in [137], varactor diodes and PIN diodes have been employed over the canonical FSS square slot design [134–136], respectively, to achieve frequency reconfigurability.

Particularly in this thesis, an unit-cell based on the design presented in [126] and [137] is proposed. The unit-cell is depicted in Fig. 5.4. Similarly to the one introduced in [126], it employs two discrete surface mount capacitors (C_d) placed over the top and bottom gaps, between the inner patch and the outer ring of a square slot canonical design. However, the unit-cell proposed in this thesis (Fig. 5.4) mainly differs from the one in [126] by having a perfect squared geometry (in [126] dimensions in X and Y directions are not equal) and, by having a very thin gap of 0.2 mm etched on the edges of the outer ring separating the metallic parts, *i.e.* $p > l$ where p represents the total length of the substrate and l the length of the ring. It should be noted that

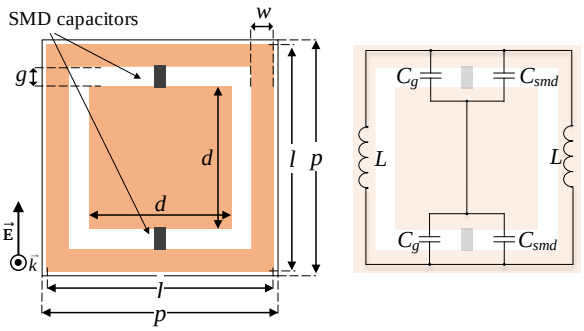

FIGURE 5.4: Square-slot unit-cell design employing SMD capacitors.

this gap was intentionally introduced to avoid the mechanical (and thus electrical) contact between adjacent unit-cells, when those are arranged side-by-side forming an array. This step was thought in advance, so that the proposed unit-cell could be used in an electronically controlled transmitarray, with independent addressable unit-cells, as reported in Chapter 6.

Due to the addition of two discrete capacitors on top of the existing gaps of the square slot FSS canonical model (Fig. 5.2), the original EC circuit model and the respective analyse equations (5.2) to (5.8) lose their significance. To the author knowledge, no proper theoretical model has been reported in the literature relating the unit-cell physical dimensions, equivalent capacitance and inductance and, the value of the loaded capacitors. However, some approximations to estimate the resonant frequency response of a square-slot loaded with capacitors have been made in [126] and in [137].

Therefore, the equation to estimate the resonant frequency response presented in [126] and given by (5.9), is considered in this work:

$$f_r = \frac{1}{2\pi.\sqrt{L_{eq}.C_{eq}}} = \frac{1}{\pi.\sqrt{L.(C_g + C_d)}}, \tag{5.9}$$

where, $L_{eq} = L/2$ and, $C_{eq} = (C_g + C_d)/2$, and L and C_g are fixed values, given by the unit-cell dimensions and C_d represents the capacitance values of the discrete SMD capacitors. When excited by an incident EM wave with a frequency close to the filter resonant frequency (f_r), and due to its band-pass frequency response, the unit-cell will allow the EM wave to propagate through with minimum insertion losses and controlled phase shifting.

TABLE 5.2
UNIT-CELL DIMENSIONS AND SUBSTRATE CHARACTERISTICS.

Unit-cell dimensions (mm)					Nelco NX9250 substrate [132]		
p	l	d	g	w	*thickness*	ε_r	$tan\delta$
33	32.8	24	1.5	3	1.5 mm	2.5	0.0017

Therefore, through an extensive set of parametric simulations, an unit-cell with the final dimensions and substrate [132] detailed in Table 5.2 exhibits a band-pass response ranging from 5 to 5.5 GHz when the capacitance (C_d) is varied from 2.8 to 0.7 pF. Nevertheless, the operation frequency of the unit-cell is considered to be of 5.35 GHz corresponding to the frequency point that crosses the pass band of all filter configurations, within the entire capacitance range, as depicted in Fig. 5.5a. In this particular case, the transmission phase shift is very low (less than 100°) along the capacitance variation range, as shown in Fig. 5.5b for $n = 1$, therefore not meeting the phase criteria of 360° defined in the theoretical analysis for beamsteering purposes.

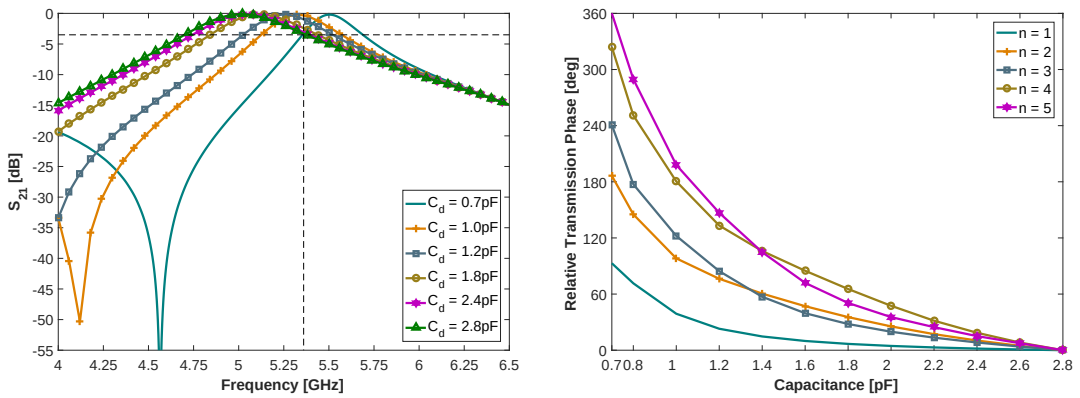

(a) (b)

FIGURE 5.5: (a) S_{21} for the unit-cell (single layer) and (b) relative transmission phase at 5.35 GHz for n-layers spaced by $\lambda/16$.

5.2.3 Transmitarray element design

In order to compensate this shortcoming, layers of unit-cells could be stacked separated by an air gap, as shown in Fig. 5.6. This allow to increase the range of the transmission phase by performing an impedance match, as reported in [13, 83, 125, 128]. In particular, [83] states that enhanced transmission in amplitude and phase shift up to 360° start to occur for a minimum of 4 stacked layers, separated at a distance of $\lambda/4$ (at the design frequency), corresponding to a quarter-wavelength impedance transformer. However, shorter separation distances (*e.g.* $\lambda/16$) can be used for extended phase requirement (Fig. 5.5b), at the expense of increasing the ripple (oscillation) in the transmission amplitude, as illustrated in Fig. 5.7a. From the depicted results, it is possible to notice the increase of the oscillation in transmission amplitude, for $n > 2$ layers, specially at the upper frequency points of the pass band (around 5.5 GHz). Additionally, it is also possible to observe the effect that the number of stacked layers have on the filtering response causing the S_{21} to be wider in the pass band (the bandwidth increases) and more selective in frequency. Therefore, a trade-off between the optimum number of stacked layers and separation distance ought to be considered to reduce the overall thickness of the apparatus while preserving the necessary phase and amplitude response for a beamsteering application.

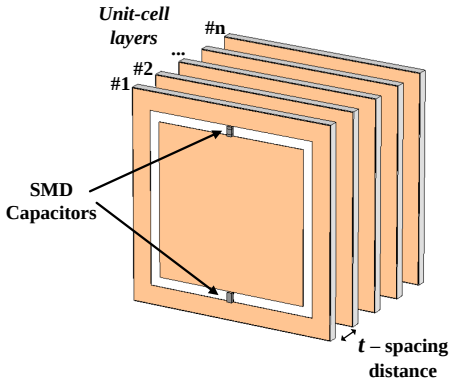

FIGURE 5.6: Stacked layers of unit-cells to increase transmission phase.

Accordingly, a parametric study is presented based on EM simulations to evaluate the best combination between number of stacked layers (n) and layer separation distance (t), against relative transmission phase ($\Delta\alpha$) to the case of $C_d = 2.8$ pF, bandwidth ($\triangle f$) and insertion losses (I_{loss}). This has been performed when 2 or more layers of unit-cells are stacked together. The number of layers varies from $n = 2$ to $n = 5$ while the separation distance varies from $t = 2.5$ to $t = 5$ mm in 0.5 mm steps. The capacitance range spans from $C_d = 0.7$ to $C_d = 2.8$ pF.

In this particular application, and considering a typical filter analysis, the bandwidth $\triangle f$, calculated using (5.10), is defined by the frequency difference between the higher -3 dB point of the 2.8 pF curve ($f_{high_{2.8pF}}$) and the lower -3 dB point of the 0.7 pF curve ($f_{low_{0.7pF}}$), both relative to the maximum value of transmission amplitude, as illustrated in Fig. 5.7b.

$$\triangle f = f_{high_{2.8pF}} - f_{low_{0.7pF}} \tag{5.10}$$

The relative transmission phase $\triangle\alpha(f_c)$ at the centre frequency, is defined by the middle point of the passband $f_c = \triangle f/2$. Furthermore, for all the parametric combinations it is characterised I_{loss} as the maximum value of insertion losses within the pass band, which in some cases is higher than -3 dB due to the oscillation in the pass band (see Fig. 5.7b). Hence, it is possible to get a fair comparison between all the parametric combinations and characterise appropriately the transmitarray element.

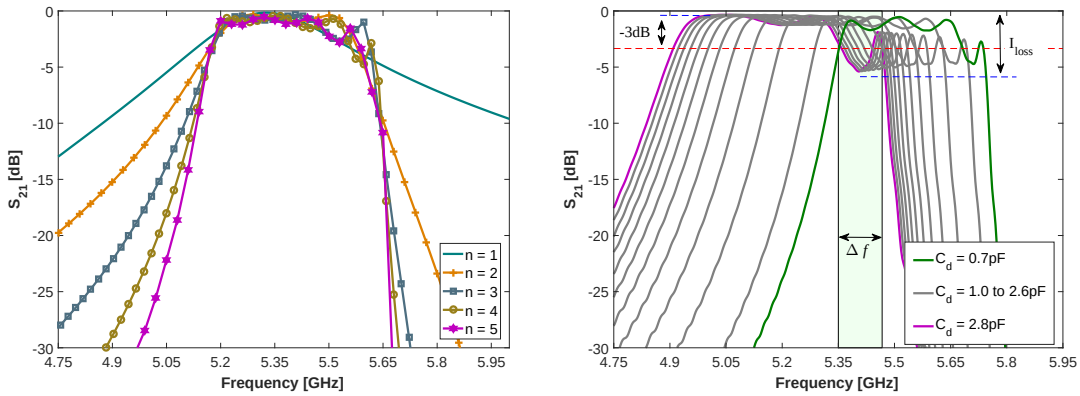

(a) (b)

FIGURE 5.7: (a) Comparison of S_{21} response for n-stacked layers separated $\lambda/16$ for $C_d = 1.0$ pF and (b) example of S_{21} analysis in the parametric study.

From the analysis of Table 5.3, it is possible to conclude that the relative transmission phase $\triangle\alpha$ increases by increasing the number of stacked layers (n) (Fig. 5.5b), as expected, regardless of the separation distance (t). Actually, with $n = 5$ layers, the $\triangle\alpha$ almost doubles when comparing with the use of $n = 2$ layers, in the interval $2.5 \leq t \leq 4$ mm. For the cases in which $t = 4.5$ mm and $t = 5$ mm with $n = 2$, results are not presented (n/a) since the bandwidth is negligible for both cases. In addition, $\triangle\alpha$ also raises by increasing the distance but this effect is not as evident as the introduction of a layer at a given separation. However, the separation distance between layers introduces a shift in the centre frequency that ranges from $f_c = 5.35 \pm 0.01$ GHz at $t = 2.5$ mm to $f_c = 5.40 \pm 0.01$ GHz at $t = 5$ mm, representing an offset of 50 MHz in relation to the initial frequency point.

Table 5.3
Simulation results for a single transmitarray element.

t (mm)	n	f_c (GHz)	$\triangle f$ (MHz)	I_{loss}(dB)	$\triangle\alpha(^\circ)$
2.5	5	5.36	140	3.39	318
	4	5.35	165	5.14	270
	3	5.35	133	2.85	201
	2	5.35	70	1.5	174
3	5	5.35	118	3.25	325
	4	5.38	160	5.45	285
	3	5.37	120	2.94	209
	2	5.36	55	1.8	179
3.5	**5**	**5.35**	**90**	**3.09**	**360**
	4	5.4	138	5.51	299
	3	5.39	100	2.82	213
	2	5.36	45	2.27	186
4	**5**	**5.38**	**65**	**2.88**	**393**
	4	5.4	115	5.39	314
	3	5.4	80	2.63	244
	2	5.37	15	2.94	196
4.5	**5**	**5.38**	**35**	**2.65**	**443**
	4	5.4	95	5.16	334
	3	5.4	55	2.4	271
	2	n/a	n/a	n/a	n/a
5	**5**	**5.40**	**80**	**6.98**	**468**
	5	**5.38**	**140**	**6.98**	**371***
	4	**5.41**	**58**	**4.97**	**364**
	3	5.41	30	2.27	300
	2	n/a	n/a	n/a	n/a

* For the case in which the capacitance ranges varies from $C_d = 0.8$ pF to $C_d = 2.8$ pF.

The bandwidth $\triangle f$ of the aggregate tends to increase with the number of stacked layers, particularly when $2 \leq n \leq 4$ are considered, but between the 4^{th} and the 5^{th} layer, it can be observed a decrease in bandwidth of around 40 MHz (on average) for the cases where $2.5 \leq t \leq 4.5$ mm. In respect to I_{loss}, relatively low insertion losses are noticed (≤ 3 dB) when the number of stacked unit-cells is less than $n = 3$. However, with $n = 4$ a peak in insertion losses is noticed with values around 5.3 dB (on average) irrespective of the separation distance. For the case in which $n = 5$ and $2.5 \leq t \leq 4.5$ mm, the I_{loss} is around 3 dB except when $t = 5$ mm.

According to this analysis, an optimum setting is achieved for $n = 5$ stacked layers, spaced at a distance of $t = 3.5$ mm ($\lambda/16$ at $f_c = 5.35$ GHz) resulting in a maximum transmission phase of $\triangle\alpha = 360°$ with a reasonably comparable values for both bandwidth ($\triangle f = 90$ MHz) and insertion loss ($I_{loss} = 3.09$ dB) obtained when the capacitance varies from $C_d = 0.7$ pF to $C_d = 2.8$ pF. Nevertheless, several other combinations of number of layers (n) *versus* separation distance (t) can be used to achieve the necessary phase for beamsteering purposes. Those cases are marked in bold in Table 5.3, however not all of them present a relatively good agreement between insertion losses and bandwidth, *e.g.* $t = 4.5$ mm with $n = 5$ and $t = 5$ mm with $n = 4$.

When comparing the curves of the relative transmission phase for the highlighted cases in Table 5.3 (Fig. 5.8a), it can be noticed that for the combination where $n = 5$ and $t = 5$ ($\triangle\alpha = 468°$), the minimum value of the capacitance range could be set at 0.8 pF, maintaining a transmission phase over 360°. Consequently, it is possible to change the lower limit of the capacitance range and, according to (5.10), increase the bandwidth since f_{low} is now defined by the -3 dB point of the 0.8 pF curve. This particular case, marked with * in Table 5.3, exhibits a S_{21} response plotted in Fig. 5.8b, with bandwidth $\triangle f = 140$ MHz and a relative transmission phase up to $\triangle\alpha = 371°$ at the centre frequency.

Therefore, for the transmitarray implementation and subsequent beamsteering analysis, two configurations based on the presented parametric study are considered and summarised in Table 5.4. These parameters will form a single transmitarray element of the 5×5 transmitarray implemented in the following section.

Table 5.4
Configurations for a single transmitarray element.

Configuration	t (mm)	n	Capacitance Range (pF)
#1	3.5	5	[0.7; 2.8]
#2	5	5	[0.8; 2.8]

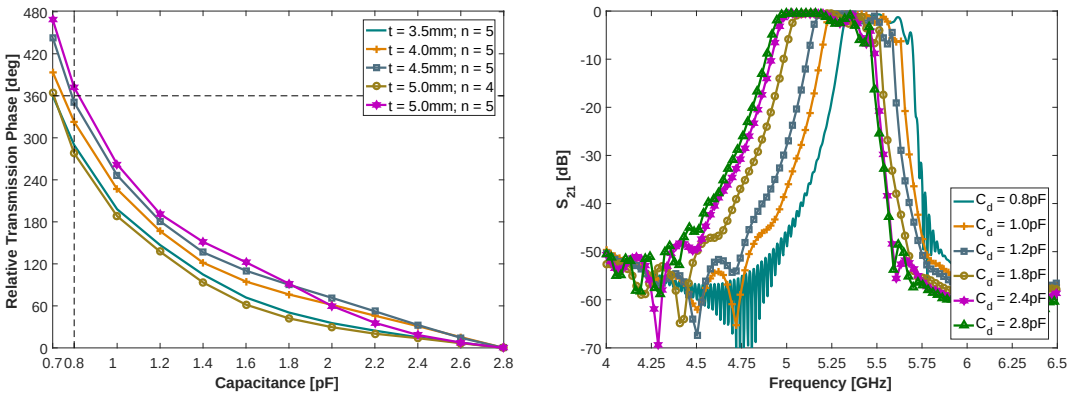

(a) (b)

FIGURE 5.8: (a) Relative transmission phase for the highlighted configurations of Table 5.3 and (b) S_{21} transmitarray response, considering the case $n = 5$ and $t = 5$ mm, within the capacitance range from 0.8 to 2.8 pF.

5.3 Beamsteering algorithm and model validation

Considering the proposal for a 5×5 transmitarray, as depicted in Fig. 5.9a, a MATLAB script was developed to implement the beamsteering algorithm and estimate the capacitance values to apply in each unit-cell of the array for a desired output angle, with Az and El components (2D beamsteering).

(a) (b)

FIGURE 5.9: (a) Model of the transmitarray in CST MWS, composed by 5×5 array elements of 5 stacked layers of unit-cells, (b) when coupled to the aperture of a realistic model of an horn antenna supported by the *Perspex* mount.

The script runs based on the equations presented in Section 4.3 for a transmitarray model with 2D beamsteering capabilities, and its data flow is summarised on the block diagram of Fig. 5.10. The script starts by calculating the progressive phase (ψ_x, ψ_y) for the requested output angle pair (Az, El), in the X and Y direction of the array

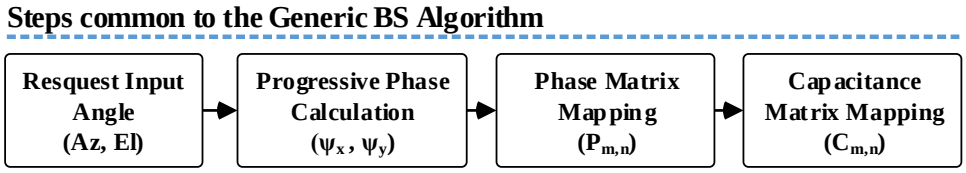

FIGURE 5.10: Block diagram of the implementation steps in the beamsteering algorithm.

and, consequently, the theoretical phase-shift necessary to apply in each transmitarray element. Additionally, the (normalised) phase-shifts of every array element are mapped in a matrix ($P_{m,n}$), ranging from 0° to 360°. The matrix has the size of the proposed structure (5×5 elements), wherein the position of first element of the matrix corresponds to the top left element of the transmitarray (when considering -z direction of Fig. 5.9a). Subsequently, the C_d values of each element are extracted by linearly interpolating (mathematical operation) the correspondent transmission phase curve of Fig. 5.8a with the phase-shifts given by the matrix $P_{m,n}$. Finally, the script returns a capacitance matrix ($C_{m,n}$) indicating the capacitance values to apply in transmitarray element.

When no beamsteering is intended, *i.e.* the main lobe of the radiation pattern remains at broadside ($Az = 0°$ and $El = 0°$ according to Fig.5.9a), all the capacitors of the transmitarray must be set to the same value (0.9 pF), in order to cancel the progressive phase between elements, and therefore any steer in direction.

As example, for the case in which the main lobe is intended to be shifted towards $Az = 23°$ and $El = 10°$, the (normalised) progressive phase matrices and the capacitance matrices, are detailed in (5.11) and (5.12) for configuration #1, and (5.13) and (5.14) for configuration #2, respectively.

$$\overline{P}_{m,n} = \begin{bmatrix} 326.1 & 244.6 & 163.1 & 81.5 & 0 \\ 2.9 & 281.4 & 199.8 & 118.3 & 36.8 \\ 39.6 & 318.2 & 236.6 & 155.1 & 73.6 \\ 76.5 & 354.9 & 273.4 & 191.9 & 110.7 \\ 113.3 & 31.7 & 310.2 & 228.7 & 147.2 \end{bmatrix}, \quad C_{m,n} = \begin{bmatrix} 0.75 & 0.9 & 1.14 & 1.54 & 2.80 \\ 2.72 & 0.82 & 1.00 & 1.34 & 1.98 \\ 1.94 & 0.76 & 0.92 & 1.17 & 1.59 \\ 1.57 & 0.71 & 0.84 & 1.02 & 1.37 \\ 1.36 & 2.07 & 0.77 & 0.93 & 1.20 \end{bmatrix}, \tag{5.11}$$

$$\overline{P}_{m,n} = \begin{bmatrix} 327 & 245.3 & 163.5 & 81.7 & 0 \\ 5.14 & 283.4 & 201.6 & 119.9 & 38.1 \\ 43.3 & 321.5 & 239.8 & 158 & 76.2 \\ 81.4 & 359.6 & 277.9 & 196.1 & 114.4 \\ 119.5 & 37.8 & 316 & 234.2 & 152.5 \end{bmatrix}, \quad C_{m,n} = \begin{bmatrix} 0.88 & 1.05 & 1.34 & 1.86 & 2.80 \\ 2.65 & 0.96 & 1.17 & 1.61 & 2.18 \\ 2.13 & 0.89 & 1.06 & 1.37 & 1.90 \\ 1.86 & 2.79 & 0.97 & 1.19 & 1.65 \\ 1.61 & 2.18 & 0.90 & 1.08 & 1.39 \end{bmatrix}, \tag{5.13}$$

In order to assess the algorithm, predict the performance of the model and understand which of the configurations (#1 or #2) would perform the best in terms of beamsteering capability, a set of simulations was performed in CST on the 5×5 transmitarray. Therefore, the simulations were firstly performed using an incident plane-wave and open boundaries on the transmitarray to rapidly evaluate the model, rather than considering a full-wave approach using the horn antenna as radiation source (as depicted in Fig. 5.9b).

From the simulation results, employing both described configurations and their respective capacitance given by (5.12) and (5.14), it has been found that for configuration #1 the transmitarray does not present a good agreement in terms of output angle resolution, when comparing with configuration #2 and theoretical formulation. This study is presented in Table 5.5 for 4 beam steered angles, with Az and El components, where Δ_{Az} and Δ_{El} represents the angular deviation in both azimuth and elevation planes from theoretical values. With configuration #1 the output steered angle presents a maximum global deviation of $-5°$ against the $-2°$ of configuration #2, within all samples. Consequently, only configuration #2 is considered for a full wave analysis and further prototype implementation.

Table 5.5
Simulated beamsteering output angles(°) using plane wave excitation.

Expected		Configuration #1				Configuration #2			
Az	El	Az	El	Δ_{Az}	Δ_{El}	Az	El	Δ_{Az}	Δ_{El}
0	0	0	0	0	0	0	0	0	0
23	10	19	8	-4	-2	21	10	-2	0
0	25	0	20	0	-5	0	23	0	-2
25	0	20	0	-5	0	25	0	0	0

5.4 Transmitarray prototyping

As a result, the final model of the transmitarray comprises 5×5 elements of 5 stacked layers of unit-cells separated 5 mm by an air gap. The transmitarray presents an overall dimension of 180 mm × 180 mm × 27.5 mm, where a margin in substrate of 7.5 mm in all directions and four holes are considered to be able to attach the transmitarray to a support structure, as illustrated in Fig. 5.9b. The separation between layers is maintained by using PTFE spacers with 5 mm of height. The support structure, made of *Perspex* ($\epsilon_r = 2.22$, $tan\delta = 0.02$ and thickness of 5mm), allow to fix the structure

with a minimum separation of 5 mm, to a standard gain horn antenna, with aperture dimension of 230 mm × 170 mm and length 421 mm. This apparatus is considered in all the simulation and experimental results. The physical prototype of the 5 × 5 transmitarray is depicted in Fig. 5.11.

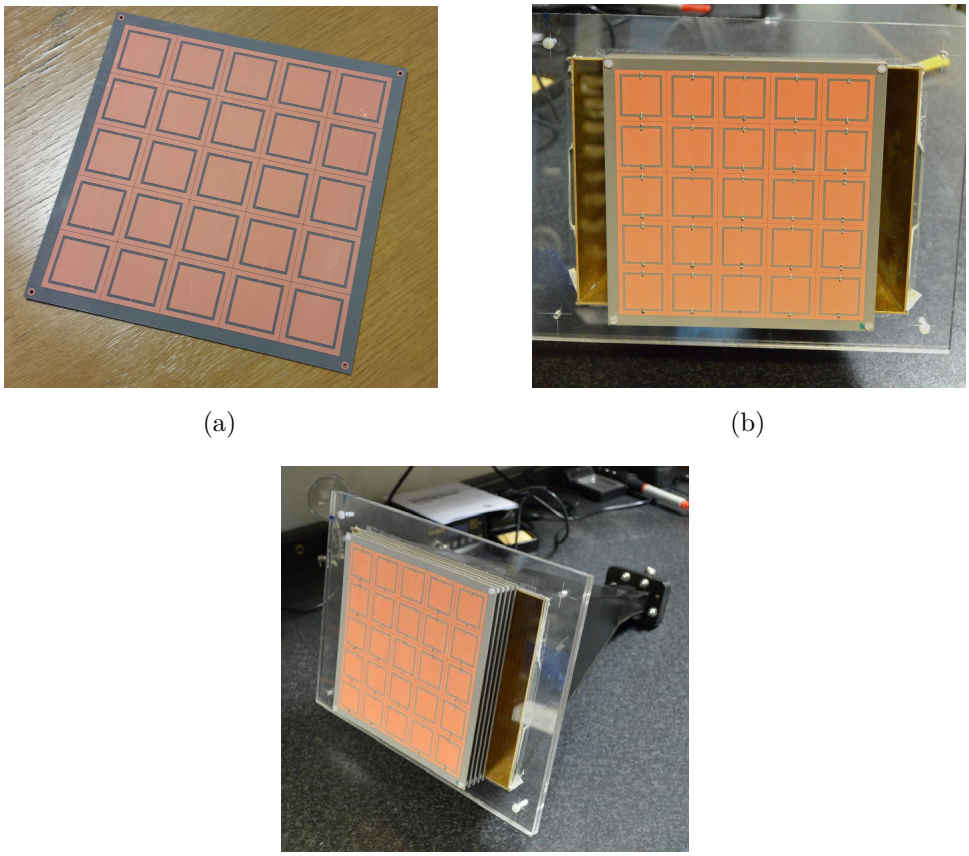

(a) (b)

(c)

FIGURE 5.11: (a) FSS prototype, (b) close up of the FSS-inspired transmitarray and (c) transmitarray coupled to the reference horn antenna using the *Perspex* mount.

5.5 Results and discussion

To assess the 2D beamsteering capability of the transmitarray, the four output angles with azimuth and elevation components of Table 5.5 are considered. For each angle, the respective capacitance matrix is applied to the transmitarray. Simulations are performed in CST MWS while experimental results are obtained using the setup described in Section 3.4. The beamsteering capability is evaluated, through the analysis

of 3D radiation patterns, in terms of main lobe steering direction (considering the higher absolute gain direction in dBi), half power beamwidth (HPBW and the side-to-main lobe level (SLL), *i.e.* the amplitude difference between the main lobe and the higher side lobe of the radiation pattern.

5.5.1 S_{11} parameter characterisation

The first set of measurements obtained were the antenna S_{11}. These were obtained for the horn antenna itself but also when the transmitarray is coupled to its aperture and all the capacitors set to the same value ($C_d = 0.9$ pF). Both sets are compared against its respective simulation results in Fig. 5.12. The results start to indicate that the horn antenna is relatively well matched ($S_{11} < -10\ dB$ [1]) within the presented frequency span (4.75 to 6 GHz). Moreover, when the transmitarray is coupled to the reference horn, the S_{11} curve takes the expected shape of a bandpass frequency response associated to the square-slot FSS. This is valid for both simulated and measured results. However, a frequency offset of around 90 MHz is clearly noticed between these set of results.

The offset is calculated by the frequency difference between the simulated and experimental S_{11} parameters (Fig. 5.12) at -10 dB. Such shift in frequency can be justified by the use of ideal lumped ports, purely capacitive, to simulate the capacitors in CST MWS, not taking into account possible intrinsic series inductance and resistance (no equivalent model for the capacitors were provided by the manufacturer) that would predict such effect. Due to this fact, simulated results will be analysed at 5.38 GHz corresponding to the centre frequency given by Table 5.3 for the referenced transmitarray element. However, to get a fair correspondence, experimental results are analysed at 5.29 GHz.

Therefore, simulated and experimental results will be presented in this document, side-by-side, to facilitate the their interpretation and further summarised in Table 5.6.

5.5.2 Beamsteering characterisation

To evaluate the beamsteering characteristics of the 5×5 transmitarray, the manufactured prototype has been coupled to the standard gain horn antenna characterised in Section 3.8. For reference, the 3D radiation patterns of the horn without the transmitarray coupled to its aperture are depicted in Fig. 3.17.

The beamsteering capability of the transmitarray was then evaluated considering 4 distinct output angle directions, steering towards (Az, El): $(0°, 0°)$, $(23°, 10°)$, $(0°, 25°)$ and finally to $(25°, 0°)$, according to the direction indicated in Fig. 5.9a.

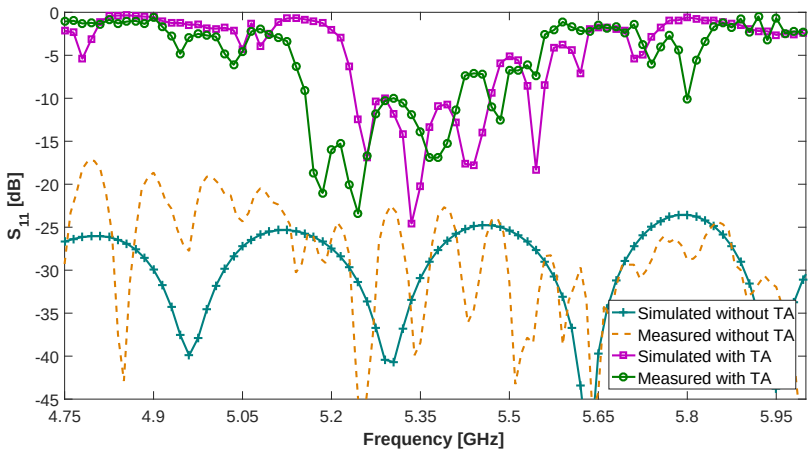

FIGURE 5.12: Simulated and measured S_{11} parameters, for the reference antenna with and without the transmitarray using $C_d = 0.9$ pF.

For each direction, the respective capacitance values have been computed using the MATLAB script described in Section 5.3. Therefore, the capacitance values given by the script were used in the simulations, whilst in the practical implementation those had to be approximated to the nearest available capacitor commercially available in the market. The correspondent theoric and real capacitor matrices to apply in the transmitarray, for each beamsteering angle, are detailed in Appendix B.

When the transmitarray is coupled to the reference antenna using the configuration previously described (all capacitors $C_d = 0.9$ pF), both simulations and experiments confirm that no steering is experienced (main lobe remains at broadside) as illustrated in Fig. 5.13a and Fig. 5.13b. Moreover, the filtering effect introduced by the structure is quite evident as depicted in the S_{11} parameter (Fig. 5.12). For this case, according to simulations the antenna has now a maximum gain of 18.7 dBi with a HPBW of 15° in Az and 21° in El, and a SLL of -15.2 dB, while for measurements, it presents an absolute gain of 17.3 dBi with a HPBW of 14° in Az and 16° in El, and a SLL of -13.7 dB. Consequently, a decrease in the gain at the broadside of around 1.9 dB in simulations and 2.8 dB in measurements is evident, when compared to the horn antenna alone. However, this difference is not only justified by the losses inserted by the transmitarray but also due the enhancement of side lobes even though SLL remains low.

By applying in the transmitarray the capacitors given by matrices (B.1) and (B.2) for simulation and experiments, respectively, the original antenna main lobe is then expected to shift in direction towards $Az = 23°$ and $El = 10°$. Simulated results (Fig. 5.14a) show the higher gain set at $Az = 22.0°$ and $El = 9°$ compared to the measured values (Fig. 5.14b) of $Az = 19.0°$ and $El = 9°$, presenting an error of 1°and 4°, respectively. The discrepancy between measured and simulated steered angles could be reduced by slightly changing the frequency of operation, setting the experiment to

5.20 GHz, resulting in $Az = 21.0°$ and $El = 11°$. For the referenced case, the absolute gain decays around 2.5 dB relative to the gain using the transmitarray at broadside, and similar effect occur in the SLL which varies proportionally in both simulated and experimental results. Nevertheless, for the experimental case, the main lobe (Fig. 5.14b) is narrower when comparing with the simulated one (Fig. 5.14a), presenting a HPBW mismatch in both Az and El, however is still reasonable specially when comparing with the HPBW of the reference antenna.

As indicated, two specific cases of beamsteering are considered by only performing a shift in elevation and azimuth planes,where the main lobe is expected to be centred at $Az = 0°$ and $El = 25°$ and $Az = 25°$ and $El = 0°$, respectively. For the elevation case, in which $Az = 0°$ and $El = 25°$ is intended, the considered capacitance matrices are detailed in (B.3) and (B.4), for simulation and experiments, respectively. The presented results, depiced in Fig. 5.15a and Fig. 5.15b, are in a good agreement with an maximum error of 3° between simulated, measured and expected angles. Both patterns are similar in shape and the main lobe gain and SLL are still proportional when comparing to the reference antenna. However, for the azimuth steering of $Az = 25°$ and $El = 0°$, which capacitance matrices are detailed in (B.5) and (B.6), the radiation pattern steered by the transmitarray (Fig. 5.16a and Fig. 5.16b), only achieves an output angle with its maximum gain direction at $Az = 19°$ and $El = 0°$, presenting a difference of 5° when comparing with the simulation results. This clearly demonstrates a limitation on the steering of the azimuthal angle, that can also be noticed for the case $Az = 23°$ and $El = 10°$.

In summary, it is possible to conclude that the proposed technique performs beam-steering with an averaged error of 3° between simulated and measured results. Such discrepancy can be justified by the capacitance difference between theoretical and real values of the discrete capacitors (Appendix B) and by their tolerance, even though the tolerance represents a relatively small part when comparing with discrepancy introduced by the theoretic-to-real conversion). Nonetheless, such angular deviation could be reduced by a fine tuning in the frequency range for the different output angles, or by compensating with change in capacitors values. Nevertheless, the accuracy of the beam steered angles is quite acceptable specially when compared with the high value of half power beamwidth. Moreover, if applicable to an automated model where capacitance could be electronically controlled *e.g.* by using varactors, such error may be decreased by pre-applying look up tables to compensate the capacitance values.

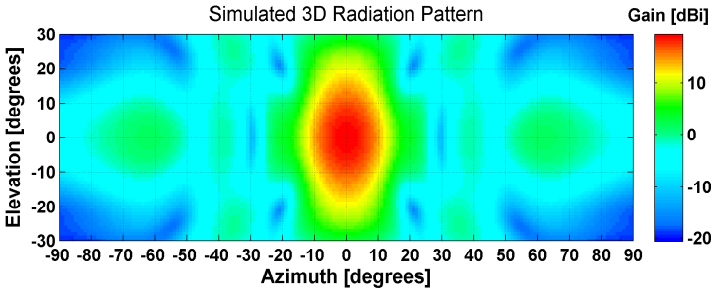

(a)

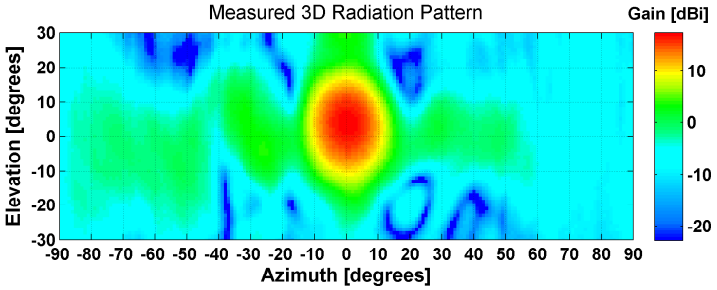

(b)

FIGURE 5.13: (a) Simulated and (b) measured 3D radiation pattern at 5.38 GHz and 5.29 GHz, respectively, with transmitarray set at broadside direction $(0°, 0°)$.

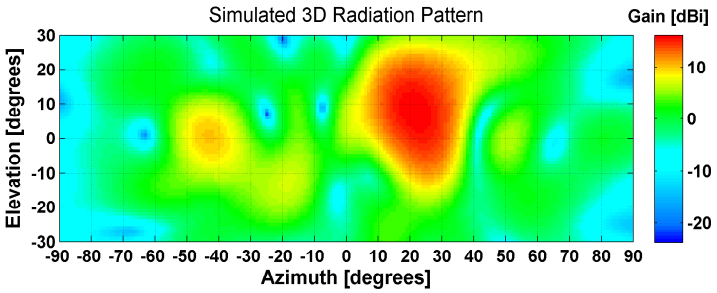

(a)

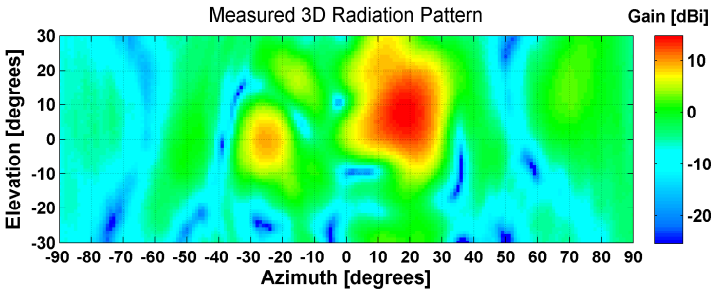

(b)

FIGURE 5.14: (a) Simulated and (b) measured 3D radiation pattern at 5.38 GHz and 5.29 GHz, respectively, with transmitarray steering at $(23°, 10°)$.

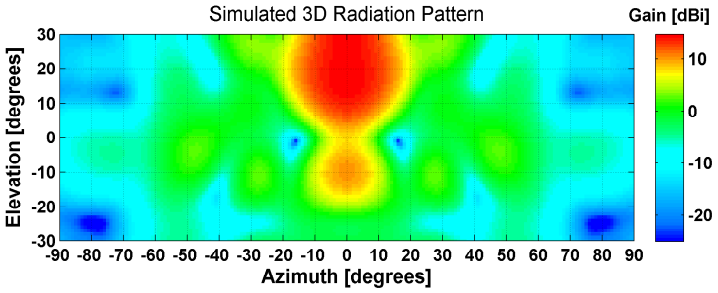

(a)

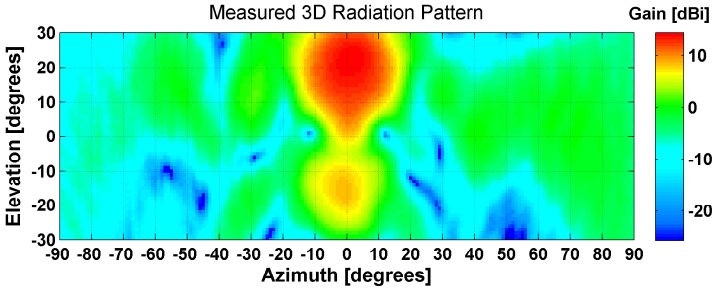

(b)

FIGURE 5.15: (a) Simulated and (b) measured 3D radiation pattern at 5.38 GHz and 5.29 GHz, respectively, with transmitarray steering at $(0°, 25°)$.

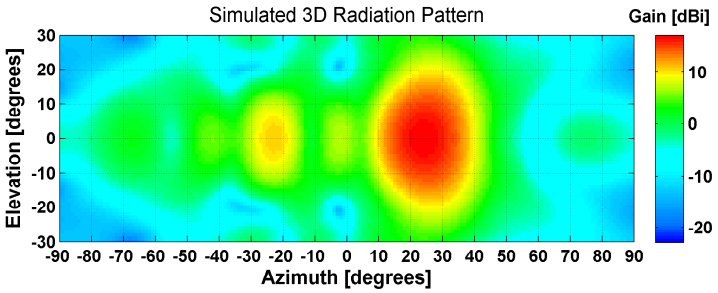

(a)

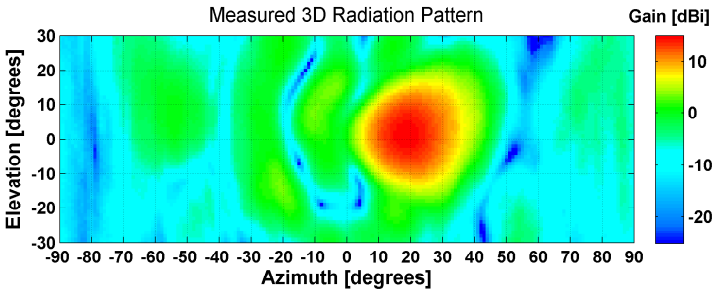

(b)

FIGURE 5.16: (a) Simulated and (b) measured 3D radiation pattern at 5.38 GHz and 5.29 GHz, respectively, with transmitarray steering at $(25°, 0°)$.

Table 5.6
Summary table for simulated and measured 3D radiation patterns.

Simulated Results @ 5.38 GHz								Experimental Results @ 5.29 GHz					
Expected		Main lobe			HPBW		SLL	Main lobe			HPBW		SLL
Az(°)	El(°)	Az(°)	El(°)	Gain (dBi)	Az(°)	El(°)	(dB)	Az(°)	El (°)	Gain (dBi)	Az(°)	El(°)	(dB)
*-	*-	0	0	20.6	17	17	-12.6	0	0	20.1	16	14	-11.9
0	0	0	0	18.7	15	21	-15.2	0	2	17.3	14	16	-13.7
23	10	22	9	16.2	20.7	25.6	-6.1	19	9	14.7	14	18	-5.3
0	25	0	22	14.8	24.4	35.7	-4.6	0	23	14.3	18	22	-5.9
25	0	24	0	16.5	19.6	23.9	-6.4	19	0	14.9	18	18	-11.5

*For the reference horn antenna without the transmitarray attached.

5.5.3 Polarisation characterisation

To characterise the effect on antenna polarisation caused by the insertion of the transmitarray, a measure of the Axial Ratio (AR) was performed inside the anechoic chamber. The AR is defined by the ratio of maximum length (OA) and minimum length (OB) of electric field of the polarised propagating EM wave, or the ratio of the major and minor axes of the polarisation ellipse [1, 15], depicted in Fig. 5.17.

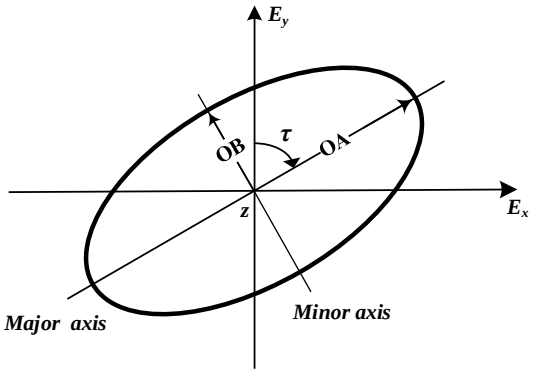

FIGURE 5.17: Polarisation ellipse (image adapted from [1]).

In fact, the AR can be calculated, in linear units, using (5.15),

$$AR = \frac{\textbf{major axis}}{\textbf{minor axis}} = \frac{OA}{OB}, \quad 1 \leq AR \leq \infty, \tag{5.15}$$

which resumes to the difference between OA and OB, if the values are considered to be in *decibels*.

To this extent, a comparative study was performed by measuring: *i*) the polarisation of the EM wave emitted by the reference horn antenna (individually); *ii*) the polarisation of the propagating wave when the transmitarray is coupled to the horn antenna and all capacitors are set at $C_d = 0.9$ pF (reference case for (0°,0°) output angle); and finally, *iii*) the polarisation of the propagating wave when the transmitarray is coupled physically rotated by 90°, in relation to the reference antenna (and maintaining $C_d = 0.9$ pF).

In this experiment, the setup utilised in last section for antenna radiation pattern were considered. The antenna under test was utilised as a receiver (although it may have been used as transmitter as indicated in [1]). The transmitter antenna was used to probe the polarisation. Measurements were obtained at 5.29 GHz. The arrangement for measurement is depicted in Fig. 5.18.

The antenna used as test probe was rotated in the plane of the polarisation (around Z axes with direction of rotation marked with τ in Fig. 5.18), which is taken to be normal to the direction of the incident field (plane xoy) [1, 15]. The S_{21} in *decibel* was recorded for every τ angle, defined from $-180 \leq \tau \leq +180$, with 1° step resolution. The resultant polarisation patterns, normalised to the maximum of the reference measurement (horn antenna), are depicted in Fig. 5.19.

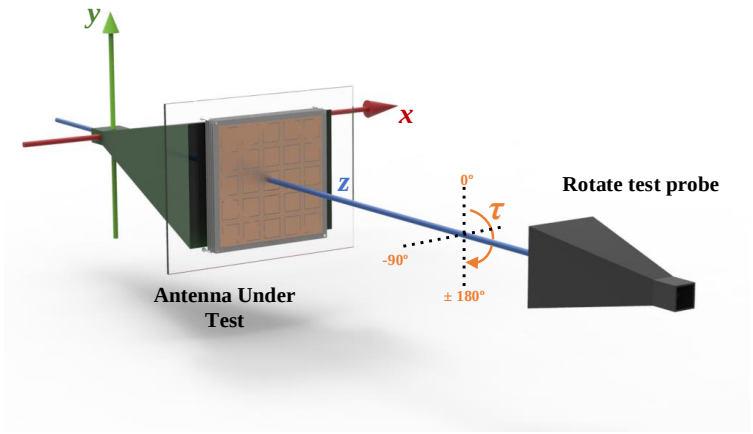

FIGURE 5.18: Antenna configuration for polarisation pattern measurement.

From the experimental results obtained for the horn (Fig. 5.19), it can clearly be observed the polarisation pattern of a typical linear polarised antenna. The maximum of radiation is set at the direction in which the E-fields vectors of both receiver and transmitter antennas are vertical and coincident. This can be seen at $\tau = 0°$ but also at $\tau = 180°$. On the other hand, the minimum of radiation is exhibited when both E-field vectors are perpendicular, *i.e.* when $\tau = \pm 90°$. Thus, according to (5.15), the AR for the horn antenna is of 25 dB.

When the transmitarray is coupled to the structure, no particular alteration can be noticed in the shape of the polarisation pattern, rather than a vertical offset of around 2.2 dB. This is explained by the fact the transmitarray was developed to operate in the vertically polarised mode (as indicated in Section 5.2.1). In fact, such offset corresponds to the insertion losses of the transmitarray structure at the considered frequency. The AR for this case is of *i.e.* $AR = 27$ dB.

Interestingly, when the transmitarray is physically rotated by 90° and both the transmitter and receiver antennas kept their original orientation, the polarisation pattern is severely affected. An attenuation of 24 dB is noticed although an AR of only 12 dB is obtained. This effect on the polarisation pattern is due to the attenuation

caused by cross-polarisation between the horn antenna and the transmitarray. Since the transmitarray is physically rotated by 90°, the propagating field is 90° out-of-polarisation to the transmitarray. This experiment clearly indicates the transmitarray do not operate significantly well for any other incident polarisation rather than the vertical one (TE mode). Table 5.7 resumes the results obtained from this characterisation.

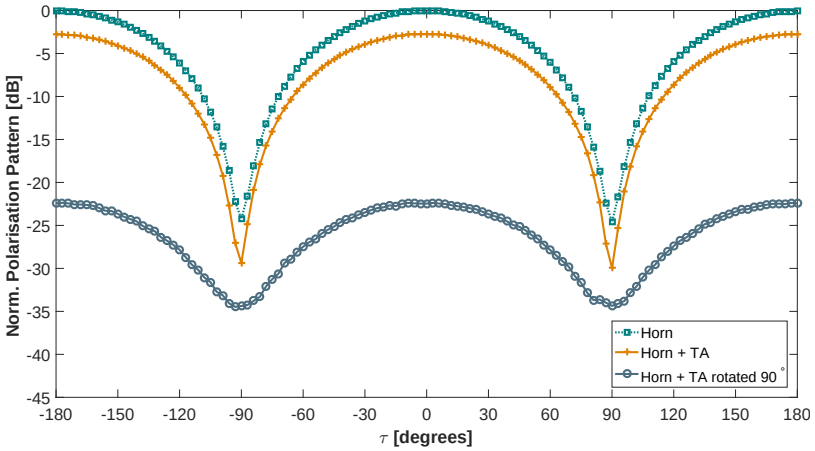

FIGURE 5.19: Normalised polarisation pattern at 5.29 GHz for the horn antenna, horn coupled with the transmitarray and, horn coupled with transmitarray rotated 90°, considering all capacitors set at $C_d = 0.9$ pF.

TABLE 5.7
MEASURED AXIAL RATIO OBTAINED AT 5.29 GHZ.

Case	OA (dB)	OB (dB)	AR (dB)
Horn antenna	0	-25	25
Horn + TA	-2.2	-29.4	27.2
Horn + TA rotated 90°	-22.4	-34.3	11.9

5.6 Interim conclusions

In this chapter, a new approach for the analysis of a transmitarray with 2D beam-steering capability using a FSS -inspired transmitarray has been presented and validated by EM simulations and experimental results carried out in a 5×5 transmitarray model.

The unit-cell that composes the transmitarray is inspired by a square slot FSS canonical model loaded with discrete SMD capacitors to modify its resonant frequency response. The unit-cell has been characterised using a full wave EM solver (CST MWS), where a parametric study evaluates the transmission phase, bandwidth and insertion losses of several layers of cells stacked together. It has been proved that by stacking up to 5 layers separated by a distance of 5 mm of air, the phase-shift between the first and the last layer can be tuned up to 360° by varying the value of the loaded capacitance.

Therefore, simulations on a transmitarray comprising 5×5 unit-cells with 5 stacked layers demonstrated that the main lobe of the radiation pattern of a horn antenna can successfully shifted towards specific directions, by changing the capacitance values in each array element. The proposed model has been validated through measurements performed on a physical prototype and compared against simulation results.

The similarity between simulated and experimental results validates the proposed model. Although an average error of 2° in output angle between theoretical and simulations, and 3° between simulated and experimental results are evident, this value is acceptable when considering high value of half power beamwidth of the main lobe of the radiation pattern.

The potential found in such application allied to the non-expensive manufacture cost motivated further developments in FSS-inspired transmitarray for beamsteering application. With a successful prove of concept on a discrete, non-reconfigurable transmitarray model, a fully electronically controlled transmitarray is therefore presented in the upcoming chapter of this thesis.

The work performed in this chapter was disseminated in one international journal publication and two international conference paper publications:

J. J. Reis; N. Copner; A. Hammoudeh; Z. Al-Daher; R.F.S. Caldeirinha; T.R. Fernandes and R. Gomes, **"FSS-inspired Transmitarray for two Dimensional Antenna Beamsteering"**, *IEEE Transactions on Antennas and Propagation*, vol. 64, no. 6, pp. 2197-2206, June 2016. doi: 10.1109/TAP.2016.2543802. **Impact Factor = 2.957, Q1;**

C. J. Reis; Z. Al-Daher; N. Copner; R.F.S. Caldeirinha and T.R. Fernandes, **"Two-Dimensional Antenna Beamsteering Using Metamaterial**

Transmitarray", *Proc. European Conf. on Antennas & Propagation - EUCAP*, Lisbon, Portugal, Vol. 1, pp. 1 - 1, April, 2015;

C. J. Reis; Z. Al-Daher; N. Copner; A. Hammoudeh; R.F.S. Caldeirinha and T.R. Fernandes, **"Two-Dimensional Transmitarray Beamsteering Using Stacked Tunable Metamaterials"**, *Proc. Loughborough Antennas and Propagation Conf. – LAPC*, Loughborough, United Kingdom, Vol. 1, pp. 495 - 499, November, 2014.

This page is intentionally left blank.

CHAPTER 6

The electronically reconfigurable transmitarray (eRT)

6.1 Introduction

This chapter presents the implementation and characterisation of a reconfigurable transmitarray with electronic beamsteering capabilities. The electronically reconfigurable transmitarray (eRT) was developed subsequently to the preliminary research performed in the passive transmitarray of stacked FSS layers, reported in the previous chapter. The functional block diagram of the implemented device is depicted in Fig. 6.1.

In detail, a proof-of-concept of an active FSS-inspired transmitarray with 2D dimensional electronic beamsteering is being described. The new model of the transmitarray was developed by employing SMD varactors diodes in the initial unit-cell model and by adding a biasing network able to feed and control all the transmitarray elements individually.

Electromagnetic simulations performed in CST MWS are presented to characterise the electronic transmitarray in terms of amplitude and phase response, and highlight the impact the proposed biasing strategy has on overall system performance, when

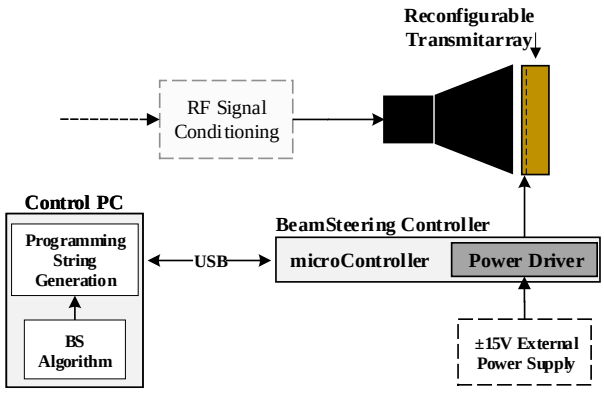

FIGURE 6.1: General block diagram for the electronically reconfigurable transmitarray.

comparing with the previous model. Additionally, the design, hardware implementation and characterisation of a beamsteering controller (BsC) which enables an intelligent and automated beamsteering is also reported in this chapter.

Finally, the experimental results obtained on a fully functional prototype of the device are presented validating the reconfigurable transmitarray model and proving its usefulness against typical beamsteering applications.

6.2 Design and simulation of the eRT

6.2.1 Active transmitarray element

The active transmitarray being described herein is an enhanced version of the passive model previously presented in Chapter 5. Namely, each element that composes the reconfigurable transmitarray was made electronically and independently controlled, so that an automated progressive phase pattern could be generated throughout the array. Depending on the phase applied to each element and consequently on the phase difference between adjacent elements (progressive phase), the original beam of a source antenna could be electronically steered to an output angle with 2D components, *i.e.* azimuth and elevation.

Accordingly, a few modifications were performed to the original stacked architecture of FSS layers in order to make it electronically reconfigurable. Namely, the discrete SMD capacitors were replaced by SMD varactor diodes, a voltage controlled capacitance. An additional 6^{th} layer responsible for providing the voltage (V_r) to control each varactor diode was also added to the stack. Through-hole through-layer vias were utilised to connect in parallel, all the 5 FSS layers to the feeding network present on the 6^{th} layer. The alterations performed in the transmitarray element are depicted in Fig. 6.2a, while substrate characteristics and dimensions of each layer are detailed in Table 6.1.

Therefore, a single element of the novel reconfigurable transmitarray is composed by 5 stacked layers of the square-slot FSS unit-cell separated at 5 mm by an air gap, corresponding to the optimum case obtained from the extensive study carried out on the passive transmitarray. The feeding layer was added to the bottom of the stack also separated at a distance of 5 mm. Two transversal copper vias were used per element, one at the centre of the middle patch and the other connected to the outer ring, thus allowing the varactor diodes (C_{up} and C_{down}) to have the same V_r at their terminals, in a reverse voltage assembly.

In the feeding layer, FR4 substrate (higher permittivity and higher loss than NX9250 - Table 6.1) was used since it was readily available for PCB production at USW facilities.

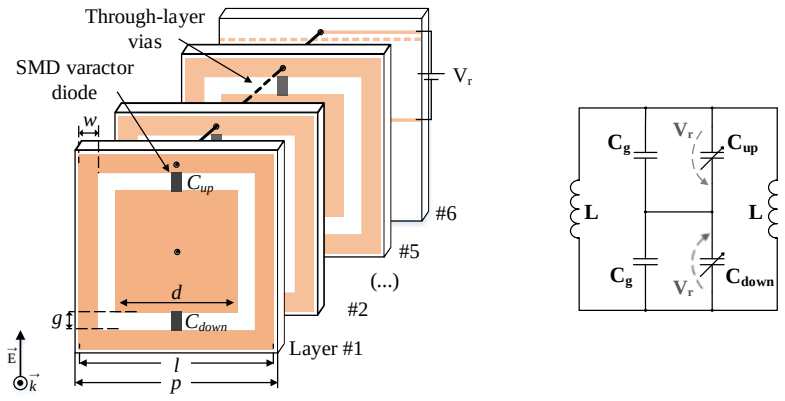

(a) (b)

FIGURE 6.2: (a) Transmitarray active element composed by 5 stacked layers of square slot FSS and by a feeding network and (b) single layer unit-cell equivalent circuit.

TABLE 6.1
RECONFIGURABLE TRANSMITARRAY ELEMENT LAYER DECOMPOSITION.

Layer		Substrate				Dimensions (mm)				
Pos. #	Type	Material	ϵ_r	$tan\delta$	t (mm)	p	l	d	g	w
[1-5]	FSS	NX9250	2.5	0.0017	1.5	33	32.8	24	1.5	3
[6]	Feeding	FR4	4.3	0.025	1.5	tracks width & spacing = 0.2				

This avoided long leading times associated to external PCB production while maintaining it low-cost, at the expense of slightly increasing the insertion losses. However, the biasing network was carefully designed to distribute the control voltage to the elements and, optimized to reduce major impact in RF performance.

To this end, routing tracks 0.2 mm wide spaced by 0.2 mm were disposed perpendicular to the incident E-field with vias coincident with the direction of the propagation, as illustrated in Fig. 6.3a . According to simulation results of Fig. 6.3c, obtained using electric/ magnetic boundaries and waveguide port excitation in CST MWS, the proposed feeding architecture yielded less impact on S_{21} than *e.g.* vertical tracks parallel to the incident E-field (Fig. 6.3b). While a horizontal distribution of routing tracks have almost no impact in S_{21}, rather than insertion losses in average around 0.4 dB due to the FR4 substrate, vertical distributed lines cause a non-desirable resonance effect that introduces higher losses affecting the operating bandwidth.

With the introduction of varactor diodes, the typical band-pass response of the square-slot FSS design (f_r), is now proportional to the control voltage V_r. The filtering

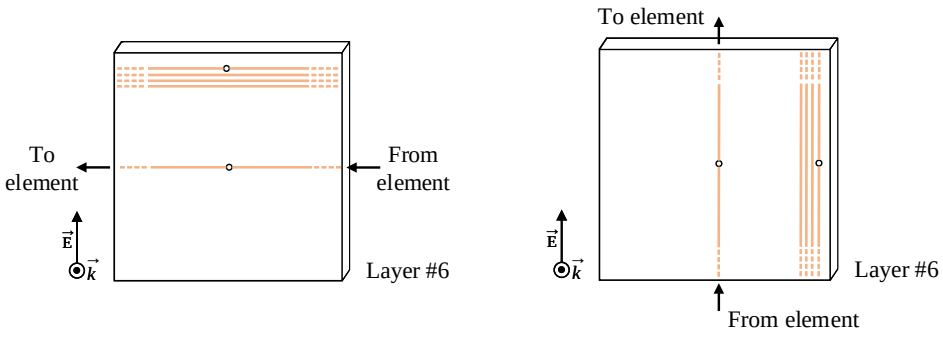

(a) (b)

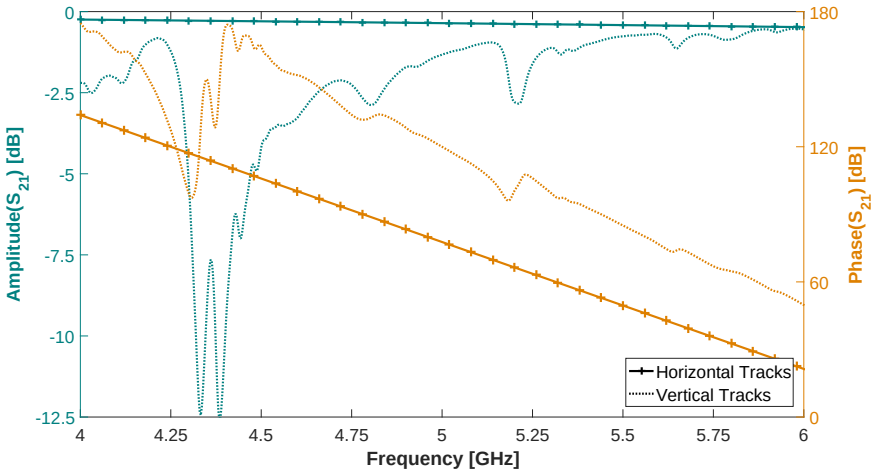

(c)

FIGURE 6.3: Routing tracks distribution for the biasing network positioned: (a) perpendicular and (b) parallel to the incident electric field and (c) respective S_{21} simulated results.

response obtained from the analysis of the unit-cell equivalent LC circuit of Fig. 6.2b is, for a single unit-cell of the active element, given by (6.1),

$$f_r(V_r) = \frac{1}{\pi.\sqrt{L.(C_g + C_{var}(V_r))}}, \tag{6.1}$$

where, L, C_g are given by the square slot design, as reported in Section 5.2.2, and $C_{var}(V_r) = C_{up} = C_{down}$ represents the capacitance value given by the varactor diode as a function of the applied reverse voltage (V_r). Following the theoretical principle, an incident EM wave that illuminates the transmitarray is re-transmitted with low attenuation but also with a controlled phase shifting ($\Delta\alpha$) proportional to V_r.

In the optimum case of the passive transmitarray, a phase shifting of $\Delta\alpha = 365°$ was obtained when 5 stacked layers separated by 5mm where considered, fulfilling the requirements to perform beamsteering. However, such phase shifting is slightly attenuated as soon as the proposed feeding network (6^{th} layer and through-layer vias) was introduced to compose active transmitarray element, as illustrated in Fig. 6.4a.

According to the simulation results (Fig. 6.4a), the relative phase shifting decreases around 45° when comparing both the passive (5 layers) and the active transmitarray element models (5 layers + feeding layer), for the useful capacitance range of 2.8 to 0.8 pF. To compensate such impact, the lower capacitance limit in the sweeping range ought to be reduced to $C_{var} = 0.78$ pF, at the expense of slightly reducing the bandwidth of a single active element. In a practical scenario, such compensation is trivial to perform by just adjusting V_r accordingly, since varactor diodes were being used.

Therefore, the proposed transmitarray element (Fig. 6.2a) exhibits a frequency response as illustrated in Fig. 6.4b, with a maximum bandwidth of $\Delta f = 100$ MHz centred at 5.36 GHz and with an enhanced phase shifting $\Delta\alpha = 360°$ when the capacitance of the varactor diode varies from 2.8 to 0.78 pF. However, although the feeding network has been designed to reduce major impact in the transmitarray element characteristics, a peak around 6.5 GHz with -40 dB is noticed when comparing the S_{21} of the novel reconfigurable element (Fig.6.4b) and the S_{21} of the passive transmitarray, depicted in Fig. 5.8b of Section 5.2.3. This impact is thought to be associated to the mutual coupling between layers (feeding layer and nearest FSS) being however neglected since it was out of the frequency of interest.

6.2.2 Composing the reconfigurable transmitarray

The reconfigurable transmitarray was composed in an array configuration of 5×5 equally separated active elements, as illustrated in Fig. 6.5a. Although the active transmitarray element (comprised of 5 FSS stacked layers and 1 layer for feeding), is fully characterised

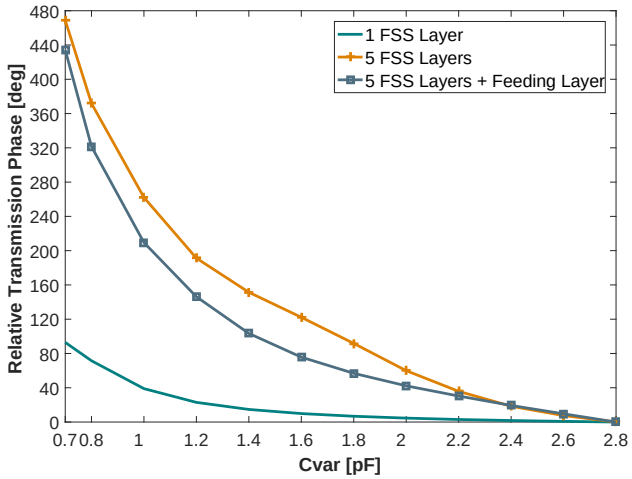

(a)

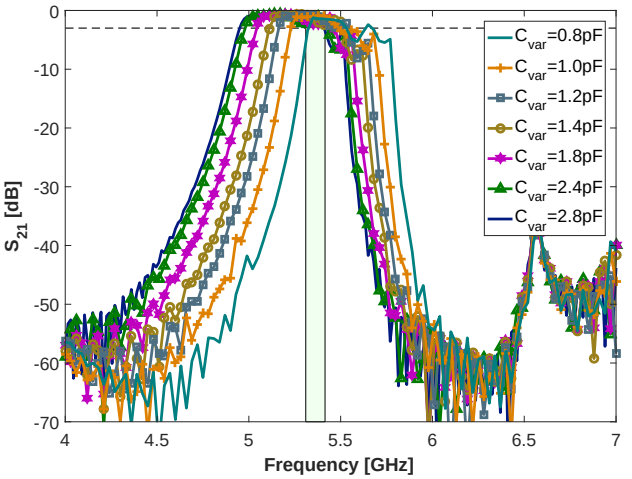

(b)

FIGURE 6.4: (a) Relative transmission phase at 5.35 GHz for 1 layer, 5 layers and, 5 layers plus the feeding network, respectively, and (b) S_{21} transmitarray element response including the feeding network (6^{th} layer and vias).

in the previous section, a few aspects in its design characteristics should be highlighted when assembling the array together. Those were intentionally implemented to provide an automated beam steerability to the transmitarray.

In particular, due to the design of the FSS unit-cells (length l smaller than periodicity p) adjacent array elements were maintained separated at a distance $s = 0.4$ mm from each other (between 1^{st} and 5^{th} layer), electrically isolating neighbouring cells, as depicted in Fig. 6.5b. Such feature, in addiction to the presented feeding strategy, allowed to address every array element of the transmitarray with the necessary control voltage V_r and consequently, with the necessary phase delay to perform 2D-beamsteering. In the feeding layer (6^{th} layer), the routing tracks are extended up to the edge of the PCB board and merged into a PCB header connector making all the pins available for output connection, as it can be seen in Fig. 6.5c. This output was responsible for the connectivity between the transmitarray and the BsC, further described in Section 6.3.2.

6.3 Prototyping the reconfigurable transmitarray

6.3.1 Transmitarray implementation

A prototype of the transmitarray presented in Fig. 6.5a was built for evaluation. It comprises the 6 stacked layers whose material and characteristics are detailed in Table 6.1. Each FSS layer presented an overall dimension of 180 mm × 180 mm × 1.5 mm whereas the feeding layer (Fig. 6.5c) was of a slightly large dimension of 225 mm × 180 mm × 1.5 mm to facilitate all the necessary pins for feeding. All layers had their sides extended by 7.5 mm and four holes placed at the corners to be able to attach layers to each other and to the *Perspex* structure, presented in Section 3.4.4.

When assembled together, 5 mm PTFE spacers were used to assure the right separation distance between layers causing the transmitarray to have a total thickness of 34 mm. Moreover, through-layer vias were implemented using copper wire of 0.5 mm of diameter, connecting all the FSS layers to the feeding plane, as illustrated in Fig. 6.6.

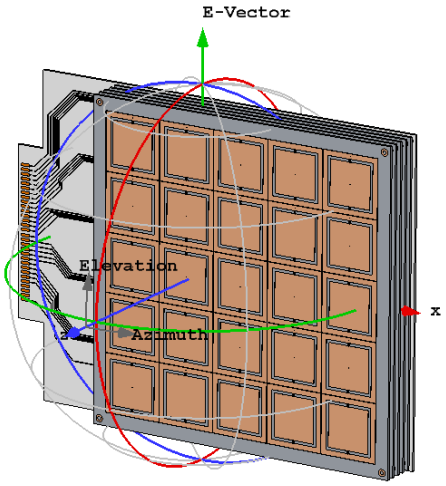

(a)

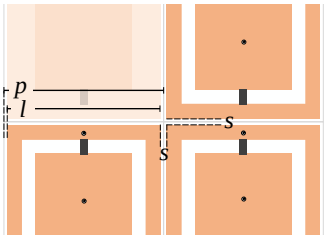

(b)

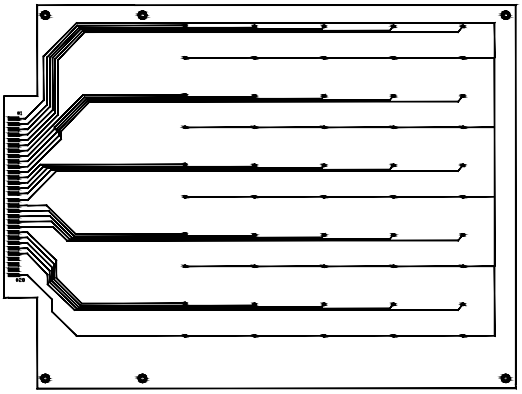

(c)

FIGURE 6.5: (a) Model of the eRT in CST composed by 5×5 active elements, (b) unit-cells disposed side-by-side physically separated by "s" and (c) illustration of the feeding network present on the 6^{th} layer.

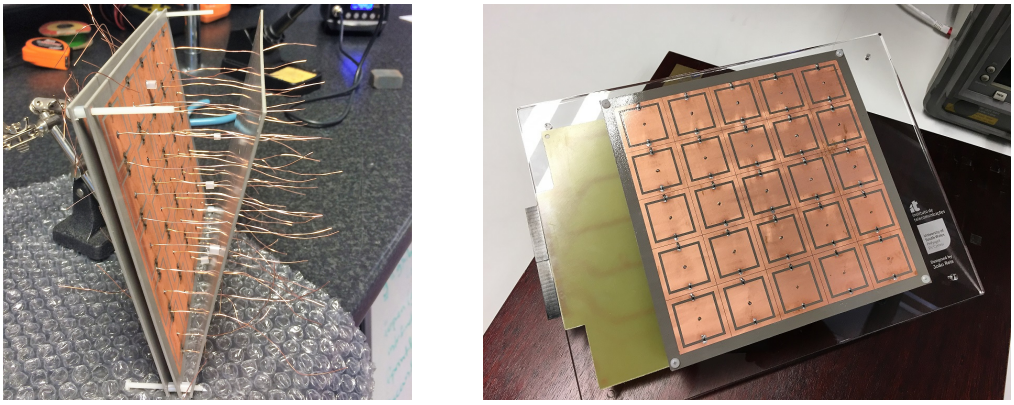

(a) (b)

FIGURE 6.6: (a) Assembly of the reconfigurable transmitarray and (b) transmitarray coupled to the *Perspex* mount.

Each FSS layer was populated with SMV1232-079LF hyperabrupt junction varactor diodes from SKYWORKS [138]. This varactor diode was particularly of interest for this application since it covered all the necessary capacitance range required for the transmitarray element ($0.78 < C_{var} < 2.8$ pF), while it presented a relatively low intrinsic series inductance $L_s = 0.7$ nH and internal resistance $R_s = 1.5\ \Omega$ [138], usually desirable for radio frequency applications. The capacitance versus reverse voltage ($C_{var}(V_r)$) values for the selected varactor are detailed in Table 6.2, following manufacture specifications [138].

TABLE 6.2
CAPACITANCE VS. REVERSE VOLTAGE FOR SMV1232-079LF VARACTOR DIODE.

C_{var} (pF)	V_r (V)	C_{var} (pF)	V_r (V)	C_{var} (pF)	V_r (V)
4.15	0	1.97	2.0	1.2	4.11
3.22	0.5	1.80	2.34	1.05	5
2.80	0.88	1.51	3.0	0.81	8
2.67	1.0	1.40	3.34	0.73	12.5
2.4	1.34	1.22	4.0	0.72	15

Due to the architecture of the proposed feeding strategy, varactor diodes are therefore electronically disposed according to the schematic of Fig. 6.7. Since a 5×5 array is considered, 25 independent V_r power supplies were necessary to control electronically the transmitarray. Subsequently, an external beamsteering controller, being described in the following section, was developed to provide the V_r and consequently set C_{var}

to each (m, n) element of the transmitarray (following the same element distribution previously defined in Section 5.3).

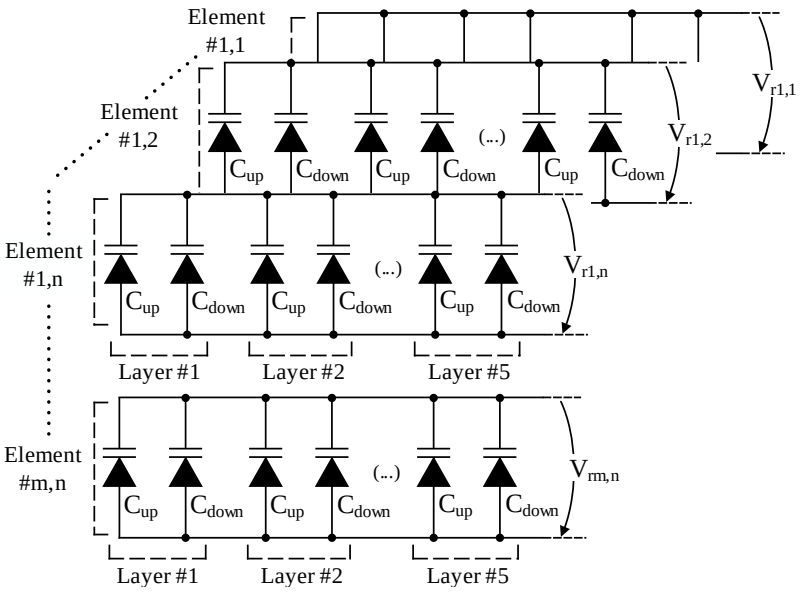

FIGURE 6.7: Schematic of transmitarray elements electronic feeding.

6.3.2 The beamsteering controller

A beamsteering controller was designed and fabricated completing all the necessary hardware components to electronically control the transmitarray. Its general block diagram is depicted in Fig. 6.8. The beamsteering controller is in charge of providing the control voltage V_r to each of the 25 elements of the reconfigurable transmitarray and consequently apply a specific progressive phase pattern through the array, according to an output steering angle inserted by the user through a MATLAB GUI (described in Section 6.3.3).

The hardware of the beamsteering controller is divided in two main parts: the Power Driver (PD) and the microController (μC). While the PD is responsible for driving the $V_{r(m,n)}$ control voltages to the transmitarray, the μC implemented with an Arduino Micro [139], was responsible for bridging the information sent from the GUI running in an control computer and the power driver.

Accordingly, after the requested output angle with (Az, El) components has been inserted in the GUI, voltage values corresponding to each (m, n) are sent to the μC via RS232 link and using a proprietary communication protocol (also described in

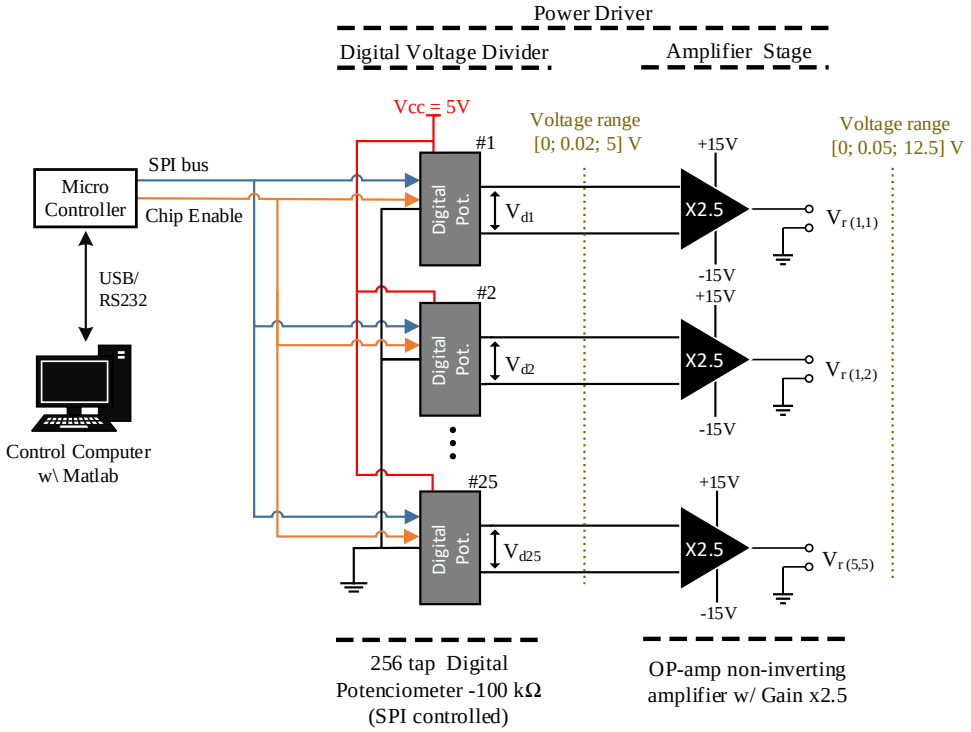

FIGURE 6.8: Beamsteering controller block diagram.

Section 6.3.3). Such information is loaded in 7 AD5204 [140] chips via Serial Peripheral Interface bus (SPI) containing a total of 28 digital potentiometers of 100 kΩ (4 per chip) with 256 taps of resolution (8-bits) each.

At this point, a digital voltage divider is implemented internally to each AD5204, according to (6.2) [140],

$$V_d(Dx) = \frac{Dx}{256} \times V_{AB} + V_B \Leftrightarrow V_d(Dx) = \frac{Dx}{256} \times 5V, \tag{6.2}$$

where V_d is the output voltage per Dx tap, $V_{AB} = 5$ V and $V_B = 0$ V. Consequently, all the outputs V_{d1} up to V_{d28} are digitally controlled from 0 up to 5 V with 0.02 V of resolution.

In a second stage, those outputs are amplified using a non-inverting Operational Amplifier (OpAmp). In particular, 7 quadruple integrated circuits LM348-N [141] fed by an external power supply (Vcc) providing ±15 V, are used along with a set of 270 $k\Omega$ and 180 $k\Omega$ resistors per output, as illustrated in Fig. 6.9. These configuration yield to a closed loop voltage gain of 2.5, according to (6.3),

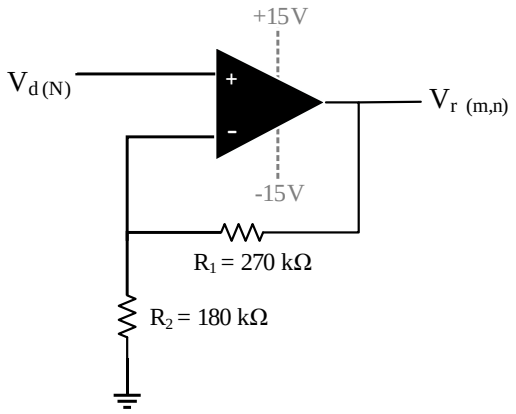

FIGURE 6.9: Non-inverting operational amplifier configuration.

$$V_1 = \frac{R_2}{R_2 + R_1} \times V_{out} \Leftrightarrow A_v = 1 + \frac{R_1}{R_2} \Leftrightarrow A_v = 1 + \frac{270\ k\Omega}{180\ k\Omega} = 2.5 \tag{6.3}$$

extending the sweep range of each output from 0 to 12.5 V with 0.05 V of resolution and, consequently, limiting the varactor tuning range from 4.15 to 0.73 pF, according to Table 6.2.

Although the BsC was developed with 28 independent voltage outputs (taking advantage of the quadruple Integrated Circuit (IC)), only 25 are being used ($V_{r(1,1)}$ to $V_{r(5,5)}$) corresponding to the number of elements of the reconfigurable transmitarray, being 3 outputs left as reserve.

The controller was developed in double-sided PCB (printed circuit board) technology and surface mount (SMD) components were used in order to reduce the overall size of the controller (95 mm × 95 mm), as illustrated in Fig. 6.10. The connectivity between the BsC and the transmitarray is performed using a 30 pin, 200 mm flex cable with an adaptor at on end to connect to the feeding layer of the transmitarray. Full schematics and PCB Gerber files can be found attached in Appendix C.

After hardware production, a test bench was performed to evaluate the operability of the developed controller. A debug program was implemented forcing all the 28 outputs of the BsC to have the same voltage values, by loading directly in the μC their associated logic levels in hexadecimal (given by (6.2)). Simultaneously, in the hardware, the outputs were measured using a multimeter at the end of each stage, *i.e.* in V_d and V_r lines.

The results of the test bench are detailed in Table 6.3, where it can be seen the beamsteering controller is performing well. The measured gain, *i.e.* V_r/V_d is approximately 2.5, as expected, and linear in the entire sweep range. However, although the measured upper limit of the V_d is only 12.33 V instead of the expected 12.5 V (due

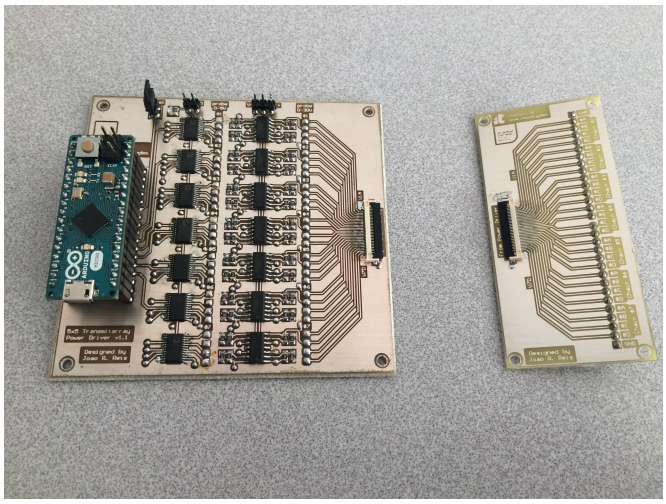

(a)

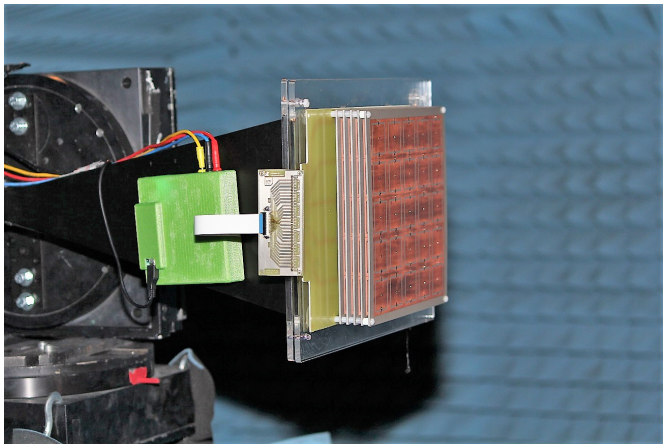

(b)

FIGURE 6.10: (a) Prototype of the beamsteering controller and (b) beamsteering controller connected to the reconfigurable transmitarray.

TABLE 6.3
MEASURED OUTPUT VOLTAGES (AVERAGE OF THE 28 OUTPUTS)

Expected V_d (V)	Logic lvl.	Hex.	V_d (V)	V_r (V)	Gain	$^*C_{var}$ (pF)
0	0	00	0.4 mV	7 mV	†17.5	4.15
1	51	33	0.99	2.47	2.495	1.735
2	102	66	1.97	4.93	2.502	1.061
3	153	99	2.96	7.4	2.5	0.844
4	204	CC	3.94	9.86	2.502	0.763
5	255	FF	4.94	12.33	2.495	0.738

* Estimated capacitance value;
† Meaningless value.

to the 0.06V difference in the 5V rail), the necessary capacitance range defined by the theoretical model ($0.78 < C_{var} < 2.8$ pF) is still achievable with the proposed hardware fulfilling the requirements for the project.

6.3.3 GUI for beamsteering control

A graphical user interface was developed in MATLAB to control, in real time, the reconfigurable transmitarray and therefore to electronically control the beamsteering. The GUI is divided in two parts, the main script (invisible to user) that runs in background all the necessary programming code, *e.g.* BS algorithm and the communication protocol scripting, and the graphical interface that visually transmits to the user relevant information about programming and control operations.

The GUI, running in the Control PC, requests to the user coordinates (in Az and El) of the direction to which the main lobe of the antenna is intended to be steered. In background, the beamsteering algorithm described in Section 5.3 computes the respective progressive phase and capacitance values (in a 5×5 matrix) to apply in each transmitarray element for the selected steering angle.

Additionally, a voltage matrix $V_{r(m,n)}$ is generated with the estimated voltage values to apply in each of the 25 transmitarray elements. Such values are obtained by linear interpolation, between the capacitance values calculated in the previous step and the varactor diode transfer function (Table 6.2 [138]).

At this stage, all the information is visually transmitted to the user including, *e.g.* the estimated wavefront direction, relative transmission phase curve, varactor diode transfer function and all the phase, capacitance and voltage information in the format of matrices, as depicted in the snapshot of Fig. 6.11.

Moreover, to proceed with transmitarray programming, the checkbox for "Program TA" must be selected. In such case, the $V_{r(m,n)}$ values are downscaled to V_d and converted

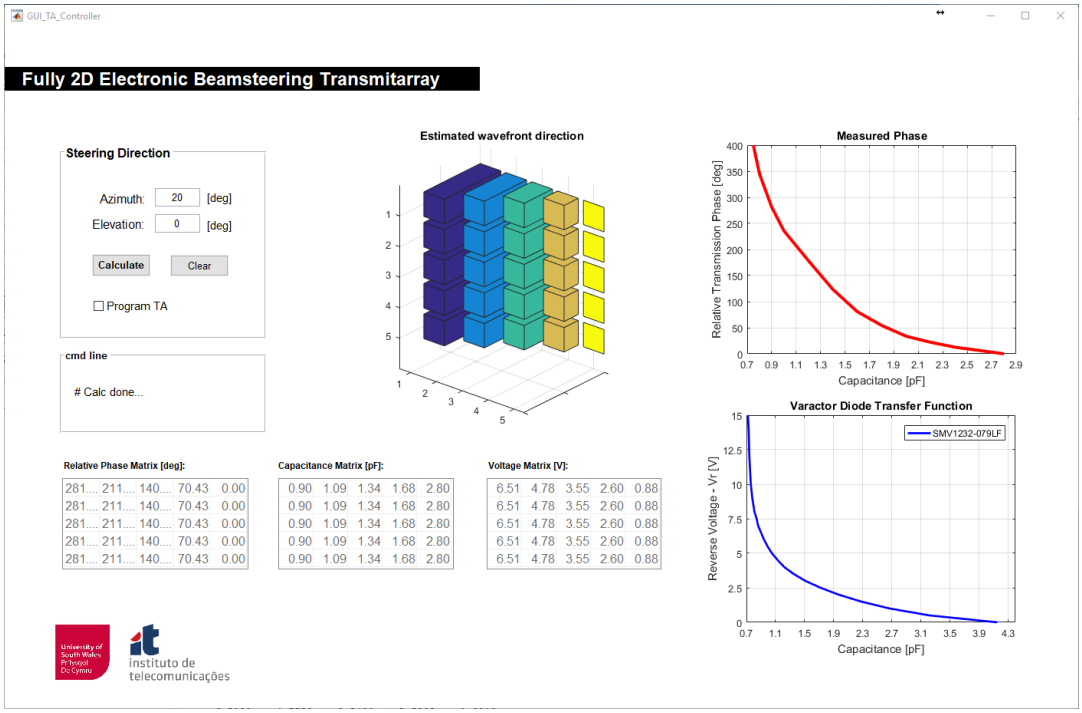

FIGURE 6.11: Snapshot of the MATLAB GUI.

to digital with 8-bits resolution (hexadecimal) respecting the process described in last section, before being sent to the controller using a proprietary communication protocol, via RS232 link (USB Port). A block diagram illustrating the programming steps implemented by the GUI is depicted in Fig. 6.12.

A communication protocol was implemented to enable the exchange of information between the Control Personal Computer (PC) (running GUI) and the Beamsteering Controller, and *vice-versa*. The protocol utilises messages in the format of text strings to communicate. To every command sent by the GUI, the BS controller replies with an acknowledgement that is displayed in GUI in *"cmd line"* (command line) field.

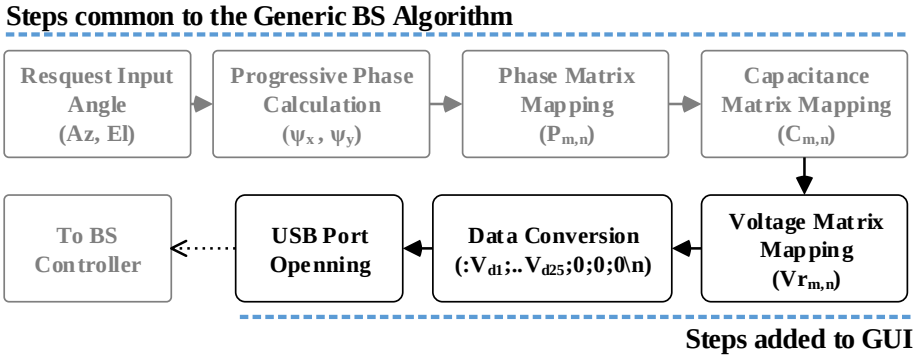

FIGURE 6.12: Block diagram of the programming steps and data flow implemented by the GUI.

The messages respect the following syntax:

<header> : <data separated by ";"> <terminator "\n">

The *header* section indicates to the BS controller which type of *data* is the string carrying. Subsequently, the *data* is introduced, separated by ";", between the different fields. Finally, the string is terminated with a "\n" to indicate the end of the message. In particular, several different *headers* have been developed to implement distinct actions:

<chipstatus> It sends the indication to turn "On" or "Off" the transmitarray power supply (power driver);

<levels> It sends the information about the voltage level of each independent transmitarray element, in hexadecimal format. The *data* string respects the syntax of "V_{d1}; V_{d2}; ... ;V_{d25};0;0;0",corresponding to the voltage of the 25 elements plus 3 spares at 0V;

<autoswitch> It enables automated and consecutive beamsteering between two distinct output angles (bouncing) pre-loaded in the μC. *Data* respects the format of "xxxxx;ttttttt", where "x" correspond to the number of iterations the beam is bouncing (up to 99999), and "t" the time the beam is hold on at each direction, in microseconds (up to 9999999). (refer to Section 7.2 for detailed information about this feature).

In Table 6.4 are detailed the correct syntax for all possible messages, including the acknowledgements sent by the BS controller in case of a successfully delivery message or in case of incorrect syntax.

Table 6.4
Message formatting and acknowledgement

Header	Data	Acknowledgement
<levels>	:V_{d1};V_{d2}; ... ;V_{25};0;0;0\n	"Levels loaded successfully!!"
<levels>	for any $V_d < 0$ or $V_d > 255$	"Error! Check input data format"
<chipstatus>	:ON\n (or :OFF\n)	"ICs are ON! (or OFF!)"
<autoswitch>	:xxxxx;ttttttt\n	"Auto Beam Switching Mode!"
if any above	empty or missing field	"Error! Check commands syntax!"

6.4 Results and discussion

After all hardware implementation, the eRT was evaluated in terms of electromagnetic characteristics including its beamsteering capability. Experimental results were obtained and compared against full wave simulations. While experiments were performed using the setup and techniques described in Chapter 3, full wave simulations were performed in CST MWS considering open boundaries and an ideal model of an horn antenna as excitation source.

6.4.1 S_{11} and S_{21} parameters characterisation

Firstly, to understand the initial behaviour of the transmitarray, the S_{11} parameters are presented and compared in Fig. 6.13, for both simulations and measurements with and without the transmitarray attached to the reference horn antenna (characterised in Section 3.8).

In particular, all the transmitarray elements were considered with the same voltage $V_r = 4.11$ V forcing an elementary case of equally distributed capacitance ($C_{var} = 1.2$ pF) along the elements, *i.e.* no beamsteering. The expected filtering effect in the S_{11} caused by the introduction of the transmitarray in front the reference antenna is clearly noticeable in both simulation and measured results. Nevertheless, a large frequency offset around 160 MHz between initial simulation (depicted in purple squared curve) and measurement (in blue dash curve) is experienced. This offset, calculated by the frequency difference between both S_{11} parameters at -10 dB, was proved to be related to the use of an ideal model of a varactor diode utilised in simulations.

In a second iteration, where the intrinsic parasitic elements of the varactor diode supplied by the manufacturer were considered, *i.e.* series inductance ($L_s = 0.7$ nH) and internal resistance ($R_s = 1.5\ \Omega$) [138], the simulated S_{11} parameter (green dotted curve) nearly matches the experimental one. This clearly indicates that a varactor diode had a higher impact than a simple SMD capacitor in the implementation of such structures, and subsequently, its intrinsic parameters must be considered from the very beginning of unit-cell design to compensate for such mismatch.

Moreover, while the series inductance of the varactor tends to introduce an offset in frequency, internal resistance (R_s) was responsible for increasing the insertion losses, as can be seen when comparing the simulated and measured S_{21} parameters of Fig.6.4b and Fig. 6.14a, respectively. As evident in Fig. 6.14a insertion losses of around 4.33 dB (on average) were noticed within all the useful capacitance/voltage range.

To this end, and for the sake of the evaluation, beamsteering capability is therefore characterised at 5.2 GHz, which represent the middle point of a 70 MHz bandwidth

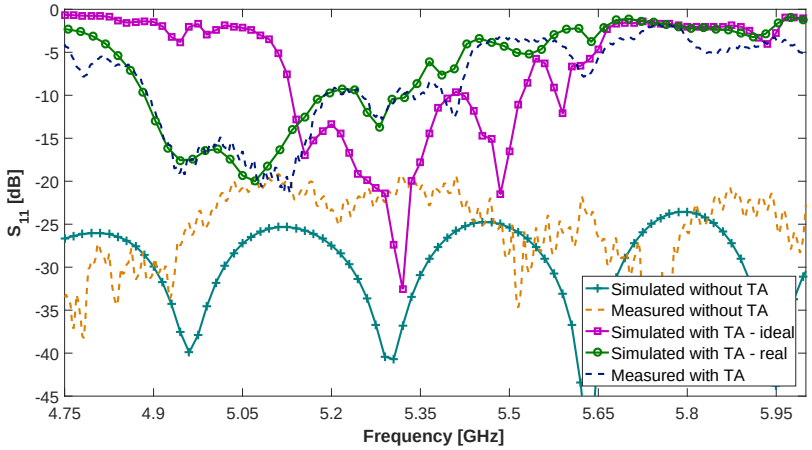

FIGURE 6.13: Simulated and measured S_{11} parameters, for the reference antenna with and without the transmitarray, with $V_r = 4.11$ V ($C_{var} = 1.2$ pF) equally distributed along the array.

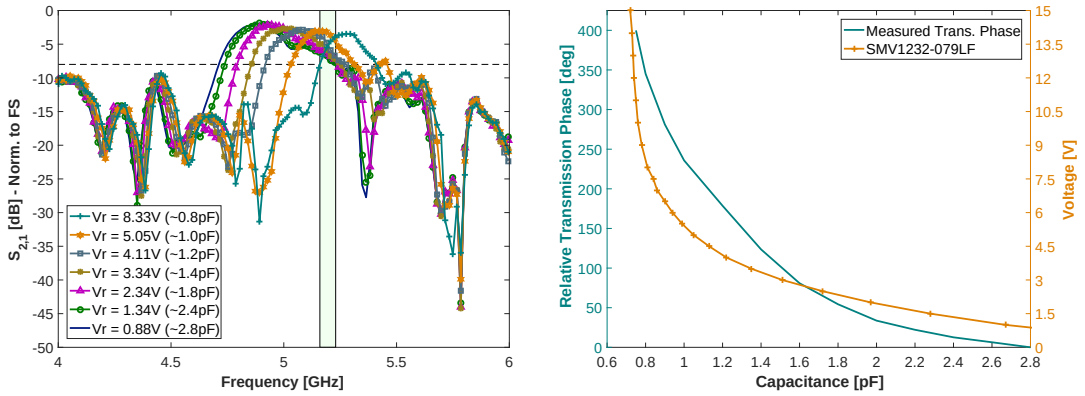

(a) (b)

FIGURE 6.14: Measured (a) S_{21} transmitarray element response and (b) Relative transmission phase at 5.2 GHz plotted against varactor transfer function.

taken at -8 dB (-3 dB below the average insertion loss) of experimental S_{21}. At this frequency point, the measured relative transmission phase of the transmitarray is depicted in Fig. 6.14b together with the varactor transfer curve whose values are in Table 6.2 [138].

6.4.2 Beamsteering characterisation

In order to characterise the capability of performing beamsteering with the proposed reconfigurable transmitarray, a set of steering angles represented by its azimuth and elevation components are considered. Simulation and experiment results for all the angles are detailed and summarised in Table 6.5. All the radiation pattern are referenced to the standard horn antenna (characterised in Section 3.8).

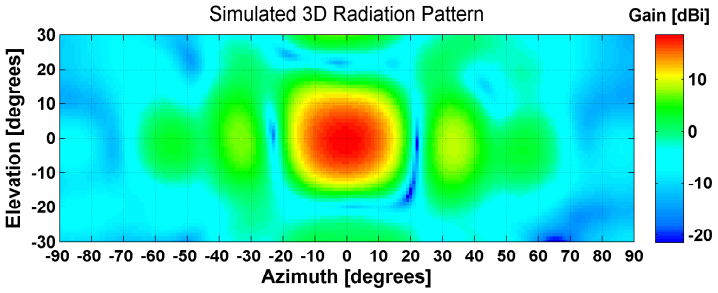

(a)

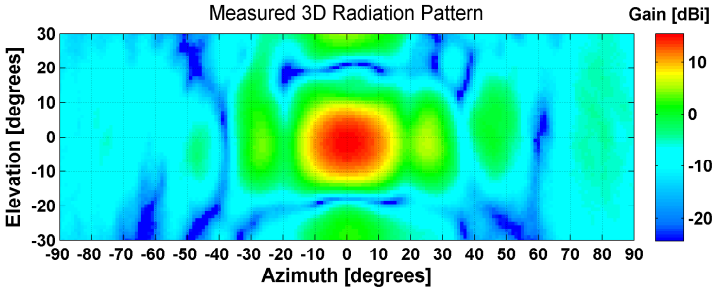

(b)

FIGURE 6.15: (a) Simulated and (b) measured 3D radiation patterns at 5.2 GHz for the transmitarray set with no beamsteering $(0°, 0°)$.

The beamsteering capability is assessed by the analysis of the main lobe steering direction (considering the higher absolute gain direction in dBi), HPBW and the SLL, *i.e.* the amplitude difference between the main lobe and the highest side lobe of the radiation pattern.

When the transmitarray is attached to the horn and the elementary case described above is applied, *i.e.* all elements with the same voltage $V_r = 4.11$ V ($C_{var} = 1.2$ pF), the main lobe of the original radiation pattern remains at broadside, *i.e.* no steering is experienced, as expected. This effect is depicted in the Fig. 6.15a and Fig. 6.15b for both simulation and experiments, respectively. Consequently, the antenna has now a maximum gain of 18.6 dBi with a HPBW of 20° in Az and 16° in El, and a SLL around -9 dB, while for measurements, it presents an absolute gain of 15.6 dBi with a HPBW of 16° in Az and 14° in El with a SLL of -9.7 dB. A decrease in gain at the broadside of around 1.6 dB in simulations and 4.3 dB in measurements is evident due to losses inserted by the transmitarray and due to the enhancement of the power of side lobes in relation to the original main lobe. This observation is in good agreement with experimental results obtained from the analysis of the S_{21} and presented in Fig. 6.14a. It is worthwhile to mention that this new transmitarray model compares with the passive one (which uses SMD capacitors – Chapter 5) by presenting approximately 1.5 dB of excess loss at the considered frequency.

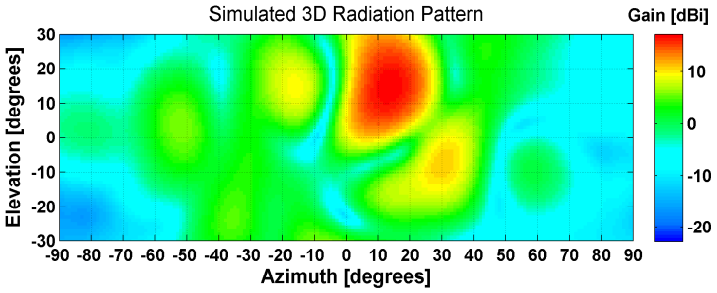

(a)

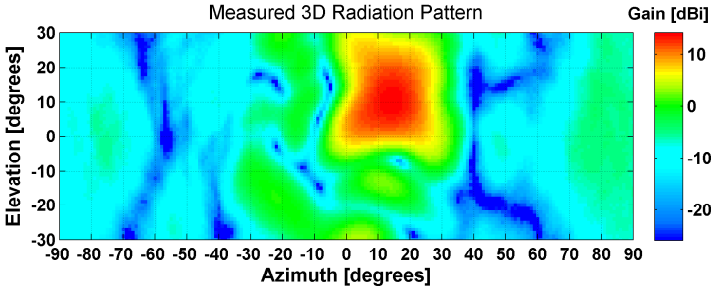

(b)

FIGURE 6.16: (a) Simulated and (b) measured 3D radiation patterns at 5.2 GHz for a requested steered angle set at $(15°, 15°)$.

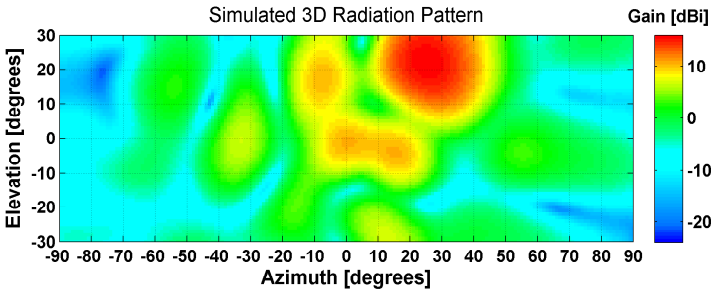

(a)

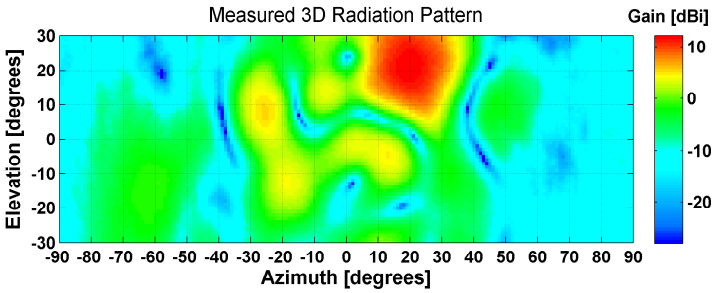

(b)

FIGURE 6.17: (a) Simulated and (b) measured 3D radiation patterns at 5.2 GHz for a requested steered angle set at $(25°, 25°)$.

Table 6.5
Summary table for simulated and measured 3D radiation patterns at 5.2 GHz.

Simulated Results								Experimental Results					
Expected		Main lobe			HPBW		SLL	Main lobe			HPBW		SLL
Az(°)	El(°)	Az(°)	El(°)	Gain (dBi)	Az(°)	El(°)	(dB)	Az(°)	El (°)	Gain (dBi)	Az(°)	El(°)	(dB)
*-	*-	0	0	20.2	17	17	-11.6	0	0	19.9	16	16	-11.3
0	0	0	0	18.6	20	16	-9	0	-2	15.6	16	14	-9.7
15	15	15	15	17.3	17	20	-7.7	15	12	14.1	18	18	-11.6
25	25	25	23	16.1	21	21	-7	21	20	12.1	19	19	-6.7

*For the reference horn antenna without the transmitarray attached.

TABLE 6.6
EXPECTED *vs.* EXPERIMENTAL STEERING ANGLES.

	Azimuth (°)		Elevation (°)	
Expected	Measured	Deviation	Measured	Deviation
0	0*	0	-2†	-2
10	10*	0	9†	1
15	12	3	12	3
20	17*	3	15†	5
25	20	5	20	5
30	22*	8	26†	4
35	25	10	–	–
40	28*	12	–	–
45	29	16	–	–

* Plotted in Fig. 6.18a;
† Plotted in Fig. 6.18b.

Furthermore, by forcing the transmitarray to have a steered output angle toward $Az = 15°$ and $El = 15°$ and further toward $Az = 25°$ and $El = 25°$, both simulated and measured results show that 2D beamsteering is achievable, thus validating the proposed transmitarray model. In fact, the simulated and measured patterns are similar in shape and the main lobe Gain and SLL are still proportional when comparing to the reference antenna, as can be seen in Fig. 6.16 and 6.17.

Nevertheless, a maximum averaged error around 5°, for both Az and El planes, is presented for the case in which $Az = 25°$ and $El = 25°$. The discrepancy is found to be consistent with results obtained for larger angular steering ranges, as detailed in Table 6.6, concluding that for steering angles larger than 15°, lookup tables must be implemented in the algorithm to compensate for such angle mismatches. In fact, this should not be seen as a limitation in the beamsteering angular range. According to the results in Fig. 6.18 which show the radiation patterns for the highlighted cases of Table 6.6 and their mirror, the effective steering might be extended up ±28° and ±26°, in the azimuth and elevation planes, respectively. This while maintaining a relatively good SLL (< -10 dB) within all steering range. For angles higher than the specified range, amplitude degradation and/ or higher side lobes start to appear, clearly indicating the steering limit of the transmitarray in each direction.

6.4.3 Angular response and beam direction sensitivity

Moreover, to evaluate the angular response of the transmitarray, the beamsteering envelope has been obtained by keeping both transmit and receive antennas fixed, aligned to each other, and electronic steering applied directly to the structure. Results depicted in Fig. 6.19 show that a tunable angular region is clearly denotable for the specified

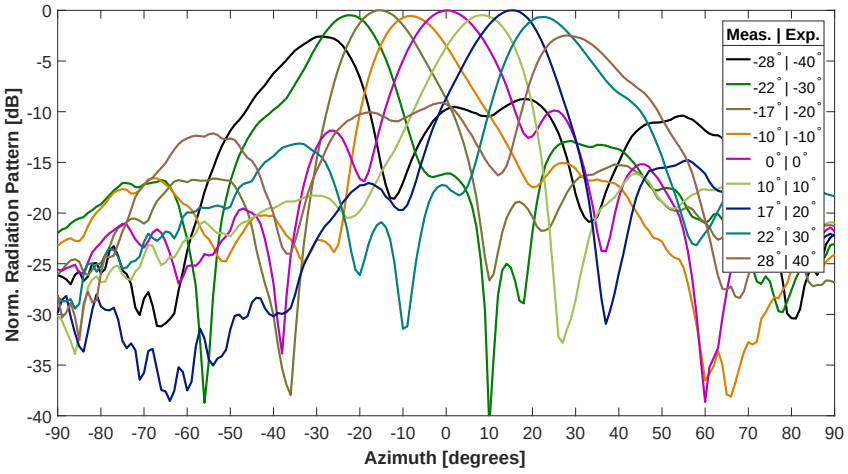

(a)

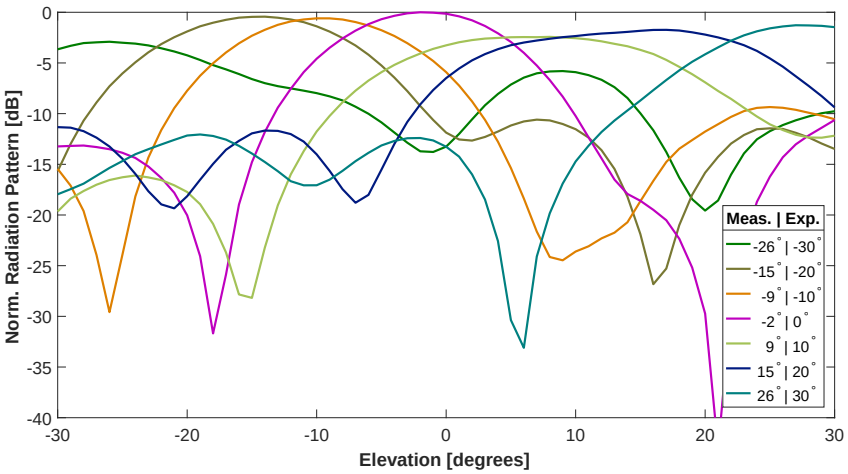

(b)

FIGURE 6.18: Measured radiation patterns for different steering angles in (a) azimuth and (b) elevation planes, normalised to the reference measurement.

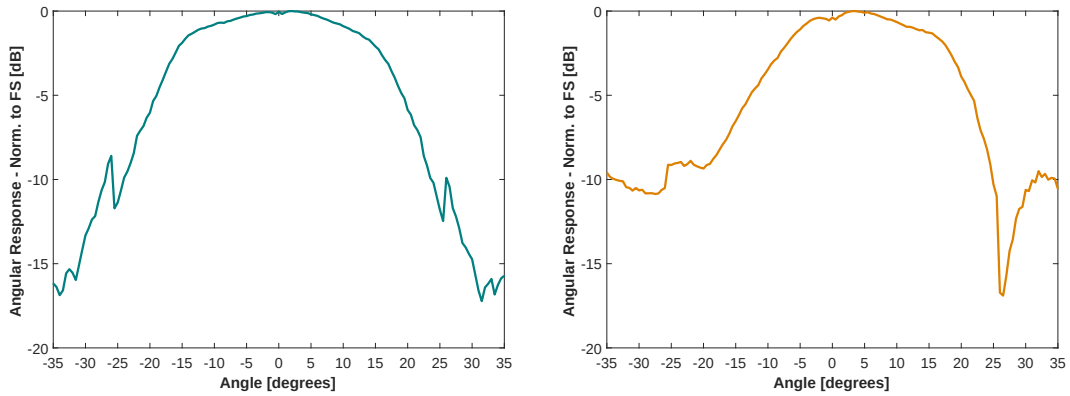

(a) (b)

FIGURE 6.19: Measured beamsteering angular response for the electronic transmitarray in (a) azimuth and (b) elevation planes.

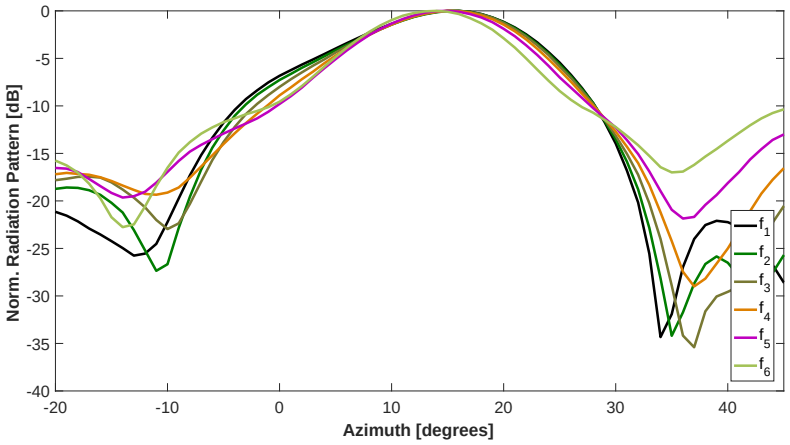

FIGURE 6.20: Angular beam sensitivity against frequency sweep for an angle steered to $Az = 20°$ (effective $Az = 17°$).

limits of both azimuth and elevation angles, and a steering resolution of 1° is found to be possible with the proposed transmitarray.

A particular effect can be noticed in Elevation plane, where a non-symmetry in the Y-axis and an offset of around $-2°$ is observed in the main centred beam, matching the equivalent 2D case of Fig. 6.18b and the 3D case ($Az = 0°$ and $El = 0°$) detailed in Table 6.5. This offset is thought to be due the routing tracks of the feeding network are not equally distributed in space in a unit-cell, *i.e.* feeding lines pass always through the upper edge of each unit-cell and none at the bottom edge as illustrated in Fig 6.5c.

An additional study was also performed in order to evaluate the beam direction sensitivity by changing the operational frequency of the signal source. This phenomenon, known as a beam squinting (please refer to Section 2.2.4), severely affects phased-array systems due to the non-linear phase-frequency characteristic. Consequently, the output angle direction is expected to deviate as a function of the operational frequency. This

TABLE 6.7
EXPERIMENTAL BEAM DIRECTION SENSITIVITY.

	Frequency (GHz)	Main-lobe direction (°)	Angular deviation (°)	HPBW (°)
f_1	5.1650	17	0	17
f_2	5.1775	17	0	16
f_3	5.1900	17	0	16
f_{ref}	5.2000	17	–	16
f_4	5.2025	16	-1	15
f_5	5.2150	16	-1	14
f_6	5.2275	15	-2	13

can be seen in Fig. 6.20, when the transmitarray is set, *e.g.* to $Az = 20°$ (effective $Az = 17°$ according to Table 6.6) and several the frequency points were considered, within bandwidth of the transmitarray. These results, summarised in Table 6.7, clearly demonstrate a radiation pattern squint of about 2° in azimuth plane, when the frequency is swept between 5.1650 GHz and 5.2275 GHz, presenting a relatively low angular sensitivity of 0.032 deg/MHz within the 70 MHz bandwidth of the eRT. However, this effect may be neglected specially when considering the 16° of HPBW.

6.4.4 Power handling capability

One of the points that may raise some concerns when using the eRT is its power handling capability. This is particularly relevant since varactor tuned FSS are placed right on the aperture of a horn antenna, which can have relatively high field strength levels and, the RF induced changes on the bias of the varactors can seriously deteriorate the response of the device. In fact, since varactor diodes are voltage dependent capacitors, the E-field generated by the antenna may alter the voltage value at their terminals, and consequently a drift in the associated capacitance can occur, altering the beamsteering characteristics of the eRT.

For example, if an Effective Isotropic Radiated Power (EIRP)[1] of 1 W is considered, an estimated E-field of approximatelly 547 V/m is presented at the terminals of varactors diodes. This E-field, calculated at a distance $r = 1.3$ cm (which corresponds distance between the horn aperture and the first FSS layer) using (6.4) as indicated in [142], may be sufficent to steer off the transmitarray from the original resonant frequency.

$$E = \frac{\sqrt{30.EIRP_w}}{r} \quad \Leftrightarrow \quad E = \frac{\sqrt{30.P_{tx}.G_{tx}}}{r} \quad [V/m]. \tag{6.4}$$

[1]EIRP is the power input required to a lossless isotropic antenna to give the same maximum power density far from the antenna as the actual transmitter [18].

Therefore experiments were performed on the fabricated prototype in order to understand the effect that high transmitted power levels have on its performance. Experiments were performed in detriment of electromagnetic simulations (in CST MWS), since the solver in consideration does not allow to control the transmitted power of the radiating ports, limiting therefore the proposed analyse. The test was then carried out by measuring the S_{11} parameter of the transmitarray antenna under different circumstances. In particular, the S_{11} were obtained for an input power (P_{tx}) swept between -30 dBm and 12.5 dBm (limited by the VNA), respectively, under two extreme conditions: firstly, when all the varactors have no applied voltage at their terminals, *i.e.* $V_r = 0$ V corresponding to $C_{var} = 4.15$ pF, and finally when the varactors are subjected to the maximum control voltage provided by the beamsteering controller, *i.e.* $V_r = 12.33$ V corresponding to $C_{var} = 0.738$ pF, as indicated in Table 6.3.

According to the experimental results depicted in Fig. 6.21, it is possible to conclude that the considered transmitted power level does not affect the performance of the eRT under the applied testing circumstances. In fact, the S_{11} curve remains unaltered when P_{tx} is increased from -30 to 12.5 dBm, for both $V_r = 0$ V and $V_r = 12.33$ V cases. This corresponds to a maximum EIRP of 32.4 dBm (1.75 W) calculated using (6.5),

$$EIRP_{dB} = P_{tx} + G_{tx}\,[dB] \quad \Leftrightarrow \quad EIRP_w = 10^{(P_{tx}+G_{tx})/10} \quad [W] \tag{6.5}$$

when considering the measured absolute gain of the reference horn antenna $G_{tx} =$ 19.9 dBm at 5.2 GHz and, to a E-field of aproximatelly 725 V/m.

Thus, it is clear that the power of EM field emitted by the radiating element does not have any impact in varactor's control,at least within the considered EIRP range, otherwise a down-shift of the filtering response would have been noticed in the S_{11} parameter.

6.5 Interim conclusions

This chapter presented the implementation and characterisation of a electrically reconfigurable transmitarray with two-dimensional beamsteering capability. In the sequence of the study performed in the passive transmitarray, the eRT was developed by employing SMD varactors diodes in each FSS unit-cell of the 5×5 array and by adding a biasing network able to feed and control all the transmitarray elements individually.

After electromagnetic simulations characterising the new transmitarray model in terms of amplitude and phase response and evaluating the impact the proposed biasing

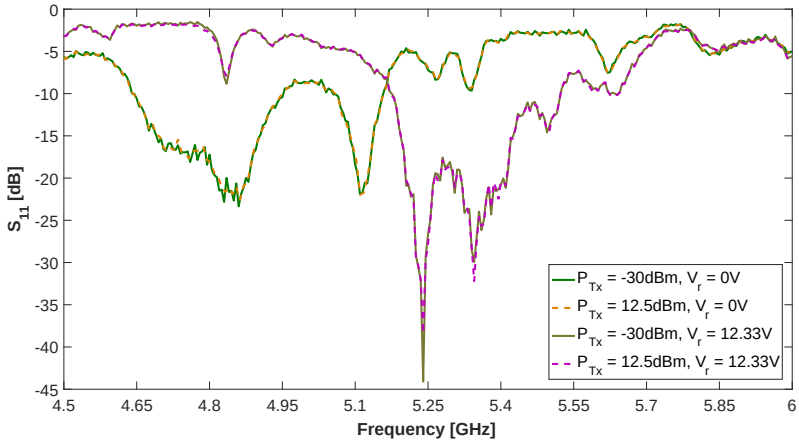

FIGURE 6.21: Measured power handling capability of the eRT.

strategy in RF performance, a prototype was developed and characterised experimentally. It comprises the FSS structure to apply in the aperture of the reference antenna but also a beamsteering controller which enables the intelligent and electronic control of the steering direction.

Moreover, to facilitate the control of transmitarray, a graphical user interface running the beamsteering algorithm was implemented in MATLAB, displaying all the necessary information to the user. After inserting the steering direction to which the main lobe of the antenna radiation pattern is intended to be steered, the GUI provides the necessary phase, capacitance and voltage values to apply in every element of the transmitarray. Such values are therefore uploaded using a proprietary communication protocol, from the control computer where GUI is running to the BS controller.

Although experimental results are found to be in good agreement with those obtained from the simulation, a down shift in frequency around 160 MHz and insertion losses of around 5 dB between the original design and the experimental prototype have been experienced. This was found to be due to the use of varactor diodes. Results have shown that a varactor diode has a significant impact on the implementation of such structures, and its intrinsic parameters, *i.e.* series inductance and internal resistance must be considered at the very beginning of unit-cell design to compensate for such impairments.

Notwithstanding, due to the developed active architecture an automated steering of the main lobe of the original radiation pattern can be performed in both elevation and azimuth planes, simultaneously. The proposed system running the algorithm without any kind of angle compensation, exhibits an error in output angles can go up to 16° when comparing theory with experiments. Nevertheless, this was compensated by applying a look-up table based on the study of Table 6.6 and in such case, practical steering angle can go up to 28° in azimuth and 26° in elevation.

Several experiments on the fabricated prototype have been performed yielding to a better characterisation of the eRT. Namely, a steering resolution of 1° has been achieved with the prototype and beam direction sensitivity against frequency of 0.032 deg/MHz was obtained. Furthermore, the power handling capability of the FSS structure was evaluated to understand if a high power transmitted radio-wave would have any impact in device performance. An a EIRP of around 1.8 W was applied to the eRT without any noticeable impact.

The work performed in this chapter was disseminated in one international journal publication, and demonstrated in real-time, in two showcases:

J. J. Reis; R.F.S. Caldeirinha, A. Hammoudeh and N. Copner, **"Electronically Reconfigurable FSS-Inspired Transmitarray for 2-D Beamsteering"**, *IEEE Transactions on Antennas and Propagation*, vol. 65, no. 9, pp. 4880-4885, Sept.2017. doi: 10.1109/TAP.2017.2723087. **Impact Factor = 2.957, Q1;**

D. Exhibitor: **"Novel Antenna Beamsteering for Wireless Applications"** – *2016 Engineering Showcase* – 20 April 2016 – University of South Wales, United Kingdom;

D. Exhibitor: **"Fully 2D Electronic Beamsteering for 5G and RADAR of the Future"** – *Techdays Aveiro 2017 Centro Exposições* – 12-14 October 2017 – Aveiro, Portugal, in a collaboration with EMScan and eNGN Technologies.

CHAPTER 7

Practical applications using the eRT

7.1 Introduction

In this chapter, the electronic model of the transmitarray developed in the last chapter of this thesis, was experimentally tested in two distinct case studies which may represent possible real-life applications. Each case study is disseminated in a specific section.

Firstly, the prototype of the eRT was evaluated under fast beamsteering angular requests. The agility of beamsteering was tested by quickly steering the beam between two distinct output angles (bouncing). The current characterisation allow to evaluate the steering-rate response of the eRT to be deployed on fast tracking applications, *e.g.* in the scope of 5G.

In the second section, the prototype was evaluated when integrated in a realistic LTE wireless communication system. The eRT was utilised as the transmitter antenna of a top-notch OFDM software defined radio, operating at 5.2 GHz, with the objective of evaluating the impact of its insertion in a high-data rate communication system.

The case studies being presented herein were dissiminated in 2 paper publications, under revision at the time of this document, corresponding to the work performed in each individual section of this chapter.

7.2 2D Agile beamsteering using the eRT

Antenna beamsteering is a desirable function in any wireless communication systems, however, the specifications for a certain applications may vary from scenario to scenario. Nevertheless, a common feature requirement of those systems is the beamsteering agility and its response to fast steering requests. For example, radio base station antennas with fast beamsteering in elevation and/ or azimuth are necessary to significantly improve the carrier to interference ratio and hence the spectral efficiency [143].

When considering the example illustrated Fig. 7.1, fast beamsteering is demanded if mobile users are needed to be covered by the antenna main beam over the time when moving, *i.e.* continuous tracking, or if multiple users must be covered by the same base station antenna at different space positions at distinct instants of time, *i.e.* using a Time Division Multiple Access (TDMA) technique. A direct example of application would be the implementation of beamsteering over a LTE TDMA system [144], since typical radio frame has a duration of 10 ms [145].

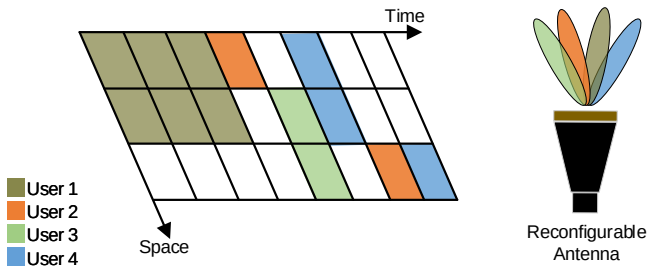

FIGURE 7.1: Example of an application scenario for fast beamsteering requests.

Novel antenna designs can be found in the literature reporting fast beamsteering [143, 146–149], from microwave [148] to millimetre wave applications [147], using phase change materials or more recently CMOS technology [149]. However, only a few of them have really reported beamsteering switching rates under experimental prototypes. Moreover, none of the work presented in Chapter 2, directly related to transmitarray design and implementations, has been tested under such demanding requests.

Therefore, it is presented in this section, the evaluation and characterisation of beamsteering agility provided by the eRT (described in Section 6) under demanding fast-steering conditions. The characterisation was performed experimentally on the physical prototype, by evaluating the maximum switching rate time that the eRT can handle when bouncing between several scanning angles pointing at distinct directions.

This experiment allows to validate the prototyped eRT to work in real communication systems where beamsteering is necessary to keep track of a mobile user, over-the-time, but also over-the-space. The timing rates associated to such operation are reported herein.

7.2.1 Experimental considerations for fast beamsteering evaluation

To characterise the eRT in terms of agility performance, the experiments carried out in this part of the research work have been performed in two distinct stages. Firstly, antenna radiation patterns have been measured, in advance, for a selection of output steered angles. Finally, the agility of the beamsteering was characterised when intermittently swithcing between two of those pre-selected directions. Both stages are detailed as follows:

Reference radiation pattern measurements

The radiation pattern were obtained using the physical setup and the measuring techniques described in Chapter 3, when the eRT was set at boresight ($Az = 0°$), and when it was set to steer towards $Az = 5°, 10°$ and $15°$. For convenience, radiation pattern for the case when the eRT is powered off was also obtained, *i.e.* $V_r = 0$ V at every transmitarray element. To simplify the analysis, only positive azimuth angles have been considered for this experiment, however, any other direction could have been chosen as soon as the steering limits of the transmitarray, characterised in Chapter 6, were respected. The measured radiation patterns are depicted in Fig. 7.2.

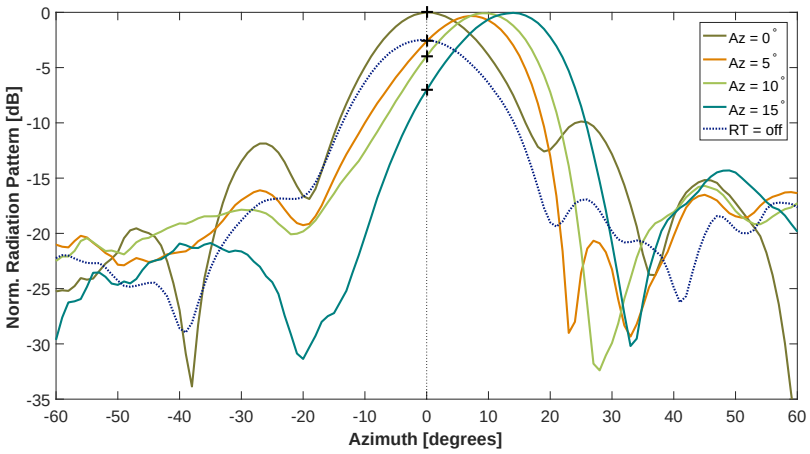

FIGURE 7.2: Measured radiation patterns in Azimuth plane for the sample beam steered angles, using the eRT.

Beamsteering analyse

The performance under fast beamsteering requests were evaluated using a slightly altered measurement setup. Namely, the arrangement of Fig. 7.3 was assembled inside the anechoic chamber, without altering the antenna initial physical positions. The new setup was assembled with the objective of evaluating the response, over-the-time, that the transmitarray exhibits under the defined circumstances.

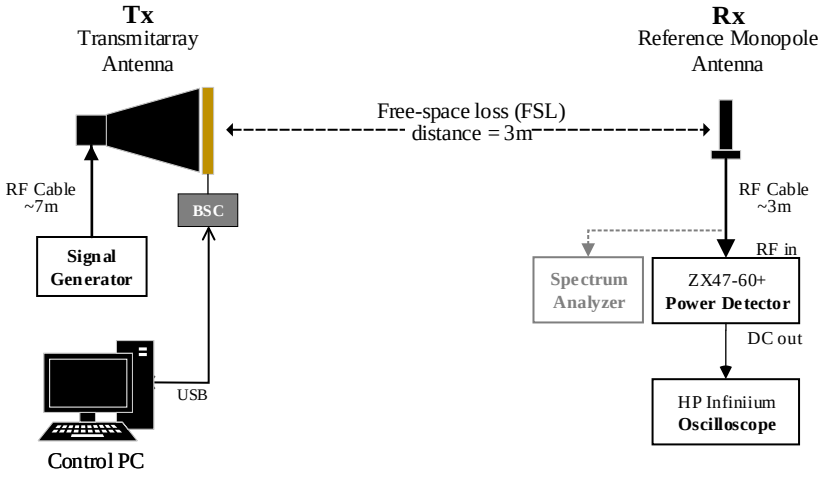

FIGURE 7.3: Side-view representation of the experimental setup utilised inside the anechoic chamber for fast beamsteering request analysis.

For instance, the eRT was used as transmitter antenna, connected to a signal generator (*Rhode & Schwarz* SMR27) which produced a RF signal at 5.2 GHz with 15 dBm. At the receiver end, a well characterised omnidirectional antenna (*SkyCross* EM-5TO6M) was connected to a spectrum analyser (*Agilent* E4407B) to measure the received power or, alternately, to a power detector (ZX47-60+) that converted the input RF signal to a DC value. Moreover, the power detector was connected to a digital oscilloscope (*HP Infiniium* 54820A with 2GSa/s) allowing to observe the DC level transitions associated to the beamsteering. Both transmitter and receiver antennas were then aligned to the maximum power direction, with the eRT electronically set at broadside direction (Az = 0° and El = 0°) and kept fixed throughout the measurements. The link budget for the new setup is presented in Table 7.1.

Therefore, since the system was calibrated prior to the fast switching measurements and, the antennas were always fixed and physically aligned throughout the measurements, the difference between received power is directly associated to the electronic beamsteering. In fact, such values correspond to the power difference between the points marked with

Table 7.1
Link budget estimation for the reference measurement system at 5.2 GHz.

Parameter	Value	Units
Transmitted power	+15	dBm
Transmitter antenna gain	+19.9	dBi
eRT gain	-4.3	dB
Receiver antenna gain	+2.3	dBi
Cable & connectors losses	+18.4	dB
Estimated FSL (3m)	+56.3	dB
Estimated received power	-41.8	dBm

Table 7.2
Received power calibration values.

β (°)	Rx. Power (dBm)	V_{rx} (V)
0	-41.8	1.66
5	-44.2	1.73
10	-45.2	1.74
15	-48.5	1.82
RT: Off	-44.1	1.73

a '+' in the radiation patterns of Fig. 7.2. The received power and its respective DC value were obtained, for the set of sample directions steered using the eRT, as detailed in Table 7.2.

7.2.2 Optimised eRT working mode

In order to avoid the introduction of any undesirable delay that may mask the switching performance of the eRT, *e.g.* delay associated to beamsteering algorithm computing time and/or to USB communication, a new working mode was created specifically for this experiment.

Accordingly, the voltage matrices corresponding to each of the considered output directions ($Az = 5°, 10°$ and $15°$) were computed, in advance, and pre-loaded directly into the beamsteering controller memory, as a lookup-tables. In addition, a new operation mode was developed in the GUI, to force the controller to switch between two of those pre-allocated angles (defined here by β for simplification) and holding it for a (T_β) period of time. To control it, a new command defined by the syntax *<autoswitch>* was then created. The command is detailed in Section 6.3.3.

This new method differs from the normal operation mode by allowing a very fast swicthing between pre-allocated angles, without having to compute and send, individually

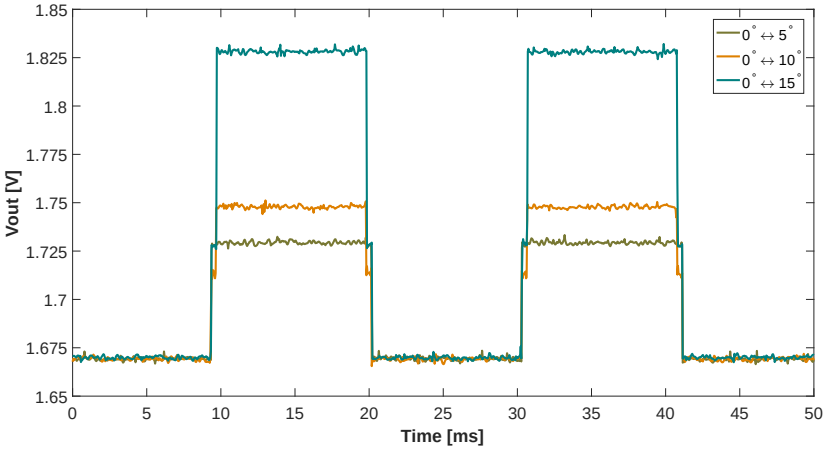

FIGURE 7.4: Measured output DC levels for a beamsteering commuted between $0° \leftrightarrow 5°$, $0° \leftrightarrow 10°$ and $0° \leftrightarrow 15°$ in the azimuth plane.

for each angle, the capacitance matrix from the host computer to the beamsteering controller, introducing therefore undisarelable communication and processing delays.

The voltage/time acquired with the oscilloscope for the beam bouncing in azimuth plane between $0° \leftrightarrow 5°$, $0° \leftrightarrow 10°$ and $0° \leftrightarrow 15°$, are illustrated in Fig. 7.4, when considering a $T_\beta = 10$ ms for $\beta = 0°, 5°, 10°$ and $15°$, respectively.

7.2.3 Results and discussion

The characterisation of the capability of the transmitarray to operate under fast beamsteering requests is performed by analysing the oscilloscope measured voltage, when considering the beamsteering between two distinct output steering directions. In this specific case study only the beam switch between $0°$ and $15°$ is considered.

The experiment started with a sample duration $T_\beta = 1$ second that was progressively shortened by a factor of 10, as depicted in Fig. 7.5. From the analyse of the results, it can be noticed that the eRT handles a beamsteering with a state duration of at least 10 ms (Fig. 7.5c), until a degradation in the scope started to become evident (Fig. 7.5d). This corresponds to a steering rate of 50 Hz, calculated using (7.1),

$$f_{steering} = \frac{1}{T_{0°} + T_{15°}}, \tag{7.1}$$

where T_β is the sample duration and ($f_{steering}$) is the steering rate.

However, when shortening the sample duration T_β to the order of microseconds (Fig. 7.5d), it can be noticed that the power related voltage, measured by the oscilloscope, starts losing the square shape and, the voltage is momentaneously set at a DC level of 1.73 V. This effect is depicted in Fig. 7.5d. In fact, the amount of time (327 μs) that

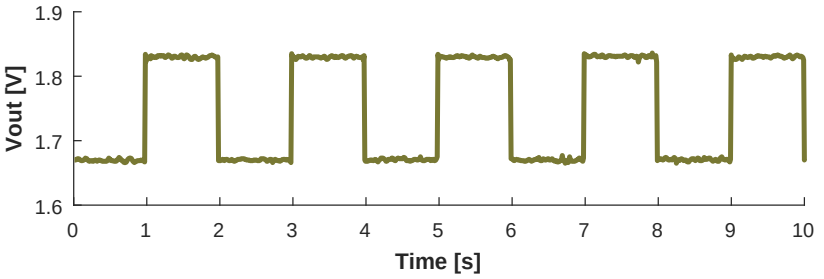

(a)

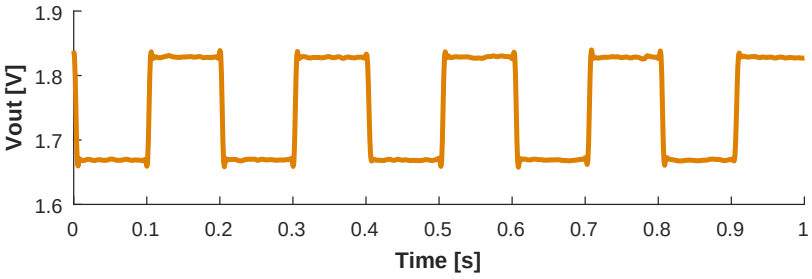

(b)

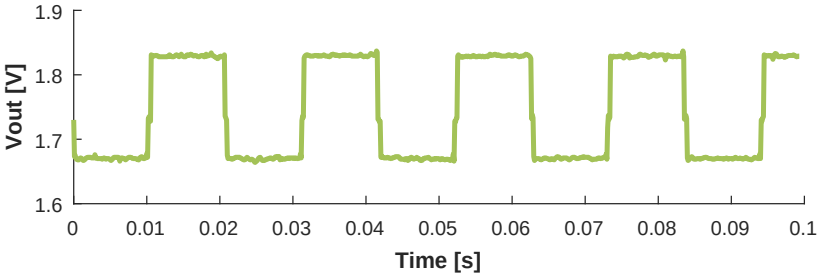

(c)

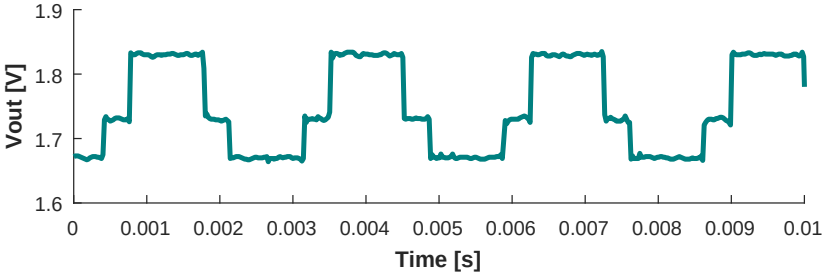

(d)

FIGURE 7.5: Oscilloscope output for beamsteering bouncing between 0° and 15°, with state times of: (a) 1s (b) 0.1s (c) 0.01s and (d) 0.001s.

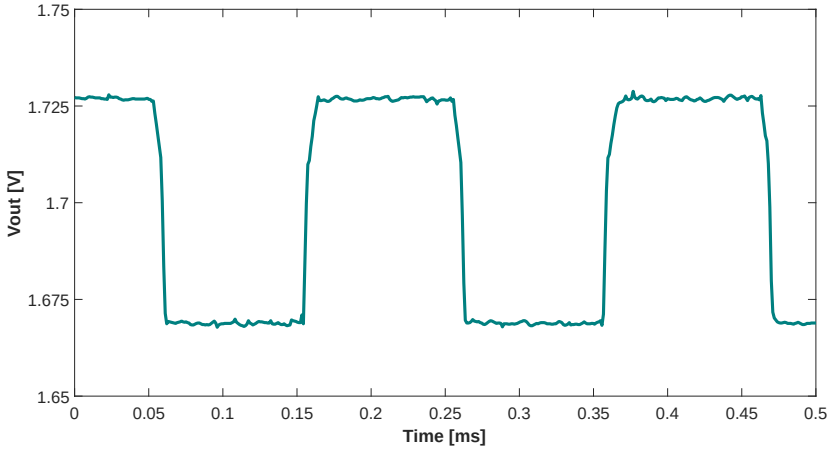

FIGURE 7.6: Maximum achieved beamsteering frequency rate using the eRT.

the state level is at 1.73 V, corresponds to the duration that the beamsteering controller takes to program the eRT. Interestingly, such voltage level corresponds to the steering state where the eRT is powered off (Fig. 7.2 and Table 7.2).

Therefore, it seems there are always delays associated to programming in which the eRT is forced to power down, before uploading the next voltage matrix. At this time scale, the limitations of the beamsteering controller start to become evident. With this findings, (7.1) should be altered to include the programming time as in (7.2), where $T_{programing} = 327$ μs.

$$f_{steering} = \frac{1}{T_{0^\circ} + T_{15^\circ} + T_{programing}}. \tag{7.2}$$

Since the firmware (code) was already optimised, the eRT structure is just a simple wire/PCB feeding line (as far as DC analyse is concerned) and the varactor diodes typically can handle switching rates down to the order of nanosecods, it can be concluded that this limitation may be related with the electronics of the beamsteering controller.

It is evident with this experiment that, for $T_\beta = 1$ ms, the beamsteering starts to be affected by the programming time (Fig. 7.5d), but with developed beamsteering controller, a steering rate of 5 kHz is still achievable the eRT is forced to switch between its Off state (no power applied to the varactors) and any other output angle β, as depicted in Fig. 7.6, although this not represent the normal operating mode. It is believed though that with a faster beamsteering controller, *e.g.* implemented with an FPGA and proper Digital-to-analogue Converter (DAC), this steering limits would be withheld.

7.2.4 Interim conclusions

In this section, the developed electronic reconfigurable transmitarray has been evaluated experimentally in terms of beamsteering agility. This has been accomplished by forcing the device to operate under fast beamsteering requests by quickly varying the control voltage at the terminals of varactor diodes.

An angular steering rate that can go up to 5kHz was achieved with the prototyped hardware under experimental conditions. Fast beamsteering is evaluated by the instant of time used to steer the main lobe of the antenna pattern towards a specific direction. According to experiments, state times of 10 ms can be easily achieved with the current hardware when steering between two distinct output directions, *e.g.* $0° \leftrightarrow 15°$ while sample durations of 0.1 ms are also possible when bouncing between the OFF state and any other angle, although this does not represent the normal operating mode. It is believed however that the reported steering switching times could be withheld, using a beamsteering controller with faster electronics, *e.g.* using an FPGA instead of a traditional micro controller.

With this characterisation, it becomes evident that the developed prototype still show its merit and it may be used in several application, as is, that require agile beamsteering in the orders of 10ms, *i.e.* in LTE systems.

7.3 OFDM Data transmission using the eRT

The 5th generation mobile network (5G) is probably the hottest topic within the wireless scientific and industry community nowadays [7–10]. The trend on wireless technology developments for 5G applications is pointing towards high data-rates, low latencies, high spectral efficiency and high bandwidths [9]. This would cover most of the requirements introduced by the 5G key applications: machine-to-machine communication, vehicle-to-vehicle, IoT [10], among others.

Therefore, a great deal of interest has been given to the development of novel wireless communication standards and technologies that enables users and devices to experience an enhanced wireless communication [150]. Part of such enhancement is expected from the introduction of antenna technologies [151–153], such as massive MIMO, beamforming, beamsteering or multi-beam antennas, but also from the deployment of novel waveforms and radio access technologies [150]. The aforementioned antenna techniques are necessary to allow agile reconfiguration of the antennas radiation pattern and thus, focusing their energy towards the receiver, *e.g.* to track moving users or to select cellular areas in function of the user spatial concentration, improving the Signal-to-noise Ratio (SNR) at the receiver. On the other hand, radio access techniques

and waveforms will contribute to meet the requirements for communication latencies and throughputs, as previously mentioned.

In this Ph.D. work, it has been proposed an alternative approach to phased antenna arrays to perform beamsteering and withdraw some of the limitations known in design of antenna arrays, and subsequently, antennas for massive MIMO. In particular, the use of a single transmitarray provides a path to reduce the complexity of antenna front-end by allowing electronic 2D beamsteering, using a single RF radiating source. However, the impact that such artificial manufactured structures may cause on a data transmission is unknown. In fact, although an extensive list of work on transmitarray devices has been presented in the literature (refer to Chapter 2), they mainly report the characteristics of a transmitarray in terms of electromagnetic performance. This is typically accomplished either through the analysis of the S_{11} and S_{21} parameters and/ or by the analysis of the antenna radiation pattern in order to obtain the maximum angular scan a transmitarray can achieve. Hence, it is lacking in the literature a proper study that allows to understand the impact that such devices may cause when connected to a (real) wireless communication system.

To this extent, the developed eRT was employed as a transmitter antenna, with two-dimensional electronic beamsteering properties, on a state-of-the-art OFDM-based SDR. The system in consideration was developed by a fellow researcher of *Instituto de Telecomunicações - Leiria, Portugal,* and it is fully characterised in [154]. The SDR is capable of transmitting data with a scalable bandwidth from 20 to 61.44 MHz, attaining close to 500 Mb/s when using high order Quadrature Amplitude Modulation (QAM) modulations [154], and thus ready for 5G applications.

In this section, a comparative analysis is presented by transmitting OFDM data over-the-air, with and without the eRT attached at the transmitter's horn antenna. This is performed when both transmitter and receiver antennas are aligned with each other but also when they are physically misaligned and the eRT is compensating for such angular mismatch. The OFDM SDR has been employed to generate data transmission using Quadrature Phase-shift Keying (QPSK) up to 256QAM modulations, at 5.2 GHz. EVM and BER are used as figures of merit to evaluate the system's performance, and consequently, the impact the eRT is having on the system.

7.3.1 OFDM-based SDR transceiver

A SDR is a programmable platform that enables the typical hardware components of a radio communication system, *e.g.* mixers, filters, amplifiers, detector, to be implemented by software, in the digital domain. Such systems are traditionally composed of a high performance DSP, *e.g.* FPGA that takes care of the heavy computation, complemented

TABLE 7.3
SDR DESIGN AND IMPLEMENTATION SPECIFICATIONS BASED ON [154].

Parameter	Value
FFT size block	1024
Loaded carriers	800
OFDM frame number	5 symbols
Full signal bandwidth	61.44 MHz
Mod. signal bandwidth	48 MHz
Subcarrier bandwidth	60 kHz
Modulation	QPSK to 256QAM
Guard time interval	256 samples
Max spectral eff.	6 bits/s/Hz/user
Maximum data-rate	288 Mbps
Digital data width	32 bits

by an RF front-end that is responsible for the radio signal conditioning inherent to transmission and reception.

Particularly, the work presented in this section makes use of the SDR presented in [154], with an updated FMCOMMS3 RF front-end, where an OFDM Single-input Single-output (SISO) transceiver is implemented using a fully pipelined hardware architecture. The presented SDR design follows the requirements of the LTE downlink physical layer [155] including all the respective algorithms for an over-the-air transmission, *e.g.* algorithms for timing and frame synchronization and, channel estimation and equalization. The main operating specifications of the OFDM SDR utilised in this work are detailed in Table 7.3.

In detail, the SDR transceiver is composed of a *Xilinx* KC705 development board loaded with a XC7K325T-2FFG900C FPGA chip and a FMCOMMS3 RF board from *Analog Devices* [156], as depicted in Fig. 7.7. This board acts as a RF front-end carrying both up- and down- conversion stages on a single chip (AD9361 [157]), enabling carrier modulation/ demodulation in frequency ranges from 70 MHz up to 6 GHz.

The SDR is controlled through a MATLAB GUI running on a control PC. The GUI communicates with the transmitter/ receiver embedded FPGA *MicroBlaze* processor via USB and configures, in real-time, the main parameters of the SDR transceiver, such as the modulation, the sampling rate of DAC/ ADC, filters roll-off and bandwidth, decimation ratio, internal automatic gain control parameters, *etc.*. The most relevant SDR analogue specifications are listed in Table 7.4. A pseudo-random data generator, internal to the SDR, generates the data that will be modulated by the 48 MHz bandwidth OFDM transceiver and passed through the entire communication loop, while at the end of the receiver, a real-time debugging tool, *Xilinx Integrated Logic Analyser*, captures

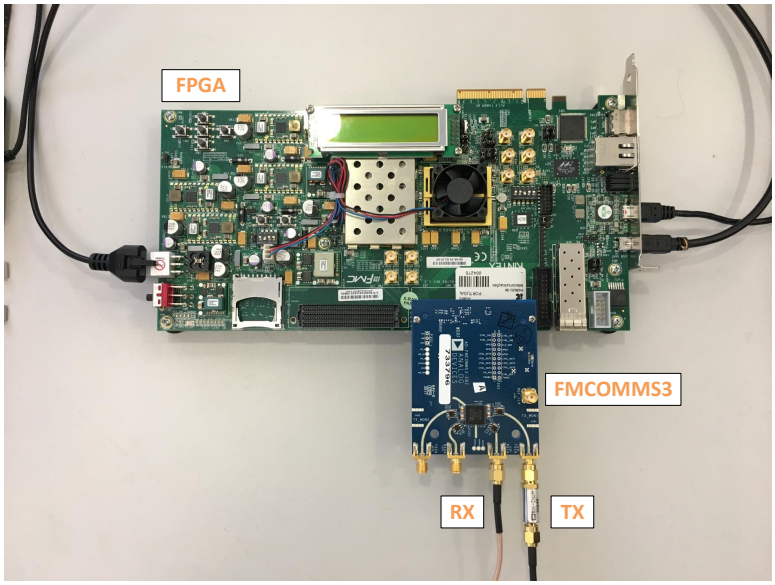

FIGURE 7.7: Photography of the SDR transceiver.

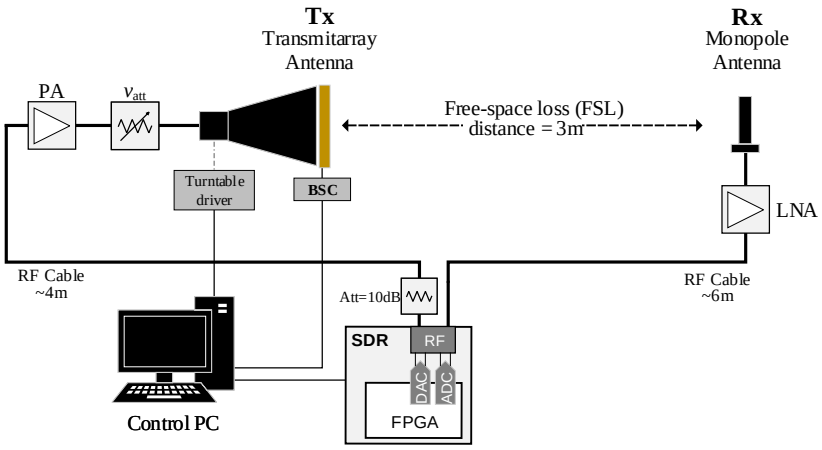

FIGURE 7.8: Block diagram of the experimental setup.

samples of the decoded data. These samples are then transferred to the PC for EVM and BER processing.

7.3.2 Measurement setup and procedure

Measurement setup

In order to evaluate the eRT operating within the SDR OFDM system, the setup of Fig. 7.8 is considered. The measurement setup has been assembled inside an anechoic chamber to avoid possible negative effects from a multi-path fading channel, emulating an Additive White Gaussian Noise (AWGN) channel. The SDR was configured to operate at 5.2 GHz, corresponding to the central frequency of the eRT.

Table 7.4
Summary of the SDR analogue specifications for a 5.2 GHz carrier frequency [156].

Feature	Value
Transmission BW	48 MHz
Tx noise floor	-157 dBm/Hz
Rx noise figure	3.5 dB
Rx sensitivity	-44 dBm*
Rx gain	67 dB
DAC/ADC sampling rate	61.44 Msamples/s
Number of DAC/ADC channels	2/2
Resolution of DAC/ADC	12 bits
RF carrier freq.	70 MHz - 6 GHz

(*) Received power level which ensures an EVM value equal to -36 dB, according to AD9361 specifications.

As it can be observed in the block diagram of the measurement setup (Fig. 7.8), the SDR (described in the last section) is utilised as a transceiver where both Transmitter (Tx)/ Receiver (Rx) channels of the FMCOMMS3 are connected, respectively, to the transmitter and receiver branches. On the transmitter side, a Power Amplifier (PA) with 35.5 dB of gain is introduced prior to a 27 dB variable attenuator (v_{att}), utilised to manually sweep the SNR (in order to plot BER curves). At the output of the Tx port, a 10 dB attenuator (Att) is introduced to back-off the operating point of the PA, and thus, reducing possible non-linear distortions associated to the high peak to average power ratio of OFDM modulation (around 10/ 15 dB) [158]. Finally, the transmitter chain terminates with a 20 dBi standard gain horn antenna (well characterised in Section 3.8) which supports the eRT. On the receiver side, a well characterised omni-directional antenna (*SkyCross* EM-5TO6M) is utilised with a Low Noise Amplifier (LNA) of 34.5 dB which is then connected to the Rx port. Both transmitter and receiver antennas are placed 3 meters apart to ensure that the measurements were performed in the antenna's far-field region.

To mimic the testing setup and estimate the dynamic range of the system, a complete link budget analysis is presented in Table 7.5. This takes into consideration the gain and losses of the components in the system, with the exclusion of the eRT insertion losses (reference measurement). For an OFDM signal with 48 MHz of bandwidth and a maximum transmission power of -23 dBm (DAC Tx power), a received power varying between -15.6 dBm and -42.6 dBm is obtained, when v_{att} varies between 0 and 27 dB, respectively, and the antennas are aligned to their maximum power direction. This setup was carefully designed to ensure that the power level at the ADC input is higher than the established Rx sensitivity of -44 dBm (in Table 7.4), maximizing the dynamic range

Table 7.5
Link budget estimation for the reference measurement system at 5.2 GHz.

Parameter	Value	Units
DAC Tx power	-23	dBm
Attenuator (Att) gain	-10	dB
Power amplifier (PA) gain	+35.5	dB
Variable attenuator (v_{att}) gain	[-27 $\leftrightarrow$ 0]	dB
Transmitter antenna gain	+19.9	dBi
Receiver antenna gain	+2.3	dBi
Low noise amplifier	+34.5	dB
Cables & connectors losses	+18.5	dB
Estimated Path Loss (3m)	+56.3	dB
Estimated Received Power	[-42.6 $\leftrightarrow$ -15.6]	dBm

of the system and ensuring that the SDR is operating at the optimal range (-36 dB of EVM).

The computer that stores and processes the decoded OFDM data (Fig. 7.8), is also responsible for controlling a motorised turntable (via turntable driver) that allows to physically rotate the transmitter antenna around its own axis, in azimuth plane, towards a direction given by β_m (where m stands for *mechanical*). Moreover, it is also responsible for controlling the eRT (via the beamsteering controller) and select the angle β_c (where c stands for *compensated*), steered by the transmitarray, *i.e.* the angle attributed to the eRT to compensate for the mechanical movement of the turntable. An illustration of the mechanical movements for system characterisation is presented in Fig. 7.9a, for ease of interpretation, while the setup inside the anechoic chamber is depicted in Fig.7.9b.

Measurements procedure

In order to assess the impact of the eRT has on a wireless communication system, a comparative study has been performed for OFDM transmitted data using QPSK and 256QAM modulation schemes, which correspond to the lowest and highest order modulations provided by the SDR system, respectively, with and without the transmitarray device coupled into the reference horn antenna.

Accordingly, two case studies have been defined:

- Case #1 - measurements using horn antenna only (reference);
- Case #2 - measurements with horn antenna coupled with eRT.

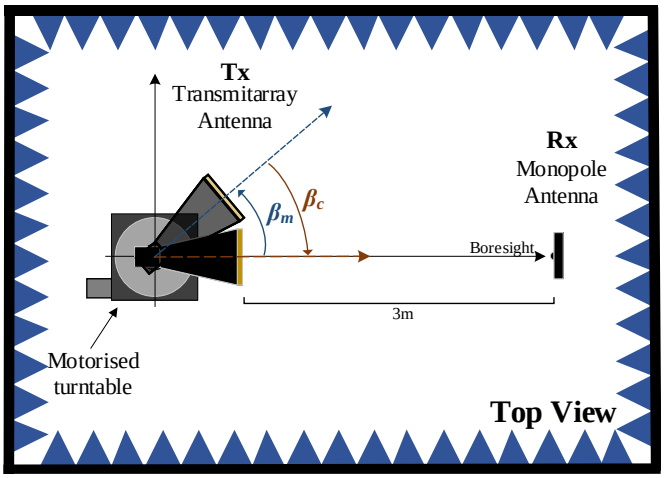

(a)

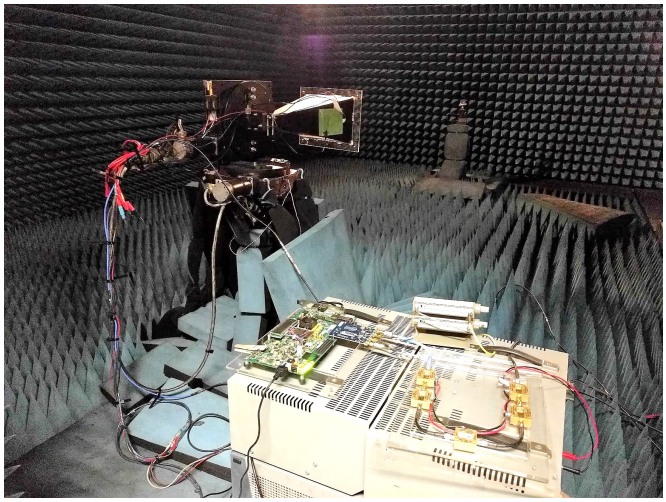

(b)

FIGURE 7.9: (a) Schematic top-view of the mechanical arrangement and (b) photography of the experimental setup inside the anechoic chamber.

TABLE 7.6
CONSIDERED CASE STUDIES FOR MEASUREMENT.

	Case #1	Case #2
Measurement type	Horn only	Horn w/ eRT
Mechanical position	$\beta_m = [0°,\ 10°,\ 22°,\ 30°]$	
Beamsteering compensation	none	$\beta_c = \beta_m$
Transmit modulations	QPSK, 256QAM	
v_{att} variation	0 to 27 dB	

For both cases, several angular points have been considered, namely, by keeping the horn antenna pointing boresight ($\beta_m = 0°$), and mechanically rotated to: $\beta_m = 10°$, $\beta_m = 22°$ and $\beta_m = 30°$, respectively. Furthermore, in the second case (case #2), the eRT is coupled into the horn antenna and programmed so it could compensate for any Tx-Rx misalignments, *i.e.* the main-lobe of the radiation pattern of the horn antenna would always be pointing at the receiver using electronic beamsteering. In this particular case, the eRT enables beamsteering compensation for: $\beta_c = \beta_m = 10°$, $\beta_c = \beta_m = 22°$ and $\beta_c = \beta_m = 30°$, respecting the diagram of Fig. 7.9a. The position that respects $\beta_c = \beta_m = 0°$ (no angular compensation) is also considered since it helps to characterise the impairments caused on the system with the insertion of the eRT (reference measurement). It should be mentioned that although only positive azimuth (β_m) angles have been considered for this experiment, any other direction could have been chosen due to the full 2D beamsteering capability of the eRT, if the steering limits of the transmitarray are respected. A summary of both case studies is presented in Table 7.6.

7.3.3 Results and discussion

In this section, the evaluation of the performance of OFDM data transmission using the eRT coupled to an standard gain horn antenna is presented. One of the measurements obtained from the experiments was the average EVM ($\overline{\text{EVM}}$) [154, 159]. The $\overline{\text{EVM}}$ is a metric that quantify the dispersion of a scatter point constellation characterising the quality of a (received) modulation.

In particular, $\overline{\text{EVM}}$ values have been computed using the mathematical formulation readily available in [154, 159] and, averaged over 30 OFDM received frames. This action has been performed for all the angular combinations defined by the case studies indicated in Table 7.6, while v_{att} is swept from 0 to 27 dB, with 3 dB steps. The respective results are presented in Table 7.7, both in decibel (dB) and percentage (%). The expected increase of $\overline{\text{EVM}}$ with incremented v_{att} is noticeable. This effect, common to both case #1 and #2, is explained by the reduction of the SNR at the receiver. A lower SNR impacts the received signal resulting in a sparser demodulated constellation,

TABLE 7.7
$\overline{\text{EVM}}$ VS. v_{att} FOR SEVERAL INPUT ANGLES WITH AND WITHOUT THE ERT

	Case #1				Case #2			
v_{att}	$\beta_m = 0°$	$\beta_m = 10°$	$\beta_m = 22°$	$\beta_m = 30°$	$\beta_c = 0°$	$\beta_c = 10°$	$\beta_c = 22°$	$\beta_c = 30°$
[dB]	[dB] | (%)	[dB] | (%)	[dB] | (%)	[dB] | (%)	[dB] | (%)	[dB] | (%)	[dB] | (%)	[dB] | (%)
0	-28.01 (3.98)	-27.19 (4.37)	-18.39 (12.4)	-9.59 (33.17)	-26.54 (4.71)	-25.85 (5.1)	-27.53 (4.2)	-26.39 (4.79)
3	-27.46 (4.24)	-25.97 (5.03)	-15.86 (16.10)	-5.79 (51.37)	-25.35 (5.40)	-23.93 (6.36)	-26.24 (4.88)	-24.55 (5.92)
6	-26.54 (4.71)	-24.36 (6.06)	-12.71 (23.15)	-2.05 (79.02)	-23.5 (6.69)	-21.63 (8.28)	-24.5 (5.95)	-22.13 (7.82)
9	-25.15 (5.53)	-22.31 (7.67)	-9.57 (33.23)	–	-21.29 (8.62)	-19.15 (11.03)	-22.23 (7.73)	-19.58 (10.49)
12	-23.32 (6.83)	-19.91 (10.11)	-5.7 (51.86)	–	-18.43 (11.99)	-16.42 (15.11)	-19.57 (10.51)	-16.58 (14.82)
15	-21.06 (8.85)	-17.12 (13.93)	–	–	-15.63 (16.53)	-13.59 (20.91)	-16.58 (14.82)	-13.38 (21.44)
18	-18.47 (11.93)	-14.05 (19.84)	–	–	-12.77 (22.99)	-9.36 (34.04)	-13.69 (20.68)	-10.19 (30.92)
21	-14.83 (18.13)	-10.94 (28.38)	–	–	-8.66 (36.91)	-6.89 (45.26)	-10.17 (31.01)	-6.77 (45.87)
24	-11.98 (25.17)	-7.73 (41.08)	–	–	-6.02 (50.02)	-3.54 (66.5)	-6.54 (47.12)	-3.13 (69.77)
27	-7.77 (40.89)	-7.68 (41.29)	–	–	-2.59 (74.18)	–	-3.1 (69.98)	–

and consequently, a larger $\overline{\text{EVM}}$. This is in agreement with the theory, since both EVM and SNR metrics can be related by (7.3) for QPSK modulation, according to [159],

$$\overline{\text{EVM}}_{RMS} \approx \sqrt{\frac{1}{SNR}} \quad \Leftrightarrow \quad \overline{\text{EVM}}|_{dB} \approx -SNR|_{dB}. \tag{7.3}$$

In fact, the decrease of $\overline{\text{EVM}}$ is more pronounced in case #1, when the antennas misalignment is forced by mechanical means. Rotating the antenna has an impact on the SNR proportional to the difference between the main-lobe gain and the gain at the considered angular offset. For example, for case #,1 where $\beta_m = 30°$, such discrimination is so large that it goes beyond the dynamic range of the proposed setup and no useful information can be extracted from the received signal for most part of v_{att} range (marked as "-" in Table7.7).

However, such limitation is mitigated with the introduction of the eRT and by enabling electronic beamsteering. With the transmitarray coupled to the horn antenna (case #2), the variation of the measured $\overline{\text{EVM}}$ is not as abrupt as in case #1. In fact, it is kept almost constant over entire angular sweep range (within ±1 dB), as it can be observed in Fig. 7.10a, for $v_{att} = 0,\ 3$ and 6, respectively. Such behaviour indicates that the eRT yields an overall system performance enhancement. For a steering angle of ±30°, the OFDM system presents an improvement of 72% in terms of demodulation error.

In fact, the inclusion of the eRT enhances the OFDM system with gains up to 20 dB of $\overline{\text{EVM}}$ performance, as depicted in Fig. 7.10b. However, for scanning angles between ±10°, the $\overline{\text{EVM}}$ is affected with a degradation of 2 dB. This corresponds to the excess loss by the introduction of the eRT, *i.e.* transmitarray insertion losses. Moreover, it can also be observed that for the entire angular sweep range of case #2, $\overline{\text{EVM}}$ values experience a reduced fluctuation of approximately ±1 dB (Fig. 7.10a), which correspond to the non-linear insertion losses that vary from angle to angle, well characterised in Section 6.4, *e.g.* the direction $\beta_c = 22°$ exhibits slightly better $\overline{\text{EVM}}$ than for the remaining positions.

The aforementioned effects can be observed on the received scatter point constellations for QPSK (Fig. 7.11a and 7.11b) and 256QAM (Fig. 7.11c and 7.11d) modulations. The modulations are presented and compared for case #1 (horn antenna only) and case #2 (horn with eRT compensating for $\beta_c = \beta_m$), for the angular case $\beta_m = 0°$ and $\beta_m = +30°$, and considering the best SNR case ($v_{att} = 0$ dB). While, for $\beta_m = 0°$, all constellations exhibit a well defined point scattering area, when $\beta_m = 30°$ is considered, relatively high distortion of the received scatter symbols is clearly visible for all modulations when the eRT is not used. In this case, constellation points are largely scattered from each other indicating, therefore, that decoded data will exhibit an high error probability. On the

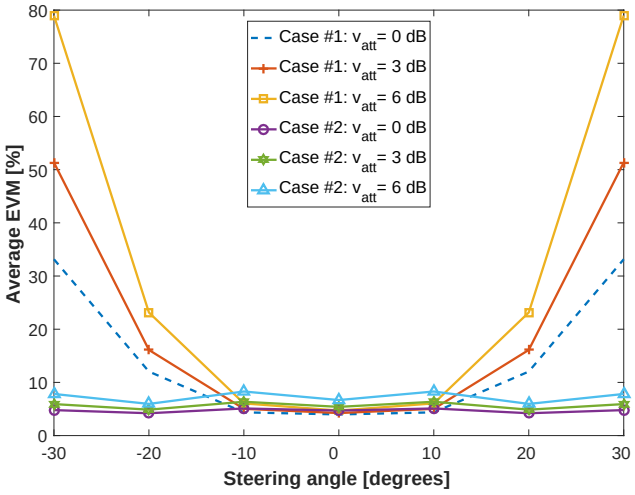

(a)

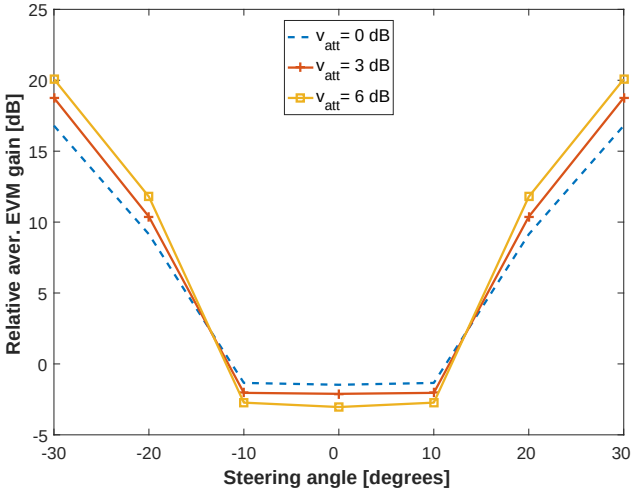

(b)

FIGURE 7.10: (a) Average EVM and (b) average EVM relative gain, for $v_{att} =$ 0 3 and 6 dB, over the considered angular steering range, when comparing the OFDM system with and without the eRT, respectively.

other hand, with the beamsteering compensation active, constellations are very similar in shape for both $\beta_m = 0°$ and $\beta_m = 30°$, as expected.

In addition to EVM analysis, BER performance has also been evaluated in this work. Such analysis allows to characterise additional distortions introduced by the transmitarray structure on the implemented wireless communication system. While EVM only characterises the quality of a demodulated constellation, BER quantifies statistically the number of errors (in bits) introduced by the eRT on the data transmission over-the-air. The BER calculation follows the *Monte Carlo* method [160], and compares both cases #1 and #2 for $\beta_m = 0°$ (reference measurement), for the lowest (QPSK) and the highest (256QAM) order modulations. From Fig. 7.12, it can be verified that experimental results with and without the eRT exhibit a good match for 256QAM only (similar BER curves). This indicates that the introduction of eRT does not effect the overall OFDM system performance.

It is worth mentioning that Fig. 7.12 shows a 256QAM result near the theoretical limit, while QPSK results have a 3 to 4 dB BER gap to the theoretical. This small gap between both the QPSK curves (Fig. 7.12) can be attributed to a number of reasons. Firstly, the eRT introduces losses, which are more notorious in this particular modulation due to the fact that any SNR fluctuation is enhanced at this low error probability (BER $<< 10^{-2}$). Secondly, the displacement between the experimental results and the AWGN theoretical curves, which are the curves that characterise the modelation scheme robustness over a white Gaussian noise channel [154], are related with OFDM algorithm implementation and RF front-end impairments. In the case of OFDM, imperfect channel estimation and compensation algorithms on the receiver side can lead to such difference, as reported in [154]. Finally, as stated in [161], the RF front-end can contribute by introducing phase noise, the PA non-linearities, the IQ imbalances, and many other hardware impairments.

7.3.4 Interim conclusions

In this section, the impact of a FSS-inspired eRT on a real-time wireless data transmission is studied. This particular characterisation presents to the literature, for the first time, the impact that such artificial structures have on a realistic data transmission. This has been accomplished through the combination of a state-of-the-art OFDM SDR transceiver, with a physical prototype of the eRT, to enable electronic beamsteering. A comparative study has been presented by transmitting modulated data using QPSK up to 256QAM modulations, over-the-air, with and without the eRT compensating for a forced mechanical antenna misalignment. The experimental results, obtained at 5.2 GHz, clearly demonstrate that the eRT do not negatively impact the data transmission (through the analysis of a BER study) but also proves the effectiveness of

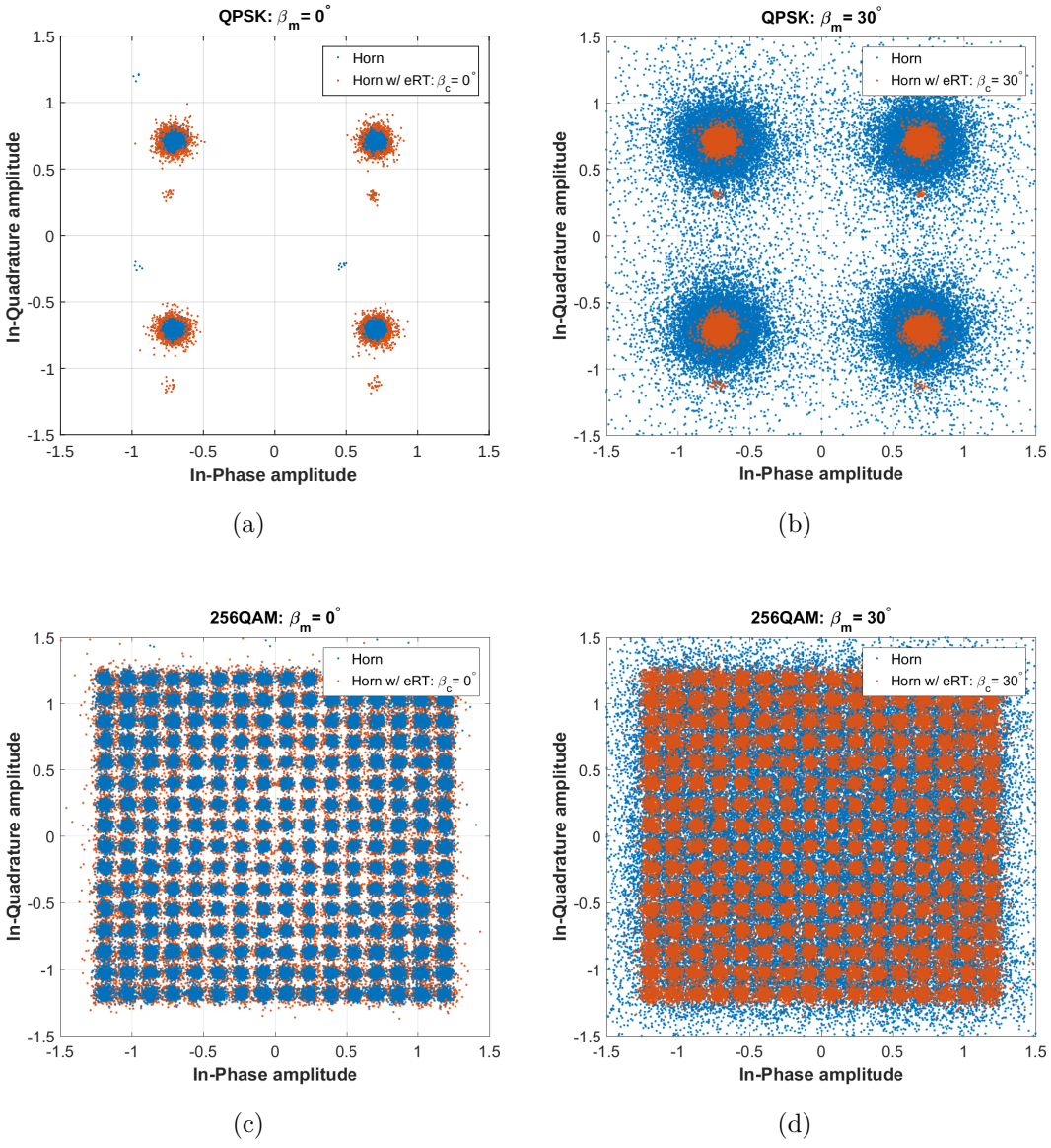

FIGURE 7.11: Received scatter point constellation for (a,b) QPSK and (c,d) 256QAM modulations using, respectively, the horn antenna aiming at $\beta_m = 0°$ with no compensation ($\beta_c = 0°$) and, using the horn antenna with the eRT aiming at $\beta_m = 30°$ with beamsteering compensation ($\beta_c = 30°$).

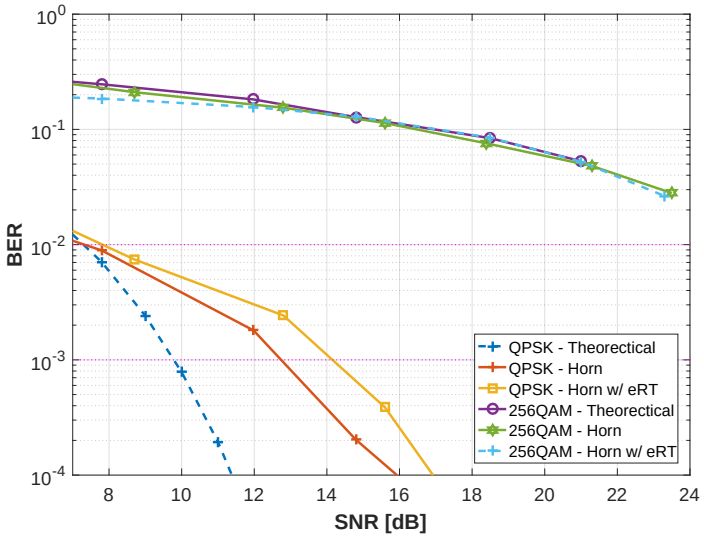

FIGURE 7.12: BER *vs.* SNR curves for QPSK and 256QAM modulations, with and without the eRT coupled into the reference horn antenna, respectively.

the eRT in the angular sweep range of ±30°, in any direction. For instance, when a ±30° antenna misalignment is induced and the eRT is compensating for such offset, the $\overline{\text{EVM}}$ undergoes only 4.8% (-26.4 dB) of degradation, as opposed to 33.2% (-9.6 dB) otherwise. This yields to 20 dB of $\overline{\text{EVM}}$ improvement for the extreme angular case. Finally, the adoption of an eRT in emerging 5G radio systems seems to be a key factor in reducing the RF circuitry burden normally required for antenna beamsteering, while enabling agile steering by electronic means, in addition to its rather low profile and light-weight. This became more important, on dynamic propagation scenarios. Thus, it represents an important step in antenna design innovation applied to real case OFDM test-bed.

7.4 Overall chapter appreciation

The work presented in this chapter puts the efforts on testing the developed transmitarray devices for 2D antenna beamsteering in possible real-case applications. This was achieved mostly under experimental circumstances on the manufactured prototypes. This option was considered as alternative to simulations, that might have also been performed to obtain the same characterisation, due to the long computing simulation times associated to the complex and electronically large model in CST MWS. The experimental validation allowed to easily explore the physical limits of the prototypes by deploying it under scenarios that mimic real applications.

The case study presented in Section 7.2, allow to characterise the agility of the beamsteering of the eRT under demanding angular requests. The eRT was experimentally

subjected to fast changes of beam direction and, the switching times reported with the current hardware were found to support switching rates up to 10 ms (supported by LTE), although some limitations are evident mainly due to the (hardware) design of the beamsteering controller.

Section 7.3 culminates all the work by employing the eRT within a real wireless communication system, as a transmitter antenna with beamsteering capability. The study performed on the structure allowed to prove the usefulness of antenna beamsteering on data transmission, but also to study the impact that introduction of FSS made of artificial materials, might have on a real transmission.

The work performed in every section of this chapter was disseminated in one international journals and one conference publications, under review at the submission time of this document, as follows:

Section 7.2: J. Reis; R.F.S. Caldeirinha; T.R. Fernandes; A. Hammoudeh and N. Copner, **"2D Agile Beamsteering using a Reconfigurable Transmitarray"**, *Proc. European Conf. on Antennas & Propagation - EuCAP*, Krakow, Poland, April 2019, (under review: submitted on Sept. 2018);

Section 7.3: J. Reis; C. Ribeiro; L. Duarte; R. Gomes; N. Copner and R.F.S. Caldeirinha, **"Performance evaluation of OFDM data transmission using an 2D beamsteering transmitarray"**, *IET Magazine on Antennas and Propagation*, (under review: submitted on Sept. 2018). **Impact Factor = 1.739, Q2**.

This page is intentionally left blank.

CHAPTER 8

Review and conclusions

8.1 Introduction

This chapter is dedicated to the summary, critical analysis and evaluation of the work undertaken during this research project, identification of the main contributions to science and possible directions for further work. The chapter is divided into four sections: *i)* review of the work developed in this Ph.D. by presenting the main developments and achievements; *ii)* overview of the major contributions conceded by this research work; *iii)* overview of the published work that contributed to the scientific knowledge; *iv)* proposals for further scientific investigation and developments, by pursuing with the main research topic of this thesis, or with relevant parallel lines of research.

8.2 Review of the thesis

The main scope of this Ph.D. thesis aimed at the investigation of novel antenna beamsteering for wireless applications. To achieve such broad objective, antenna transmitarrays were presented as alternative to the most traditional beamsteering techniques presented in the literature. In particular, transmitarrays inspired on Frequency Selective Surfaces unit-cells have been studied, designed, simulated and finally manufactured, yielding to two manufactured fully functional prototypes. The prototypes have been characterised experimentally, in a proper controlled environment, to prove the concept and validate the usefulness of the proposed methodology for antenna beamsteering. Finally, the electronic model of the developed prototype have been employed in several real-case scenarios that may be part of potential use-case applications. The outcome of this work is reported in distinct chapters of this thesis, herein presented for review:

Chapter 1 provided an introduction to this research work by identifying the background and subsequent motivation that lead to its initial definition. The line of research is defined by exploring the concept of transmitarrays, as alternative to antenna phased arrays for beamsteering realisation. This concept was adopted from the beginning of this research and it is the distinctive key feature of this work, by performing beamsteering using a single directive radiating antenna controlled by an artificial structure composed of frequency selective surfaces. This chapter then enumerated the main original research objectives and thesis document structure.

In Chapter 2 was presented an extensive literature review addressing many different topics of relevance towards the execution of this research work. It starts by introducing and reviewing work on traditional antenna beamsteering systems, including reconfigurable antennas, phased arrays, switch-beam and smart antennas, followed by presenting alternative methodologies utilised to steer the main lobe of antenna radiation pattern, of which transmitarrays are included. The scope of the presented literature is narrowing down throughout the chapter. A proper state-of-the-art on transmitarray systems is finally presented, summarising the most up-to-date contents of the literature on this topic. Passive and reconfigurable (active) transmitarray and unit-cells designs for antenna beamsteering and wavefront polarisation control, built based on either microstrip patch, metamaterials and frequency selective surfaces are presented, summarised and compared each other.

In Chapter 3, the measurement systems used for evaluating the EM performance of the transmitarray prototypes were introduced. All measurements were performed in the controlled environment of an anechoic chamber, with all relevant mechanical and RF hardware being described in this chapter. An evaluation of the available measurement system dynamic range for antenna radiation patterns characterisation was provided. The measurement normalisation procedures were also described as well as the post-processing methods implemented to analyse the measured data.

Chapter 4 introduced the mathematical formulation to perform beamsteering using a transmitarray. The mathematical models for both 1D and 2D antenna beamsteering are described and further validated on an ideal transmitarray model composed of ideal permittivity elements. Initial electromagnetic simulations, using a full-wave electromagnetic solver, are included to characterise the performance of the proposed model.

The contents of Chapter 5 are related to developments of a passive, none-reconfigurable, transmitarray for 2D antenna beamsteering. Following the requirements of the theoretical model introduced in last chapter, a controlled phase shift is applied to each individual transmitarray element, to enable the steering of the main lobe of an original antenna pattern in both elevation and azimuth planes. Therefore, it is presented and described in this chapter all the procedures taken into consideration to develop a transmitarray,

from the unit-cell design, to the composition of a 5×5 transmitarray device. The proposed model, inspired on Frequency Selective Surfaces, is developed, simulated and finally optimized through a complete parametric study based on EM simulations using CST MWS, that allowed to evaluate and characterise the transmitarray performance against unit-cell design parameters. The final model of the transmitarray yielded the construction of a prototype that was proved to successfully realise 2D antenna beam-steering, under an experimentally controlled environment (anechoic chamber). The work being presented in this chapter resulted in two peer-review international conference publications and a paper publication on a highly reputed international journal.

Chapter 6 presented the implementation and evaluation of a reconfigurable transmitarray with two-dimensional electronically beamsteering capability. This model was developed subsequently to the preliminary research performed in the passive transmitarray. An eRT was developed by employing varactor diodes on the initial unit-cell model (originally loaded with discrete capacitors), and by adding a biasing network able to feed and control all the transmitarray elements individually. Electromagnetic simulations were performed to characterise the new model in terms of amplitude and phase response, and evaluate the impact that the proposed biasing strategy had on overall system performance. A prototype of the transmitarray was built and characterised experimentally inside of an anechoic chamber with the help of a beamsteering controller. The latter was developed to control the reconfigurable transmitarray by controlling the phase value of each transmitarray element and enable the intelligent and automated control of the direction of the antenna main beam. The content presented in this chapter resulted in a paper publication in a highly reputed international journal.

Chapter 7 was organised in a slightly different manner than the previous ones. It is composed of two sections, each testing the usage of the electronic model of the transmitarray under a different scenario of application. The results being reported were obtained experimentally, using a particular measurement setup inside the anechoic chamber. In Section 7.2, the eRT was evaluated experimentally in terms of beamsteering agility and steering response. The results obtained on the prototype helped to understand and characterise the commutation rates achievable by the eRT, when switching between different output angle directions and, what are the timing constraints associated to such fast angular switching. Finally, in Section 7.3, the eRT was employed as a transmitter antenna, with two-dimensional electronic beamsteering properties, on a state-of-the-art OFDM-based SDR. The SDR is capable of transmitting data at high data rates using high order QAM modulations. A comparative analysis was presented by transmitting OFDM data over-the-air, with and without the eRT attached at the transmitter's horn antenna to evaluate the impact the eRT had on the system. To the date of this document, the work developed in this chapter resulted in: one published (user review)

peer-reviewed conference publications Section 7.2); and, one submitted publication on highly reputed international journal (relative to the work presented in Section 7.3).

8.3 Conclusions

The work developed under this research programme several contributed particularly on two distinct areas: *i)* Antenna beamsteering for wireless applications; and *ii)* transmitarray design and characterisation. The research work presented in this document was thoroughly supported by simulations and measurement campaigns, allowing to extract several critical observations and conclusions drawn. The main contributions to each area may be summarised below.

8.3.1 Contribution to beamsteering systems

Although the backgrounds on antenna beamsteering are well reported in the literature, this Ph.D. work contributed with the introduction of a novel alternative technique to realise 2D antenna beamsteering. This was achieved by exploring the concept of transmitarrays.

A theoretical model that allow to predict the performance of a 2D beamsteering transmitarray was introduced and further validated against EM simulations, on a ideal model of a transmitarray. With the proposed methodology, beamsteering is enabled in the two main antenna planes, by using a single directive radiating source only. Due to this fact, a significant reduction of either the complexity of the RF front-end, and its associated cost is expected when compared with the most mainstream techniques (*e.g.* phased arrays, switch-beam antennas).

The proposed theoretical model served as base to the design and implementation of the transmitarrays models being presented along this document.

8.3.2 Contribution to transmitarray designs and implementation

The outcome of this research work culminated in the construction of two fully functional transmitarray prototypes (one passive, one reconfigurable), for antenna beamsteering.

In particular, the design presented in Chapter 5, on the square-slot FSS unit-cell, yield to the construction and experimental characterisation of a passive transmitarray prototype with 2D beamsteering capabilities. This part of the work contributed to the literature with 3 direct paper publications which disseminate: design procures, results of extensive parametric simulations and, finally, validation of the simulations against experimental results.

With the experience obtained on the passive model, an electronically reconfigurable transmitarray was finally proposed. The work carried out in this model is mostly described in Chapter 6, which not only reports the feeding strategy design, simulation and optimisation, but it also describes the drivers and the firmware/software implementation that allowed to automatically control the direction of the main beam of the radiation pattern. The work performed using the electronically reconfigurable transmitarrays directly contributed to scientific community with to 4 publication (2 of which under review at the time of the submission of this document) and 2 live demonstrators in national exhibitions.

8.3.3 Contribution to measurements

This research work included extensive measurement campaigns in the controlled environment of an anechoic chamber available at both host institutions: *University at South Wales, Treforest, United Kingdom* and *Instituto de Telecomunicações - Leiria, Portugal*. Different measurement techniques were used to characterise the manufactured prototypes in terms of frequency response, but also regarding to their radiation properties. Most of the measurements were obtained from 4.0 to 6.0 GHz covering the specific operation bandwidths of the manufactured devices. A total of two prototypes were manufactured, corresponding to the passive and the active (reconfigurable) model of the transmitarray. The measurement allowed to demonstrate that two dimensional antenna beamsteering is achievable by coupling artificial man-made structures to commercially available, (directive) antennas, instead of using the most the typical antenna array structures. This measurements added to the literature new raw data regarding antenna radiation pattern resultant from the beamsteering characteristics provided by such structures. Moreover, this work also contribute by presenting to the literature, for the first time, measurements results of the usage of an electronically reconfigurable device on a real wireless communication system. The presented result disseminated the impact that such structures may have caused when used within a real wireless system, transmitting and receiving OFDM modulated data.

8.4 Contribution to the knowledge

The research work carried out in this Ph.D. has contributed to the knowledge with relevant scientific publication in several recognised international Journals [J] and international conferences [C], supporting and covering most of the topics being address in the different chapters of this thesis. It has also contributed with several live demonstrators [D] in relevant national and international events.

8.4.1 Direct contributions

At the submission time of this document, the work being presented in this thesis contributed directly to the knowledge with a total of three journal papers (one of which under review), nine peer-reviewed conference papers (two of which under review) and several live demonstrators. The contributions are listed below in increasing order of date. Samples of the published papers can be found on-line in various digital libraries, namely in *IEEE Xplore* website.

Papers in international journals:

J1. J. Reis; N. Copner; A. Hammoudeh; Z. Al-Daher; R.F.S. Caldeirinha; T.R. Fernandes and R. Gomes, **"FSS-inspired Transmitarray for two Dimensional Antenna Beamsteering"**, *IEEE Transactions on Antennas and Propagation*, vol. 64, no. 6, pp. 2197-2206, June 2016. doi: 10.1109/TAP.2016.2543802. **Impact Factor = 2.957, Q1;**

J2. J. Reis; R.F.S. Caldeirinha, A. Hammoudeh and N. Copner, **"Electronically Reconfigurable FSS-Inspired Transmitarray for 2-D Beamsteering"**, *IEEE Transactions on Antennas and Propagation*, vol. 65, no. 9, pp. 4880-4885, Sept.2017. doi: 10.1109/TAP.2017.2723087. **Impact Factor = 2.957, Q1;**

J3. J. Reis; C. Ribeiro; L. Duarte; R. Gomes; N. Copner and R.F.S. Caldeirinha, **"Performance evaluation of OFDM data transmission using an 2D beamsteering transmitarray"**, *IET Magazine on Antennas and Propagation*, (under review: submitted on Sept. 2018). **Impact Factor = 1.739, Q2**.

Papers in international conferences:

C1. J. Reis; Z. Al-Daher; N. Copner; A. Hammoudeh; R.F.S. Caldeirinha and T.R. Fernandes, **"Two-Dimensional Transmitarray Beamsteering Using Stacked Tunable Metamaterials"**, *Proc. Loughborough Antennas and Propagation Conf. – LAPC*, Loughborough, United Kingdom, Vol. 1, pp. 495 - 499, November, 2014;

C2. J. Reis; Z. Al-Daher; N. Copner; R.F.S. Caldeirinha and T.R. Fernandes, **"Two-Dimensional Antenna Beamsteering Using Metamaterial Transmitarray"**, *Proc. European Conf. on Antennas & Propagation - EUCAP*, Lisbon, Portugal, Vol. 1, pp. 1 - 1, April, 2015;

C3. J. Reis; R.F.S. Caldeirinha; T.R. Fernandes and A. Hammoudeh, **"Enabling Spatial Diversity and Beamsteering with Reduced RF-chains using Re-**

configurable Transmitarrays", *Proc. European Conf. on Antennas & Propagation - EUCAP*, Paris, France, March 2017.

C4. J. Reis; R.F.S. Caldeirinha; M. Vala; A. Sardo and A. Hammoudeh, **"Electronically Reconfigurable Active Metamaterials for 2D Beamsteering"**, *XII Iberian Meeting on Computational Electromagnetics - EIEC2018*, Coimbra, Portugal, May 2018.

C5. J. Reis; R.F.S. Caldeirinha; A. Hammoudeh and Nigel Copner, **"Measurements and Modelling of Spatial Diversity using 2D Transmittarrays"**, *IEEE International Symposium on Personal, Indoor and Mobile Radio Communications*, Bologna, Italy, September, 2018;

C6. M. Vala; J.Reis; A. Sardo and R.F.S. Caldeirinha, **"Electronic reconfigurable beam redirecting metasurfaces for outdoor-indoor radio coverage enhancement"**, *IEEE International Symposium on Personal, Indoor and Mobile Radio Communications*, Bologna, Italy, September, 2018;

C7. M. Vala; J. Reis and R.F.S. Caldeirinha, **"A 28 GHz Fully 2D Electronic Beamsteering Transmitarray for 5G and Future RADAR Applications"**, *Proc. Loughborough Antennas and Propagation Conf. – LAPC*, Loughborough, United Kingdom, November, 2018;

C8. J. Reis; R.F.S. Caldeirinha; T.R. Fernandes; A. Hammoudeh and N. Copner, **"2D Agile Beamsteering using a Reconfigurable Transmitarray"**, *Proc. European Conf. on Antennas & Propagation - EuCAP*, Krakow, Poland, April 2019, (under review: submitted on Sept. 2018);

C9. J. Reis; M. Vala and R.F.S. Caldeirinha; **"Novel Electronically Reconfigurable Transmitarray for 2D Beamsteering: Emerging Applications"**, *Proc. European Conf. on Antennas & Propagation - EuCAP*, Krakow, Poland, April 2019, (under review: submitted on Sept. 2018).

Live demonstrators/ showcases:

D1. Exhibitor: **"Novel Antenna Beamsteering for Wireless Applications"** – *2016 Engineering Showcase* – 20 April 2016 – University of South Wales, United Kingdom;

D2. Exhibitor: **"Fully 2D Electronic Beamsteering for 5G and RADAR of the Future"** – *Techdays Aveiro 2017* – 12-14 October 2017 – Aveiro-Expo, Aveiro, Portugal, in a collaboration with EMScan and eNGN Technologies.

D3. Poster only: **"Fully 2D Electronic Beamsteering for 5G and RADAR of the Future"** – *Ciencia Viva 2018* – 2-4 July 2018 – Lisbon Congress Centre, Lisbon, Portugal;

8.4.2 Indirect contributions

The author has also contributed to other relevant research work that resulted in several international publications in connection to the work presented in this thesis.

Papers as co-author in international journals:

J1. R. Gomes; A. Hammoudeh; R.F.S. Caldeirinha, Z. Al-Daher; T.R. Fernandes and J. Reis, **"Towards 5G: Performance evaluation 60GHz UWB OFDM communications under both channel and RF impairments"**, *Physical Communication*, 2017; **Impact Factor = 1.583, Q2**.

J2. R.Gomes; J.Reis; Z. Al-Daher; A. Hammoudeh and R.F.S. Caldeirinha, **5G: Performance and Evaluation of FS-FBMC against OFDM for High Data Rate Applications at 60 GHz**, *IET Signal Processing*, 2016, DOI: 10.1049/iet-spr.2016.0671. **Impact Factor = 1.298, Q2**.

Papers as co-author in international conferences:

C1. D. Ferreira; R.F.S. Caldeirinha; I. Cuinas; T.R. Fernandes and J. Reis, **"A Square Loop Frequency Selective Surface Parametric Study for EC Model Optimisation"**, *Proc. Loughborough Antennas and Propagation Conf. – LAPC*, Loughborough, United Kingdom, Vol. 1, pp. 1 - 4, November, 2014;

8.5 Recommendations for further work

With the results obtained and presented in this thesis, possible extensions for further development may be suggested in identified lines of research. As such, proposals are grouped according to these lines: *i)* novel unit-cell designs for transmitarrays; *ii)* extension of the work to (other) 5G frequencies of interest; *iii)* the application of the eRT in hybrid beamsteering MIMO systems; *iv)* the implementation of transmitarrays for *RADAR of the future* applications, and finally, v) development of electronic reconfigurable beam redirecting metasurfaces for outdoor-indoor radio coverage enhancement. Relevant improvements on the current work and novel ideas for the usage of transmitarrays with beamsteering capability are still feasible and worthy of research:

- Study and development of novel unit-cell designs for transmitarray applications. The unit-cell design presented in this work was based on the the canonical square-slot model of frequency selective surfaces. This choice was based on the fact that the square slot is one of the most reported unit-cells in the literature, with several design guide-lines and, therefore, a good base for initial design and prove-of-concept. Although it was proved to be successfully applied to the construction of transmitarrays for 2D beamsteering, its limitations are evident, namely regarding to narrow bandwidth. It would be worth to study and develop novel unit-cell designs that may overcome this issue, for example by exploring other FSS shapes, such as the hexagonal FSS that tend to be more broadband. With this suggestion, it could also be explored the possibility of providing to the unit-cell, the capability of controlling the polarisation of the radiating wave so it can be, *e.g.* swappable, in real-time, between RHCP and LHCP, or at least raise the constraint of the transmitarray being only operable for vertical polarisation. Nonetheless, based on the experience obtained from this research, the unit-cell to be developed must be designed to support a bias layout to feed and control whatever element is selected for phase variation: varactors diodes, PIN diodes or others, if the development of an electronic model of a transmitarray is the priority.

- In the early stage of this Ph.D., 5G was just a concept for a novel generation for wireless communications. The original ideas behind 5G have evolved and in the past year, novel directions for what 5G would be about started to become evident. To date, 5G systems are being aimed to operate at 27 GHz, instead of the sub-6 GHz band as originally thought. Due to this fact, it would be of interest to adapt and develop the concept for 2D beamsteering using transmitarrays, to the frequency of operations finally targeted for 5G communication. With this being said, novel transmitarray structures to operate at 27 GHz have a huge demand.

  In fact, some time has already been dedicated to this topic, and preliminary research on a unit-cell to operate at those frequencies have already been undertaken. In Fig. 8.1a and Fig. 8.1b are report some of the results on a square-slot transmitarray element, obtained following the premisses left by this Ph.D work. This new structure works similar to the previous one, that is using off-the-shelf varactor diodes to control the phase in each unit stacked cell. However, in order to achieve full control over the relative transmission phase using 5 layers, lower capacitance values were used, as shown in Fig. 8.1a, between 0.3 and 2.8 pF, as opposed to the ones used for the structure at 5.2 GHz (between 0.7 and 2.8 pF). The distance between layers was set 1.5 mm. Those results indicate that beamsteering would be practicable with a transmitarray implemented based on such element, however some concerns have been raised due to the small dimensions on the unit-cell for such frequencies (Table 8.1). The implementation of transmitarray at higher

frequencies (>30 GHz) may become impracticable using standard PCB techniques (integrated technology such as CMOS may be a possibility) and impracticable to load discrete surface mount devices, since the increase of the operating frequency makes the overall size of the unit-cell to decrease in proportion.

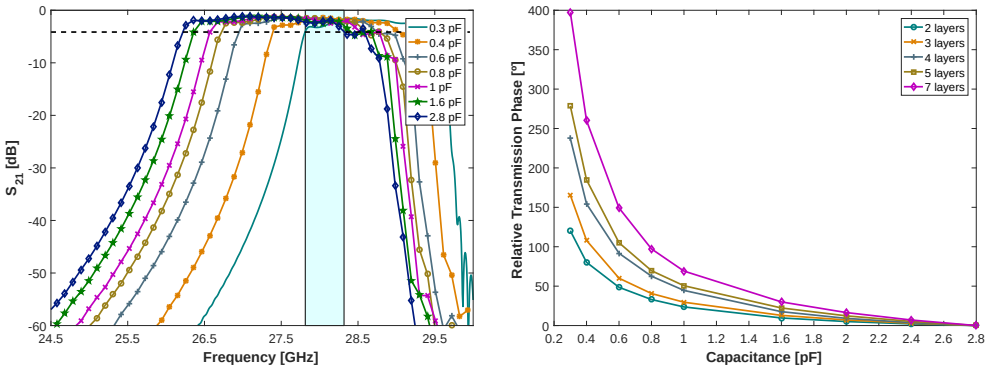

(a) (b)

FIGURE 8.1: Preliminary simulation results on a transmitarray element for 27 GHz 5G antenna applications: (a) array element S_{21} response and, (b) relative transmission phase.

TABLE 8.1
UNIT-CELL DIMENSIONS AND SUBSTRATE CHARACTERISTICS OF A 27 GHZ TRANSMITARRAY ELEMENT.

Unit cell dimensions (mm)					Nelco NX9250 substrate		
p	l	d	g	w	thickness	ε_r	tanδ
5.75	5.55	4.06	0.34	0.41	0.635 mm	2.5	0.0017

- A new vision on novel and hybrid transmission schemes, namely by delving into the properties of the eRT, have already been introduced in author' publication [C3.] and [C5.], mentioned in Section 8.4. The initial concept have been tested for a spatial diversity scenario where the burden of the RF front-end was reduced with savings that scale to 1 : (4 × N) front-ends. However, this idea may also be explored to other transmission schemes:

  – Single User (SU)-MIMO with beamsteering: To activate MIMO, two eRTs aggregated to two distinct RF chains must be considered as illustrated in Fig. 8.2a. Although a single RF chain is used per radiation element, an overall reduction of at least 1:4 in hardware is experienced and beamsteering with *Azimuth-over-*

Elevation is still possible. This clearly shows the advantage of the proposed scheme in comparison with the equivalent planar case able to produce beamsteering with two components. Moreover, if neglecting the tracking of a single use, *i.e.* discarding the beamsteering, MU-MIMO in TDMA can be achieved. Two users can be covered, by two antennas (MIMO) at two subsequent instants of time.

– Multi-user (MU)-MIMO with beamsteering: As it has been noticed, due to the beamsteering properties of the eRT, the number of MIMO combinations increase with the number or eRT devices. When three or more eRT antennas with 2D-beamsteering capability fed individually by an RF-chain, there are a considerable amount of beam combinations that can cover a certain user, at a certain instant of time. For example in Fig. 8.2b, several users under the same network cell, are able to be individually addressed and a direct connection between user and base station are possible, consequently enabling MU-MIMO.

Nonetheless, this novel topologies must always be accompanied with a MIMO encoder/decoder or with a specific SDR transceiver for MIMO that implement all the necessary algorithms for channel estimation, and direction of arrival, while at the same time will be controlling the eRT to perform autonomous beamsteering.

- The implementation of transmitarrays for *RADAR of the future*: RADAR technology has been implemented for years in many different areas and applications like automotive, military, surveillance, stealth, sensors for detection, automation control, medical applications, among others [162, 163]. Although widely implemented, somehow the RF system design for RADAR has not changed accordingly with the advanced state-of-the-art of other areas. The concept of *RADAR of the future* aims to evolve the RADAR to a new other level, *e.g.* by integrating new concepts such as: intelligent signal coding, MIMO RADAR, digital beamforming and array imaging.

  To this extent, it could be explored the application of the developed eRT on future RADAR systems. The concept to be explored is depicted in Fig. 8.3. Much like on the past topic about hybrid transmission schemes, the eRT could be used and associated to an SDR system, to enable digital processing RADAR schemes (as in [164]) with automated beamsteering. Besides the fact that eRT helps to reduce the RF burden of a wireless system, its small, compact and lightweight form factor is a plus for the mentioned applications.

- Electronic reconfigurable beam redirecting metasurfaces for outdoor-indoor radio coverage enhancement. Due to the capability of controlling the direction of an wavefront, and thus proceeding with far-field beam re-direction, electronic transmitarrays may be applied on the concept of a smart wall. This idea may find applicability in mobile radio, particularly, for outdoor-indoor radio coverage

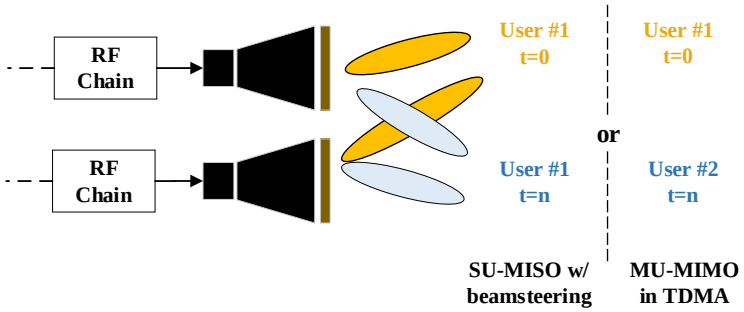

(a)

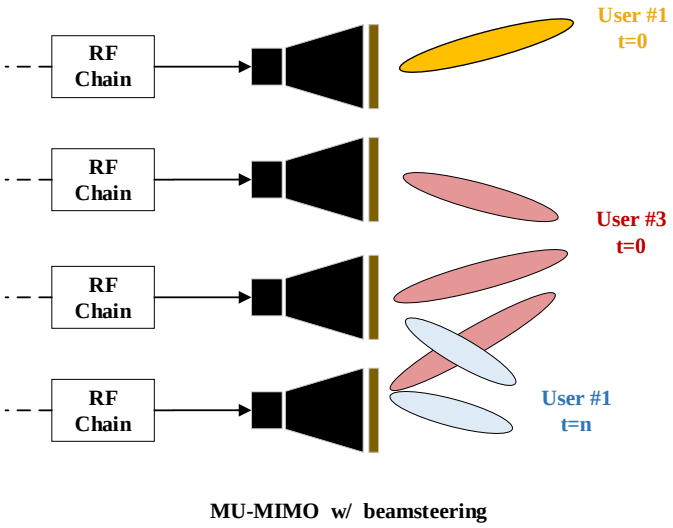

(b)

FIGURE 8.2: Novel hybrid transmission schemes to explore with the usage of eRT: (a) SU-MIMO with beamsteering or MU-MIMO in TDMA and (b) MU-MIMO with beamsteering.

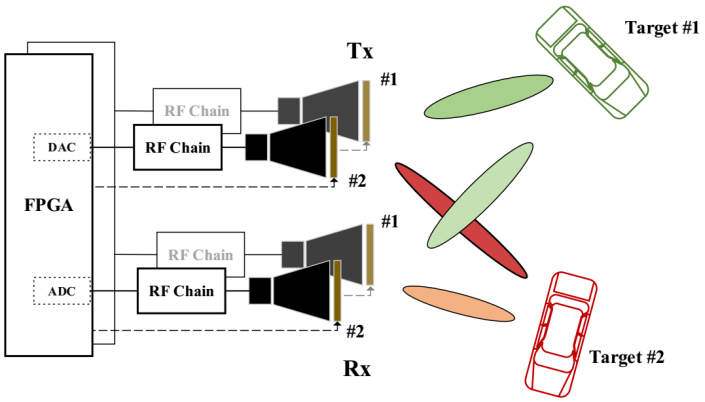

FIGURE 8.3: eRT envisaged for *RADAR of the future* applications.

enhancement by re-directing radio signals coming from the exterior, *e.g.* LTE signal, to a mobile used inside a building.

In fact, initial measurement trials in the anechoic chamber were already undertaken to study the feasibility of using eRT in such application scenarios. A specific test fixture to hold the eRT through an open window was initially characterised to serve as reference for further comparison with and without the eRT on it. A metal plate has also been measured to make sure that the obtained measured results are not in anyway contaminated with unwanted reflections or diffractions around the wedges of the test fixture. Measurement results are presented in Fig. 8.4a, where the effect of the structure is visible at around 5.2 GHz. For each setup, the turntable of the receiver antenna is rotated from $-60°$ to $60°$ at 5.2 GHz, in order to obtain the radiation pattern of the test fixture, the metallic plate and the FSS (*i.e.* the eRT). In Fig. 8.4b one may can observe that the received signal is only emanated from the structure. By controlling the smart wall with a computer, it is possible to redirect the main beam of the incoming wave to any direction in both planes beyond the wall. As shown in Fig. 8.4c, the main lobe of the incoming wave was successfully shifted from $0°$ to $5°$, $10°$, $20°$ and $30°$.

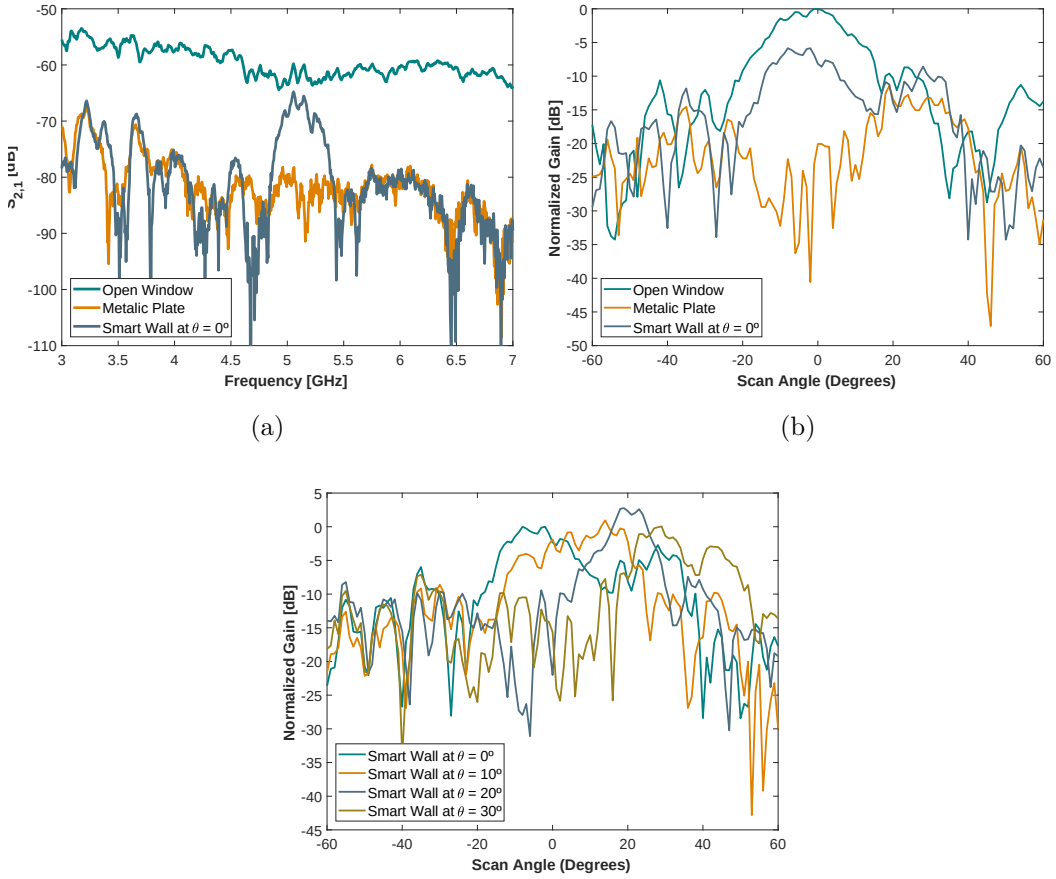

(a) (b)

(c)

FIGURE 8.4: (a) Measured radiation power for each setup from 3 to 7 GHz, (b) measured radiation pattern for each setup from $-60°$ to $60°$ at 5.2 GHz and, (c) measured radiation pattern for a Smart Wall tuned to $0°$, $10°$, $20°$ and $30°$

References

[1] C. A. Balanis, *Antenna Theory: Analysis and Design, 3rd Edition.* John Wiley & Sons, 2005, vol. 72.

[2] L. Brennan, "Angular Accuracy of a Phased Array Radar," *IRE Transactions on Antennas and Propagation*, vol. 9, no. 3, pp. 268–275, May 1961.

[3] K. Molz, "The AN/FPS-85 Satellite Tracking Phased Array Radar," *IEEE Transactions on Aerospace*, vol. 2, no. 2, pp. 135–138, April 1964.

[4] W. Von Aulock, "Properties of Phased Arrays," *Proceedings of the IRE*, vol. 48, no. 10, pp. 1715–1727, Oct 1960.

[5] R. J. Mailloux, *Phased Array Antenna Handbook.* Artech House, Incorporated, 2005.

[6] A. Bhattacharyya, *Phased Array Antennas: Floquet Analysis, Synthesis, Bfns and Active Array Systems*, ser. Wiley Series in Microwave and Optical Engineering. Wiley, 2006.

[7] J. G. Andrews, S. Buzzi, W. Choi, S. V. Hanly, A. Lozano, A. C. K. Soong, and J. C. Zhang, "What will 5G be?" *IEEE Journal on Selected Areas in Communications*, vol. 32, no. 6, pp. 1065–1082, June 2014.

[8] E. Dahlman, S. Parkvall, D. Astély, and H. Tullberg, "Advanced Antenna Solutions for 5G Wireless Access," in *2014 48th Asilomar Conference on Signals, Systems and Computers*, Nov 2014, pp. 810–814.

[9] S. Bronckers, A. Roc'h, and B. Smolders, "Wireless Receiver Architectures Towards 5G: Where Are We?" *IEEE Circuits and Systems Magazine*, vol. 17, no. 3, pp. 6–16, thirdquarter 2017.

[10] G. A. Akpakwu, B. J. Silva, G. P. Hancke, and A. M. Abu-Mahfouz, "A Survey on 5G Networks for the Internet of Things: Communication Technologies and Challenges," *IEEE Access*, vol. 6, pp. 3619–3647, 2018.

[11] F. Capolino, *Applications of Metamaterials.* CRC Press, 2009.

[12] Y. Dong and T. Itoh, "Metamaterial-Based Antennas," *Proceedings of the IEEE*, vol. 100, no. 7, pp. 2271–2285, July 2012.

[13] B. A. Munk, *Frequency Selective Surfaces: Theory and Design.* John Wiley & Sons, 2005.

[14] J. Vardaxoglou, *Frequency Selective Surfaces: Analysis and Design.* Research Studies Press, 1997.

[15] IEEE, "IEEE Standard Test Procedures for Antennas," *ANSI/IEEE Std 149-1979*, p. 01, 1979.

[16] [Online]. Available: https://www.ifixit.com/Guide/iPhone+6+Plus++5GHz+Wi-Fi+Antenna+Replacement/29806

[17] [Online]. Available: https://theaerialman.co.uk/satellite-dish-installers-bristol/satellite-dish-installers-bristol/

[18] C. A. Balanis, *Modern Antenna Handbook*. New York, NY, USA: Wiley-Interscience, 2008.

[19] S. J. Orfanidis, *Electromagnetic Waves and Antennas*, R. University, Ed., 2014.

[20] S. Jahani, J. Rashed-Mohassel, and M. Shahabadi, "Miniaturization of Circular Patch Antennas Using MNG Metamaterials," *IEEE Antennas and Wireless Propagation Letters*, vol. 9, pp. 1194–1196, 2010.

[21] M. Li, K. M. Luk, L. Ge, and K. Zhang, "Miniaturization of Magnetoelectric Dipole Antenna by Using Metamaterial Loading," *IEEE Transactions on Antennas and Propagation*, vol. 64, no. 11, pp. 4914–4918, Nov 2016.

[22] F. Farzami, K. Forooraghi, and M. Norooziarab, "Miniaturization of a Microstrip Antenna Using a Compact and Thin Magneto-Dielectric Substrate," *IEEE Antennas and Wireless Propagation Letters*, vol. 10, pp. 1540–1542, 2011.

[23] K. Han, M. Swaminathan, R. Pulugurtha, H. Sharma, R. Tummala, S. Yang, and V. Nair, "Magneto-Dielectric Nanocomposite for Antenna Miniaturization and SAR Reduction," *IEEE Antennas and Wireless Propagation Letters*, vol. 15, pp. 72–75, 2016.

[24] S. M. Haque and K. M. Parvez, "Slot Antenna Miniaturization Using Slit, Strip, and Loop Loading Techniques," *IEEE Transactions on Antennas and Propagation*, vol. 65, no. 5, pp. 2215–2221, May 2017.

[25] M. Sano, K. Yamada, and M. Higaki, "Design of an Electrically Small Antenna Using a Broadside-coupled Split Ring Resonator," in *2017 IEEE International Symposium on Antennas and Propagation USNC/URSI National Radio Science Meeting*, July 2017, pp. 537–538.

[26] S. X. Ta and T. K. Nguyen, "Ar Bandwidth and Gain Enhancements of Patch Antenna Using Single Dielectric Superstrate," *Electronics Letters*, vol. 53, no. 15, pp. 1015–1017, 2017.

[27] Q. L. Li, S. W. Cheung, D. Wu, and T. I. Yuk, "Microwave Lens Using Periodic Dielectric Sheets for Antenna-Gain Enhancement," *IEEE Transactions on Antennas and Propagation*, vol. 65, no. 4, pp. 2068–2073, April 2017.

[28] S. J. Franson and R. W. Ziolkowski, "Gigabit per Second Data Transfer in High-Gain Metamaterial Structures at 60 GHz," *IEEE Transactions on Antennas and Propagation*, vol. 57, no. 10, pp. 2913–2925, Oct 2009.

[29] M. A. Amiri, C. A. Balanis, and C. R. Birtcher, "Gain and Bandwidth Enhancement of a Spiral Antenna Using a Circularly Symmetric HIS," *IEEE Antennas and Wireless Propagation Letters*, vol. 16, pp. 1080–1083, 2017.

[30] W. E. McKinzie, D. M. Nair, B. A. Thrasher, M. A. Smith, E. D. Hughes, and J. M. Parisi, "60-GHz 2x2 LTCC Patch Antenna Array With an Integrated EBG Structure for Gain Enhancement," *IEEE Antennas and Wireless Propagation Letters*, vol. 15, pp. 1522–1525, 2016.

[31] A. Mellita, D. S. Chandu, and S. S. Karthikeyan, "Gain Enhancement of a Microstrip Patch Antenna Using a Novel Frequency Selective Surface," in *2017 Twenty-third National Conference on Communications (NCC)*, March 2017, pp. 1–4.

[32] B. Wu, W. Wang, J. Pacheco, X. Chen, T. Grzegorczyk, and J. A. Kong, "A Study of Using Metamaterials As Antenna Substrate to Enhance Gain," *Electromagnetic Research*, pp. 295–328, 2005.

[33] A. Dadgarpour, A. A. Kishk, and T. A. Denidni, "Gain Enhancement of Planar Antenna Enabled by Array of Split-Ring Resonators," *IEEE Transactions on Antennas and Propagation*, vol. 64, no. 8, pp. 3682–3687, Aug 2016.

[34] C. G. Christodoulou, Y. Tawk, S. A. Lane, and S. R. Erwin, "Reconfigurable Antennas for Wireless and Space Applications," *Proceedings of the IEEE*, vol. 100, no. 7, pp. 2250–2261, July 2012.

[35] Y. J. Sung, "Frequency and Polarisation Reconfigurability from an Open-loop Square Ring Antenna," *IET Microwaves, Antennas Propagation*, vol. 6, no. 5, pp. 505–509, April 2012.

[36] A. Tariq and H. Ghafouri-Shiraz, "Frequency-Reconfigurable Monopole Antennas," *IEEE Transactions on Antennas and Propagation*, vol. 60, no. 1, pp. 44–50, Jan 2012.

[37] S. Zhu, D. G. Holtby, K. L. Ford, A. Tennant, and R. J. Langley, "Compact Low Frequency Varactor Loaded Tunable SRR Antenna," *IEEE Transactions on Antennas and Propagation*, vol. 61, no. 4, pp. 2301–2304, April 2013.

[38] R. Jakoby, P. Scheele, S. Muller, and C. Weil, "Nonlinear Dielectrics for Tunable Microwave Components," in *15th International Conference on Microwaves, Radar and Wireless Communications (IEEE Cat. No.04EX824)*, vol. 2, May 2004, pp. 369–378 Vol.2.

[39] N. C. Papanicolaou, M. A. Christou, and A. C. Polycarpou, "Frequency-agile Microstrip Patch Antenna on a Biased Liquid Crystal Substrate," *Electronics Letters*, vol. 51, no. 3, pp. 202–204, 2015.

[40] F. A. Ghaffar, J. R. Bray, and A. Shamim, "Theory and Design of a Tunable Antenna on a Partially Magnetized Ferrite LTCC Substrate," *IEEE Transactions on Antennas and Propagation*, vol. 62, no. 3, pp. 1238–1245, March 2014.

[41] T. J. Jung, I. J. Hyeon, C. W. Baek, and S. Lim, "Circular/Linear Polarization Reconfigurable Antenna on Simplified RF-MEMS Packaging Platform in K-Band," *IEEE Transactions on Antennas and Propagation*, vol. 60, no. 11, pp. 5039–5045, Nov 2012.

[42] W. Yang, W. Che, H. Jin, W. Feng, and Q. Xue, "A Polarization-Reconfigurable Dipole Antenna Using Polarization Rotation AMC Structure," *IEEE Transactions on Antennas and Propagation*, vol. 63, no. 12, pp. 5305–5315, Dec 2015.

[43] B. Liang, B. Sanz-Izquierdo, E. A. Parker, and J. C. Batchelor, "A Frequency and Polarization Reconfigurable Circularly Polarized Antenna Using Active EBG Structure for Satellite Navigation," *IEEE Transactions on Antennas and Propagation*, vol. 63, no. 1, pp. 33–40, Jan 2015.

[44] S. W. Lee and Y. J. Sung, "Simple Polarization-Reconfigurable Antenna With T-Shaped Feed," *IEEE Antennas and Wireless Propagation Letters*, vol. 15, pp. 114–117, 2016.

[45] Z. C. Hao, K. K. Fan, and H. Wang, "A Planar Polarization-Reconfigurable Antenna," *IEEE Transactions on Antennas and Propagation*, vol. 65, no. 4, pp. 1624–1632, April 2017.

[46] H. L. Zhu, S. W. Cheung, X. H. Liu, and T. I. Yuk, "Design of Polarization Reconfigurable Antenna Using Metasurface," *IEEE Transactions on Antennas and Propagation*, vol. 62, no. 6, pp. 2891–2898, June 2014.

[47] K. Kandasamy, B. Majumder, J. Mukherjee, and K. P. Ray, "Low-RCS and Polarization-Reconfigurable Antenna Using Cross-Slot-Based Metasurface," *IEEE Antennas and Wireless Propagation Letters*, vol. 14, pp. 1638–1641, 2015.

[48] T. Veijalainen, "Beam Steering in Millimeter Wave Radio Links for Small Cell Mobile Backhaul," 2014. [Online]. Available: https://aaltodoc.aalto.fi/bitstream/handle/123456789/13566/master_Veijalainen_Teemu_2014.pdf

[49] Z. W. Kao-Cheng Huang, *Millimeter Wave Communication Systems.* Wiley-IEEE Press, 2011.

[50] D. Pozar, *Microwave Engineering.* Wiley, 2012.

[51] A. Chakraborty and B. Gupta, "Paradigm Phase Shift: RF MEMS Phase Shifters: An Overview," *IEEE Microwave Magazine*, vol. 18, no. 1, pp. 22–41, Jan 2017.

[52] Wikiwand. (2017) PAVE PAWS. [Online]. Available: http://www.wikiwand.com/en/PAVE_PAWS

[53] B. H. Ku, P. Schmalenberg, O. Inac, O. D. Gurbuz, J. S. Lee, K. Shiozaki, and G. M. Rebeiz, "A 77-81GHz 16-Element Phased-Array Receiver With 50deg Beam Scanning for Advanced Automotive Radars," *IEEE Transactions on Microwave Theory and Techniques*, vol. 62, no. 11, pp. 2823–2832, Nov 2014.

[54] Wikiwand. (2017) Phased array. [Online]. Available: http://www.wikiwand.com/en/Phased_array#

[55] P. Cabrol and P. Pietraski, "60 GHz Patch Antenna Array on Low Cost Liquid-crystal Polymer (LCP) Substrate," in *IEEE Long Island Systems, Applications and Technology (LISAT) Conference 2014*, May 2014, pp. 1–6.

[56] P. F. Li, S. W. Qu, S. Yang, and Z. P. Nie, "Microstrip Array Antenna With 2-D Steerable Focus in Near-Field Region," *IEEE Transactions on Antennas and Propagation*, vol. 65, no. 9, pp. 4607–4617, Sept 2017.

[57] CST – Computer Simulation Tecnology. Microstrip Patch Array Design. [Online]. Available: https://www.cst.com/solutions/article/microstrip-patch-array-design

[58] A. Artemenko, A. Mozharovskiy, A. Maltsev, R. Maslennikov, A. Sevastyanov, and V. Ssorin, "Experimental Characterization of E-Band Two-Dimensional Electronically Beam-Steerable Integrated Lens Antennas," *IEEE Antennas and Wireless Propagation Letters*, vol. 12, pp. 1188–1191, 2013.

[59] H. Wang, Z. Zhang, Y. Li, and M. F. Iskander, "A Switched Beam Antenna With Shaped Radiation Pattern and Interleaving Array Architecture," *IEEE Transactions on Antennas and Propagation*, vol. 63, no. 7, pp. 2914–2921, July 2015.

[60] M. S. Sharawi, S. Deif, and A. Shamim, "An Electronically Controlled 8-Element Switched Beam Planar Array," *IEEE Antennas and Wireless Propagation Letters*, vol. 14, pp. 1350–1353, 2015.

[61] I. Slomian, K. Wincza, and S. Gruszczynski, "Circularly Polarized Switched-Beam Antenna Arrays With Reduced Sidelobe Level," *IEEE Antennas and Wireless Propagation Letters*, vol. 15, pp. 1213–1216, 2016.

[62] S. Cheng, P. Rantakari, R. Malmqvist, C. Samuelsson, T. Vaha-Heikkila, A. Rydberg, and J. Varis, "Switched Beam Antenna Based on RF MEMS SPDT Switch on Quartz Substrate," *IEEE Antennas and Wireless Propagation Letters*, vol. 8, pp. 383–386, 2009.

[63] Z. Li, E. Ahmed, A. M. Eltawil, and B. A. Cetiner, "A Beam-Steering Reconfigurable Antenna for WLAN Applications," *IEEE Transactions on Antennas and Propagation*, vol. 63, no. 1, pp. 24–32, Jan 2015.

[64] M. S. Alam and A. M. Abbosh, "Beam-Steerable Planar Antenna Using Circular Disc and Four PIN-Controlled Tapered Stubs for WiMAX and WLAN Applications," *IEEE Antennas and Wireless Propagation Letters*, vol. 15, pp. 980–983, 2016.

[65] P. Lotfi, S. Soltani, and R. D. Murch, "Printed Endfire Beam-Steerable Pixel Antenna," *IEEE Transactions on Antennas and Propagation*, vol. 65, no. 8, pp. 3913–3923, Aug 2017.

[66] J. Butler, "Beam-forming Matrix Simplifies Design of Electronically Scanned Antennas," *Electronic Design*, vol. 9, no. 8, pp. 170–173, 1961.

[67] T. A. Denidni and T. E. Libar, "Wide Band Four-port Butler Matrix for Switched Multibeam Antenna Arrays," in *14th IEEE Proceedings on Personal, Indoor and Mobile Radio Communications, 2003. PIMRC 2003.*, vol. 3, Sept 2003, pp. 2461–2464 vol.3.

[68] C. H. Tseng, C. J. Chen, and T. H. Chu, "A Low-Cost 60-GHz Switched-Beam Patch Antenna Array With Butler Matrix Network," *IEEE Antennas and Wireless Propagation Letters*, vol. 7, pp. 432–435, 2008.

[69] W. Rotman and R. Turner, "Wide-angle Microwave Lens for Line Source Applications," *IEEE Transactions on Antennas and Propagation*, vol. 11, no. 6, pp. 623–632, November 1963.

[70] O. Kilic and S. J. Weiss, "Rotman Lens Applications for the US Army: A Review of History, Present, and Future," *URSI Radio Science Bulletin*, vol. 2010, no. 332, pp. 10–23, June 2010.

[71] S. K. Garakoui, E. A. M. Klumperink, B. Nauta, and F. E. van Vliet, "Phased-array Antenna Beam Squinting Related to Frequency Dependency of Delay Circuits," in *2011 8th European Radar Conference*, Oct 2011, pp. 416–419.

[72] M. Longbrake, "True Time-delay Beamsteering for Radar," in *2012 IEEE National Aerospace and Electronics Conference (NAECON)*, July 2012, pp. 246–249.

[73] S. Akiba, M. Oishi, Y. Nishikawa, J. Hirokawa, and M. Ando, "Photonic Approach to Beam Steering of Phased Array Antenna," in *2013 International Symposium on Electromagnetic Theory*, May 2013, pp. 448–451.

[74] T. P. McKenna, J. A. Nanzer, and T. R. Clark, "Photonic Beamsteering of a Millimeter-Wave Array With 10-Gb/s Data Transmission," *IEEE Photonics Technology Letters*, vol. 26, no. 14, pp. 1407–1410, July 2014.

[75] X. Ye, F. Zhang, and S. Pan, "Optical True Time Delay Unit for Multi-beamforming," *Opt. Express*, vol. 23, no. 8, pp. 10 002–10 008, Apr 2015. [Online]. Available: http://www.opticsexpress.org/abstract.cfm?URI=oe-23-8-10002

[76] X. Ye, D. Zhu, Y. Zhang, S. Li, and S. Pan, "Analysis of Photonics-Based RF Beamforming With Large Instantaneous Bandwidth," *Journal of Lightwave Technology*, vol. 35, no. 23, pp. 5010–5019, Dec 2017.

[77] C. A. Balanis and P. L. Loannides, *Introduction to Smart Antennas.* Morgan and Claypool Publishers LLC, jan 2007, vol. 2, no. 1.

[78] A. K. Agrawal and E. L. Holzman, "Beamformer Architectures for Active Phased-array Radar Antennas," *IEEE Transactions on Antennas and Propagation*, vol. 47, no. 3, pp. 432–442, Mar 1999.

[79] D. Rodrigo, L. Jofre, and B. Cetiner, "Circular Beam-Steering Reconfigurable Antenna With Liquid Metal Parasitics," *IEEE Transactions on Antennas and Propagation*, vol. 60, no. 4, pp. 1796–1802, April 2012.

[80] A. A. Gheethan, A. Dey, and G. Mumcu, "Passive Feed Network Designs for Microfluidic Beam-Scanning Focal Plane Arrays and Their Performance Evaluation," *IEEE Transactions on Antennas and Propagation*, vol. 63, no. 8, pp. 3452–3464, Aug 2015.

[81] E. Erdil, K. Topalli, N. Esmaeilzad, O. Zorlu, H. Kulah, and O. Civi, "A Reconfigurable Nested Ring-split Ring Transmitarray Unit Cell by Microfluidic Technology," in *2014 8th European Conference on Antennas and Propagation (EuCAP)*, April 2014, pp. 124–127.

[82] E. Erdil, K. Topalli, N. Esmaeilzad, O. Zorlu, H. Kulah, and O. Aydin Civi, "Reconfigurable Nested Ring-Split Ring Transmitarray Unit Cell Employing the Element Rotation Method by Microfluidics," *IEEE Transactions on Antennas and Propagation*, vol. 63, no. 3, pp. 1163–1167, March 2015.

[83] J. Y. Lau, "Reconfigurable Transmitarray Antennas," Ph.D. dissertation, University of Toronto, 2012. [Online]. Available: https://tspace.library.utoronto.ca/bitstream/1807/32802/3/Lau_Jonathan_Y_201206_PhD_thesis.pdf

[84] L. D. Palma, "Reconfigurable Transmitarray Antennas at Millimeter-Wave Frequencies," Ph.D., 2015. [Online]. Available: https://tel.archives-ouvertes.fr/tel-01308275/file/DI_PALMA_Luca.pdf

[85] J. Shaker, M. R. Chaharmir, and J. Ethier, *Reflectarray Antennas: Analysis, Design, Fabrication, and Measurement.* Artech House, 2013, vol. 1.

[86] J. Huang and J. A. Encinar, *Reflectarray Antennas.* John Wiley & Sons, 2007, vol. 9.

[87] S. Hum and J. Perruisseau-Carrier, "Reconfigurable Reflectarrays and Array Lenses for Dynamic Antenna Beam Control: A Review," *IEEE Transactions on Antennas and Propagation*, vol. 62, no. 1, pp. 183–198, Jan 2014.

[88] C. Balanis, *Advanced Engineering Electromagnetics*, ser. CourseSmart Series. Wiley, 2012.

[89] R. A. Shelby, D. R. Smith, and S. Schultz, "Experimental Verification of a Negative Index of Refraction," *Science*, vol. 292, no. 5514, pp. 77–79, 2001.

[90] D. Ferreira, R. Caldeirinha, I. Cuiñas, and T. Fernandes, "Square Loop and Slot Frequency Selective Surfaces Study for Equivalent Circuit Model Optimization," *IEEE Transactions on Antennas and Propagation*, vol. 63, no. 9, pp. 3947–3955, Sept 2015.

[91] D. Sievenpiper, J. Schaffner, R. Loo, G. Tangonan, S. Ontiveros, and R. Harold, "A Tunable Impedance Surface Performing as a Reconfigurable Beam Steering Reflector," *IEEE Transactions on Antennas and Propagation*, vol. 50, no. 3, pp. 384–390, Mar 2002.

[92] D. Sievenpiper and J. Schaffner, "Beam Steering Microwave Reflector Based on Electrically Tunable Impedance Surface," *Electronics Letters*, vol. 38, no. 21, pp. 1237–1238, Oct 2002.

[93] E. Carrasco, M. Barba, and J. Encinar, "X-Band Reflectarray Antenna With Switching-Beam Using PIN Diodes and Gathered Elements," *IEEE Transactions on Antennas and Propagation*, vol. 60, no. 12, pp. 5700–5708, Dec 2012.

[94] E. Carrasco, M. Barba, B. Reig, C. Dieppedale, and J. Encinar, "Characterization of a Reflectarray Gathered Element With Electronic Control Using Ohmic RF MEMS and Patches Aperture-Coupled to a Delay Line," *IEEE Transactions on Antennas and Propagation*, vol. 60, no. 9, pp. 4190–4201, Sept 2012.

[95] D. M. Pozar, S. D. Targonski, and H. Syrigos, "Design of Millimeter Wave Microstrip Reflectarrays," *IEEE Transactions on Antennas and Propagation*, vol. 45, no. 2, pp. 287–296, Feb 1997.

[96] B. Mencagli, G. RV, L. Marcaccioli, and R. Sorrentino, "Design of Large mm-Wave Beam-scanning Reflectarrays," in *The European Conference on Wireless Technology, 2005*, Oct 2005, pp. 475–478.

[97] B. Ma, L. Yan, M. Xia, C. Wang, and L. Cui, "Design of Reflectarray Antenna Using Double Square Ring Elements," in *2011 IEEE International Conference on Microwave Technology Computational Electromagnetics (ICMTCE)*, May 2011, pp. 213–216.

[98] D. McGrath, "Planar Three-Dimensional Constrained Lenses," *IEEE Transactions on Antennas and Propagation*, vol. 34, no. 1, pp. 46–50, Jan 1986.

[99] H. Kaouach, L. Dussopt, J. Lanteri, T. Koleck, and R. Sauleau, "Circularly-polarized Discrete Lens Antennas in the 60-GHz Band," in *2010 Conference Proceedings ICECom*, Sept 2010, pp. 1–4.

[100] L. Dussopt, H. Kaouach, J. Lanteri, and R. Sauleau, "Circularly-polarized Discrete Lens Antennas in the 60-GHz Band," in *Radio Engineering*, vol. 20, Dec 2011, pp. 733–738.

[101] L. D. Palma, A. Clemente, L. Dussopt, R. Sauleau, P. Potier, and P. Pouliguen, "Circularly Polarized Transmitarray With Sequential Rotation in Ka-Band," *IEEE Transactions on Antennas and Propagation*, vol. 63, no. 11, pp. 5118–5124, Nov 2015.

[102] C. Pfeiffer and A. Grbic, "Millimeter-Wave Transmitarrays for Wavefront and Polarization Control," *IEEE Transactions on Microwave Theory and Techniques*, vol. 61, no. 12, pp. 4407–4417, Dec 2013.

[103] X. Zhong, L. Chen, Y. Shi, and X. Shi, "Design of Multiple-Polarization Transmitarray Antenna Using Rectangle Ring Slot Elements," *IEEE Antennas and Wireless Propagation Letters*, vol. 15, pp. 1803–1806, 2016.

[104] C. Huang, W. Pan, X. Ma, and X. Luo, "1-Bit Reconfigurable Circularly Polarized Transmitarray in X-Band," *IEEE Antennas and Wireless Propagation Letters*, vol. 15, pp. 448–451, 2016.

[105] C. Huang, W. Pan, and X. Luo, "Low-Loss Circularly Polarized Transmitarray for Beam Steering Application," *IEEE Transactions on Antennas and Propagation*, vol. 64, no. 10, pp. 4471–4476, Oct 2016.

[106] L. D. Palma, A. Clemente, L. Dussopt, R. Sauleau, P. Potier, and P. Pouliguen, "Circularly-Polarized Reconfigurable Transmitarray in Ka-Band With Beam Scanning and Polarization Switching Capabilities," *IEEE Transactions on Antennas and Propagation*, vol. 65, no. 2, pp. 529–540, Feb 2017.

[107] P. Padilla, A. Munoz-Acevedo, M. Sierra-Castaner, and M. Sierra-Perez, "Electronically Reconfigurable Transmitarray at Ku Band for Microwave Applications," *IEEE Transactions on Antennas and Propagation*, vol. 58, no. 8, pp. 2571–2579, Aug 2010.

[108] J. Y. Lau and S. V. Hum, "Analysis and Characterization of a Multipole Reconfigurable Transmitarray Element," *IEEE Transactions on Antennas and Propagation*, vol. 59, no. 1, pp. 70–79, Jan 2011.

[109] J. Lau and S. Hum, "A Planar Reconfigurable Aperture With Lens and Reflectarray Modes of Operation," *IEEE Transactions on Microwave Theory and Techniques*, vol. 58, no. 12, pp. 3547–3555, Dec 2010.

[110] ——, "A Wideband Reconfigurable Transmitarray Element," *IEEE Transactions on Antennas and Propagation*, vol. 60, no. 3, pp. 1303–1311, March 2012.

[111] ——, "Reconfigurable Transmitarray Design Approaches for Beamforming Applications," *IEEE Transactions on Antennas and Propagation*, vol. 60, no. 12, pp. 5679–5689, Dec 2012.

[112] A. Clemente, L. Dussopt, R. Sauleau, P. Potier, and P. Pouliguen, "1-bit Reconfigurable Unit Cell Based on PIN Diodes for Transmit-array Applications in X-band," *IEEE Transactions on Antennas and Propagation*, vol. 60, no. 5, pp. 2260–2269, May 2012.

[113] ——, "Wideband 400-Element Electronically Reconfigurable Transmitarray in X Band," *IEEE Transactions on Antennas and Propagation*, vol. 61, no. 10, pp. 5017–5027, Oct 2013.

[114] A. Clemente, L. Dussopt, B. Reig, R. Sauleau, P. Potier, and P. Pouliguen, "Reconfigurable Unit-cells for Beam-scanning Transmitarrays in X Band," in *2013 7th European Conference on Antennas and Propagation (EuCAP)*, April 2013, pp. 1783–1787.

[115] Y. Sun, Z. Li, W. Zhu, Z. Ji, and Q. Wang, "New Steerable Antenna with Controllable Metamaterial," in *EuMC 2012 European Microwave Conference*, Oct 2012, pp. 936–939.

[116] T. Jiang, Z. Wang, D. Li, J. Pan, B. Zhang, J. Huangfu, Y. Salamin, C. Li, and L. Ran, "Low-DC Voltage-Controlled Steering-Antenna Radome Utilizing Tunable Active Metamaterial," *IEEE Transactions on Microwave Theory and Techniques*, vol. 60, no. 1, pp. 170–178, Jan. 2012.

[117] N. Marcuvitz, *Waveguide Handbook*. Stevenage, U.K.: Peregrinus,, 1986.

[118] K. Sarabandi and N. Behdad, "A Frequency Selective Surface With Miniaturized Elements," *IEEE Transactions on Antennas and Propagation*, vol. 55, no. 5, pp. 1239–1245, May 2007.

[119] A. Edalati and T. Denidni, "Beam-switching Antenna Based on Active Frequency Selective Surfaces," in *2011 IEEE International Symposium on Antennas and Propagation (APSURSI)*, July 2011, pp. 2254–2257.

[120] H. Zhou, S. Qu, B. Lin, J. Wang, H. Ma, Z. Xu, W. Peng, and P. Bai, "Filter-Antenna Consisting of Conical FSS Radome and Monopole Antenna," *IEEE Transactions on Antennas and Propagation*, vol. 60, no. 6, pp. 3040–3045, June 2012.

[121] M. Niroo-Jazi and T. Denidni, "Electronically Sweeping-Beam Antenna Using a New Cylindrical Frequency-Selective Surface," *IEEE Transactions on Antennas and Propagation*, vol. 61, no. 2, pp. 666–676, Feb 2013.

[122] C. G. Ryan, M. Chaharmir, J. Shaker, J. Bray, Y. Antar, and A. Ittipiboon, "A Wideband Transmitarray Using Dual-Resonant Double Square Rings," *IEEE Transactions on Antennas and Propagation*, vol. 58, no. 5, pp. 1486–1493, May 2010.

[123] I. Russo, D. Gaetano, L. Boccia, G. Amendola, and G. Di Massa, "Investigation on the Transmission Beam-Steering Capabilities of Tunable Impedance Surfaces," in *EuMC 2009 European Microwave Conference*, Sept 2009, pp. 1033–1036.

[124] I. Russo, L. Boccia, G. Amendola, and G. Di Massa, "Tunable Pass-band FSS for Beam Steering Applications," in *2010 Proceedings of the Fourth European Conference on Antennas and Propagation (EuCAP)*, April 2010, pp. 1–4.

[125] L. Boccia, I. Russo, G. Amendola, and G. Di Massa, "Multilayer Antenna-Filter Antenna for Beam-Steering Transmit-Array Applications," *IEEE Transactions on Microwave Theory and Techniques*, vol. 60, no. 7, pp. 2287–2300, July 2012.

[126] W. Pan, C. Huang, P. Chen, M. Pu, X. Ma, and X. Luo, "A Beam Steering Horn Antenna Using Active Frequency Selective Surface," *IEEE Transactions on Antennas and Propagation*, vol. 61, no. 12, pp. 6218–6223, Dec 2013.

[127] M. Sazegar, Y. Zheng, C. Kohler, H. Maune, M. Nikfalazar, J. Binder, and R. Jakoby, "Beam Steering Transmitarray Using Tunable Frequency Selective Surface With Integrated Ferroelectric Varactors," *IEEE Transactions on Antennas and Propagation*, vol. 60, no. 12, pp. 5690–5699, Dec 2012.

[128] A. Alu and N. Engheta, "Evanescent Growth and Tunneling through Stacks of Frequency Selective Surfaces," *IEEE Antennas and Wireless Propagation Letters*, vol. 4, pp. 417–420, 2005.

[129] E. . C. A. Chambers. (2010) EB-100 – Eccosorb VHP-NRL – Very High Performance Broadband Pyramidal Absorber. [Available online].

[130] F. Microwave. Dual Polarized Horn Series DP241. [Online]. Available: https://flann.com/wp-content/uploads/2015/09/Series-DP241.pdf

[131] G. Masters and S. Gregson, "Coordinate System Plotting for Antenna Measurements," *AMTA Symposium*, 2007.

[132] N. P. Inc. Nelco N9000 PTFE Laminates - Park Advanced Circuitry Materials. [Online]. Available: http://elmechanics.com/pdf_manufacturers/100/N9000.pdf

[133] L. Kong, S. Li, T. Zhang, J. Zhai, F. Boey, and J. Ma, "Electrically Tunable Dielectric Materials and Strategies to Improve Their Performances," *Progress in Materials Science*, vol. 55, no. 8, pp. 840 – 893, 2010.

[134] G. H. Sung, K. W. Sowerby, M. J. Neve, and A. G. Williamson, "A Frequency-Selective Wall for Interference Reduction in Wireless Indoor Environments," *IEEE Antennas and Propagation Magazine*, vol. 48, no. 5, pp. 29–37, Oct 2006.

[135] N. Qasem and R. Seager, "Indoor Band Pass Frequency Selective Wall Paper Equivalent Circuit and Ways to Enhance Wireless Signal," in *2011 Loughborough Antennas Propagation Conference*, Nov 2011, pp. 1–4.

[136] Y. Z. Wenxing Li, Chunming Wang and Y. Li, "A Miniaturized Frequency Selective Surface Based on Square Loop Aperture Element," *International Journal of Antennas and Propagation*, vol. 2014, 2014.

[137] K. C. S. il Kwak and Y. J. Yoon, "Equivalent Circuit Modeling of Active Frequency Selective Surfaces," in *2008 IEEE Radio and Wireless Symposium*, Jan 2008, pp. 663–666.

[138] SKYWORKS. (2012, 6) Data Sheet SMV123x Series: Hyperabrupt Junction Tuning Varactors. [Available online]. [Online]. Available: http://www.skyworksinc.com/uploads/documents/SMV123x_Series_200058V.pdf

[139] Arduino. (2016, 1) Arduino micro datasheet. [Available online]. [Online]. Available: https://store.arduino.cc/arduino-micro

[140] A. Devices. (2016, 2) 5204/5206 datasheet. [Available online]. [Online]. Available: http://www.analog.com/media/en/technical-documentation/data-sheets/AD5204_5206.pdf

[141] T. Instruments. (2016, 2) LM345-N Datasheet. [Available online]. [Online]. Available: http://www.ti.com/lit/ds/symlink/lm348.pdf

[142] SEMTECH. Calculating Radiated Power and Field Strength for Conducted Power Measurements . [Online]. Available: https://www.semtech.com/uploads/documents/semtech_acs_rad_pwr_field_strength.pdf

[143] M. Andersson, B. Goransson, I. Skarin, K. From, S. Cheng, E. Ojefors, P. Hallbjorner, L. Manholm, and A. Rydberg, "Antennas with Fast Beam Steering for High Spectral Efficiency in Broadband Cellular Systems," in *2006 European Conference on Wireless Technology*, Sept 2006, pp. 12–15.

[144] Y. Ye, D. Wu, Z. Shu, and Y. Qian, "Overview of LTE Spectrum Sharing Technologies," *IEEE Access*, vol. 4, pp. 8105–8115, 2016.

[145] M. O. Kayali, Z. Shmeiss, H. Safa, and W. El-Hajj, "Downlink Scheduling in LTE: Challenges, Improvement, and Analysis," in *2017 13th International Wireless Communications and Mobile Computing Conference (IWCMC)*, June 2017, pp. 323–328.

[146] A. Mirkamali, R. Deban, F. Siaka, and J. J. Laurin, "Fast and Low-cost Beam Steering Using an Agile Mechanical Feed System for Exciting Circular Arrays," *IET Microwaves, Antennas Propagation*, vol. 10, no. 4, pp. 378–384, 2016.

[147] R. Bonjour, M. Singleton, S. A. Gebrewold, Y. Salamin, F. C. Abrecht, B. Baeuerle, A. Josten, P. Leuchtmann, C. Hafner, and J. Leuthold, "Ultra-Fast Millimeter Wave Beam Steering," *IEEE Journal of Quantum Electronics*, vol. 52, no. 1, pp. 1–8, Jan 2016.

[148] D. E. Anagnostou, G. Goussetis, D. Torres, and N. Sepulveda, "Ultra-fast Reconfigurable Antennas with Phase Change Materials," in *2017 International Workshop on Antenna Technology: Small Antennas, Innovative Structures, and Applications (iWAT)*, March 2017, pp. 146–147.

[149] I. Y. Lee and D. Im, "Low-power SOI CMOS Antenna Switch Driver Circuit RF Leakage Suppression and Fast Switching Time," *Electronics Letters*, vol. 53, no. 5, pp. 293–294, 2017.

[150] M. Shafi, A. F. Molisch, P. J. Smith, T. Haustein, P. Zhu, P. D. Silva, F. Tufvesson, A. Benjebbour, and G. Wunder, "5G: A Tutorial Overview of Standards, Trials, Challenges, Deployment, and Practice," *IEEE Journal on Selected Areas in Communications*, vol. 35, no. 6, pp. 1201–1221, June 2017.

[151] F.-L. Luo and C. Zhang, *Massive MIMO for 5G: Theory, Implementation and Prototyping*. Wiley-IEEE Press, 2016.

[152] D. Muirhead, M. A. Imran, and K. Arshad, "A Survey of the Challenges, Opportunities and Use of Multiple Antennas in Current and Future 5G Small Cell Base Stations," *IEEE Access*, vol. 4, pp. 2952–2964, 2016.

[153] S. Malkowsky, J. Vieira, L. Liu, P. Harris, K. Nieman, N. Kundargi, I. C. Wong, F. Tufvesson, V. Owall, and O. Edfors, "The World 2019s First Real-Time Testbed for Massive MIMO: Design, Implementation, and Validation," *IEEE Access*, vol. 5, pp. 9073–9088, 2017.

[154] C. Ribeiro and A. Gameiro, "A Software-defined Radio FPGA Implementation of OFDM-based PHY Transceiver for 5G," *Analog Integrated Circuits and Signal Processing*, vol. 91, no. 2, pp. 343–351, May 2017.

[155] 3GPPgroup. LTE – 3GPP webpage. [Online]. Available: http://www.3gpp.org/technologies/keywords-acronyms/98-lte

[156] A. Devices. AD-FMCOMMS3-EBZ User Guide. [Online]. Available: https://wiki.analog.com/resources/eval/user-guides/ad-fmcomms3-ebz

[157] ——. AD9361 RF Agile Transceiver. [Online]. Available: http://www.analog.com/media/en/technical-documentation/data-sheets/AD9361.pdf

[158] R. Gomes, Z. Al-Daher, A. Hammoudeh, K. Sobaihi, R. Caldeirinha, and T. Fernandes, "Performance and Evaluation of OFDM and SC - FDE over an AWGN Propagation Channel under RF Impairments Using Simulink at 60GHz," in *2014 Loughborough Antennas and Propagation Conference (LAPC)*, Nov 2014, pp. 685–689.

[159] H. A. Mahmoud and H. Arslan, "Error Vector Magnitude to SNR Conversion for Nondata-aided Receivers," *IEEE Transactions on Wireless Communications*, vol. 8, no. 5, pp. 2694–2704, May 2009.

[160] Agilent EEsof EDA. (2018) Presentation on Error Rate Simulations. [Online]. Available: http://literature.cdn.keysight.com/litweb/pdf/5989-9111EN.pdf

[161] R. Gomes, A. Hammoudeh, R. F. Caldeirinha, Z. Al-Daher, T. Fernandes, and J. Reis, "Towards 5G: Performance Evaluation of 60GHz UWB OFDM Communications under both Channel and RF impairments," *Physical Communication*, vol. 25, pp. 527 – 538, 2017.

[162] W. Wiesbeck, "The Radar of the Future," in *2013 European Radar Conference*, Oct 2013, pp. 137–140.

[163] W. Wiesbeck, L. Sit, M. Younis, T. Rommel, G. Krieger, and A. Moreira, "Radar 2020: The Future of Radar Systems," in *2015 IEEE International Geoscience and Remote Sensing Symposium (IGARSS)*, July 2015, pp. 188–191.

[164] J. Moghaddasi and K. Wu, "Multifunctional Transceiver for Future Radar Sensing and Radio Communicating Data-Fusion Platform," *IEEE Access*, vol. 4, pp. 818–838, 2016.

APPENDIX A

CST port model for the $N \times N$ dielectric slab model

This appendix presents and summarises, a set of simulations performed solely on the excitation port utilised in the CST MWS models of Section 4.4.3. The excitation port produces an impinging wave that illuminates a dielectric slab composed of $N \times N$ ideal dielectric elements of dimensions $p = t = 33$ mm.

Depending on the considered size of the $N \times N$ array, the excitation port vary proportionally in dimensions, as indicated in Table A.1.

The considered EM wave generated by the excitation port, produces in the far-field, the radiation patterns depicted in Fig. A.1. Those have their gain and main lobe direction and HPBW summarised in Table A.1.

These data may assist with the interpretation of the beamsteering radiation patterns of Table 4.4 in Section 4.4.3.

Table A.1
Far-field radiation pattern characteristics for excitation ports with different size.

$N \times N$ array	Port dimension	Main lobe			HPBW	
		$Az(^\circ)$	$El(^\circ)$	Gain (dBi)	$Az(^\circ)$	$El(^\circ)$
2×2	$66mm \times 66mm$	0	0	10.7	55	54.5
4×4	$132m \times 132mm$	0	0	16.6	30.2	24
6×6	$198mm \times 198mm$	0	0	20.3	18.5	16.8
8×8	$264mm \times 264mm$	0	0	22.8	11.5	15.3
10×10	$330mm \times 330mm$	0	0	24.8	12.3	9.1

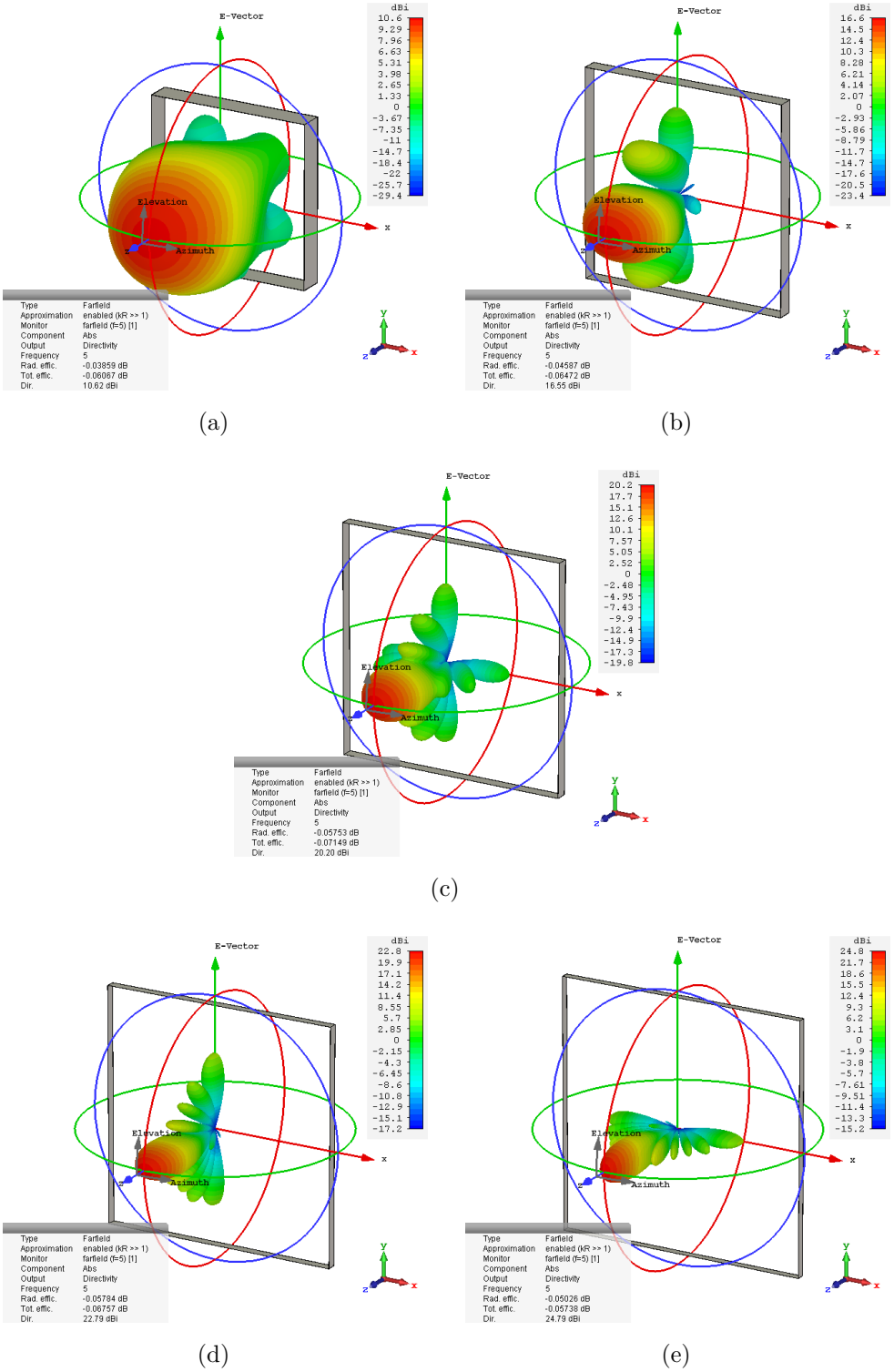

FIGURE A.1: (a-e) Snapshot of the far-field resultant from an excitation port that illuminates the dielectric slab with dimension of 2×2, 4×4, 8×8 and 10×10 elements of dimensions $p = t = 33$ mm.

APPENDIX B

Capacitors matrix for the FSS-inspired transmitarray

This appendix presents the capacitor values employed in the FSS transmitarray of Section 5.5.2, in simulations using the theorectical values given from the MATLAB script (C_{theory}) and, in experiments, using the nearest capacitor values available in the market (C_{real}), for the output angle directions defined by (Az, El): $(23°, 10°)$, $(0°, 25°)$ and $(25°, 0°)$, as follows:

Steering towards $(23°, 10°)$:

$$C_{theory} = \begin{bmatrix} 0.88 & 1.05 & 1.34 & 1.86 & 2.80 \\ 2.65 & 0.96 & 1.17 & 1.61 & 2.18 \\ 2.13 & 0.89 & 1.06 & 1.37 & 1.90 \\ 1.86 & 2.79 & 0.97 & 1.19 & 1.65 \\ 1.61 & 2.18 & 0.90 & 1.08 & 1.39 \end{bmatrix}, \quad (B.1)$$

$$C_{real} = \begin{bmatrix} 0.9 & 1.0 & 1.3 & 1.9 & 2.8 \\ 2.7 & 1.0 & 1.2 & 1.6 & 2.1 \\ 2.1 & 0.9 & 1.0 & 1.4 & 1.9 \\ 1.9 & 2.8 & 1.0 & 1.2 & 1.7 \\ 1.6 & 2.2 & 0.9 & 1.0 & 1.4 \end{bmatrix}, \quad (B.2)$$

Steering towards $(0°, 25°)$:

$$C_{theory} = \begin{bmatrix} 0,79 & 0,79 & 0,79 & 0,79 & 0,79 \\ 0,95 & 0,95 & 0,95 & 0,95 & 0,95 \\ 1,22 & 1,22 & 1,22 & 1,22 & 1,22 \\ 1,66 & 1,66 & 1,66 & 1,66 & 1,66 \\ 2,80 & 2,80 & 2,80 & 2,80 & 2,80 \end{bmatrix}, \quad (B.3)$$

$$C_{real} = \begin{bmatrix} 0.8 & 0.8 & 0.8 & 0.8 & 0.8 \\ 0.9 & 0.9 & 0.9 & 0.9 & 0.9 \\ 1.2 & 1.2 & 1.2 & 1.2 & 1.2 \\ 1.7 & 1.7 & 1.7 & 1.7 & 1.7 \\ 2.8 & 2.8 & 2.8 & 2.8 & 2.8 \end{bmatrix}, \quad (B.4)$$

Steering towards $(25°, 0°)$:

$$C_{theory} = \begin{bmatrix} 0,79 & 0,95 & 1,22 & 1,66 & 2,80 \\ 0,79 & 0,95 & 1,22 & 1,66 & 2,80 \\ 0,79 & 0,95 & 1,22 & 1,66 & 2,80 \\ 0,79 & 0,95 & 1,22 & 1,66 & 2,80 \\ 0,79 & 0,95 & 1,22 & 1,66 & 2,80 \end{bmatrix}, \quad (B.5)$$

$$C_{real} = \begin{bmatrix} 0.8 & 0.9 & 1.2 & 1.7 & 2.8 \\ 0.8 & 0.9 & 1.2 & 1.7 & 2.8 \\ 0.8 & 0.9 & 1.2 & 1.7 & 2.8 \\ 0.8 & 0.9 & 1.2 & 1.7 & 2.8 \\ 0.8 & 0.9 & 1.2 & 1.7 & 2.8 \end{bmatrix}, \quad (B.6)$$

This page is intentionally left blank.

APPENDIX C

PCB Schematics and Gerber Files

C.1 Beamsteering Controller Schematics

- Bottom Level;
- Middle Level;
- Top Level.

C.2 Beamsteering Controller Gerbers

To scale gerbers:

- Main board - top layer;
- Main board - bottom layer;
- Molex adaptor - top layer.

C.3 Transmitarray Gerbers

To scale gerbers

- 5×5 FSS-inspired transmitarray;
- Feeding network for the eRT.

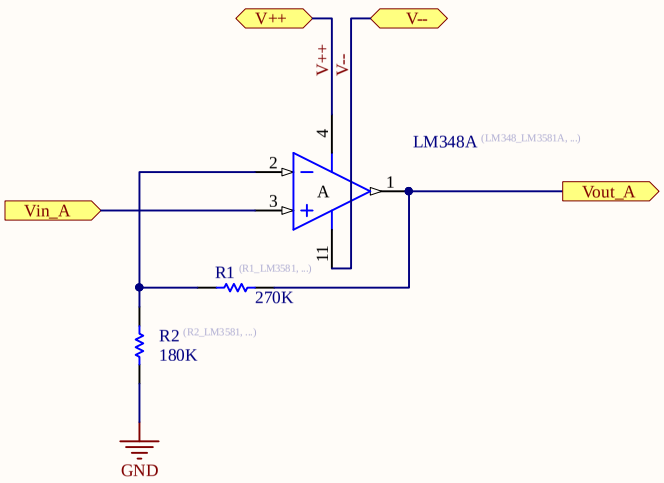

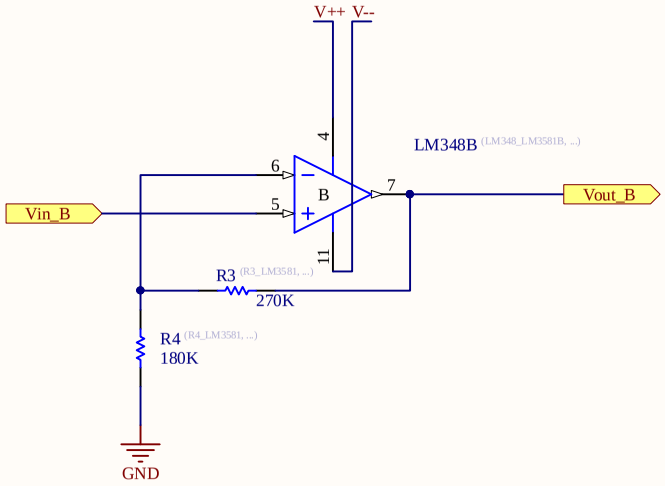

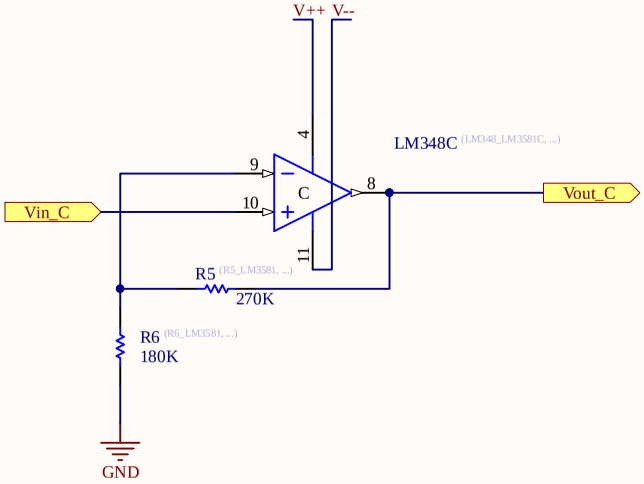

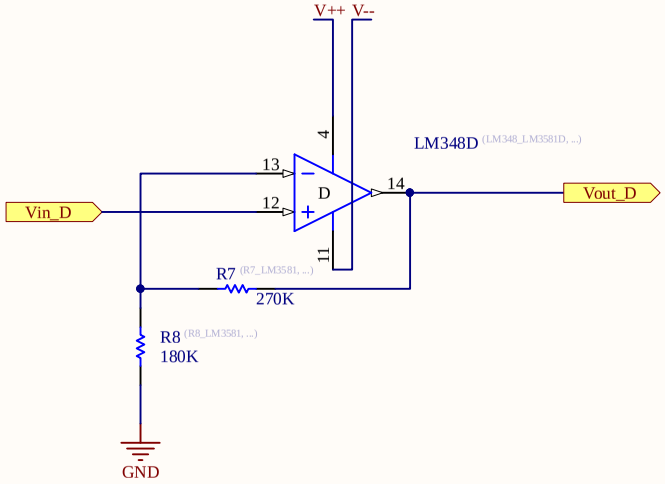

NON-INVERTING OPAMP

V+ = V-
Zo = inf

Vo = A (V+ - V-)

V- = R1/(R1+R2) * Vout

Vin = V+ = V-

Vout/Vin = A = (R1+R2)/R2 =
= (1 + R2/R1)

For:

R1= R3 = R5 = R7 = 270 kohm

and

R2 = R4 = R6 = R8 = 180 kohm

A = 2.5 (Gain)

Title: Bottom Level (LM358-N)		
Size: A4	Number:	Revision:
Date: 20/02/2018		Sheet of
File: D:\Dropbox\..\ampopstage.SchDoc		Drawn By:

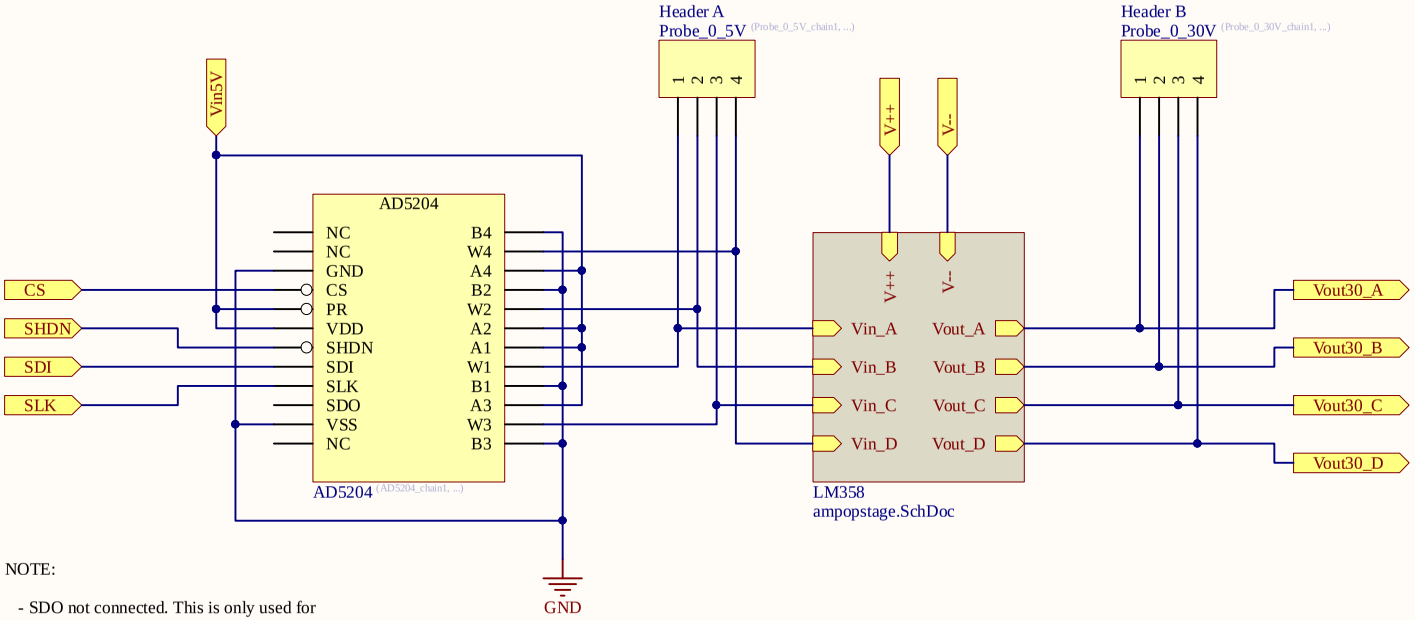

NOTE:

- SDO not connected. This is only used for daisy chain SPI communication not used in my case.
- PR connected to Vin5V (HIGH) to assure that is not reset at midscale (level=128). This avoid plus 8 Arduino pins

NOTE2:

- Quadruple AD5204 for a Quadruple LM348-N.

Title	Middle Level (AD5204 + LM358-N)		
Size A4	Number		Revision
Date:	20/02/2018	Sheet of	
File:	D:\Dropbox\..\TopLevel.SchDoc	Drawn By:	

Arduino to PCB interface (SPI)

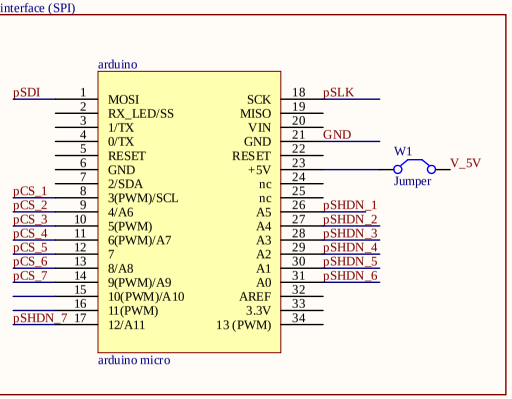

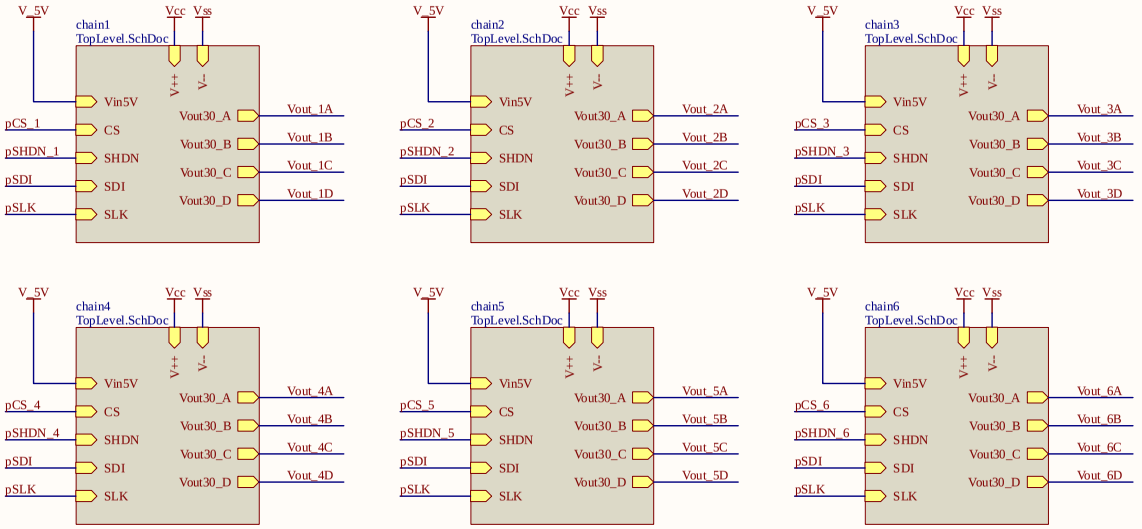

External 5V input

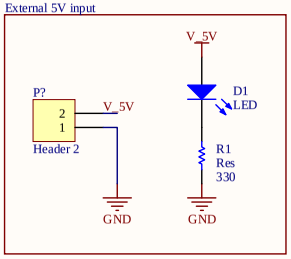

OPamp diff input

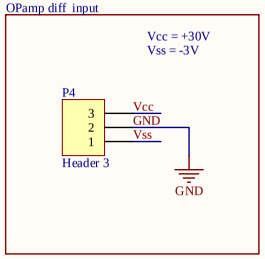

PCB to Transmitarray Interface (Molex flat cable)

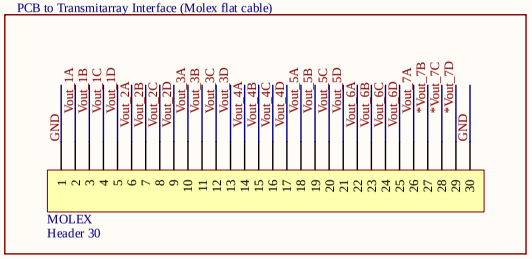

Current calculation in 5V rail:

Ipot = 60uA; Itotpot = 7 * 60 = 0.42mA;

Imaxwipper = I1tap = 5V/(100K/256) = 12.8mA; Itotwippers = 7*4*12.8mA = 0.3584A

Iled = 10mA;

Itotal = 0.36A;

NOTE:

- Quadruple AD5204 and LM348;
- Each component has 4 branchs. To achieve 25 outputs (Vouts) 7 IC's are being used.
- 3 Vout (7B, 7C and 7D) as reserve.

Title: Top Level		
Size: A3	Number:	Revision:
Date: 20/02/2018		Sheet of
File: D:\Dropbox\..\TopTopLevel.SchDoc		Drawn By:

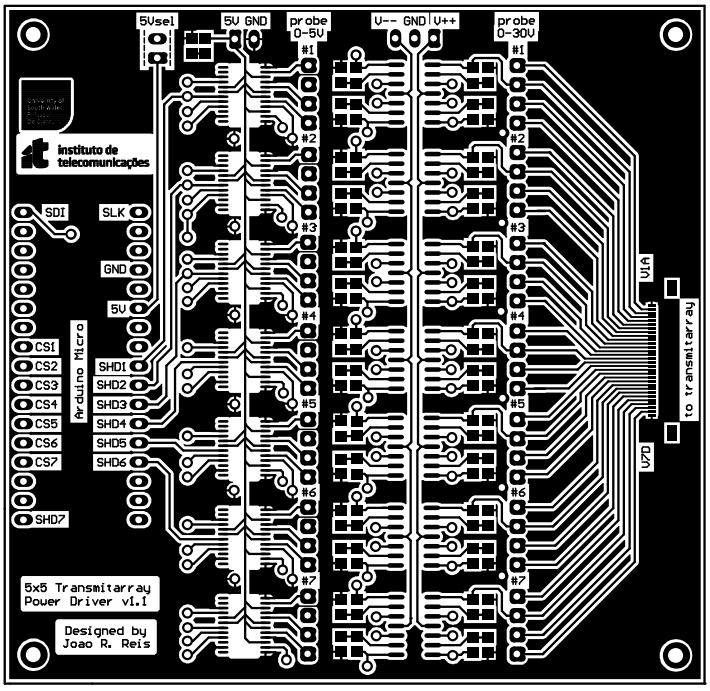

Main board - Top layer (to scale).

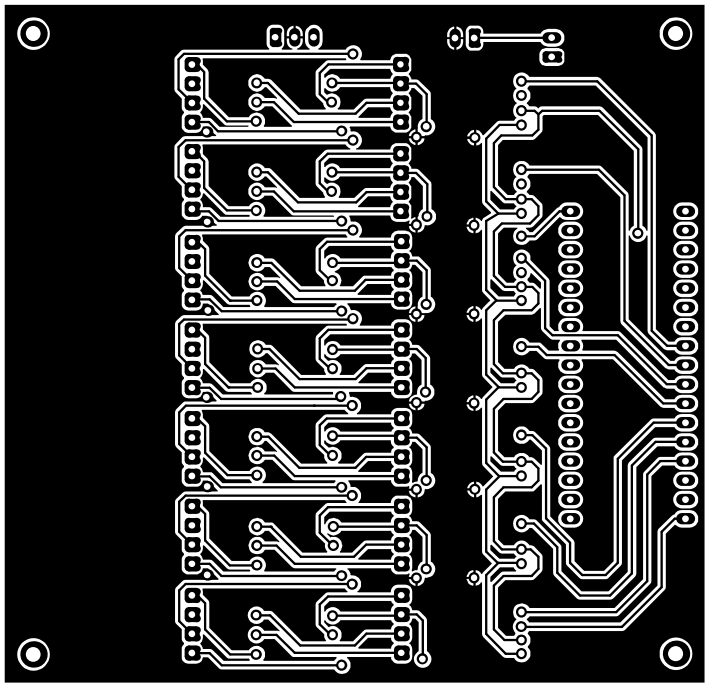

Main board - Bottom layer (to scale).

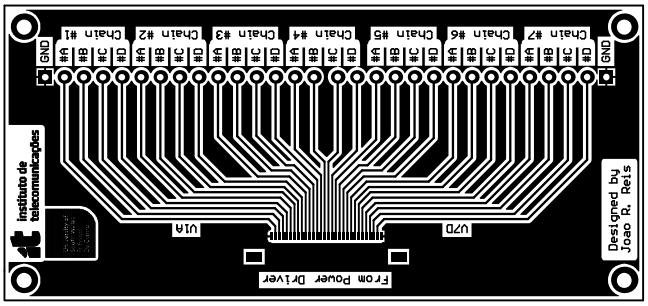

Molex adaptor - Top layer (to scale).

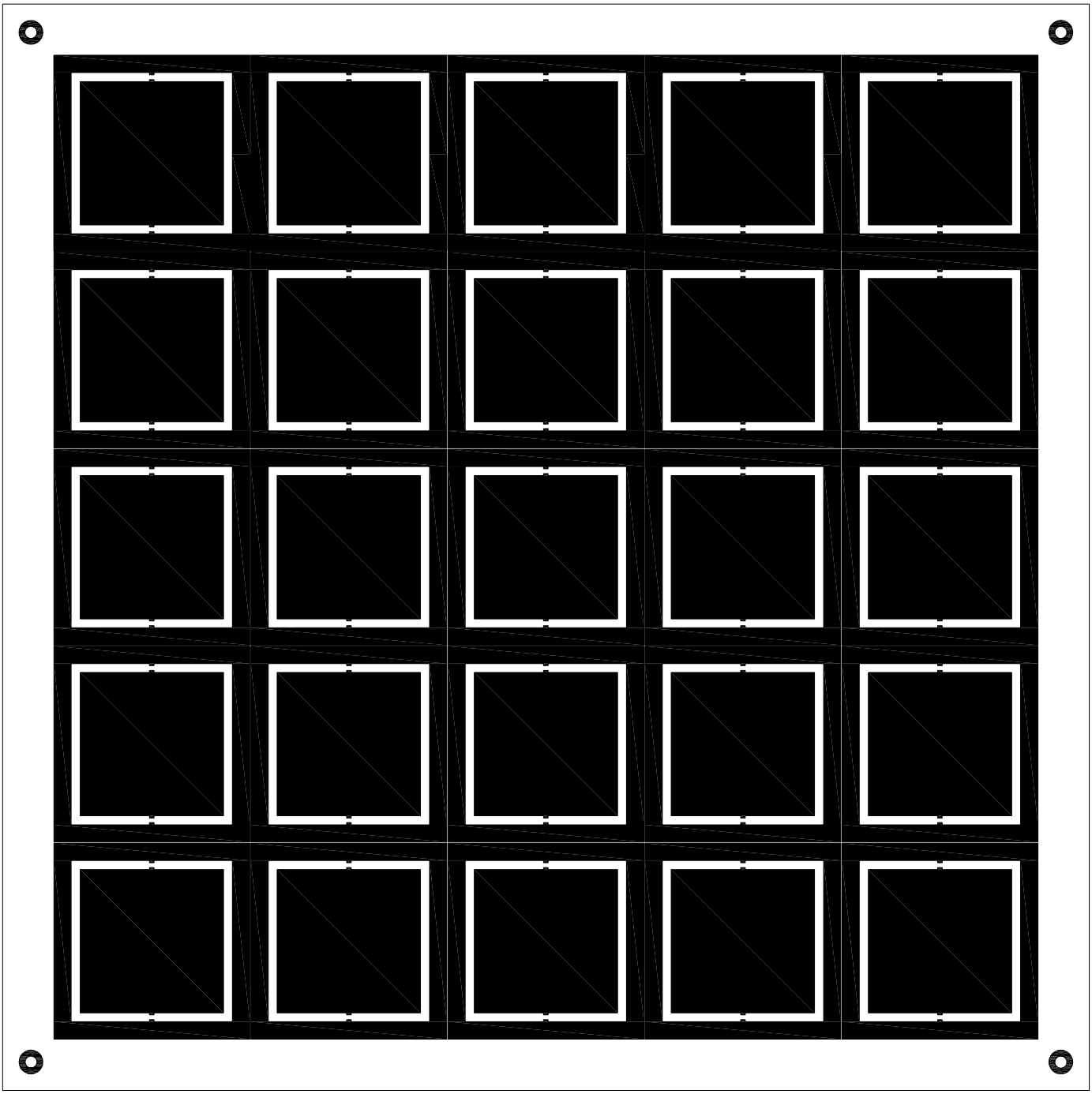

Transmitarray - Top layer (to scale).

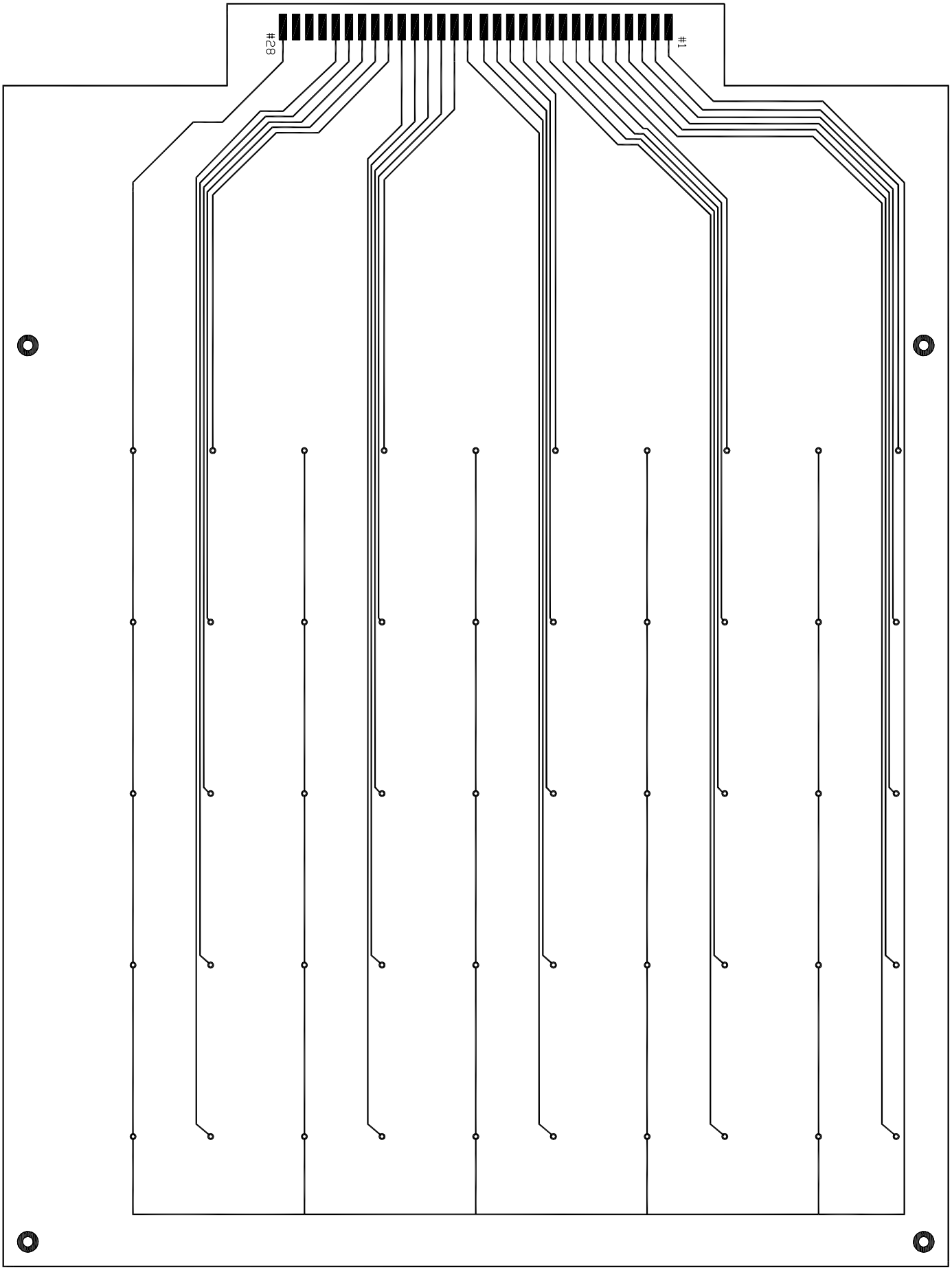

Feeding network - Top layer (to scale).

This page is intentionally left blank.